MAPPING CHANGES IN YELLOWSTONE'S GEOTHERMAL AREAS

by

Shannon Lea Savage

A dissertation submitted in partial fulfillment
of the requirements for the degree

of

Doctor of Philosophy

in

Ecology and Environmental Sciences

MONTANA STATE UNIVERSITY
Bozeman, Montana

August 2009

APPROVAL

of a dissertation submitted by

Shannon Lea Savage

This dissertation has been read by each member of the dissertation committee and has been found to be satisfactory regarding content, English usage, format, citation, bibliographic style, and consistency, and is ready for submission to the Division of Graduate Education.

Dr. Rick L. Lawrence
Dr. Stephan G. Custer

Approved for the Department of Land Resources and Environmental Sciences

Dr. Bruce D. Maxwell

Approved for the Division of Graduate Education

Dr. Carl A. Fox

STATEMENT OF PERMISSION TO USE

In presenting this dissertation in partial fulfillment of the requirements for a doctoral degree at Montana State University, I agree that the Library shall make it available to borrowers under rules of the Library. I further agree that copying of this dissertation is allowable only for scholarly purposes, consistent with "fair use" as prescribed in the U.S. Copyright Law. Requests for extensive copying or reproduction of this dissertation should be referred to ProQuest Information and Learning, 300 North Zeeb Road, Ann Arbor, Michigan 48106, to whom I have granted "the exclusive right to reproduce and distribute my dissertation in and from microform along with the non-exclusive right to reproduce and distribute my abstract in any format in whole or in part."

Shannon Lea Savage

August 2009

To my parents, whose support and
confidence have always lifted me up.

ACKNOWLEDGEMENTS

I would like to thank Rick Lawrence for his guidance, his support, his willingness to put up with my moodiness, and especially his confidence that I would be able to make this happen (from the beginning and through the difficult times). Steve Custer has provided excellent guidance and is my inspiration to find a job I am passionate about. My committee stuck with me even through my lowest points, so I extend tremendous gratitude to Dave Roberts and Dave Ward. Scott Powell agreed to join the committee at the last minute and provided excellent advice when I came to him with convoluted questions. Joe Shaw, who is officially my graduate representative, has been instrumental in my understanding of thermal remote sensing, and his knowledge and willingness to help has been greatly appreciated. I extend special thanks to Yellowstone National Park, and its geologists, Hank Heasler and Cheryl Jawrowski, who provided the funding for this project through a Cooperative Ecological Study Unit (CESU) agreement between Yellowstone National Park's Geology program and Montana State University (CESU task agreement number: J1580050584). My family and friends have been stellar support these past 3½ -years. Their encouragement and support always helped me face another day at the lab. I also appreciate the warmth, support, empathy, and sympathy that have been extended to me by my lab mates, Jennifer Watts, Natalie Campos, and Steve Jay. Finally, and most importantly, I thank Jeff, my favorite student, simply for being there – I'm not sure I could have done this without him.

TABLE OF CONTENTS

TABLE OF CONTENTS - CONTINUED

LIST OF TABLES

Table Page

LIST OF TABLES - CONTINUED

Table Page

LIST OF TABLES - CONTINUED

Table Page

LIST OF TABLES - CONTINUED

Table Page

LIST OF TABLES - CONTINUED

Table Page

LIST OF FIGURES

Figure Page

LIST OF FIGURES - CONTINUED

Figure Page

LIST OF FIGURES - CONTINUED

Figure Page

LIST OF FIGURES - CONTINUED

Figure Page

LIST OF FIGURES - CONTINUED

Figure Page

LIST OF FIGURES - CONTINUED

Figure Page

LIST OF FIGURES - CONTINUED

Figure Page

ABSTRACT

Yellowstone National Park (YNP) contains the world's largest concentration of geothermal features, and is legally mandated to protect and monitor these natural features. Remote sensing is a component of the current geothermal monitoring plan. Landsat satellite data have a substantial historical archive and will be collected into the future, making it the only available thermal imagery for historical analysis and long-term monitoring of geothermal areas in the entirety of YNP. Landsat imagery from Thematic Mapper (TM) and Enhanced Thematic Mapper Plus (ETM+) sensors was explored as a tool for mapping geothermal heat flux and geothermally active areas within YNP and to develop a change analysis technique for scientists to utilize with additional Landsat data available from 1978 through the foreseeable future.

Terrestrial emittance and estimates of geothermal heat flux were calculated for the entirety of YNP with two Landsat images from 2007 (TM) and 2002 (ETM+). Terrestrial emittance for fourteen summer dates from 1986 to 2007 was calculated for defined geothermal areas and utilized in a change analysis. Spatial and temporal change trajectories of terrestrial emittance were examined. Trajectories of locations with known change events were also examined. Relationships between the temporal clusters and spatial groupings and several change vectors (distance to geologic faults, distance to large water bodies, and distance to earthquake swarms) were explored. Finally, TM data from 2007 were used to classify geothermally active areas inside the defined geothermal areas as well as throughout YNP and a 30-km buffer around YNP.

Estimations of geothermal heat flux were inaccurate due to inherent limitations of Landsat data combined with complexities arising from the effects of solar radiation and spatial and temporal variation of vegetation, microbes, steam outflows, and other features at each geothermal area. Terrestrial emittance, however, was estimated with acceptable results. The change analysis showed a relationship between absolute difference in terrestrial emittance and earthquake swarms, with 34% of the variation explained. Accuracies for the classifications of geothermally active areas were poor, but the method used for classification, random forest, could be a suitable method given higher resolution thermal imagery and better reference data.

CHAPTER 1

INTRODUCTION

The greatest concentration of geysers, hot springs, fumaroles, and mud pots in the world are found in Yellowstone National Park (YNP), in Wyoming, Montana, and Idaho, USA (Waring *et al*., 1983). Millions of people visit YNP every year to see the natural wonders therein, including a wide variety of wildlife, beautiful landscapes, and a stunning array of geothermal features, not the least of which is the well-known Old Faithful Geyser. Not only is YNP a popular tourist attraction, but it is a one-of-a-kind scientific laboratory that the National Park Service is mandated to preserve, protect, and monitor.

Hundreds of scientists have studied and continue to study the geothermal features in hopes of new and exciting scientific discoveries. One well-known discovery was that of *Thermus aquaticus*, a heat-loving microbe found in several springs in YNP, including Mushroom Spring and Perpetual Spouter (Brock and Freeze, 1969). *Thermus aquaticus* was instrumental in the development of an important technique for DNA research, the polymerase chain reaction (often referred to as PCR), a process that has applications ranging from crime-scene forensics to diagnosis of diseases and is a multimillion dollar making patent (Brock, 1997). Many more important discoveries might be waiting in the heated waters spread throughout YNP.

Over 12,000 geothermal features exist in YNP and over 6,300 ha are classified as geothermally active areas within its boundaries. Changes in the hydrogeothermal flow in

these areas are expressed on the surface as the appearance and disappearance of geothermal features. An unnamed spring, for instance, appeared next to Narrow Gauge Spring in Mammoth Hot Springs during the summer of 1998 and Brimstone Basin became dormant (Langford, 1972; Nordstrom *et al.*, 2009). Understanding the patterns of spatial change in the geothermal areas of YNP is important for scientists and managers, both from the perspective of understanding changes in the system as a whole and potentially for assessment of visitor safety. Spatial changes, however, are difficult to monitor on a regular basis over an area as large as YNP and the surrounding geothermally active areas. Not only might changes in geothermal activity within YNP be interconnected with impacts on geothermal features outside YNP (such as potential geothermal energy development in the Corwin Springs, Montana, and Island Park, Idaho known geothermal resource areas), but there is not enough time, personnel, or money to visit every geothermal area in YNP on an annual basis – or even on a decadal basis.

Remote sensing is a proven technique for mapping change over large areas. Remote sensing uses satellite or airborne imagery to collect information over great expanses of land. Landsat satellite imagery is often used for mapping large areas. Landsat data cover the entire globe and are available from 1972 to the present and will be available into the foreseeable future (NASA, 2009). Two Landsat satellites are currently in orbit collecting data: Landsat 5 with the Thematic Mapper sensor (TM) and Landsat 7 with the Enhanced Thematic Mapper Plus sensor (ETM+). A third satellite, Landsat 8, is expected to be launched into orbit in 2012. One Landsat scene covers the entirety of YNP (a swath of 185 km), and the TM and ETM+ sensors collect information from

reflective (visible, near infrared, and middle infrared) and emitted (thermal infrared) bands of the electromagnetic spectrum every 16 days, making it an ideal source of imagery for monitoring geothermal areas over time in YNP. These data have the potential to classify geothermally active areas, estimate geothermal heat flux (GHF) (the convective heat change in water and steam in geothermal systems), and analyze patterns of spatial change in these geothermal elements in YNP (Oppenheimer *et al*., 1993; Harris *et al*., 1998; Watson *et al.*, 2008).

The development of an inexpensive, accurate, reproducible, and automated procedure for mapping geothermally active areas and geothermal heat flux across political boundaries at a scale useful for YNP-wide studies might open doors for many more important geothermal and ecological studies in YNP. Scientists and managers would be able to monitor the landscape, observe spatial and temporal changes, and make scientifically sound management decisions appropriate for visitor safety, preservation of geothermal features in geothermally active areas, and research planning.

The first goal of this project was to evaluate the utility of Landsat TM and ETM+ thermal imagery for monitoring GHF within the boundaries of YNP, examined in Chapter 2. A second goal was to conduct a change analysis of the spatial distribution of terrestrial emittance within YNP's defined geothermal areas over two decades, examined in Chapter 3. The final goal was to assess the ability of Landsat TM imagery combined with random forest and target detection classification methods to classify geothermally active areas accurately within YNP's defined geothermal areas as well as throughout

YNP and 30-km beyond its boundary, examined in Chapter 4. Chapter 5 provides a summary of this dissertation.

Literature Cited

Brock, T.D. 1997. The value of basic research: Discovery of *Thermus aquaticus* and other extreme thermophiles. *Genetics*, 146(5): 1207-1210.

Brock, T.D. and H. Freeze. 1969. *Thermus aquaticus* gen. n. and sp. N., a non-sporulating extreme thermophile. *Journal of Bacteriology*, 98(1): 289-297.

Harris, A.J.L., L.P. Flynn, L. Keszthelyi, P.J. Mouginis-Mark, S.K. Rowland, and J.A. Resing. 1998. Calculation of lava effusion rates from Landsat TM data. *Bulletin of Volcanology*, 60(1): 52-71.

Langford, N.P. 1972. The Discovery of Yellowstone Park: Journal of the Washburn Expedition to the Yellowstone and Firehole Rivers in the Year 1870. University of Nebraska Press, Lincoln, Nebraska, 125 pp.

NASA. 2009. The Landsat Data Continuity Mission. Last accessed on 28 March 2009. http://ldcm.nasa.gov/about.html.

Nordstrom, D.K., R.B. McCleskey, and J.W. Ball. 2009. Sulfur geochemistry of hydrothermal waters in Yellowstone National Park: IV Acid-sulfate waters. *Applied Geochemistry*, 24(2): 191-207.

Oppenheimer, C., D.A. Rothery, and P.W. Francis. 1993. Thermal distributions at fumarole fields: implications for remote sensing of active volcanoes. *Journal of Volcanology and Geothermal Research*, 55(1-2): 97-115.

Waring, G.A., R.R. Blankenship, and R. Bentall. 1983. Thermal springs of the United States and other countries of the world – a summary. U.S.G.S. Professional Paper 492, U.S. Geological Survey, Alexandria, Virginia, 401 pp.

Watson, F.G.R., R.E. Lockwood, W.B. Newman, T.N. Anderson, and R.A. Garrott. 2008. Development and comparison of Landsat radiometric and snowpack model inversion techniques for estimating geothermal heat flux. *Remote Sensing of Environment*, 112(2): 471-481.

CHAPTER 2

EVALUATING THE USE OF LANDSAT IMAGERY FOR MAPPING HEAT FLOW IN YELLOWSTONE NATIONAL PARK

Introduction

Yellowstone National Park (YNP), located in Wyoming, Montana, and Idaho, became the world's first national park primarily because of its geothermal features. The land was set aside for the "benefit and enjoyment of the people" and to "provide for the preservation from injury or spoliation of all timber, mineral deposits, natural curiosities, or wonders within said park, and their retention in their natural condition" (Yellowstone Park Act, 1872). Currently there are recognized threats to the geothermal features of YNP, including potential geothermal development in Idaho and Montana, and oil, gas, and groundwater development in Wyoming, Montana, and Idaho (Sorey, 1991; Custer *et al.*, 1993; Heasler *et al.*, 2004). The National Park Service (NPS) is legally mandated to monitor and protect geothermal features within its units, and YNP in and of itself is listed as a significant geothermal feature (Geothermal Steam Act, 1970 as amended in 1988).

Geothermal heat flux (GHF) is the heat change in water and steam in geothermal systems and is radiated, or emitted, from the surface of the Earth. It represents only heat coming from below the surface and it does not include any accumulated indirect or direct solar heating effects such as convection from air currents, and conduction of solar effects on soil (indirect), or solar heating due to variations in topography such as south-facing slopes (direct). GHF can be measured from bore holes (Sorey, 1991), by estimation from

other indirect measurements such as chloride flux (Fournier *et al.*, 1975; Norton and Friedman, 1985; Friedman and Norton, 2007), or by utilizing thermal sensors (Boomer *et al.*, 2002). Terrestrial emittance represents the heat emitted from the ground and is composed of GHF and includes direct and indirect solar radiation effects.

Chloride flux has been used as a proxy to determine GHF in YNP (Fournier *et al.*, 1975; Norton and Friedman, 1985; Friedman and Norton, 2007). Measurements of the rate of flow and chloride content of rivers draining hot spring areas have been made at U.S. Geological Survey (USGS) gauging stations located throughout YNP since 1966 These measurements were used to calculate heat flow in various regions of YNP. The GHF of YNP has been estimated to be 1,800 mWm^{-2}, thirty times the continental average (Fournier *et al.*, 1975; Smith and Siegel, 2000; Waite and Smith, 2002).

More recently, on October 9, 2002, two airborne multi-spectral imagery data sets were acquired of the Norris Geyser Basin area (one flight near solar noon and the other at night) (Hardy, 2005; Seielstad and Queen, 2009). These data were collected to identify, classify, and map geothermal features. Five spectral bands were acquired and utilized in the image processing: one thermal infrared (TIR), one near infrared (NIR), and three from the visible portion of the electromagnetic spectrum (EMS). The developed methods demonstrated that a geothermal gradient could be classified, mapped, and defined using high-resolution airborne thermal imagery. These methods, however, are currently impractical to apply to the entirety of YNP due to time and cost constraints. Researchers at the University of Montana are continuing this project by testing additional airborne remote sensing methods at Norris Geyser Basin and surrounding areas, while researchers

at Utah State University are testing other airborne methods at Upper Geyser Basin and surrounding areas.

Multispectral Landsat satellite imagery has been used to map geothermal heat and activity in a variety of situations. Landsat Thematic Mapper (TM) and Enhanced Thematic Mapper Plus (ETM+) imagery have been used successfully to map and analyze volcanic features (Andres and Rose, 1995; Kaneko and Wooster, 1999; Flynn *et al.*, 2001; Urai, 2002; Patrick *et al.*, 2004). Many studies have used TM and ETM+ data to map lineaments (*e.g.*, fault lines) as part of the process of finding geothermal areas (Bourgeois *et al.*, 2000; Song *et al.*, 2005) and to map minerals such as iron oxide and hydrothermally altered soil (Carranza and Hale, 2002; Daneshfar *et al.*, 2006; Dogan, 2008).

Landsat thermal imagery, however, has rarely been used to assess the spatial distribution of GHF in YNP, and in one instance, only one image was used for a snapshot of GHF (Watson *et al.*, 2008). The method developed by Watson *et al.*, 2008 to quantify the intensity of surficial geothermal activity at YNP, was developed with 2000 Landsat ETM+ imagery, and the results suggested good potential for geothermal monitoring. Thermal radiance data from ETM+ imagery were utilized to estimate terrestrial emittance. Estimates of non-geothermal-related heat were incorporated with terrestrial emittance to subsequently measure and create a map of continuous variations in residual terrestrial emittance (*i.e.*, no solar effects) that was hypothesized to estimate a lower bound for GHF.

The Watson *et al.*, 2008 method utilized a spectral library of "light yellowish brown loamy sand" from the NASA Jet Propulsion Laboratory (JPL) to estimate a single emissivity value for the entire image. This method might be improved upon by assigning emissivity on a pixel-by-pixel basis rather than using a single value. Emissivity can be estimated from a Normalized Difference Vegetation Index (NDVI) that uses the red and NIR Landsat bands to represent amounts of healthy green vegetation (Brunsell and Gillies, 2002). The estimated emissivity can be applied to the calculation of terrestrial emittance, and thus to estimations of GHF.

Landsat data can be valuable for calculation of GHF in YNP. The method suggested in this paper is not highly parameterized – it requires only three Landsat bands and some atmospheric correction coefficients. Emissivity is incorporated per pixel rather than as one value across the entire image, potentially increasing the precision of the GHF calculations. Finally, one Landsat image covers the entire area of YNP. Landsat data provide the means to calculate GHF for all of YNP and has the potential to enable scientists to identify locations that might need to be studied in more depth.

Using Landsat data to estimate GHF presents many challenges. Solar radiation and related topographic effects have substantial impacts on total emittance calculations since, for example, south-facing slopes that have no GHF will often have high terrestrial emittance values (Watson, 1975; Kohl, 1999; Gruber *et al.*, 2004). The effect of surface albedo is also an important component and problematic in the calculation of GHF, because dark areas such as large parking lots (*e.g.*, in the Old Faithful area) or recently burned areas absorb and re-emit large amounts of solar radiation than bright surfaces,

resulting in high terrestrial emittance readings that might not include a GHF component (Watson, 1975; Coolbaugh *et al.*, 2007).

The Landsat ETM+ sensor is superior to the Landsat TM sensor because its thermal sensor is kept calibrated by a more stable radiative cooler and it has finer spatial resolution (NASA, 2009). There are only four years of complete data available from Landsat ETM+, while Landsat TM is 25 years old and its thermal sensor has deteriorated over the years. This deterioration also might make changes in GHF more difficult to detect. The pixel resolution for both ETM+ (60 m) and TM (120 m) thermal data is much coarser than for the reflective data from both sensors (30 m). When one pixel is 60 m on a side (3,600 m^2) or 120 m on a side (14,400 m^2), effects from small geothermal features or areas are averaged over the pixel. Also, due to the large pixel size it is impractical to accurately calibrate to ground temperatures collected at a single point, and impossible to do with historical imagery.

The main purpose of this project was to evaluate the utility of Landsat TM and ETM+ thermal data for monitoring GHF. An effective method would enable the calculation of terrestrial emittance and GHF covering the entirety of YNP that could be applied to additional Landsat images for use in monitoring and change analyses. Previous studies in YNP have been for a single date and/or over limited geographic areas.

Methods

Study Area

YNP encompasses approximately 890,000 ha (Figure 2.1). Elevation ranges from 1,567 m to 3,458 m (Spatial Analysis Center, 1998). Vegetation includes grassland, brushland, and forest, with bare ground interspersed. Average precipitation is 25-30 cm in the lower elevations and up to 203 cm in the higher elevations (Spatial Analysis Center, 2000), with warm, dry summers and cold, wet winters (Western Regional Climate Center, 2005).

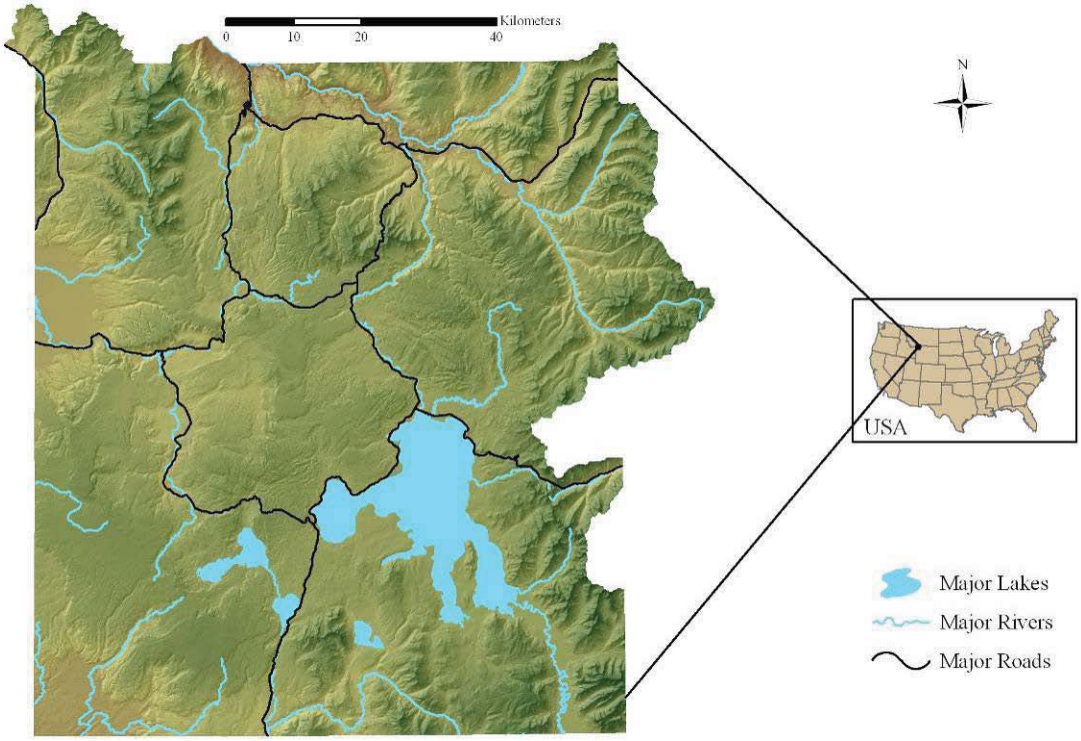

Figure 2.1: Location map for Yellowstone National Park displayed with a shaded relief background.

Data Acquisition

YNP is centered within one Landsat scene at Path 38 Row 29. A TM scene from 25 June 2007 was acquired from the USGS Earth Resources Observation and Science (EROS) Data Center and an ETM+ scene from 5 July 2002 was acquired from MontanaView (MontanaView, 2008). These scenes were chosen because they were the most recent, complete, mostly cloud-free (less than 5%) summer scenes available for each sensor.

Landsat data are now available for free download from the USGS EROS Data Center. Landsat TM data are available from July 1982 to present, while ETM+ data are available in complete form from April 1999 until May 2003 (prior to the failure of the scan line corrector) and with scan line gaps from the end of May 2003 to present. The TM images, despite 25 years of sensor degradation, are commonly used as replacements for ETM+ data after May 2003.

TM and ETM+ satellite sensors collect data in seven spectral bands, one of which is in the TIR portion of the EMS (10.4 to 12.5 μm). The TM instrument collects TIR data in 120-m pixels, while the ETM+ instrument collects TIR in 60-m pixels. Both TM and ETM+ TIR data are provided as 60-m pixels from the EROS Data Center. Both instruments collect the remaining six spectral bands in 28.5-m pixels (resampled to 30 m by 30 m on a side, or 900 m^2, by EROS Data Center). In addition the ETM+ instrument collects a panchromatic band in 15-m pixels.

Image Preprocessing

Each image was clipped to the YNP boundary. Clouds and cloud shadows were masked by on-screen digitizing. Elevations greater than 2,700 m were masked to remove snow from the input data. The COSine Transformation (COST) (Chavez, 1996) method of dark object subtraction atmospheric and radiometric correction was applied to the original raw data values of the six reflective bands of each image. The original Landsat raw data values are represented by digital numbers (or DNs) with values from 0 to 255 (8-bit radiometric resolution). The dark object DN values were chosen by examining the image histogram for each of the six reflective bands. The DN value where the histogram increased to more than 100 pixels was assigned the dark object value. These values along with information from the Landsat header files were used to convert the images to surface reflectance values for Landsat bands 1, 2, 3, 4, 5, and 7 at a 30-m pixel size (Utah State University, 2008).

NDVI was used to estimate fractional vegetation (Fr, unitless) based on the method by Brunsell and Gillies (2002). Fractional vegetation represents the percentage of vegetation within a pixel and is derived from NDVI as follows:

$$Fr = [(NDVI - NDVI_0)/(NDVI_{max} - NDVI_0)]^2 \quad (2.1)$$

where $NDVI_0$ represents bare soil and $NDVI_{max}$ represents scene-specific maximum vegetation. Assuming average broad-band emissivity for bare soil of 0.97 (from the "light yellowish brown loamy sand" and "white gypsum dune sand" JPL spectral libraries (NASA, 2008)) and emissivity for vegetation of 0.98 (from the "coniferous vegetation"

JPL spectral library (NASA, 2008)), emissivity (ε, unitless) per pixel (excepting water pixels) was estimated from the Fr:

$$\varepsilon = Fr*\varepsilon_v + (1 - Fr)*\varepsilon_s \quad (2.2)$$

where ε_v represents vegetation emissivity and ε_s represents soil emissivity. Water pixels were assigned an average broad-band emissivity value of 0.99 (Shaw and Marston, 2000). To match the lower-resolution TIR imagery, the resulting emissivity image was subsequently degraded to 60-m and 120-m pixels by averaging the 30-m pixel values.

Potential annual direct incident solar radiation (SR) was calculated from a 30-m digital elevation model (DEM) of the study area (McCune and Keon, 2002) to take solar effects into account. This equation incorporated the slope, aspect, and latitude of the terrain and returns SR in units of MJ cm^{-2} yr^{-1}:

$$SR = 0.339 + 0.808(\cos(L)*\cos(S)) - 0.196(\sin(L)*\sin(S)) - 0.482(\cos(A)*\sin(S)) \quad (2.3)$$

where L = latitude in radians, S = slope in radians, and A = folded aspect in radians east of north (this rescales 0-360° to 0-180°, so NE = NW, E = W, and so on, so that north/south contrasts would be emphasized, a critical issue in the Yellowstone ecosystem (Parmenter *et al.*, 2003)). The output values were multiplied by 316.89 $Js^{-1}m^{-2}$ to arrive at SR in Wm^{-2}. This image was degraded to 60-m and 120-m pixel images.

Albedo was calculated from five of the six reflective Landsat bands (Liang, 2000). The green band (band 2) was excluded because it does not improve the R^2 of the

regression test presented in Liang (2000). The surface reflectance values calculated from the DNs were applied to the following shortwave albedo calculation (unitless):

$$\alpha_{short} = 0.356\alpha_1 + 0.130\ \alpha_3 + 0.373\ \alpha_4 + 0.085\ \alpha_5 + 0.072\ \alpha_7 - 0.0018 \quad (2.4)$$

where $\alpha_{\#}$ refers to the Landsat band (Liang, 2000).

GHF Calculation Procedures

The raw TIR data (band 6) for each image were converted to at-satellite radiance (L_λ, $Wm^{-2}sr^{-1}\mu m^{-1}$) using published calibration factors (Chander *et al.*, 2009). Radiance was converted to top-of-atmosphere emittance (M_{toa}, Wm^{-2}) by integrating over the bandwidth (from 10.4 μm to 12.5 μm = 2.1 μm) and the projected solid angle of the hemisphere (π sr):

$$M_{toa,\ 6H} = 2.1\pi L_\lambda \quad (2.5)$$

MODerate resolution atmospheric TRANsmission (ModTran) was utilized to estimate atmospheric transmittance (τ) and upwelling atmospheric emittance (M_{up}, Wm^{-2}) for a "Mid Latitude Summer" model atmosphere (Ontar Corporation, 2001). Following the Watson method (Watson *et al.*, 2008), surface emittance integrated over band 6 ($M_{surf,\ 6H}$, Wm^{-2}) was estimated:

$$M_{surf,6H} = (M_{toa,6H} - M_{up})/\tau \quad (2.6)$$

where $M_{up} = 4.64\ Wm^{-2}$ and $\tau = 89.39\%$. The fitted coefficients from Watson's regression model were utilized to estimate broad-band surface emittance (M_{surf}, Wm^{-2}):

$$M_{surf} = (0.004812M_{surf,6H})^2 + 2.653M_{surf,6H} + 181.8 \quad (2.7)$$

Terrestrial emittance (M_{terr}, Wm^{-2}) was estimated using the NDVI-derived emissivity values and downwelling atmospheric emittance (M_{down}, Wm^{-2}) calculated with ModTran for a "Mid Latitude Summer" model atmosphere:

$$M_{terr} = M_{surf} - (1 - \varepsilon)M_{down} \quad (2.8)$$

where ε ranges from 0.97 to 0.99, and $M_{down} = 240\ Wm^{-2}$.

Estimates of GHF were calculated in three different ways. The first estimate utilized the mean M_{terr} value for non-geothermal ground within YNP for each date (mean $M_{terr,NG}$) based on the defined geothermal area boundaries (defined by staff at YNP and based on locations of geothermal features and geothermally influenced ground) (Spatial Analysis Center, 2005). By subtracting the mean non-geothermal value, the resulting positive values should on average represent geothermal heat:

$$GHF_M = M_{terr} - \text{mean } M_{terr,NG} \quad (2.9)$$

Based on the assumption that solar radiation directly and indirectly heats the ground and can be confused with geothermal heat emitted from the ground, a second estimate of GHF was calculated for each image to account for solar effects:

$$GHF_{SR} = M_{terr} - SR \quad (2.10)$$

A third estimate of GHF was calculated by incorporating albedo into equation 2.8 so that locations with low albedo and high absorption of solar radiation, for instance a recent fire scar, would not result in falsely high GHF:

$$GHF_{\alpha} = M_{terr} - (SR * (1 - \alpha_{short})) \quad (2.11)$$

where $1 - \alpha_{short}$ is absorption based on Kirchoff's law (Elachi, 1987).

Field validation of these equations was not conducted because precise field measurement of GHF would require multiple samples at each test site and an extensive number of test sites throughout the study area, many of which have limited access because of safety and resource protection issues. The results of the equations, however, could be evaluated in several ways for reasonableness. First, summary statistics of the four methods, M_{terr}, GHF_M, GHF_{SR}, and GHF_{α}, were calculated for each date. Values of all pixels within the defined geothermal areas were compared to the 57-year average annual air temperature of YNP (4.64 °C, or 337.6 Wm^{-2}) (Western Regional Climate Center, 2005) to ascertain which method had the most pixels above that average. Second, the 2002 image was subtracted from the 2007 image for each method so the range of change between years could be observed. The differenced images were also visually inspected to determine the extent to which each method accounted for solar effects. Third, the hottest 10% and coolest 10% of the pixels within YNP were calculated, mapped, and visually evaluated for spatial patterns. These hottest and coolest pixels were also clipped to the defined geothermal areas in order to evaluate which method contained the most of the hottest pixels and the least of the coolest pixels within areas that are

expected to be mostly hot. Fourth, the number of the top 10% hottest pixels in which points from the Thermal Inventory Project fell was tabulated for two of the four methods (M_{terr} and GHF_{α}) to find which method corresponded most to geothermal feature locations (the Thermal Inventory Project is a multi-year National Park Service-sponsored project with the goal of collecting a precise GPS measurement of every geothermal feature in YNP, with over 12,000 points collected thus far). Fifth, the mean value of three of the four methods (M_{terr}, GHF_{SR}, and GHF_{α}) was calculated for all areas within YNP but outside the defined geothermal areas and again for only pixels within the defined geothermal areas. The differences between the means of the defined geothermal area pixels and those outside the defined geothermal areas were calculated and compared among methods to determine which showed the largest difference and thus had more hot pixels within the defined geothermal areas.

Comparison to Airborne Data

The M_{terr} values for the July 2002 image in the Norris Geyser Basin area were compared to the summary statistics and heat flow values from a nighttime airborne thermal image of the same area from October 2002 (Hardy, 2005; Seielstad and Queen, 2009). The Hardy (2005) data originally had a pixel resolution of 0.76 m on a side. These pixels were degraded to 60 m on a side to match the Landsat data. Two extents were examined: (1) the entire extent of the Hardy data, and (2) the boundary of Norris Geyser Basin according to the defined geothermal areas (Spatial Analysis Center, 2005). Summary statistics and total heat flow were calculated for the four images and compared.

Results

GHF in YNP

The 2002 ETM+ mean M_{terr} value for non-geothermal areas in YNP was 368.7 Wm^{-2}, while the 2007 TM mean M_{terr} value for non-geothermal areas in YNP was 353.0 Wm^{-2}. SR values in YNP ranged from 0.0 to 363.0 Wm^{-2} with a mean of 275.0 Wm^{-2}. Albedo values for YNP in 2002 ranged from 0.0 to 0.6 and from 0.0 to 0.5 in 2007.

The calculated maximum and mean values for the four methods were higher in 2002 than 2007 for all but GHF_M (Tables 2.1 and 2.2). The calculated minimum values were all higher in 2002. The M_{terr}, GHF_{SR}, and GHF_{α} mean values in 2002 were approximately 13-16 Wm^{-2} greater than in 2007. The GHF_M values in 2007, on the other hand, were slightly higher than the 2002 values (approximately 1.0 Wm^{-2}). The 2002 M_{terr} values were the hottest overall, while the 2002 GHF_M values were the coolest overall. The widest range of values was observed in the 2002 GHF_{α} at 363.2 Wm^{-2}, with the next widest range in the 2002 GHF_{SR} at 352.1 Wm^{-2}.

Table 2.1: Summary statistics for terrestrial emittance (M_{terr}), mean non-geothermal value corrected geothermal heat flux (GHF_M), potential annual direct incident solar radiation corrected geothermal heat flux (GHF_{SR}), and albedo and potential annual direct incident solar radiation corrected geothermal heat flux (GHF_{α}) for Yellowstone National Park on 5 July 2002 (Wm^{-2}).

Equation	Min	Max	Mean	Median	Mode	Std. Dev.
(2.8) M_{terr}	305.8	446.7	366.7	364.7	352.7	17.8
(2.9) GHF_M	-63.0	78.0	-2.1	-4.0	-16.0	17.8
(2.10) GHF_{SR}	5.9	358.0	90.4	84.3	77.4	32.5
(2.11) GHF_{α}	14.8	378.0	121.0	118.0	111.3	32.4

Table 2.2: Summary statistics for terrestrial emittance (M_{terr}), mean non-geothermal value corrected geothermal heat flux (GHF_M), potential annual direct incident solar radiation corrected geothermal heat flux (GHF_{SR}), and albedo and potential annual direct incident solar radiation corrected geothermal heat flux (GHF_α) for Yellowstone National Park on 25 June 2007 (Wm^{-2}).

Equation	Min	Max	Mean	Median	Mode	Std. Dev.
(2.8) M_{terr}	303.8	433.4	353.1	351.9	353.4	14.8
(2.9) GHF_M	-49.9	79.6	-0.7	-1.9	-0.3	14.8
(2.10) GHF_{SR}	4.6	351.0	76.8	70.9	65.5	31.5
(2.11) GHF_α	14.1	350.7	105.6	102.2	103.5	31.1

The calculated M_{terr} values were up to three times higher than the values of the GHF models (Tables 2.1 and 2.2). The majority of M_{terr} values (median values of 364.7 Wm^{-2} in 2002 and 351.9 Wm^{-2} in 2007) were higher than the average annual air temperature in YNP of 4.64 °C (337.6 Wm^{-2}) (Western Regional Climate Center, 2005), while all pixel values calculated with the GHF_M, GHF_{SR}, and GHF_α were lower than the average annual air temperature. The GHF_M values were largely below zero with the lowest maximum values of the four methods. The values for GHF_α were higher than the GHF_{SR} values for all but the maximum values in 2007.

The mean difference between 2002 and 2007 GHF_M values was 0.0 Wm^{-2}, while the mean difference between 2002 and 2007 M_{terr}, GHF_{SR}, and GHF_α values were near -15.0 Wm^{-2} (Table 2.3). The maximum value of the difference in M_{terr} was less than half that of GHF_α and less than one third that of GHF_{SR}. The range in difference values was largest for GHF_{SR}, more than three times the smallest values (M_{terr} and GHF_M). Linear artifacts were observed in the difference maps of GHF_{SR} and GHF_α, while the M_{terr} and GHF_M difference maps appeared to have no linear artifacts (Figure 2.2).

Table 2.3: Summary statistics for differenced images (2007 minus 2002) of terrestrial emittance (M_{terr}), mean non-geothermal value corrected geothermal heat flux (GHF_M), potential annual direct incident solar radiation corrected geothermal heat flux (GHF_{SR}), and albedo and potential annual direct incident solar radiation corrected geothermal heat flux (GHF_α) for Yellowstone National Park (Wm^{-2})

Equation	Min	Max	Mean	Median	Mode	Std. Dev.	Range
(2.8) M_{terr}	-81.9	71.0	-15.0	-15.0	-15.6	8.8	152.9
(2.9) GHF_M	-66.9	86.0	0.0	0.0	-0.6	8.8	152.9
(2.10) GHF_{SR}	-273.5	217.4	-15.1	-16.5	-14.6	14.0	490.9
(2.11) GHF_α	-253.8	186.5	-16.1	-16.4	-18.2	13.8	430.3

M_{terr} and GHF_M values, in addition to having the same standard deviation (Tables 2.1, 2.2, and 2.3), were visually identical (Figures 2.3 and 2.4) as a result of subtracting a constant for each year. The hottest M_{terr} and GHF_M pixels were found primarily in the 1988 fire scars and the Northern Range of YNP, while the coolest pixels appeared to be on north-facing slopes. The hottest GHF_{SR} pixels, on the other hand, were focused in the Northern Range and north-facing slopes while the coolest pixels were on the south-facing slopes. The hottest GHF_α pixels were also located in the Northern Range and north-facing slopes, with more pixels visible in 1988 fire scars than GHF_{SR}, especially in 2002. The coolest GHF_α pixels were mostly on south-facing slopes and near Yellowstone Lake.

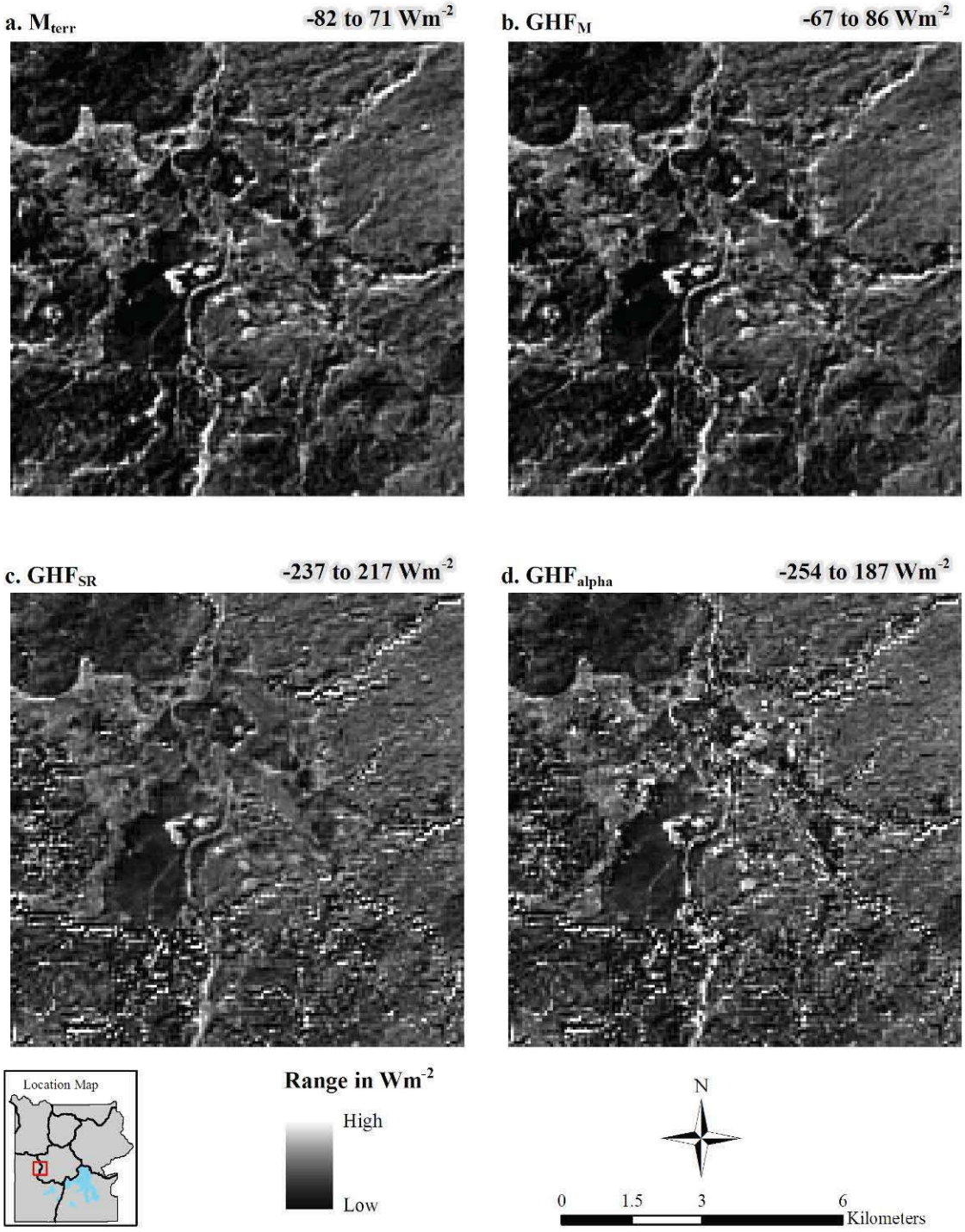

Figure 2.2: Difference images (2007 minus 2002) of (a) terrestrial emittance (M_{terr}), (b) mean non-geothermal value corrected geothermal heat flux (GHF_M), (c) potential annual direct incident solar radiation corrected geothermal heat flux (GHF_{SR}), and (d) albedo and potential annual direct incident solar radiation corrected geothermal heat flux (GHF_{α}) at Midway and Lower Geyser Basins in Yellowstone National Park (values are in Wm^{-2})

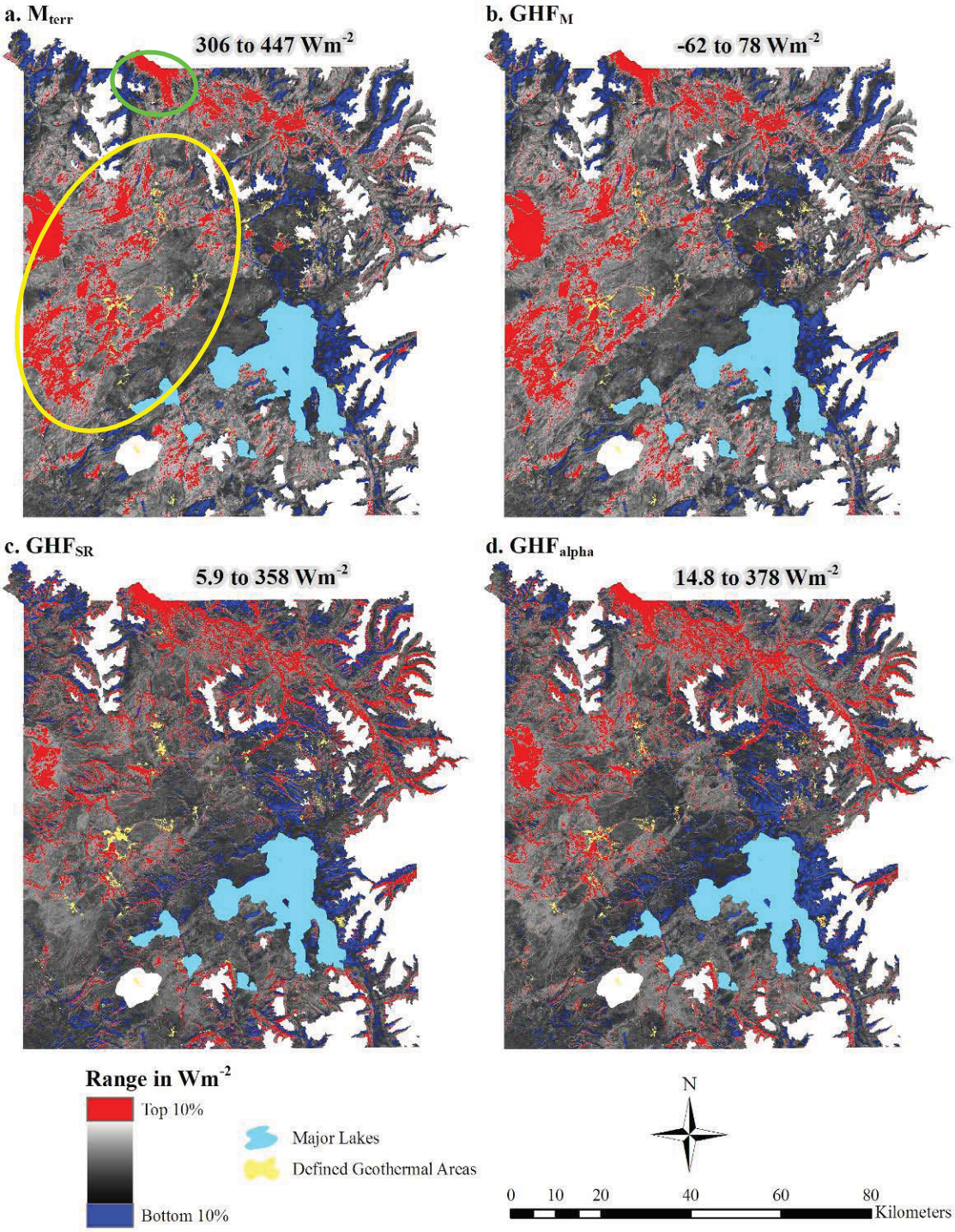

Figure 2.3: Top 10% and bottom 10% of the range of values of (a) terrestrial emittance (with many of the 1988 fire scars circled in yellow and a portion of the Northern Range circled in green (M_{terr}), (b) mean non-geothermal value corrected geothermal heat flux (GHF_M), (c) potential annual direct incident solar radiation corrected geothermal heat flux (GHF_{SR}), and (d) albedo and potential annual direct incident solar radiation corrected geothermal heat flux (GHF_{α}) for Yellowstone National Park on 5 July 2002 (Wm^{-2}). White areas were snow or cloud-covered.

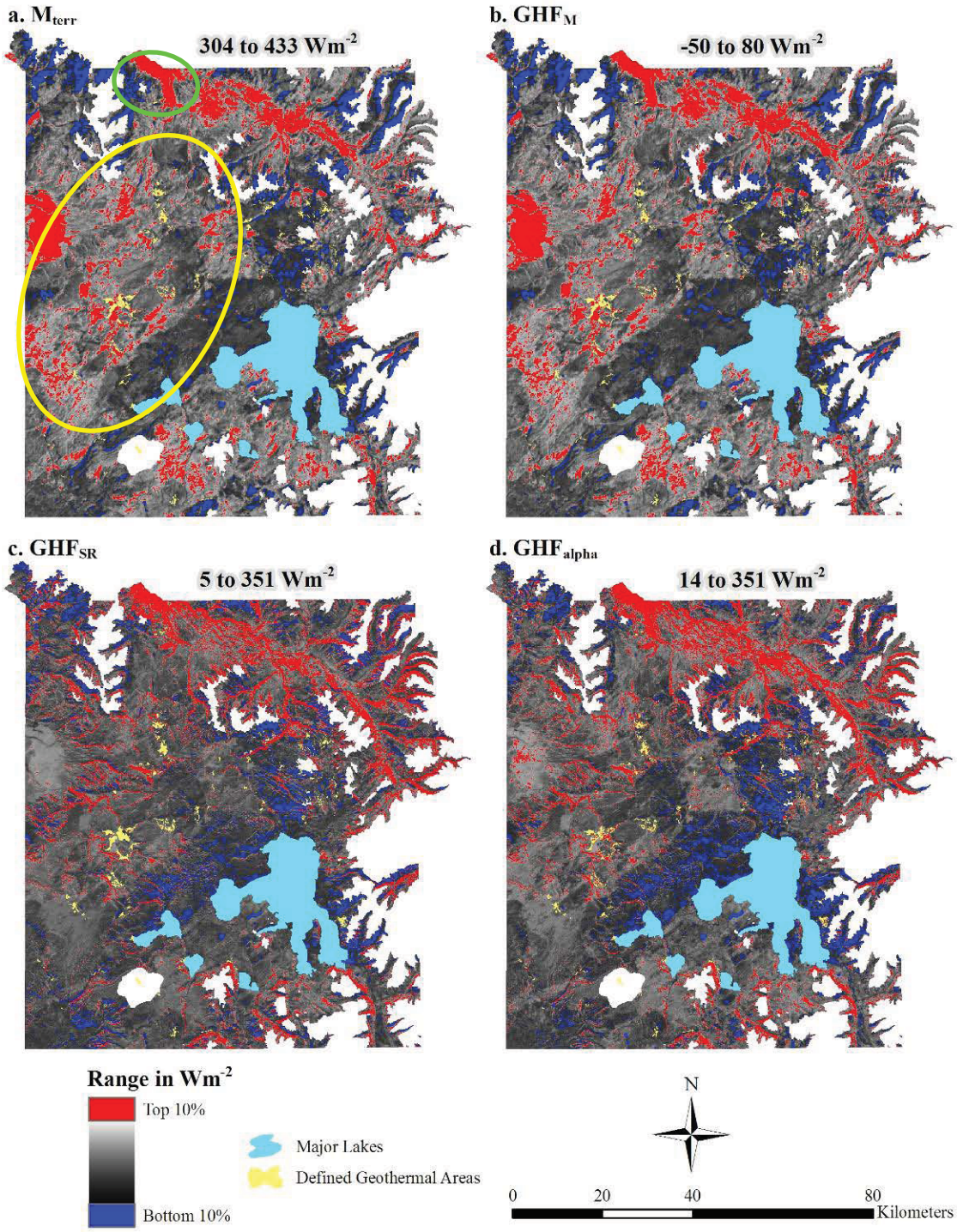

Figure 2.4: Top 10% and bottom 10% of the range of values of (a) terrestrial emittance (with many of the 1988 fire scars circled in yellow and a portion of the Northern Range circled in green (M_{terr}), (b) mean non-geothermal value corrected geothermal heat flux (GHF_M), (c) potential annual direct incident solar radiation corrected geothermal heat flux (GHF_{SR}), and (d) albedo and potential annual direct incident solar radiation corrected geothermal heat flux (GHF_α) for Yellowstone National Park on 25 June 2007 (Wm^{-2}). White areas were snow or cloud-covered.

When the four methods discussed above (M_{terr}, GHF_M, GHF_{SR}, and GHF_α) were compared, the GHF_α method resulted in more of the hottest 10% of the pixels within the defined geothermal areas. The 60-m resolution 2002 GHF_α image had 4,879 of the hottest pixels within the defined geothermal areas (21.7%), as compared to 1,452 pixels for GHF_{SR} (6.4%) and 3,949 pixels for GHF_M and M_{terr} (17.5%). The 120-m resolution 2007 GHF_α image had 1,027 of the hottest pixels within the defined geothermal areas (19.4%), as compared to 255 pixels for GHF_{SR} (4.8%) and 678 pixels for GHF_M and M_{terr} (12.8%). The M_{terr} and GHF_M methods resulted in less of the coolest 10% of the pixels within the defined geothermal areas. The 60-m resolution 2002 M_{terr} and GHF_M images had 333 of the coolest pixels within the defined geothermal areas (1.5%), as compared to 774 pixels for GHF_{SR} (3.4%) and 453 pixels for GHF_α (2.0%). The 120-m resolution 2007 M_{terr} and GHF_M images had 42 of the coolest pixels within the defined geothermal areas (0.8%), as compared to 193 pixels for GHF_{SR} (3.6%) and 111 pixels for GHF_α (2.1%).

Over 12,000 individual geothermal features have been located by the Thermal Inventory Project. The hottest 10% of GHF_α pixels coincided with more of these Thermal Inventory Project points than did the hottest 10% of the M_{terr} pixels (Table 2.4). In 2002, the hottest 10% of GHF_α coincided with more than twice as many Thermal Inventory Project points as did the hottest 10% of M_{terr}. In 2007, the hottest 10% of GHF_α coincided with just under twice as many Thermal Inventory Project points as did the hottest 10% of M_{terr}.

Table 2.4: Coincidence of the hottest 10% of terrestrial emittance (M_{terr}) and albedo and potential annual direct incident solar radiation corrected geothermal heat flux (GHF_{α}) with Thermal Inventory Project points in 2002 and 2007.

Method	Year	Number of coincident Thermal Inventory Project points
(2.8) M_{terr}	2002	1,661
(2.11) GHF_{α}	2002	3,642
(2.8) M_{terr}	2007	1,385
(2.11) GHF_{α}	2007	2,566

The GHF_{α} method produced the largest difference when the mean values of pixels outside the defined geothermal areas were subtracted from the mean values of only the pixels within the defined geothermal areas (Tables 2.5 and 2.6), indicating more hot pixels within the defined geothermal areas with this method. The M_{terr} method had a larger difference than GHF_{SR}, but had less than half the difference of GHF_{α}.

Table 2.5: 5 July 2002 differences of average Wm^{-2} values inside the defined geothermal areas and average Wm^{-2} values outside the defined geothermal areas for terrestrial emittance (M_{terr}), potential annual direct incident solar radiation corrected geothermal heat flux (GHF_{SR}), and albedo and potential annual direct incident solar radiation corrected geothermal heat flux (GHF_{α}).

Equation	Inside Average	Outside Average	Difference
(2.8) M_{terr}	377.3	368.8	8.5
(2.10) GHF_{SR}	92.4	88.6	3.9
(2.11) GHF_{α}	135.6	117.8	17.8

Table 2.6: 25 June 2007 differences of average Wm^{-2} values inside the defined geothermal areas and average Wm^{-2} values outside the defined geothermal areas for terrestrial emittance (M_{terr}), potential annual direct incident solar radiation corrected geothermal heat flux (GHF_{SR}), and albedo and potential annual direct incident solar radiation corrected geothermal heat flux (GHF_{α}).

Equation	Inside Average	Outside Average	Difference
(2.8) M_{terr}	360.2	353.8	6.4
(2.10) GHF_{SR}	74.3	73.6	0.7
(2.11) GHF_{α}	117.2	101.8	15.4

Comparison to Airborne Data in the Norris Geyser Basin Area

The summary statistics of M_{terr} values were similar to the Hardy heat flow summary statistics (Table 2.7). The Hardy (2005) data had higher values overall than the

M_{terr} data, with the maximum values much higher and the minimum values only slightly higher. The range of the Hardy data was more than double the range of the M_{terr} data. The total heat flow values for M_{terr} were within an order of magnitude of the Hardy heat flow data for both the full Hardy data extent and a subset that covers just Norris Geyser Basin (Table 2.8).

Table 2.7: Comparison of October 2002 Hardy (2005) heat data summary statistics to July 2002 estimated terrestrial emittance (M_{terr}) summary statistics (values in Wm^{-2}). Information from the full 2002 Hardy data and Norris Geyser Basin extents are displayed.

Hardy full data extent	**Min**	**Max**	**Mean**	**Median**	**Mode**	**Std. Dev.**
Hardy data 60 m	342.2	664.3	407.7	401.3	387.5	35.7
M_{terr} 60 m	338.2	418.5	378.2	377.1	376.4	13.7

Norris Geyser Basin	**Min**	**Max**	**Mean**	**Median**	**Mode**	**Std. Dev.**
Hardy data 60 m	361.8	664.3	432.0	426.7	418.5	37.0
M_{terr} 60 m	353.4	418.5	387.5	387.7	393.3	11.9

Table 2.8: Comparison of October 2002 Hardy (2005) total heat flow and power values to July 2002 estimated terrestrial emittance (M_{terr}) heat flow and power values. All M_{terr} values are within an order of magnitude of the Hardy data.

	Hardy Heat Flow	**M_{terr} Heat Flow**
Hardy data extent	407.7 Wm^{-2}	378.2 Wm^{-2}
Norris Geyser Basin	432.0 Wm^{-2}	387.5 Wm^{-2}

	Hardy Power	**M_{terr} Power**	**Area of Analysis**
Hardy data extent	7.0 GW	6.5 GW	17,125,200 m^2
Norris Geyser Basin	1.5 GW	1.4 GW	3,502,800 m^2

Discussion

Incorporating estimated emissivity on a pixel-by-pixel basis rather than as an average over the entire image produced locally precise terrestrial emittance and GHF estimates by accounting for differences in emissivity due to varying amount of vegetation

in each pixel. By deriving emissivity values from the finer spatial resolution reflective Landsat bands, more detail was incorporated into the M_{terr} values than if the thermal band had been used alone.

The M_{terr} values calculated for the July 2002 Landsat image were within the same order of magnitude of the heat flow values calculated by Hardy (2005) for the nighttime airborne October 2002 image of Norris Geyser Basin and surrounding area, providing some confirmation that the calculations used in this project were consistent with previous analysis. Solar radiation was not taken into account for either image. While there are fewer solar radiation effects during a nighttime image, there are still accumulated effects from the sun heating the ground the previous day, week, month, and year. The similarities between the daytime and nighttime readings are, therefore, expected, and show that Landsat can be used to calculate terrestrial emittance with comparable results to higher spatial resolution sensors.

The M_{terr} and Hardy heat flow values were larger for Norris Geyser Basin than for the larger extent, as expected. Reducing the study area to the smaller Norris Geyser Basin included less non-geothermal-ground, thus more heat would be emitted per area than in a larger, mostly non-geothermal-ground study area.

The M_{terr} and Hardy values were similar, but the differences are also noteworthy. Since the Landsat image was from July and solar radiation was not taken into account, M_{terr} values were expected to be greater than the Hardy heat flow values, but they were not. This is most likely due to the different data collection and processing methods. The Hardy data were derived directly from raw DNs and temperature calibration data. No

atmospheric corrections were needed since the data were collected with a low-elevation airborne flight. The M_{terr} data, on the other hand, were not calibrated to ground temperature, and needed atmospheric corrections since they were collected from space.

Estimating terrestrial emittance requires only three Landsat bands and atmospheric and radiometric corrections. Terrestrial emittance includes all the types of heat emitted from the ground: GHF, direct incident solar radiation, and indirect solar effects, including convection from air currents, and soil conduction of solar energy. Mean annual air temperature is a good representation of ground water temperature. Mean M_{terr} values were similar to, but slightly higher than, the average annual air temperature of YNP (Western Regional Climate Center, 2005), demonstrating that the model includes geothermal as well as non-geothermal heat. Many of the hottest M_{terr} pixels were located on low-elevation flat and south-facing slopes (in the Northern Range), and within 1988 fire scars that have been revegetated with thick stands of young lodgepole pine (*Pinus contorta*) intermixed with down and standing grey and white snags. The GHF_M model simply subtracted one value across the image, therefore demonstrating the exact same spatial pattern as M_{terr} but with lower values (Figures 2.3.a and b, and 2.4.a and b). This model should have resulted in relatively fewer high values that represent only geothermal heat, however, due to the effects of direct and indirect solar radiation, GHF_M was an inferior model for estimating true GHF. High values of GHF_M were observed both in geothermal areas and on south-facing slopes with no geothermal activity, with many of the highest values not in the defined geothermal areas.

There are many parameters that must be included in a GHF calculation that are not readily available or straightforwardly modeled, including sensible and latent heat exchange with the atmosphere and advected heat flux in precipitation and runoff (Watson *et al.*, 2008). Many of the direct solar radiation effects were modeled with the equation for SR (McCune and Keon, 2002). An estimation of GHF that included direct solar radiation was expected to remove many of the non-geothermal effects observed in M_{terr} and GHF_M. The method used to estimate GHF_{SR} removed some, but not all, of the effects from direct solar radiation. The high M_{terr} and GHF_M values from fire scars were reduced in the GHF_{SR} model (white circles in Figures 2.5.c and 2.6.c), however, the model over-compensated for solar and topographic effects on north-facing slopes, creating falsely warm regions (arrows in Figures 2.5.c and 2.6.c). It also reduced the geothermal heat signal from within the defined geothermal areas (*e.g.*, black circles in Figures 2.5.b and c and 2.6.b and c, in the area of Grand Prismatic and Excelsior Geyser). The SR model represented annual direct incident solar radiation, and since the Landsat images used were acquired during the summer when solar elevation was high, the annual calculation over-adjusted for north-facing slopes. This model corrected a number of the solar radiation effects that were abundant in the M_{terr} model, however, it did not correct all solar radiation and albedo effects and over-corrected direct solar radiation in some locations. This model demonstrated potential for using Landsat data to estimate GHF.

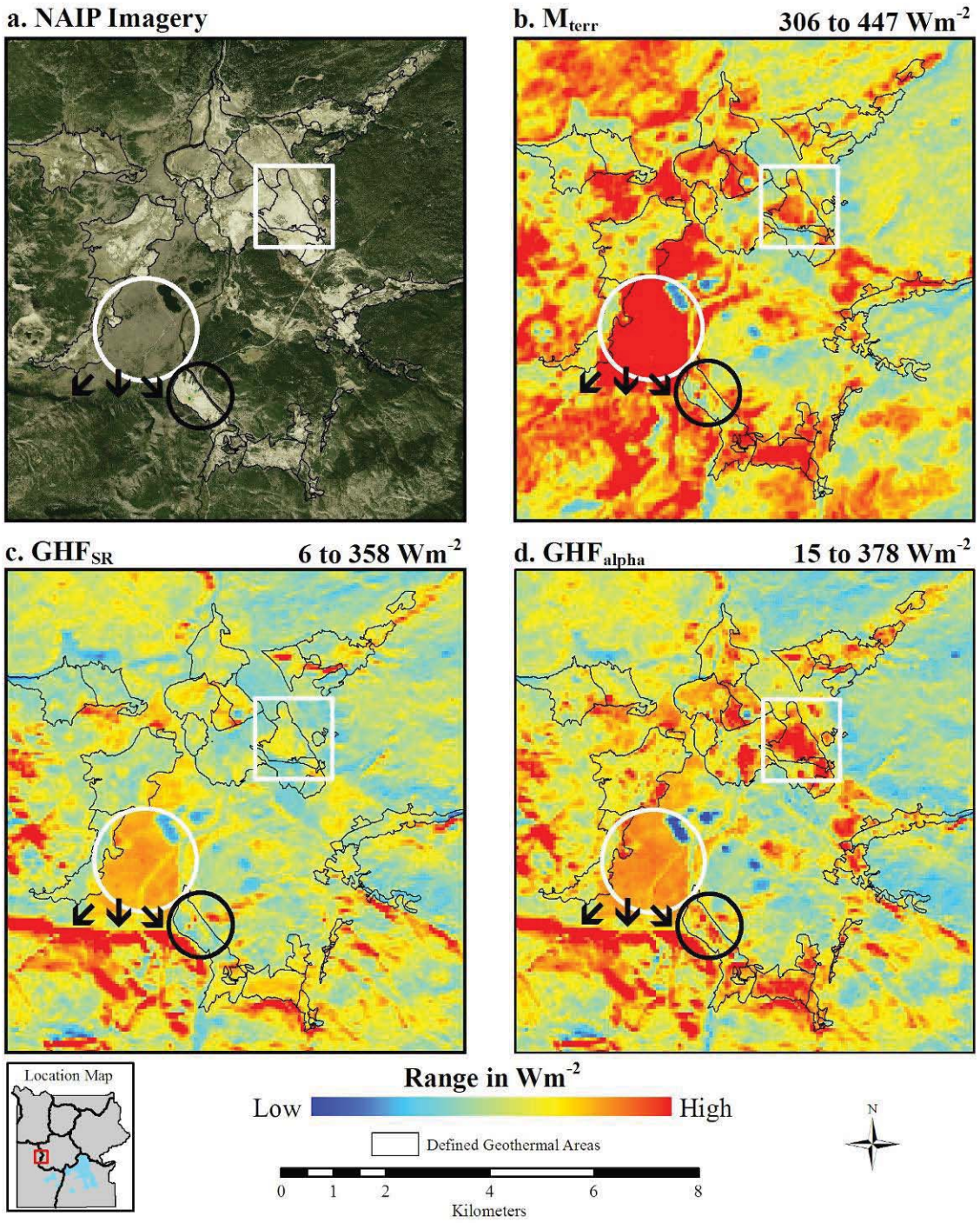

Figure 2.5: (a) National Agriculture Imagery Program (NAIP) imagery of Lower and Midway Geyser Basins, with Grand Prismatic Spring and Excelsior Geyser circled in black, a north-facing slope indicated by black arrows, a fire scar circled in white, and a geothermal barren shown in a white box; (b) terrestrial emittance (M_{terr}), (c) potential annual direct incident solar radiation corrected geothermal heat flux minus (GHF_{SR}), and (d) albedo and potential annual direct incident solar radiation corrected geothermal heat flux (GHF_{α}) on 5 July 2002 (in Wm^{-2}).

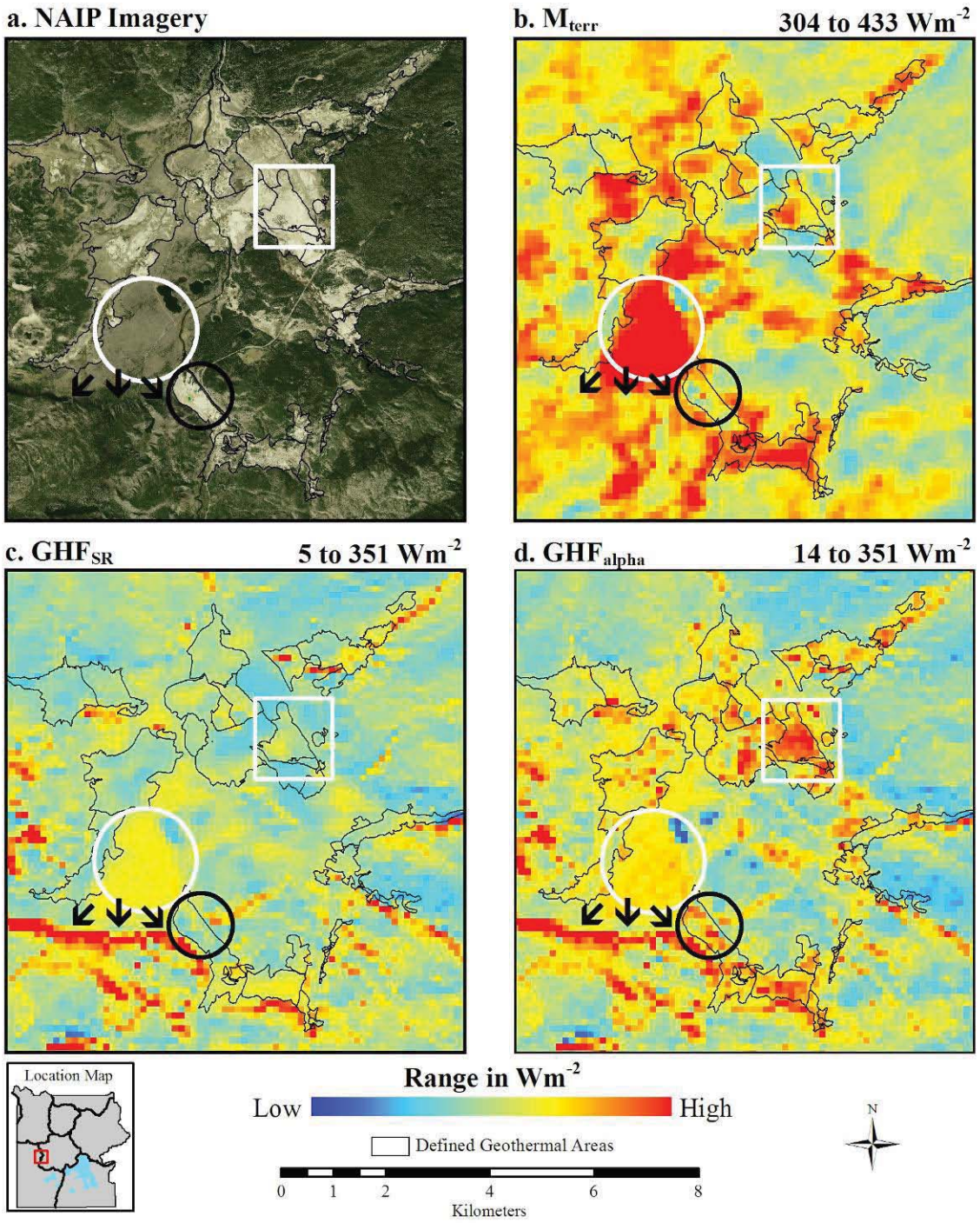

Figure 2.6: (a) National Agriculture Imagery Program (NAIP) imagery of Lower and Midway Geyser Basins, with Grand Prismatic Spring and Excelsior Geyser circled in black, a north-facing slope indicated by black arrows, a fire scar circled in white, and a geothermal barren shown in a white box; (b) terrestrial emittance (M_{terr}), (c) potential annual direct incident solar radiation corrected geothermal heat flux minus (GHF_{SR}), and (d) albedo and potential annual direct incident solar radiation corrected geothermal heat flux (GHF_{α}) on 25 June 2007 (in Wm^{-2}).

Combining the effects of albedo with SR improved the GHF_{SR} model. More geothermal heat signatures were observed within the defined geothermal areas in the GHF_{α} model than in the GHF_{SR} model. Most of the geothermally active areas in YNP are white or grey surfaces with high albedos and low solar absorption. The equation for GHF_{α} appears to calculate the values for these active areas well (black circles in Figures 2.5.d and 2.6.d), but also possibly calculates values too high for white geothermal barrens (white boxes in Figures 2.5.d and 2.6.d). Most high values within fire scars were decreased in this model, although the north-facing slopes were still falsely warm (arrows in Figures 2.5.d and 2.6.d). The GHF_{α} model shows promise, but without proper ground calibration it is uncertain to what extent it might be overcorrecting for direct solar and albedo effects. Indirect solar effects that are not included in this model must be accounted for as well.

When the four methods reviewed in this chapter were compared, no one method was consistently superior. M_{terr} and GHF_{α} tended to produce more reasonable results than GHF_M and GHF_{SR}, however, the results from comparisons were inconclusive as to whether M_{terr} or GHF_{α} were more reasonable. GHF_{α} had more of the hottest 10% of the pixels within the defined geothermal areas, but M_{terr} had fewer of the coolest 10% of the pixels within the defined geothermal areas. All of the M_{terr} pixels had values higher than the average annual air temperature, but all of the GHF_{α} pixels had values lower than the average annual air temperature. The hottest 10% of GHF_{α} pixels coincided with approximately double the number of Thermal Inventory Project points that the hottest 10% of M_{terr} pixels. The difference in mean value inside the defined geothermal areas

compared to the mean value outside the geothermal areas for GHF_{α} was more than double that of M_{terr}. Finally, the 2007 minus 2002 difference images indicated a very large range of change along with linear data artifacts in the GHF_{α} image, but a much smaller range of change and no linear data artifacts in the M_{terr} image.

This study established that estimation of absolute GHF with Landsat imagery is not possible without several additional parameters. Direct and indirect solar radiation and albedo remain as serious concerns and must be considered in future studies of this nature. Obtaining accurate absolute values of GHF with Landsat imagery will require thermal ground calibration as well as methods of accounting for surface albedo and variations in solar radiation, both direct and indirect. Due to these unaccounted for effects, M_{terr} is unsatisfactory as a measure of absolute GHF. For change analysis within the defined geothermal areas, however, M_{terr} is likely the most appropriate thermal measure, even though the method comparisons were inconclusive. Albedo and solar radiation effects within the M_{terr} model tend to be relatively constant across the image over time, unless there has been a significant land cover change such as a fire. Therefore, these effects are largely cancelled out for change analysis, with any differences between dates potentially related to changes in GHF. Utilizing M_{terr} for change analysis over recent decades is a prudent choice, since, in addition to the reasons outlined above, a version of M_{terr} has been field validated (Watson *et al.*, 2008), it is the least-modified Landsat thermal data, it requires no field data collection (impossible for historic images), and it has no linear data artifacts.

Literature Cited

Andres, R.J. and W.I. Rose. 1995. Description of thermal anomalies on two active Guatemalan volcanoes using Landsat Thematic Mapper imagery. *Photogrammetric Engineering & Remote Sensing*, 61(6): 775-782.

Boomer, S.M., D.P. Lodge, B.E. Dutton, and B. Pierson. 2002. Molecular characterization of novel red green nonsulfur bacteria from five distinct hot springs communities in Yellowstone National Park. *Applied and Environmental Microbiology*, 68(1): 346-355.

Bourgeois, O., O. Dauteuil, and B. Van Vliet-Lanoe. 2000. Geothermal control on flow patterns in the last glacial maximum ice sheet of Iceland. *Earth Surface Processes and Landforms*, 25(1): 59-76.

Brunsell, N.A. and R.R. Gillies. 2002. Incorporating surface emissivity into a thermal atmospheric correction. *Photogrammetric Engineering & Remote Sensing*, 68(12): 1263-1269.

Carranza, E.J.M. and M. Hale. 2002. Mineral imaging with Landsat Thematic Mapper data for hydrothermal alteration mapping in heavily vegetated terrane. *International Journal of Remote Sensing*, 23(22): 4827-4852.

Chander, G., B.L. Markham, and D.L. Helder. 2009. Summary of current radiometric calibration coefficients for Landsat MSS, TM, ETM+, and EO-1 ALI sensors. *Remote Sensing of Environment*, 113(5): 893-903.

Chavez, P.S.J. 1996. Image-based atmospheric corrections - revisited and revised. *Photogrammetric Engineering & Remote Sensing*, 62(9): 1025-1036.

Coolbaugh, M.F., C. Kratt, A. Fallacaro, W.M. Calvin, and J.V. Taranik. 2007. Detection of geothermal anomalies using Advanced Spaceborne Thermal Emission and Reflection Radiometer (ASTER) thermal infrared images at Bradys Hot Springs, Nevada, USA. *Remote Sensing of Environment*, 106(3): 350-359.

Custer, S.G., D.E. Michels, W. Sill, J.L. Sonderegger, W. Weight, and W. Woessner. 1993. Recommended Boundary for Controlled Groundwater Area in Montana Near Yellowstone Park, U.S. Department of the Interior National Park Service, Fort Collins, CO.

Daneshfar, B., A. Desrochers, and P. Budkewitsch. 2006. Mineral-potential mapping for MVT deposits with limited data sets using Landsat data and geological evidence in the Borden Basin, Northern Baffin Island, Nanuvut, Canada. *Natural Resources Research*, 15(3): 129-149.

Dogan, H.M. 2008. Applications of remote sensing and geographic information systems to assess ferrous minerals and iron oxide of Tokat province in Turkey. *International Journal of Remote Sensing*, 29(1): 221-233.

Elachi, C. 1987. Introduction to the Physics and Techniques of Remote Sensing. John Wiley & Sons, New York, NY, 413 pp.

Flynn, L.P., A.J.L. Harris, and R. Wright. 2001. Improved identification of volcanic features using Landsat 7 ETM+. *Remote Sensing of Environment*, 78(1-2): 180-193.

Fournier, R.O., D.E. White, and A.H. Truesdell. 1975. Convective heat flow in Yellowstone National Park, Proceedings of the Second United Nations Symposium on the Development and Use of Geothermal Resources, pp. 731-739.

Friedman, I. and D.R. Norton. 2007. Is Yellowstone losing its steam? - Chloride flux out of Yellowstone National Park. Chapter I in Professional Paper 1717, U.S. Geological Survey, pp. 272-297.

Gruber, S., M. Hoelzle, and W. Haeberli. 2004. Rock-wall temperatures in the Alps: Modeling their topographic distribution and regional differences. *Permafrost and Periglacial Processes*, 15(3): 299-307.

Hardy, C.C. 2005. "Characterizing thermal features from multi-spectral remote sensing data using dynamic calibration procedures", University of Montana, Missoula, MT, 153 pp.

Heasler, H., C. Jaworowski, and D. Susong. 2004. A geothermal monitoring plan for Yellowstone National Park, Yellowstone Center for Resources, Yellowstone National Park, Wyoming, 24pp.

Kaneko, T. and M.J. Wooster. 1999. Landsat infrared analysis of fumarole activity at Unzen Volcano: time-series comparison with gas and magma fluxes. *Journal of Volcanology and Geothermal Research*, 89(1-4): 57-64.

Kohl, T. 1999. Transient thermal effects below complex topographies. *Tectonophysics*, 306(3-4): 311-324.

Liang, S. 2000. Narrowband to broadband conversions of land surface albedo: I Algorithms. *Remote Sensing of Environment*, 76(2): 213-238.

McCune, B. and D. Keon. 2002. Equations for potential annual direct incident radiation and heat load. *Journal of Vegetation Science*, 13(4): 603-606.

MontanaView. 2008. MontanaView Supporting Remote Sensing. Last accessed on 8 April 2009. http://montanaview.org/.

NASA. 2008. ASTER Spectral Library. Last accessed on 3 March 2009. http://speclib.jpl.nasa.gov/.

NASA. 2009. Landsat 7 Science Data Users Handbook. Last accessed on 6 April 2009. http://landsathandbook.gsfc.nasa.gov/handbook.html.

Norton, D.R. and I Friedman. 1985. Chlorid flux out of Yellowstone National Park. *Journal of Volcanology and Geothermal Research*, 26(3-4): 231-250.

Ontar Corporation. 2001. PcModWin 4.0 Ver 1.01: User Interface Environment for MODTRAN 4.0. Ontar Corporation, North Andover, Massachusetts. Last accessed on 29 June 2009. www.ontar.com

Parmenter, A.W., A. Hansen, R.E. Kennedy, W. Cohen, U. Langner, R. Lawrence, B. Maxwell, A. Gallant, and R. Aspinall. 2003. Land use and land cover change in the greater Yellowstone Ecosystem: 1975-1995. *Ecological Applications*, 13(3): 687-703.

Patrick, M., K. Dean, and J. Dehn. 2004. Active mud volcanism observed with Landsat 7 ETM+. *Journal of Volcanology and Geothermal Research*, 131(3-4): 307-320.

Seielstad, C. and L. Queen. 2009. Thermal remote monitoring of the Norris Geyser Basin, Yellowstone National Park. Final Report for the National Park Service Cooperative Ecosystem Studies Unit, Agreement No. H1200040001, 38 pp.

Shaw, J.A. and C. Marston. 2000. Polarized infrared emissivity for a rough water surface. *Optics Express*, 7(11): 375-380.

Smith, R.B. and L.J. Siegel. 2000. Windows Into the Earth -The Geologic Story of Yellowstone and Grand Teton National Parks. Oxford University Press, New York, NY, 242 pp.

Song, Y., H.-C. Kim, B.-W. Yum, and E. Ahn. 2005. Direct-use geothermal development in Korea: Country update 2000-2004, Proceedings of the World Geothermal Congress, pp. 1-7.

Sorey, M.L. Effects of potential geothermal development in the Corwin Springs Known geothermal resources area, Montana, on the thermal features of Yellowstone National Park. Water-Resources Investigations Report 91-4052, U.S. Geological Survey, Menlo Park, California, 204 pp.

Spatial Analysis Center. 1998. 30-meter elevation data for Yellowstone National Park, Wyoming, Montana, Idaho. Digital Spatial Data, Yellowstone Center for Resources, Yellowstone National Park, Wyoming.

Spatial Analysis Center. 2000. Precipitation in Yellowstone National Park, Wyoming, Montana, Idaho. Digital Spatial Data, Yellowstone Center for Resources, Yellowstone National Park, Wyoming.

Spatial Analysis Center. 2005. Hydrogeothermal Areas of Yellowstone National Park, Wyoming, Montana, Idaho. Digital Spatial Data, Yellowstone Center for Resources, Yellowstone National Park, Wyoming.

Urai, M. 2002. Heat discharge estimation using satellite remote sensing data on the Iwodake volcano in Satsuma-Iwojima, Japan. *Earth Planets Space*, 54(3): 211-216.

Utah State University. 2008. Image Standardization: At-sensor Reflectance and COST Correction. Last accessed on 8 April 2009. http://earth.gis.usu.edu/imagestd/.

Waite, G.P. and R.B. Smith. 2002. Seismic evidence for fluid migration accompanying subsidence of the Yellowstone caldera. *Journal of Geophysical Research*, 107(B9, 2177): ESE 1-1 to ESE 1-15.

Watson, F.G.R., R.E. Lockwood, W.B. Newman, T.N. Anderson, and R.A. Garrott. 2008. Development and comparison of Landsat radiometric and snowpack model inversion techniques for estimating geothermal heat flux. *Remote Sensing of Environment*, 112(2): 471-481.

Watson, K. 1975. Geologic applications of thermal infrared images. *Proceedings of the IEEE*, 63(1): 128-137.

Western Regional Climate Center. 2005. Period of record monthly climate summary - Yellowstone Park, Wyoming (489905). Last accessed on 6 April 2009. http://www.wrcc.dri.edu/cgi-bin/cliRECtM.pl?wyyell.

CHAPTER 3

ANALYZING CHANGE IN YELLOWSTONE'S TERRESTRIAL EMITTANCE WITH LANDSAT IMAGERY

Introduction

Geothermal features are one of the main reasons that Yellowstone National Park (YNP) was established as the world's first national park. The National Park Service (NPS) is legally mandated to monitor and protect geothermal features within its units, and YNP, in addition to containing the greatest concentration of geothermal features in the world (Waring *et al.*, 1983), is listed as a significant geothermal feature itself (Geothermal Steam Act, 1970 as amended in 1988).

Geothermal heat flux (GHF) is an important aspect in the dynamics of geothermal features. GHF is heat change in water and steam in geothermal systems which is radiated from the surface of the Earth. It represents only heat coming from below the surface and does not include accumulated indirect or direct solar heating effects such as convection from air currents and soil conduction of solar effects (indirect), or solar heating due to variations in topography (direct). In contrast, terrestrial emittance, or M_{terr} as defined in Chapter 2, represents all heat emitted from the ground and is composed of GHF as well as direct and indirect solar radiation effects. GHF_{α}, also defined in Chapter 2, attempts to account for solar effects and appears to do so, with caveats, relative to M_{terr} at a YNP-wide scale (Equation 2.11 and Figures 2.2.d and 2.3.d). Change analysis within specific geothermal areas, however, requires data with low variability for unchanged features at local scales, allowing for the observation of actual change rather than data noise. M_{terr}

has several advantages over GHF_{α} for analyzing change in YNP's geothermal areas. First, a version of M_{terr} has been field verified (Watson *et al.*, 2008), while GHF_{α} has had no field verification. Second, the spatial patterns of GHF_{α} are substantially different from those of the less variable M_{terr}, including data striping artifacts, and overly high values on north-facing slopes. Lastly, all things being equal, the level of uncertainty in the data increases with each additional processing step, and M_{terr} requires less processing than GHF_{α}.

YNP scientists can study changes in M_{terr} values to examine changes in behavior of geothermal features or to monitor for changes in heat flux that might be occurring in response to land management practices within and outside of YNP. New features regularly emerge and active features become inactive. The geothermal features of YNP must be monitored on a regular basis to be able to assess changes that might occur over days or decades. Having multiple dates of M_{terr} readings would allow YNP scientists to study patterns in M_{terr} change and to try to relate them to possible factors that might cause change.

Ideas abound as to why geothermal features change, with seismic activity near and far being the most widely accepted hypothesis (Rojstaczer *et al.*, 2003). Changes in geyser activity within YNP were observed shortly after the 2002 7.9 magnitude Denali fault earthquake in Alaska, 3,100 km away (Husen *et al.*, 2004). Local earthquake swarms were also associated with geothermal activity change. It has been suggested that earth movement near or within geothermal features can shake open vent blockages (Husen *et al.*, 2004) or seal vents and fractures, thus changing geothermal activity

(Dobson *et al.*, 2003). Changes in climate are also thought to have an effect on geothermal features. Drought and changes in barometric pressure can change ground water levels. Geothermal features are linked with subterranean ground water (Bryan, 2001). Changes in GHF observed in Barrow, Alaska from 1971 to 1992 have been attributed to an increase in surface temperatures and decrease in soil moisture (Oechel *et al.*, 1995). Relationships between geologic faults and geothermal features activity have been observed outside the 640,000-year-old caldera boundary in YNP (Pierce and Morgan, 1992; Finn and Morgan, 2002). "Heavy breathing" (regular uplift and subsidence) of the 640,000-year-old caldera in YNP has been modeled over recent millennia and associated with hydrogeothermal activity (Pierce *et al.*, 2007). Recognized external threats to the geothermal features of YNP include potential geothermal development in Idaho and Montana, and oil, gas, and groundwater development in Wyoming, Montana, and Idaho (Sorey, 1991; Custer *et al.*, 1993; Heasler *et al.*, 2004).

Details of change within geothermal *systems* (*i.e.*, large areas of GHF as opposed to individual features), however, are poorly known. Knowledge about system-wide change might provide scientific insight into patterns that would help advance the understanding of processes in important geothermal systems. A better understanding of these systems would help inform scientists when management activities (both inside and outside YNP) are affecting geothermal resources, would help with placement of visitor information, and would be an important planning tool for placing infrastructure in YNP. Finally, there is a growing demand for alternative energy in the United States and the development of widespread geothermal energy is likely. The impact of geothermal

energy development outside YNP on geothermal features inside YNP will become an increasingly important issue. A geothermal monitoring plan that combines remote sensing of geothermal features with the inventory, monitoring, and assessment of both groundwater and chloride flux has been proposed for YNP to address these issues (Heasler *et al.*, 2004). Remote sensing is an important element of the plan since it is an excellent way to assess historic change and has great potential to provide methods for future monitoring.

Geothermal resources at YNP have been studied in several different ways in the past. Nearly 12,000 individual features in YNP have been catalogued since 1998 (Spatial Analysis Center, 2008). The next greatest concentration of geothermal features is estimated to be over 500 in Iceland and nearly 70 in New Zealand (Waring *et al.*, 1983). Rick Hutchinson, geologist for YNP from 1976 to 1996, spent many years studying the geothermal areas in YNP and during that time produced maps of geothermal area boundaries. Those maps have subsequently been updated and checked for accuracy by staff at YNP's Spatial Analysis Center to produce the most up-to-date digital map of defined geothermal areas (Spatial Analysis Center, 2005). Finally, chloride flux has been used as a proxy to determine convective heat flow in various regions of YNP (Fournier *et al.*, 1975; Norton and Friedman, 1985; Friedman and Norton, 2007). These studies can be used as guidelines for current and future studies.

Several ongoing studies are using airborne multi-spectral digital imagery to classify geothermal features in Norris Geyser Basin and surrounding area (Hardy, 2005; Seielstad and Queen, 2009) and Upper and Midway Geyser Basins and surrounding areas

(Neale, 2008). A method of quantifying the intensity of surficial geothermal activity in YNP was developed with 2004 Landsat imagery and has good potential for geothermal monitoring (Watson *et al.*, 2008). Portions of the Watson method were utilized in Chapter 2 in an attempt to map M_{terr} and GHF for YNP.

Landsat satellite imagery has been used successfully to perform many types of change analysis, making it a reasonable tool for monitoring M_{terr} at YNP over time. The short-wave infrared (SWIR) bands from the Landsat Thematic Mapper (TM) sensor could distinguish high-temperature fumarole vents and active lava bodies at Momotombo volcano in Nicaragua from 1989 to 1990 and Vulcano volcano in Italy from 1988 to 1989 (Oppenheimer *et al.*, 1993). GHF was used to detect lava flowing in tubes at Kilauea volcano in July and October of 1991 utilizing TM data and laboratory measurements (Harris *et al.*, 1998).

While most methods of change detection make comparisons of only two dates (Lu *et al.*, 2003), some recent studies have successfully analyzed change trends over multiple years. Change curves were developed with Landsat TM data to analyze change in vegetation on Mount St. Helens for 15 years following its eruption on 18 May 1980 (Lawrence and Ripple, 1999). Unsupervised statistical clustering was utilized to identify different vegetation cover trajectories (*e.g.*, slowly increasing cover in early years, and rapidly increasing cover in later years of the study period) (Lawrence and Ripple, 1999). Forest disturbance was detected and labeled with a trajectory-based change detection analysis of an 18-date time series of Landsat Enhanced Thematic Mapper Plus (ETM+) and TM data in Western Oregon (Kennedy *et al.*, 2007). Hypothesized temporal

trajectories were fit to the observed temporal trajectory of the SWIR band (band 5 of TM and ETM+) for each pixel in the image. The method effectively automated the delineation of four hypothesized change trajectories (Disturbance, Disturbance and Revegetation, Revegetation, and Revegetation to Stable State) over a 20-year time period (Kennedy *et al.*, 2007). There are no known multi-date or trajectory-based studies of geothermal heat in YNP.

The two main purposes of this project were: (1) to calculate M_{terr} in the defined geothermal areas of YNP for 14 different years, and (2) to assess the changes in spatial distribution of M_{terr} in YNP's defined geothermal areas over two decades. The value in this study lies in the near-annual observations of M_{terr} over multiple decades covering all defined geothermal areas in YNP. The few studies done in YNP previously on this topic have been for a single date (Watson *et al*., 2008) and/or over limited geographic areas (Hardy, 2005; Seielstad and Queen, 2009).

Methods

Study Area

YNP encompasses approximately 890,000 ha in Wyoming, Montana, and Idaho, USA (Figure 3.1). Elevation ranges from 1,567 m to 3,458 m (Spatial Analysis Center, 1998). Vegetation includes grassland, brushland, and forest, interspersed with bare ground. Average precipitation ranges from 25-30 cm in the lower elevations and up to 203 cm in the higher elevations (Spatial Analysis Center, 2000), with warm, dry summers and cold, wet winters (Western Regional Climate Center, 2005).

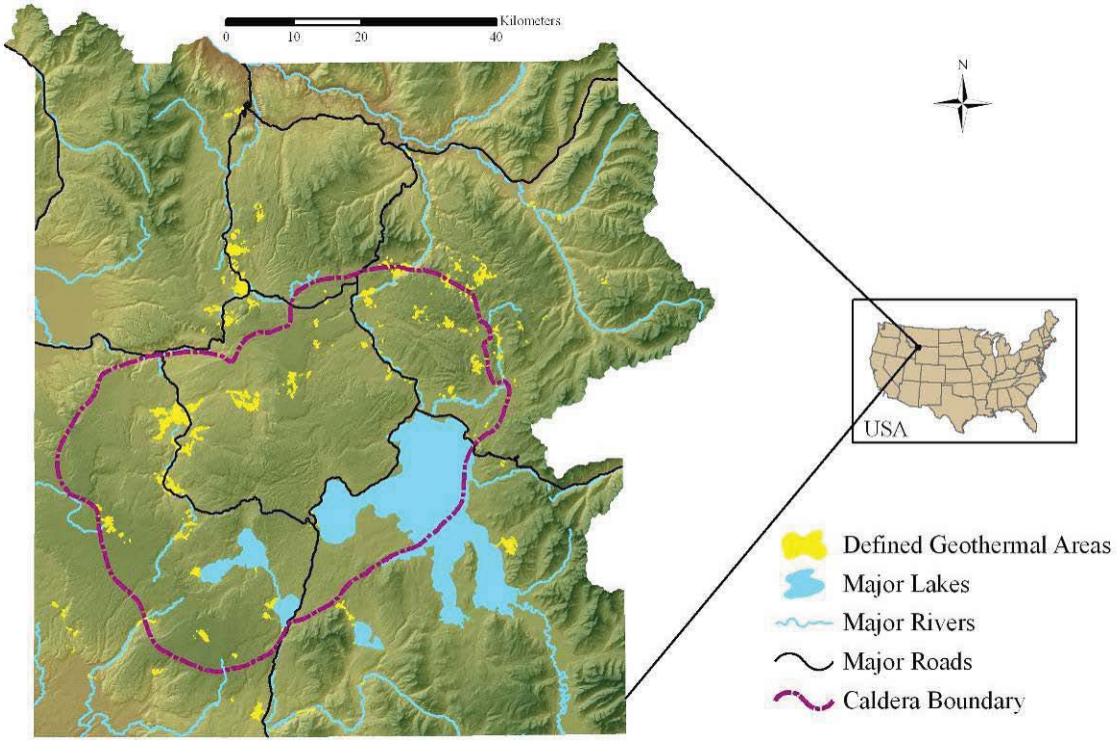

Figure 3.1: Location map for Yellowstone National Park and the currently defined geothermal areas displayed with a shaded relief background.

The currently defined geothermal areas, at 6,343 ha, comprise less than 1% of the entire area of YNP (Figure 3.1). More than 60% of the defined geothermal areas are within the 640,000-year-old caldera boundary. Elevation in these areas ranges from 1,728 m to 2,775 m (Spatial Analysis Center, 1998). The majority of the vegetation within geothermal areas is grassland, however, brushland, forest, and bare ground are also found. Average precipitation in the geothermal areas ranges from 35-203 cm (Spatial Analysis Center, 2000).

Data Acquisition

YNP is centered within one Landsat scene at Path 38 Row 29. Fourteen Landsat TM and Enhanced Thematic Mapper Plus (ETM+) summer images from 1986 to 2007

were acquired from various sources (Table 3.1). These images were chosen based on snow-free summer anniversary dates and lack of clouds. Image dates range from 25 June to 2 August resulting in anniversary dates within 5-½ weeks of one another. Two of the images are cloud free, while the remaining 12 have less than 5% cloud cover.

Table 3.1: Landsat images used in this study. Images marked with * are cloud free.

Acquisition Date (1980s)	**Sensor**	**Acquisition Date (1990s)**	**Sensor**	**Acquisition Date (2000s)**	**Sensor**
17 July 1986	TM5	15 July 1991	TM5	15 July 2000	ETM+
2 August 1989	TM4	12 July 1996	TM5	2 July 2001	ETM+
		15 July 1997	TM5	5 July 2002	ETM+
		18 July 1998	TM5	1 August 2003	TM5
		13 July 1999*	ETM+	21 July 2005*	TM5
				8 July 2006	TM5
				25 June 2007	TM5

Several ancillary data sets were required for analysis. A 30-m digital elevation model (DEM) and digital spatial data of the defined geothermal areas were provided by YNP. Digital spatial hydrology data were downloaded from the USGS National Hydrology Dataset (NHD) (USGS, 2008). Geologic fault data were downloaded from a USGS Open File Report (Christiansen and Wahl, 1999). Earthquake data were downloaded for all years in the study from the Yellowstone Volcano Observatory/University of Utah Earthquake Information Center (University of Utah, 2009). Information included with each earthquake was (1) location, (2) date, (3) time, and (4) magnitude. Magnitude values were converted to linear amplitude by taking 10 to the power of the magnitude (*i.e.*, if the magnitude was 2.24, amplitude = $10^{2.24}$ = 173.78). Average air temperature and precipitation information was downloaded from the Canyon

SNOTEL (SNOwpack TELemetry) site since it was the station nearest the center of YNP that had data for the entire study period (NRCS, 2009).

Image Preprocessing

Geometric registration of all images is vital when comparing different images in a change analysis. A "master" TM image (7 September 2005; downloaded from MontanaView; CC resampling) was chosen that aligned well with National Agriculture Imagery Program (NAIP) imagery (root mean square error (RMSE) = 0.4128 pixels, or less than 15 m) and roads and trails data recorded with high-precision GPS units by YNP staff. The 14 summer images used for this project were geometrically registered to the master image, with an RMSE for each registration of less than 0.5 pixels (15 m).

Each image was clipped to the defined geothermal area boundaries study area. Clouds and snow were masked manually through on-screen digitizing. The methods described in Chapter 2 to calculate M_{terr} from the red, near-infrared (NIR), and thermal-infrared (TIR) Landsat bands were followed, including atmospheric and radiometric correction (Chavez, 1996; Utah State University, 2008), estimating emissivity per pixel (Brunsell and Gillies, 2002) (Equations 2.1 and 2.2), and calculating M_{terr} (Watson *et al.*, 2008) (Equations 2.5 – 2.8). All resulting M_{terr} images had 120-m spatial resolution.

Thirteen M_{terr} difference (ΔM_{terr}) images were created by subtracting the absolute value of a pixel in one image from the absolute value of the same pixel in the next image (*e.g.*, 1989 image value minus 1986 image value). Absolute difference was calculated rather than relative difference because change in any direction would be informative to

the main questions of the study, and it is likely that triggers of geothermal change might cause increases in heat flow in some areas and decreases in others.

The sensitivity of calculated M_{terr} to a change of one raw digital number (DN)(the original Landsat band values that range from 0 to 255) was calculated by finding the average value of M_{terr} change per one DN change for each year. This sensitivity value is highly dependent on actual ground temperature since emittance is related to temperature to the 4^{th} power in the Stefan-Boltzman Law ($M = \varepsilon\sigma T^4$, where M is emittance, ε is emissivity, $\sigma = 5.67 \text{ X } 10^{-8}$ $Wm^{-2}K^{-4}$, and T is temperature in units Kelvin); thus sensitivity was calculated by finding the difference in M_{terr} for all pairs of DNs with a difference of one, then averaging those differences across the image.

Change Analysis

Any pixel covered with snow or clouds in any of the 14 images was excluded from the change analysis. The multitemporal data were clustered using the unsupervised ISODATA algorithm to create 24 clusters based on temporal change, rather than spatial location (Figure 3.2). Each pixel can be plotted as an M_{terr} value for each date in multiple temporal dimensions. A location with low M_{terr} values for all dates, for example, would be located graphically near the origin, while a location with high M_{terr} values for all dates would be located graphically far from the origin on all temporal axes (Figure 3.2). These temporal clusters are not necessarily spatially contiguous, but rather are groups of pixels that have similar temporal patterns regardless of geographic location. Summary statistics of the clusters were tabulated and graphed to examine the data for trends over the 21-year period. The cluster means were normalized by subtracting the mean M_{terr} value for each

date in order to account for overall trends in the data and focus on geothermal change. Linear regression models were computed with the mean M_{terr} as the response variable and air temperature and precipitation from Canyon SNOTEL data as the predictor variables to determine correlation. The trajectories of individual clusters were examined visually for trends or anomalous patterns.

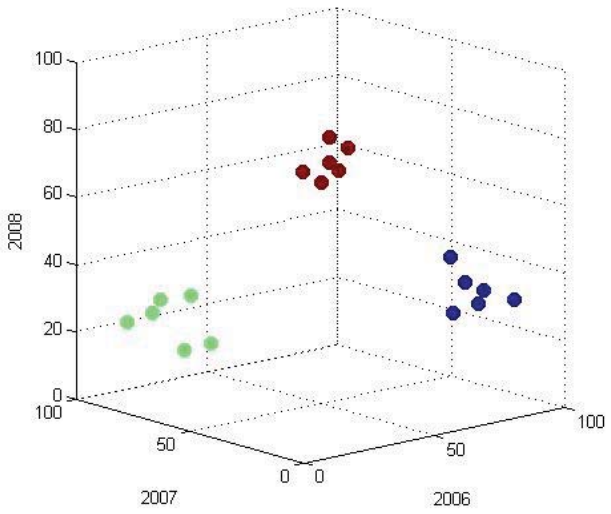

Figure 3.2: Three example temporal clusters for the time period from 2006 to 2008. Values are unitless and based on randomly generated artificial data. Cluster A (in blue) starts high in 2006, dramatically decreases in 2007 and remains fairly low in 2008. Cluster B (in green) starts low in 2006, dramatically increases in 2007, and dramatically decreases in 2008. Cluster C (in red) starts high in 2006, stays high in 2007, and decreases in 2008.

Twenty spatial groupings, each defined by YNP as "gross location of the thermal area within the park" (Spatial Analysis Center, 2005) and encompassing no less than 144,000 m^2, were analyzed in the same manner as the 24 clusters. Several of the groupings were selected for additional analysis to compare to one another over the 21-year period because of their hypothetical relationships or lack thereof (*e.g.*, it is speculated that Mammoth Hot Springs and Norris Geyser Basin "share plumbing" (Bargar, 1978; White *et al.*, 1988), and it is also speculated that geothermal activity

within the caldera differs from that without (Pierce and Morgan, 1992; Morgan *et al.*, 2003)).

Comparison to Known Change Events

Where change has been documented (Table 3.2), 9 pixels (1 pixel where the feature resides, and the 8 surrounding pixels) were extracted from each date in the 14-component multitemporal image to examine their trajectories against known change. These data were normalized in the same manner as the temporal clusters and spatial groupings. Graphs of the normalized M_{terr} over time were plotted and examined for expected trajectories of change. These were also compared to the trajectory of the average of 9 random pixels from Brimstone Basin, where there has been no geothermal heat emitted for over 100 years (Langford, 1972), and therefore very little change should be observed. In addition, GHF_{α} was calculated for Brimstone Basin and normalized in the same manner as above so its trajectory could be compared to the normalized M_{terr} trajectory to verify that M_{terr} was the appropriate choice of model to use for change analysis.

Table 3.2: Known change events in geothermal activity in Yellowstone National Park.

Date(s) of change	Location of change	Description of change
Summer 1998	Narrow Gauge Spring in Mammoth Hot Springs	New feature appeared and began spreading over trail
1999	Minerva Terrace in Mammoth Hot Springs	Water stopped flowing and heat was no longer emitted
July 2003	Porkchop Geyser in Norris Geyser Basin	Increased ground temperature; trail closed and rerouted
July and September 2006	Jewel Geyser in Biscuit Basin	Possible hydrothermal explosions

All of the geothermal features listed in Table 3.2 are considerably less than one pixel in extent. There are several potential barriers to the study of known change events with Landsat data. The changes witnessed on the ground in features only meters in size might not be discernable in a pixel of 120-m size. The changes also might not be detectable with the temporal resolution used. The changes might have lasted only days, weeks, or months, but not have occurred near enough to an image date to be sensed by the Landsat sensor. These features, although much smaller than the spatial resolution of Landsat data, were inspected to determine whether Landsat data were sensitive enough to detect these known changes and possibly other undocumented changes.

Spatial Pattern Analysis

Several images were created that represented distance to potentially important features, including geologic faults, large water bodies (defined as 14,400 m^2 or larger (at least one 120-m pixel)), and earthquake swarms (Figures 3.3, 3.4, and 3.5). The linear nature of geologic faults, if associated with M_{terr}, might be visible in the spatial patterns of M_{terr}. During periods of drought, large water bodies might be the best source of groundwater recharge, thus increased distance from large water bodies could affect the spatial patterns of M_{terr}. Earthquakes, both near and far, have been shown to affect the behavior of geothermal features in YNP (Rojstaczer *et al*., 2003; Husen *et al*., 2004).

Earthquake swarms are typically defined as a group of consecutive seismic events within a relatively short time period with no identifiable main shock (Spicak, 2000). For this study, in order to find at least one swarm per year, earthquake swarms were defined as (a) three or more earthquakes of any magnitude (b) within one week of each other (c)

in an obvious visual spatial cluster (d) with a maximum distance between earthquakes of 3 km and (e) a lag time between the last earthquake and the image date of no more than 100 days (in order to observe expected ground water changes for several weeks to months after an earthquake (Rojstaczer and Wolf, 1992; Rojstaczer *et al*., 1995)). The output values of the distance images represented the distance in number of pixels to the nearest feature of interest. Mean distances to the features were tabulated for the 24 temporal clusters and 20 spatial groupings to determine which clusters and spatial groupings were nearest to the potentially important features of interest.

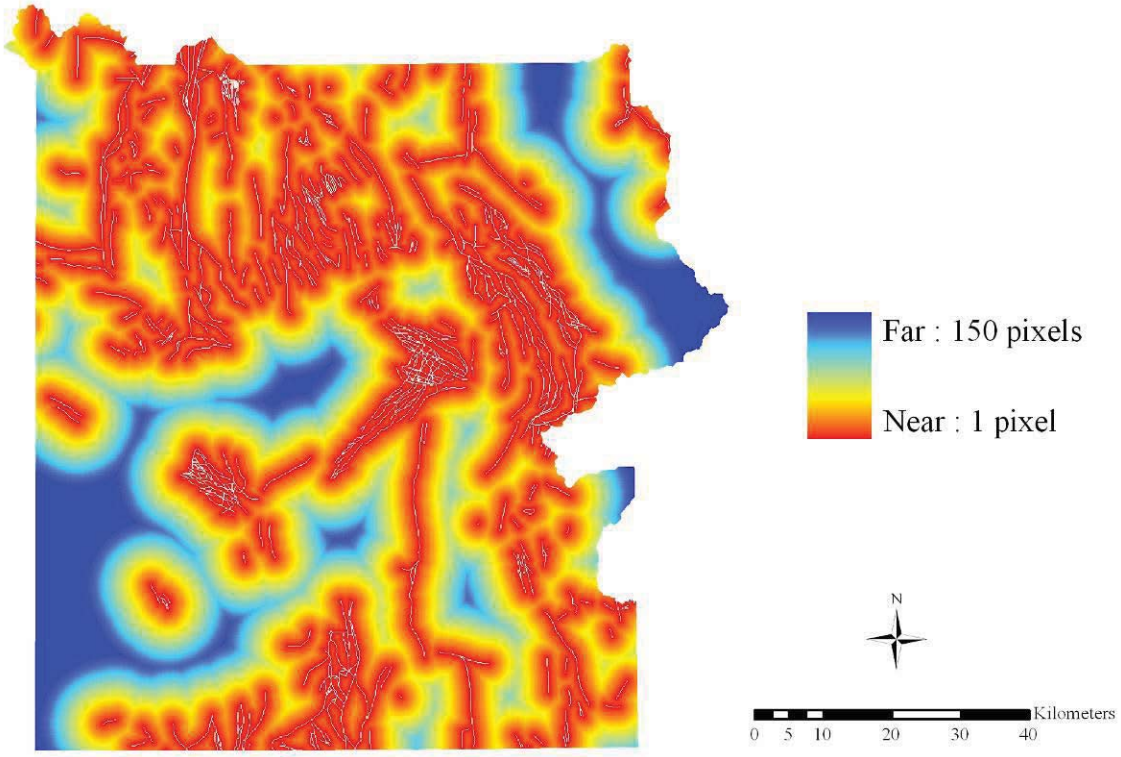

Figure 3.3: Distance to geologic faults from every pixel in Yellowstone National Park. White pixels coincide with geologic faults.

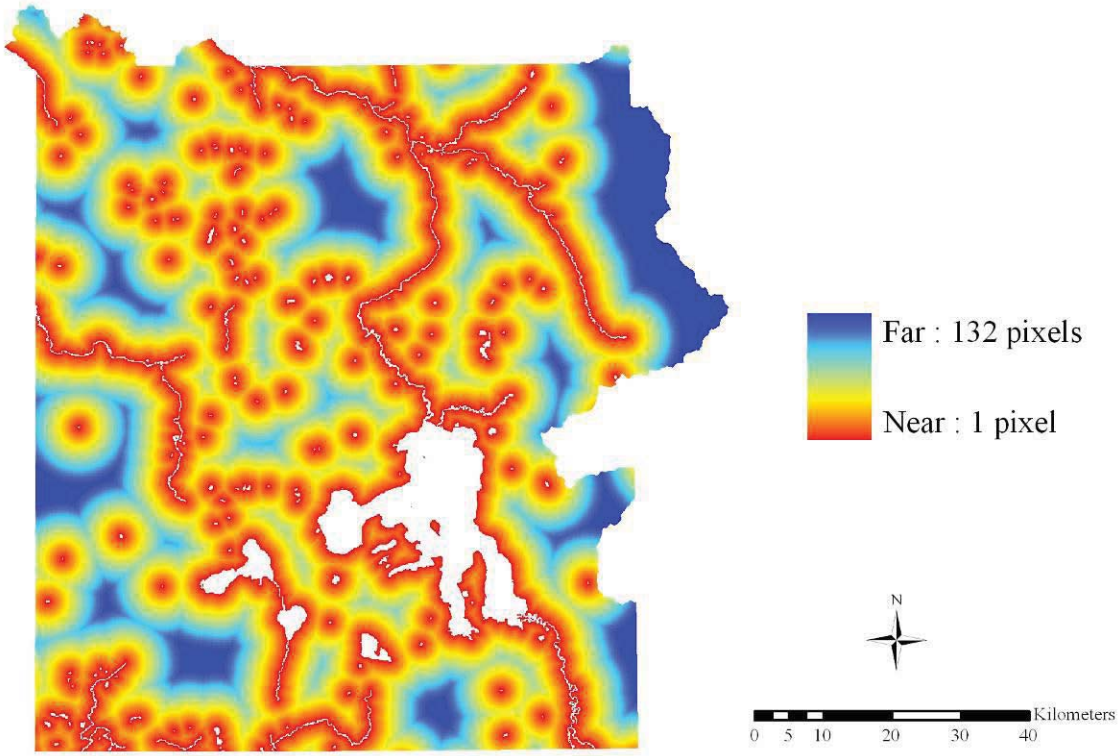

Figure 3.4: Distance to large water bodies from every pixel in Yellowstone National Park. White pixels coincide with large water bodies.

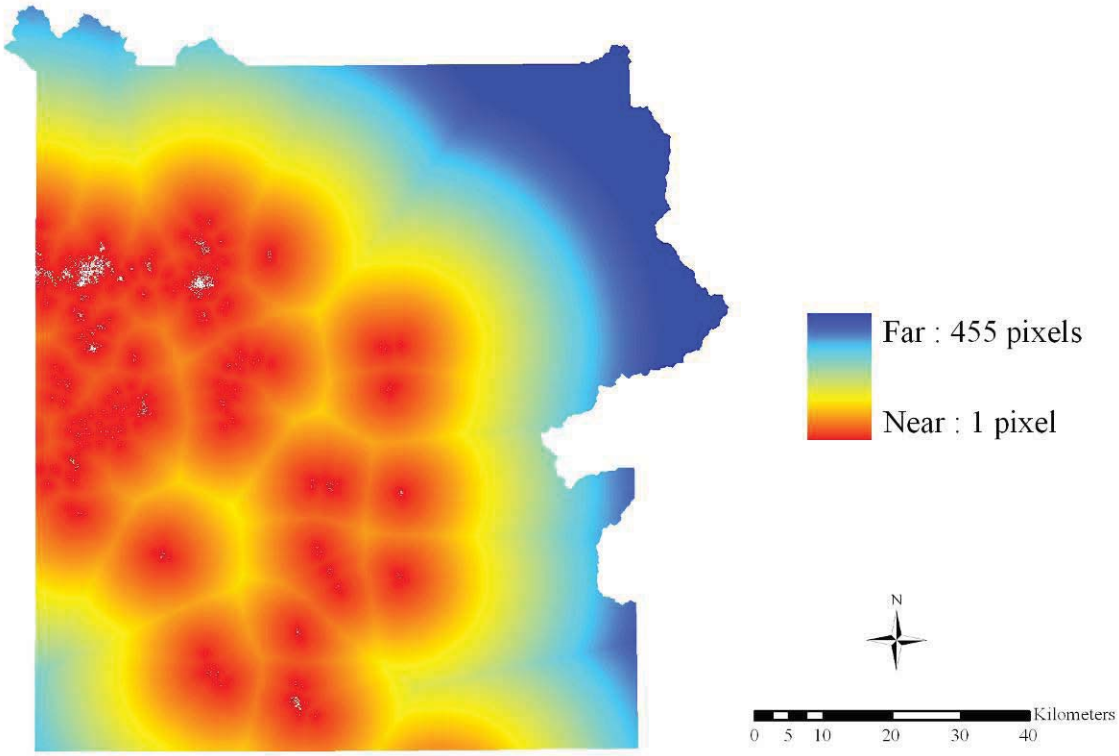

Figure 3.5: Distance to earthquake swarms from every pixel in Yellowstone National Park. White pixels coincide with earthquakes.

Three or more earthquake swarms were identified for each of 12 study years, totaling 71 swarms (yearly swarm statistics are in Table 3.3; all 71 swarms are listed in Appendix A). No swarms were identified for 1986 since it was the earliest image and there was no earlier image from which to assess change, or for 1989 since there were no earthquakes that fit the definition of a swarm during that year. A distance to swarm image was created for each of the 71 swarms and subsequently clipped to the spatial groupings boundaries so that the number of pixels to be examined was 7,431.

Table 3.3: Earthquake swarm information by year. Values were derived from information from each of the 71 earthquake swarms.

Year	Number of swarms	Highest number of earthquakes	Highest maximum amplitude	Highest mean amplitude	Highest median amplitude	Longest duration (days)	Shortest duration (days)	Longest lag time (days)	Shortest lag time (days)
2007	5	26	43.65	17.92	12.17	28	1	79	5
2006	8	76	316.23	23.79	7.85	23	1	94	5
2005	6	49	812.83	79.85	31.62	16	1	91	5
2003	6	14	28.84	14.84	14.13	22	1	81	8
2002	8	31	34.67	18.95	20.42	16	1	98	4
2001	8	39	302.00	243.11	234.42	24	1	73	2
2000	5	30	9,549.93	1,121.52	138.04	20	1	51	3
1999	7	746	17,782.79	1,670.22	251.19	30	1	82	1
1998	3	39	758.58	284.32	269.15	15	1	38	2
1997	7	356	48,977.88	1,087.12	691.83	37	1	68	1
1996	5	25	6,918.31	1,928.03	758.58	21	1	47	1
1991	3	7	1,023.29	462.05	338.84	2	1	72	5

The correlation of earthquake swarm characteristics to ΔM_{terr} was tested with regression analyses of spatial grouping swarm data that had seven predictor variables (distance to swarm, number of earthquakes in the swarm, maximum amplitude, mean amplitude, median amplitude, duration of the swarm, and lag time between final earthquake and image date) and one response variable (ΔM_{terr}). All 71 swarms could not be used in one regression analysis since multiple swarms per year would not add true variance, but instead duplicate the response variable. The most important swarm per year, therefore, was chosen for eight different backwards and forwards stepwise regression analyses based on the following selection criteria: (1) most earthquakes, (2) highest maximum amplitude, (3) highest mean amplitude, (4) highest median amplitude,

(5) longest duration of swarm, (6) shortest duration of swarm, (7) longest lag time, and (8) shortest lag time.

Results

Terrestrial Emittance

The highest M_{terr} value calculated for all the study years was the maximum for 1999 at 440.53 Wm^{-2}, while the lowest value was the minimum for 1986 at 306.21 Wm^{-2} (Table 3.4 and Figure 3.6). The highest average M_{terr} value was 389.62 in 2000. The general pattern of mean M_{terr} values shows an increase up to 2000 and a subsequent decrease. Images of M_{terr} for all 14 dates can be seen in Appendix B.

Table 3.4: Summary statistics of terrestrial emittance (M_{terr}) calculations in the defined geothermal areas for each of the 14 years in the 21-year study period (Wm^{-2}). A pattern emerges with a general increase in M_{terr} up to 2000 followed by a general decrease in M_{terr}.

Year	Min	Max	Mean	Median	Mode	Std. Dev.
1986	306.21	384.84	328.17	328.32	324.64	7.68
1989	310.34	402.57	338.10	336.64	338.44	12.37
1991	324.80	414.57	361.96	360.57	351.45	13.19
1996	322.72	399.77	359.09	358.24	368.77	13.41
1997	313.82	412.18	355.84	354.55	363.38	11.98
1998	325.28	424.73	369.23	368.01	378.11	12.43
1999	336.70	440.53	386.95	386.18	386.59	14.81
2000	343.55	436.98	389.62	388.81	381.87	14.32
2001	314.83	440.28	382.79	381.48	374.62	14.84
2002	331.11	426.66	377.11	376.27	375.90	14.73
2003	331.01	434.25	372.87	372.14	379.00	14.34
2005	321.32	427.22	378.01	376.75	373.86	14.82
2006	325.74	409.08	359.08	358.94	364.48	11.09
2007	313.55	413.58	359.76	359.66	359.66	10.81

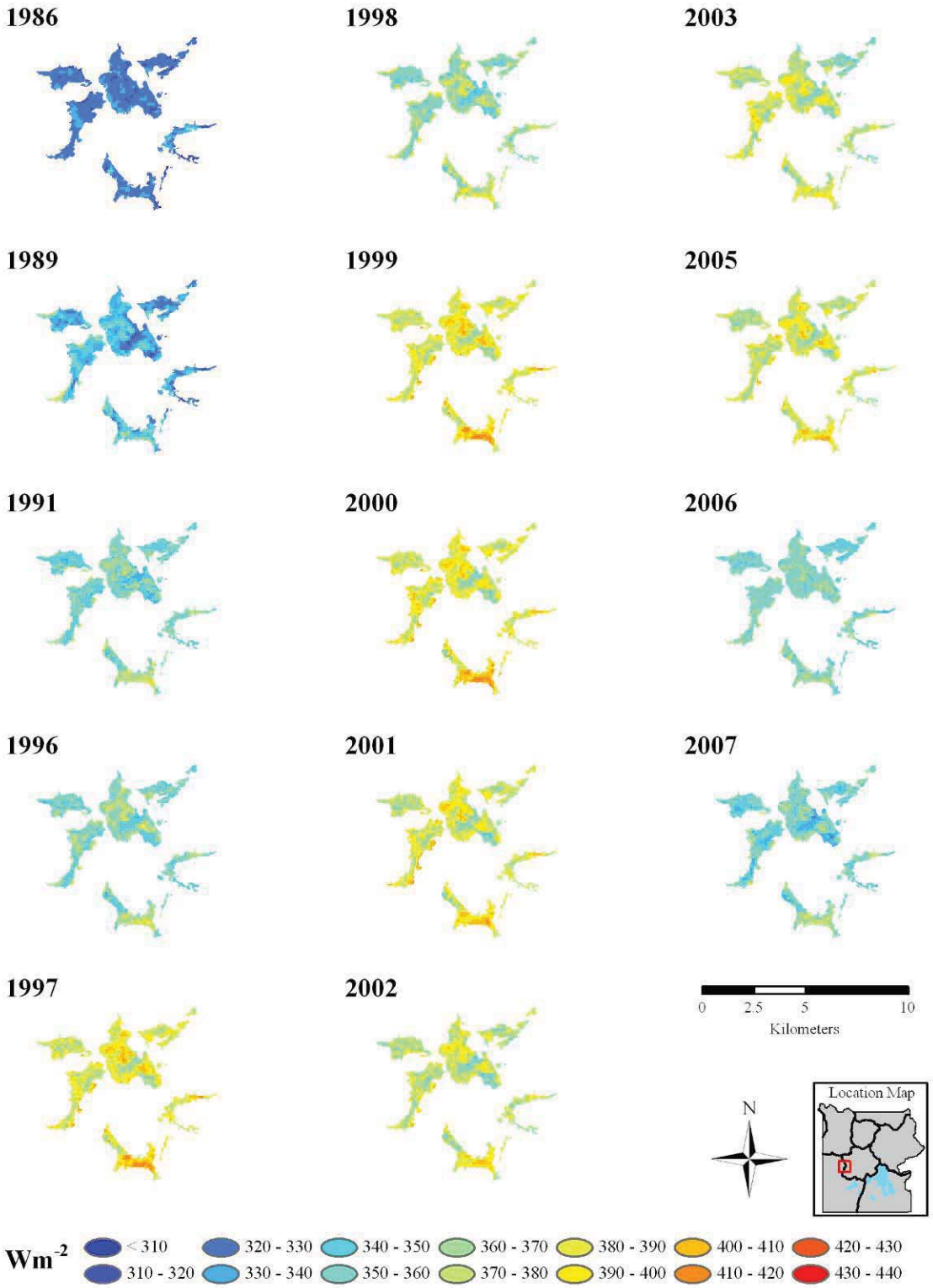

Figure 3.6: Terrestrial emittance (M_{terr}) values for Lower Geyser Basin for each of the 14 years in the 21-year study period. A pattern emerges with a general increase in M_{terr} up to 2000 followed by a general decrease in M_{terr}.

Change Analysis

The average sensitivity of M_{terr} for a change of one DN over the 14 years of imagery was 1.14 Wm^{-2}. The sensitivity ranged from -18.35 to 16.38 Wm^{-2}. The negative sensitivity values were a result of emissivity differences at each pixel.

The 24 temporal clusters ranged in size from 662,400 m^2 to 4,492,800 m^2. The 20 spatial groupings ranged from 489,600 m^2 in the Tower Junction group to 20,044,800 m^2 in the Mirror Plateau group. The trajectories of temporal clusters and spatial groupings were similar in shape, with a general upward trend to 2000 and a subsequent downward trend with substantial inter-annual variation (Figures 3.7 and 3.8) (Individual trajectory graphs are located in Appendix C and Appendix D). The overall trend of both the clusters and the spatial groupings showed increases of approximately 20 to 40 Wm^{-2} from 1986 to 2007.

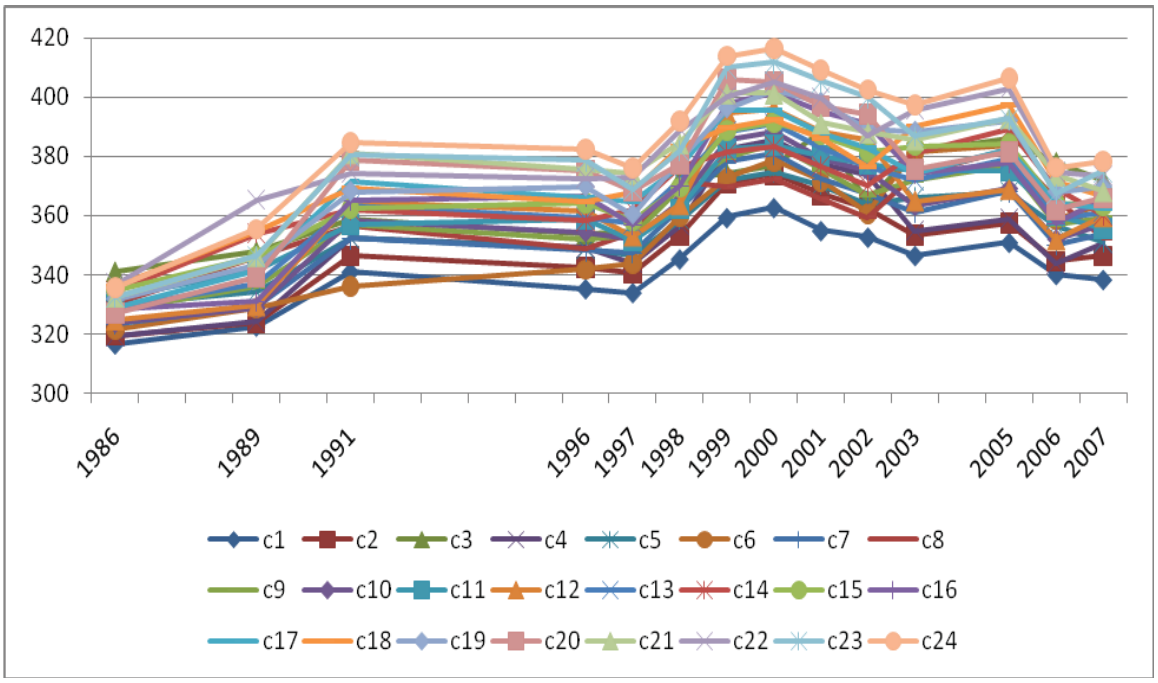

Figure 3.7: Trajectories of 24 temporal clusters of 14 dates of terrestrial emittance (M_{terr})(Wm^{-2}). Each trajectory follows a similar general pattern, increasing to 2000 and decreasing to 2007.

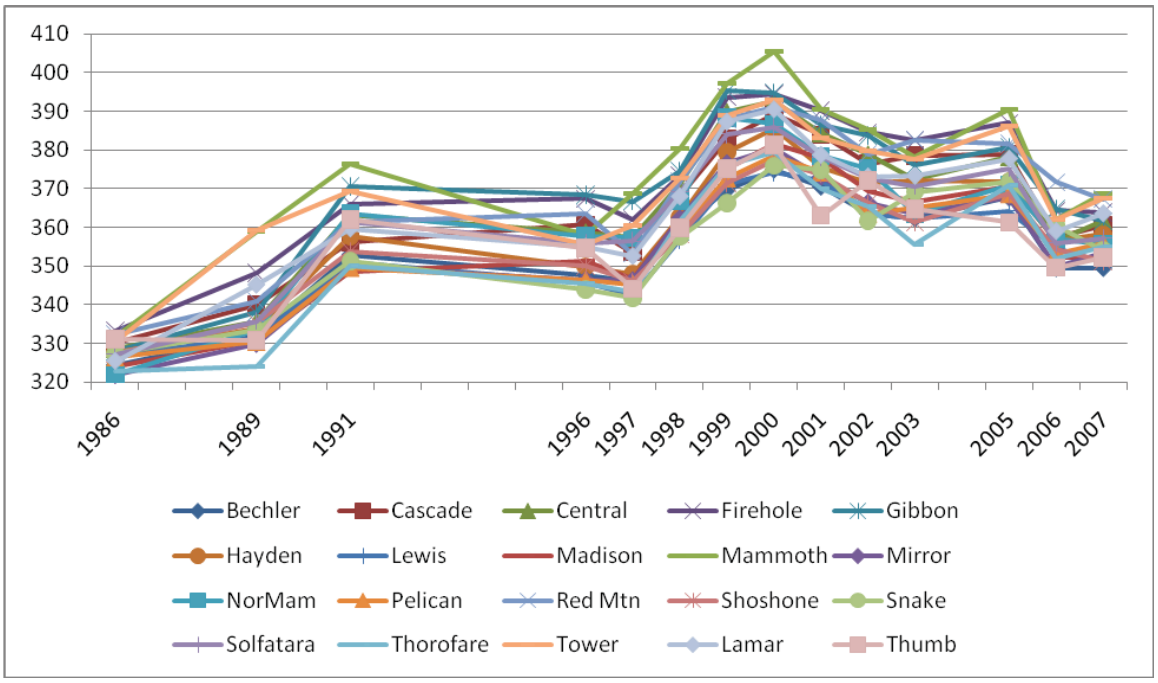

Figure 3.8: Trajectories of 20 spatial groupings of 14 dates of terrestrial emittance (M_{terr})(Wm^{-2}). Each trajectory follows a similar general pattern, increasing to 2000 and decreasing to 2007.

Part of the overall trend might be explained by differences in air temperature. The average temperature in °C for the week prior to the date of each image was obtained from the Canyon SNOTEL data (Table 3.5). A linear regression model with mean M_{terr} as the response variable and the SNOTEL air temperature as the predictor variable was computed for the clusters and for the spatial groupings. The resulting R^2 for the clusters was 0.2636, while the R^2 for the spatial groupings was 0.2607. When percent of normal water-year-to-date precipitation for the image date was added to either regression, there was little improvement.

Table 3.5: Average terrestrial emittance (M_{terr}) in Wm^{-2}, air temperature in °C, and percent of normal precipitation for 14 image dates. The average M_{terr} values are slightly different for the spatial groupings since fewer pixels were used than in the clusters.

Date	M_{terr} clusters	M_{terr} spatial groupings	Temperature	% Precipitation
2 August 1989	338.1	338.2	12.9	100.0
15 July 1991	362.0	362.0	12.0	103.1
12 July 1996	359.1	359.2	13.8	130.4
15 July 1997	355.8	356.0	10.5	139.3
18 July 1998	369.2	369.3	14.9	97.2
13 July 1999	387.0	387.2	13.3	112.7
15 July 2000	389.6	389.8	13.8	96.5
2 July 2001	382.8	382.9	15.0	81.8
5 July 2002	377.1	377.3	14.9	94.4
1 August 2003	372.9	372.9	16.0	84.5
21 July 2005	378.0	378.0	15.5	76.6
8 July 2006	359.1	359.0	13.4	91.9
25 June 2007	359.8	359.8	12.6	85.7

The M_{terr} data were normalized by removing the background variability explained by air temperature as well as other unknown factors by subtracting individual M_{terr} date means from the cluster means (Figures 3.9 and 3.10) (Individual trajectory graphs are

located in Appendix E and Appendix F). The clusters and spatial groupings showed more variability after normalizing for background effects. Cluster 6 appeared to have the largest variation of the temporal clusters (lowest measurement of -26 Wm^{-2} in 1991 and highest measurement of 8 Wm^{-2} in 2003), with a range of 34.1 Wm^{-2}. The Tower Junction spatial group appeared to have the largest variation of the spatial groupings (lowest measurement of -4 Wm^{-2} in 1996 and highest measurement of 21 Wm^{-2} in 1989), with a range of 24.8 Wm^{-2}.

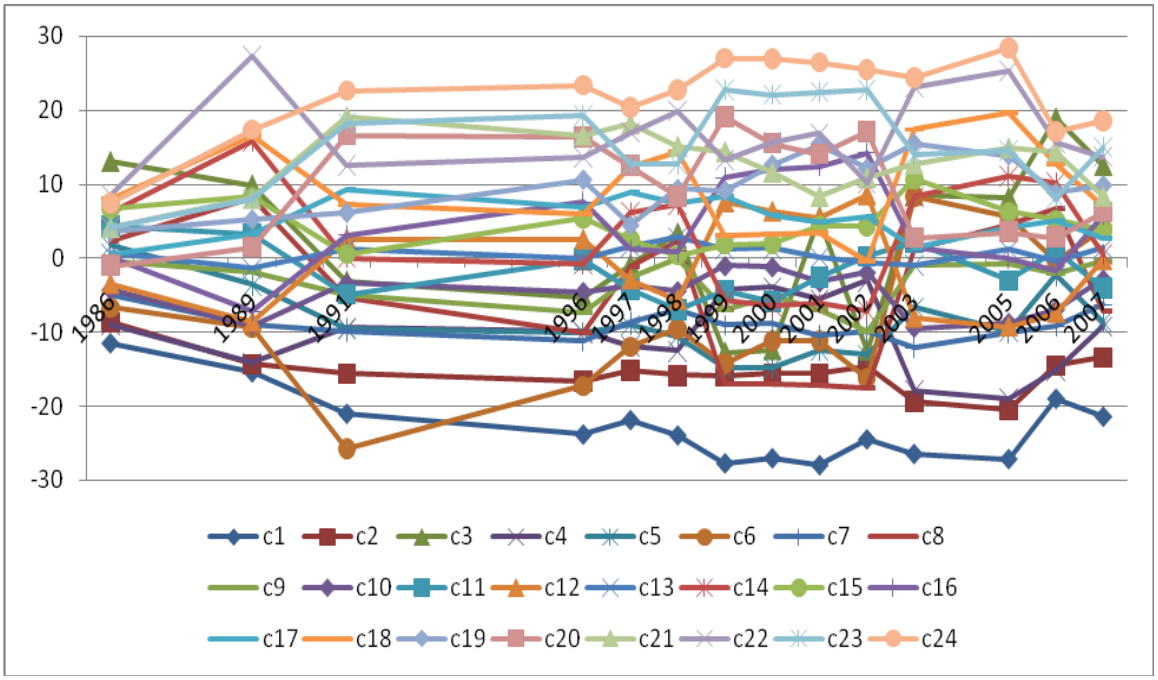

Figure 3.9: Trajectories of 24 temporal clusters, normalized by terrestrial emittance (M_{terr}) date mean. Y-axis is difference from the date mean in Wm^{-2}. Cluster 6 appears to have the largest variation, with a range of 34.1 Wm^{-2}.

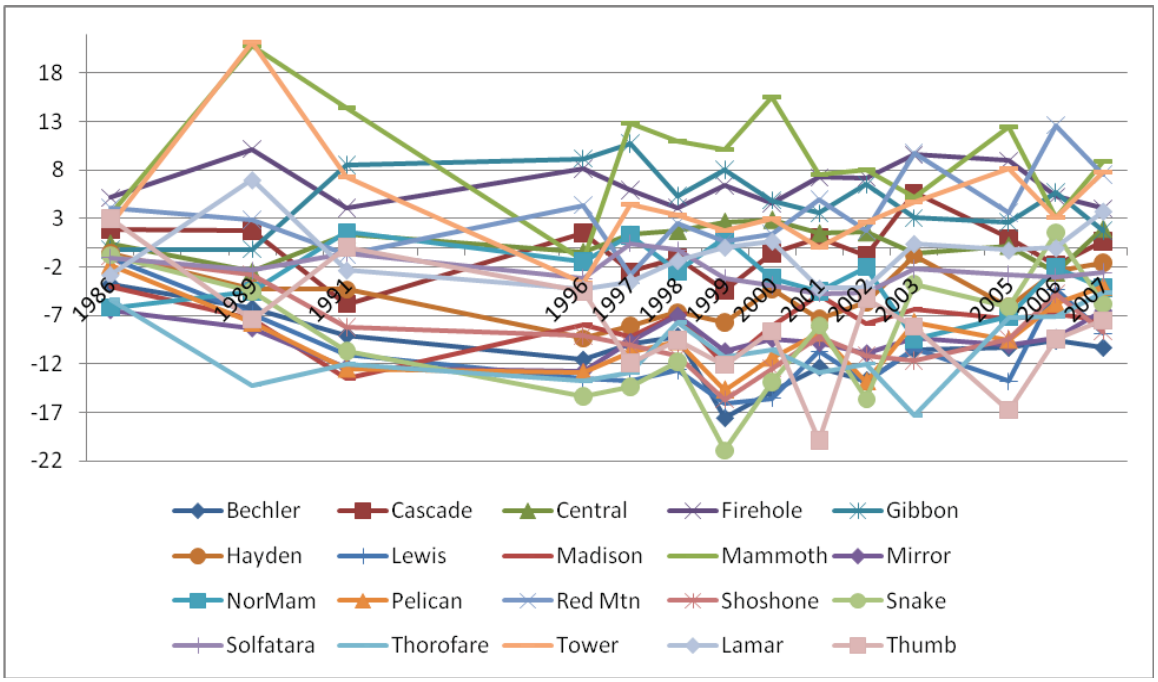

Figure 3.10: Trajectories of 20 spatial groupings, normalized by terrestrial emittance (M_{terr}) date mean. Y-axis is difference from the date mean in Wm^{-2}. The Tower Junction group appears to have the largest variation with a range of 24.8 Wm^{-2}.

Clusters were separated into groups of similar normalized trends (Figure 3.11), while the spatial groupings were separated by suggested relationships (Figure 3.12) (*e.g.*, Bargar (1978) and White *et al*. (1988) speculate that Mammoth Hot Springs and Norris Geyser Basin "share plumbing", and Pierce and Morgan (1992) and Morgan *et al*. (2003) speculate that geothermal activity within the caldera differs from that without) for further examination of trajectories. The clusters appeared to differentiate primarily with respect to mean M_{terr} and not visible changes on the ground over time. The spatial grouping trajectories appeared to show dramatic differences between spatial groupings, although, after further visual inspection, these changes did not represent dramatic visual differences on the ground (*e.g.*, dead vegetation where M_{terr} increased substantially).

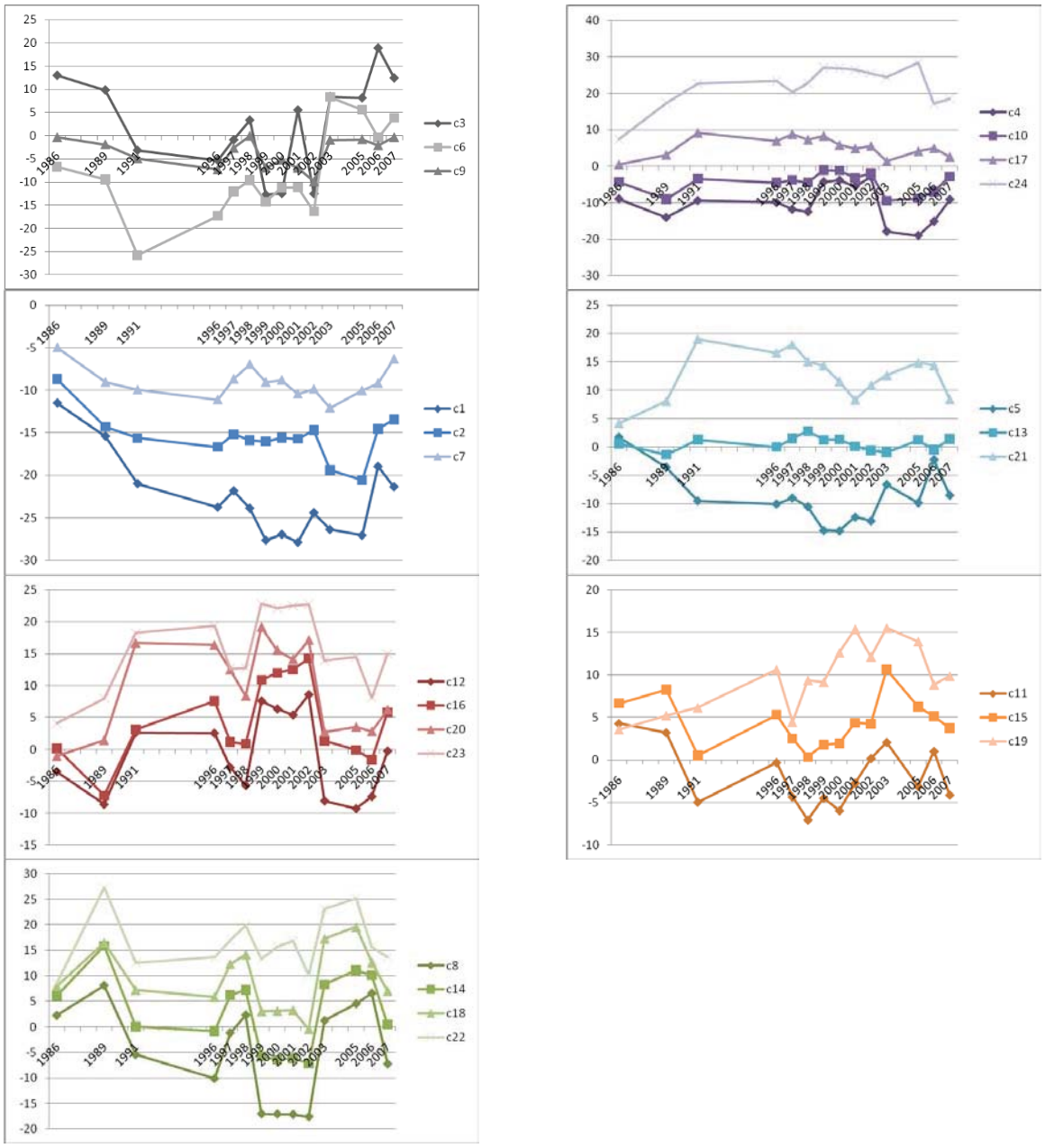

Figure 3.11: 24 normalized temporal clusters grouped by trajectory. Y-axis is difference from the date mean in Wm^{-2}.

a. Gibbon Canyon, Mammoth Area, and Norris-Mammoth Corridor

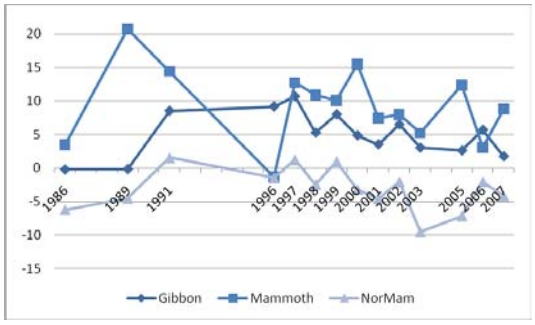

b. Firehole River Drainage and Gibbon Canyon

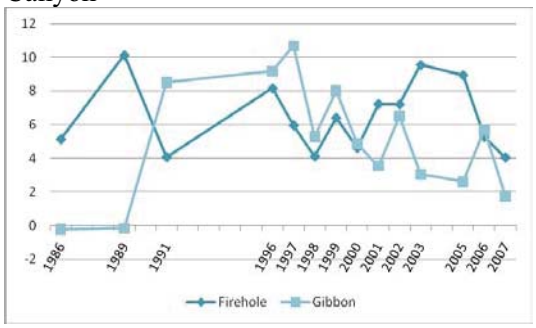

c. Lewis Canyon and Madison Plateau

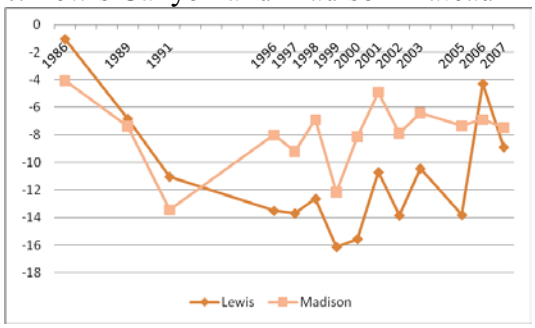

Figure 3.12: Normalized terrestrial emittance (M_{terr}) trajectories for (a) Gibbon Canyon, Mammoth Area, and Norris-Mammoth Corridor; (b) Firehole River Drainage and Gibbon Canyon; (c) Lewis Canyon and Madison Plateau. Y-axis is difference from the date mean in Wm^{-2}.

The Gibbon Canyon group and the Norris Mammoth Corridor group appear to have similar trajectories over the 21-year period, with slight differences in direction from 1991 to 1996 and 2003 to 2005, and a correlation of 0.802 (Figure 3.12.a). The Mammoth Area group trajectory, on the other hand, is not similar to and has low correlations with Gibbon Canyon (-0.137) and Norris Mammoth Corridor (0.149) trajectories (Figure 3.12.a). The trajectories of the Firehole River Drainage group that lies completely within the caldera boundary and the Gibbon Canyon group that lies completely outside the caldera boundary have a correlation of -0.235 yet are similar in that both are warmer than average (except for the first two negative values for Gibbon

Canyon) (Figure 3.12.b). The trajectories are also similar in direction of change from 1997 to 2000 but have few similarities beyond this. The trajectories of the Lewis Canyon group (outside the caldera) and the Madison Plateau group (inside the caldera) have a correlation of 0.527 and are similar in that they are both negative values and have almost identical directions of change (Figure 3.12.c). The differences lie in the direction of change between 1991 and 1996 and the magnitude of change, especially from 2005 to 2006.

Comparison to Known Change Events

Institutional knowledge of changes in geothermal activity was compared to changes in M_{terr} values over time. In the Mammoth Hot Springs area, a large spring near Narrow Gauge appeared during the summer of 1998. An increase in M_{terr} from 1998 to 1999 was observed at Narrow gauge and surrounding areas (Figure 3.13.a). Also in Mammoth Hot Springs, water stopped flowing and steam stopped being emitted at Minerva Terrace in 1999. It remains inactive today (May 2009). A decrease in M_{terr} from 1998 to 1999 was observed at Minerva Terrace, with a very slight decrease in the surrounding area (Figure 3.13.b).

a. Narrow Gauge Spring (range = 23 Wm^{-2})

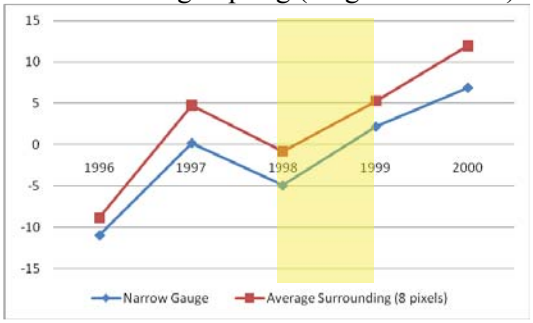

b. Minerva Terraces (range = 28 Wm^{-2})

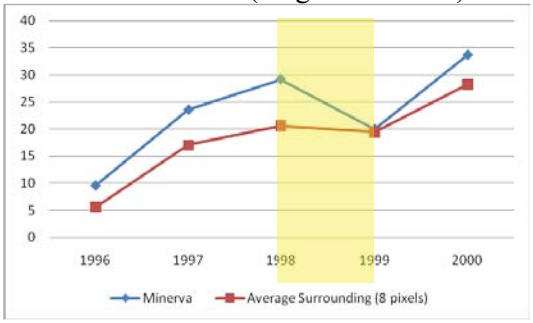

c. Porkchop Geyser (range = 13 Wm^{-2})

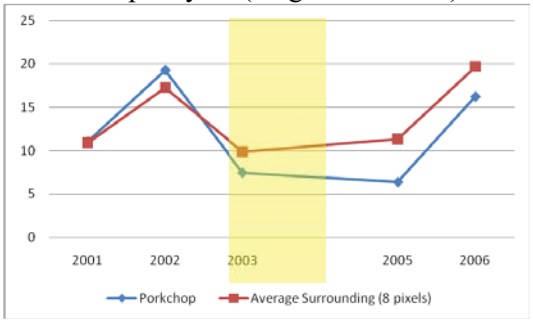

d. Jewel Geyser (range = 21 Wm^{-2})

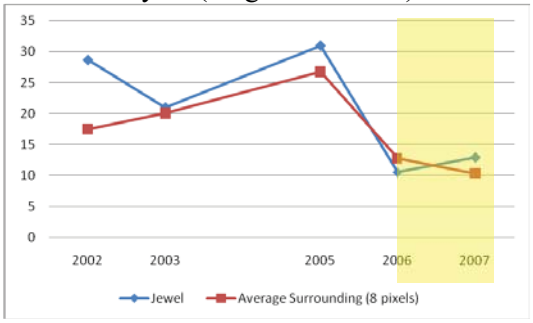

e. Brimstone Basin M_{terr} (range = 12 Wm^{-2})

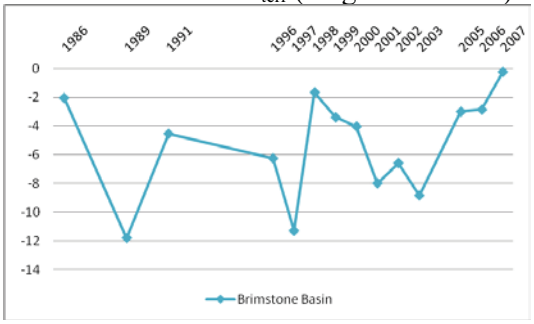

f. Brimstone Basin GHF_{α} (range = 87 Wm^{-2})

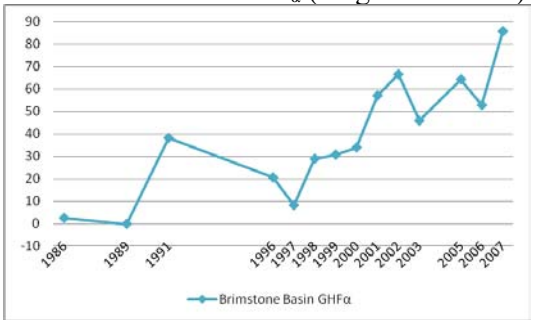

Figure 3.13: Changes in terrestrial emittance (M_{terr}) at (a) Narrow Gauge in Mammoth Hot Springs; (b) Minerva Terraces in Mammoth Hot Springs; (c) Porkchop Geyser in Norris Geyser Basin; (d) Jewel Geyser in Biscuit Basin; (e) Brimstone Basin; (f) Brimstone Basin GHFα. Y-axis is difference from the date mean in Wm^{-2}. Known change events are highlighted in yellow.

During the summer of 2003 the ground near Porkchop Geyser in Norris Geyser Basin increased in temperature enough that YNP staff were required to close parts of the path and build boardwalks so visitors would not burn their feet. A decrease in M_{terr} from 2002 to 2003 and a very slight decrease from 2003 to 2005 were observed in the pixel that contained Porkchop Geyser, while there was a slight increase from 2003 to 2005 in the surrounding area (Figure 3.13.c). Whether an increase occurred between 2003 and 2004 is unknown because of the lack of imagery from 2004. Both the pixel that contained Porkchop Geyser and the surrounding area showed a large increase from 2005 to 2006.

Possible hydrothermal explosions occurred near Jewel Geyser in Biscuit Basin on 14 July 2006 and 23 September 2006. The 2006 Landsat image was acquired on 8 July, six days prior to the first geothermal event. A decrease in M_{terr} values near Jewel Geyser from 2005 to 2006 and a continued but less significant decrease from 2006 to 2007 were observed, while the pixel that contained Jewel Geyser actually increased slightly from 2006 to 2007 (Figure 3.13.d).

Brimstone Basin, was geothermally inactive during the study period, and therefore should have relatively constant emittance, except for solar radiation effects, but does indicate some M_{terr} variability during the study period (Figure 3.13.e). When the ranges of change and means of M_{terr} for the five locations above were compared, Brimstone Basin had the smallest range of values as well as the smallest mean (Table 3.6). The range of change of GHF_{α} in Brimstone Basin, however, was nearly 8 times

larger than that of M_{terr} (Table 3.6) and the trajectory had a distinct upward trend (Figure 3.13.f).

Table 3.6: Summary statistics of changes in terrestrial emittance (M_{terr}) for 1 pixel and 9 pixels surrounding Narrow Gauge (NG), Minerva Terrace (Min), Porkchop Geyser (PC), and Jewel Geyser (Jwl), and terrestrial emittance (M_{terr}) and albedo and potential annual direct incident solar radiation corrected geothermal heat flux (GHF_{α}) of 9 pixels in Brimstone Basin (Brs). Values are difference from the date mean in Wm^{-2}.

	NG (1)	**NG (9)**	**Min (1)**	**Min (9)**	**PC (1)**	**PC (9)**	**Jwl (1)**	**Jwl (9)**	**Brs M_{terr}**	**Brs GHF_{α}**
Min	-10.99	-9.10	2.44	2.78	1.05	5.57	10.50	7.49	-11.80	-2.03
Max	12.86	13.84	33.66	28.79	24.47	21.15	30.97	29.91	-0.22	84.05
Mean	-1.29	2.09	20.71	17.16	11.28	13.38	20.75	18.91	-5.32	36.94
Range	23.85	22.93	31.22	26.01	23.43	15.58	20.47	22.42	11.58	86.08

Spatial Pattern Analysis

Of the 24 temporal clusters that had higher M_{terr} values (generally higher numbered clusters), most were scattered across the western portion of the image and the clusters that had lower M_{terr} values (generally lower numbered clusters) tended to be scattered in the eastern portion of the image (Figure 3.14). Clusters with middle values were distributed throughout the image. The 20 spatial groupings were mostly contiguous (*i.e.*, one polygon) but several groups were very dispersed across the landscape (*e.g.*, Central Plateau and Mirror Plateau) (Figure 3.15).

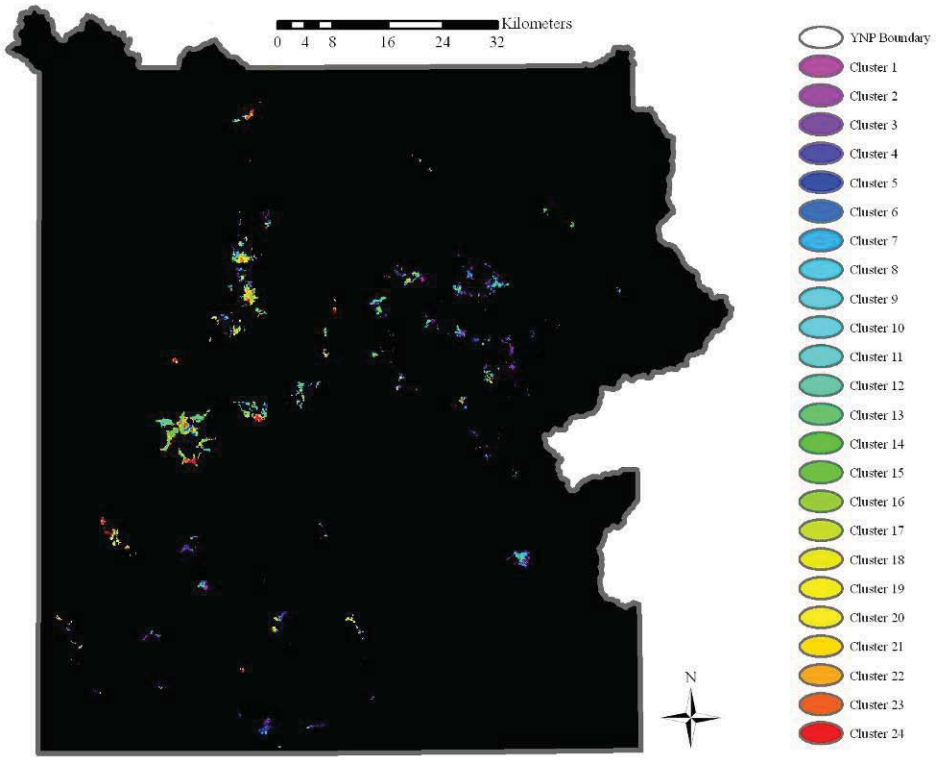

Figure 3.14: 24 temporal clusters of terrestrial emittance (Mterr) over a 21-year period in Yellowstone National Park. Clusters were created with an unsupervised classification of 14 M_{terr} images.

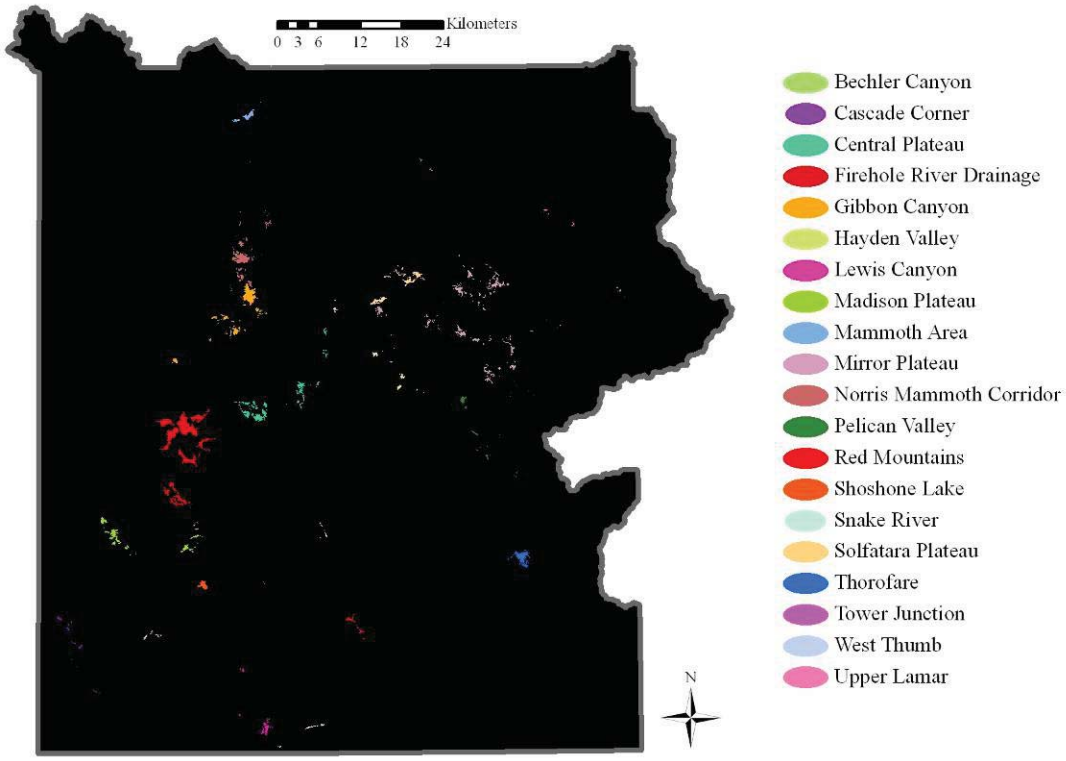

Figure 3.15: 20 spatial groupings of terrestrial emittance (M_{terr}) over a 21-year period in Yellowstone National Park. Groupings were derived from the defined geothermal areas and encompass no less than 144,000 m^2.

The average distance of each cluster from geologic faults indicated that Cluster 6 was the closest to geologic faults, with an average distance of 772 m, while Cluster 11 was the furthest away at 4,965 m (Figure 3.16). The average distance of all clusters to geologic faults was 3,032 m. Cluster 6 is smaller (46 pixels) and more cohesive than most of the other clusters, whereas Cluster 11 is one of the largest (257 pixels) and the most widely distributed of the clusters. The Red Mountains spatial grouping was on average the closest to geologic faults at 309 m, with the Cascade Corner group on average the furthest away at 11,845 m, and the average distance of all spatial groupings to geologic faults at 3,180 m (Figure 3.17). The Red Mountains group had a slightly linear shape and was intersected by faults. The Cascade Corner group also had a slightly

linear shape, however, there were no faults in the vicinity of this group. (See Appendix G for calculated distances for all clusters and spatial groupings)

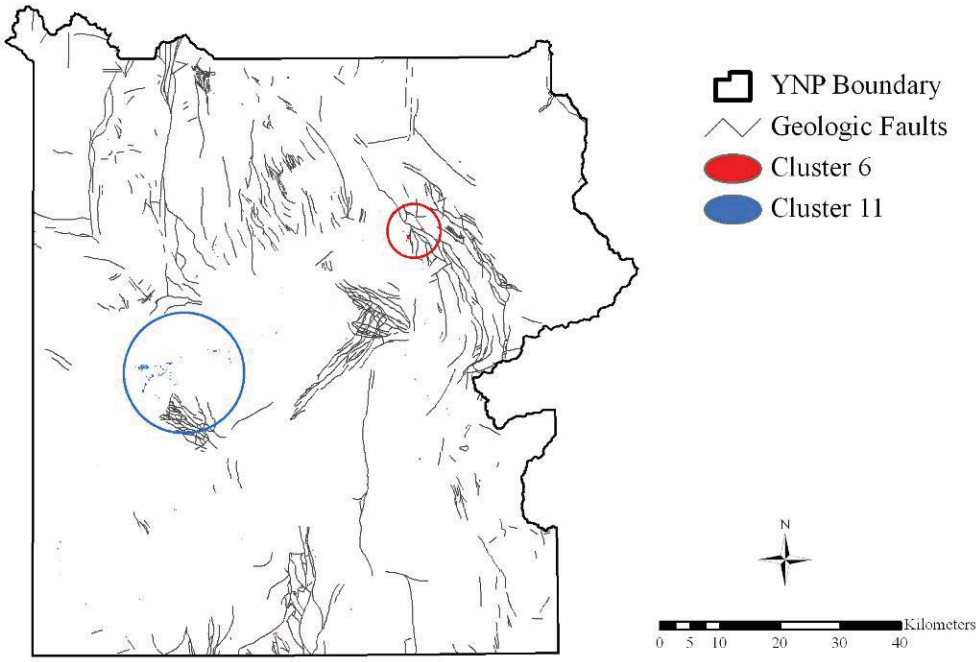

Figure 3.16: Clusters 6 and 11 with geologic faults in Yellowstone National Park (YNP). The majority of each cluster is circled. Cluster 6 was on average the closest to geologic faults at 772 m, while Cluster 11 was on average the furthest away from geologic faults at 4,965 m.

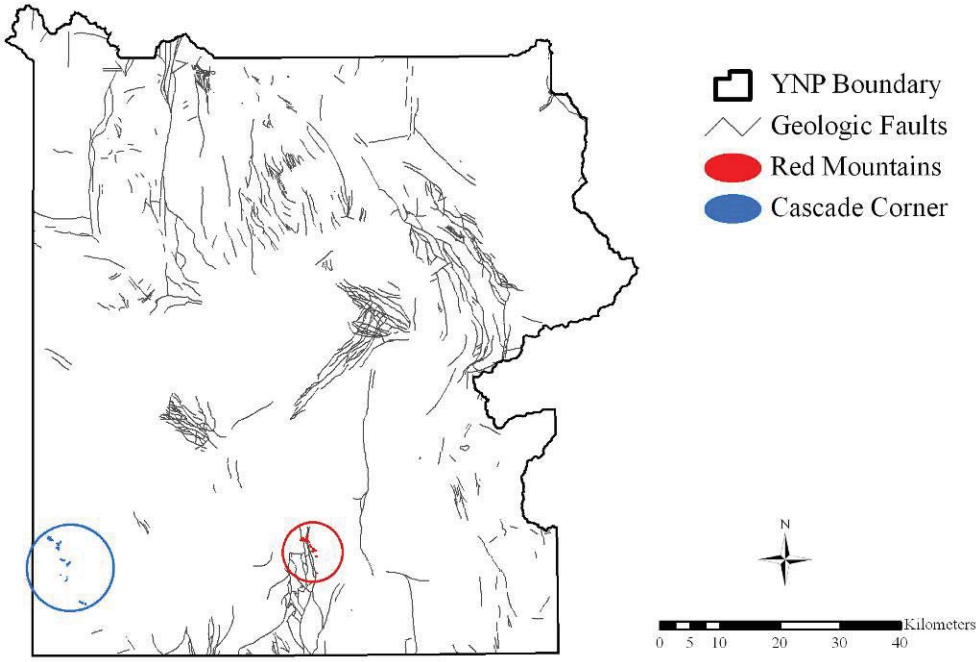

Figure 3.17: The Red Mountains group and Cascade Corner group with geologic faults in Yellowstone National Park (YNP). Groups are circled. The Red Mountains group was on average the closest to geologic faults at 309 m, while the Cascade Corner group was on average the furthest from geologic faults at 4,264 m.

The average distance of each cluster from large water bodies indicated that Cluster 15 was the closest to large water bodies at 1,046 m, while Cluster 6 was the furthest away at 3,125 m (Figure 3.18). The average distance of all clusters to large water bodies was 1553 m. Much of Cluster 15 is near Midway and Lower Geyser Basins and many water bodies. Cluster 6, on the other hand, is compact and appeared far from large water bodies. The Snake River spatial grouping was on average the closest to large water bodies at 78 m, with the Bechler Canyon group on average the furthest away at 5,458 m, and the average distance of all spatial groupings to large water bodies at 1,563 m (Figure 3.19). The Snake River group follows the Snake River for the most part. The Bechler Canyon group is in the southwest corner of YNP and very distant from most

large water bodies. (See Appendix G for calculated distances for all clusters and spatial groupings)

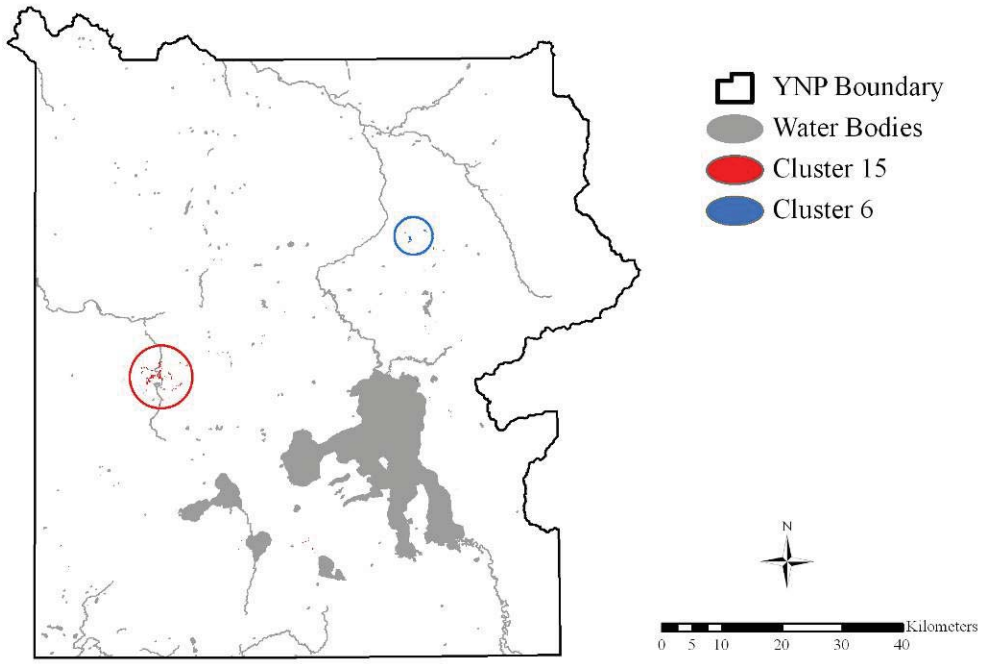

Figure 3.18: Clusters 15 and 6 with large water bodies in Yellowstone National Park (YNP). The majority of each cluster is circled. Cluster 15 was on average the closest to large water bodies at 1,046 m, while Cluster 6 was on average the furthest away from large water bodies at 2,125 m.

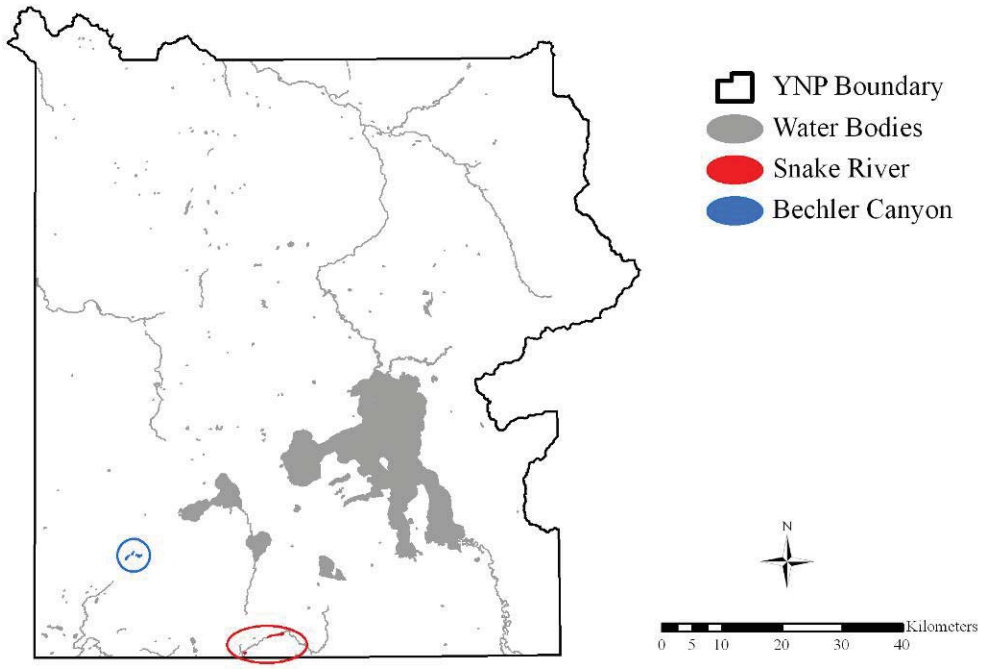

Figure 3.19: The Snake River group and Bechler Canyon group with large water bodies in Yellowstone National Park (YNP). Groups are circled. The Snake River group was on average the closest to large water bodies at 78 m, while the Bechler Canyon group was on average the furthest away from large water bodies at 5,458 m.

The average distance of each cluster from earthquake swarms indicated that Cluster 21 was the closest to earthquakes at 3,654 m, while Cluster 6 was the furthest away at 12,506 m (Figure 3.20). The average distance of all clusters to earthquake swarms was 7,276 m. Much of Cluster 21 was widely dispersed in the northwest portion of YNP, where many of the earthquake swarms occurred. Cluster 6, on the other hand, was compact, in the northeast portion of YNP, and appeared very distant from the majority of the earthquake swarms. The Hayden Valley spatial grouping was on average the closest to earthquake swarms at 1,412 m, with the Upper Lamar group on average the furthest away at 30,233 m, and the average distance of all spatial groupings to earthquake swarms at 9,547 m (Figure 3.21). The Hayden Valley group is intersected by swarms from 2002 and 2005. The Upper Lamar group is in the northeast portion of YNP, similar

to Cluster 6, and very distant from any of the earthquake swarms. (See Appendix G for calculated distances for all clusters and spatial groupings).

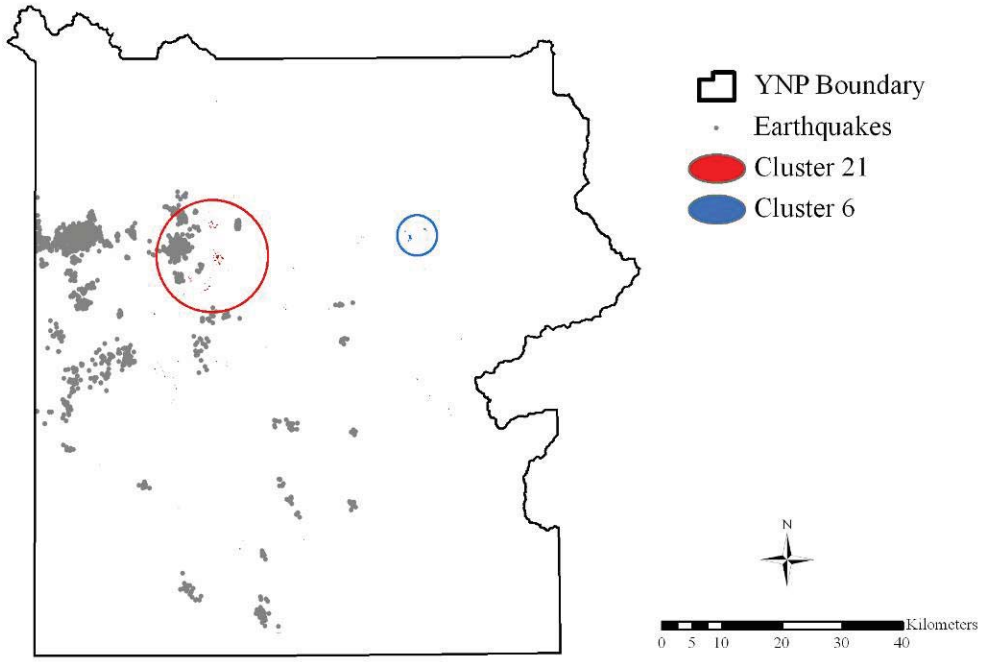

Figure 3.20: Clusters 21 and 6 with earthquake swarms in Yellowstone National Park (YNP). The majority of each cluster is circled. Cluster 21 was on average the closest to earthquake swarms at 3,654 m, while Cluster 6 was on average the furthest away from earthquake swarms at 12, 506 m.

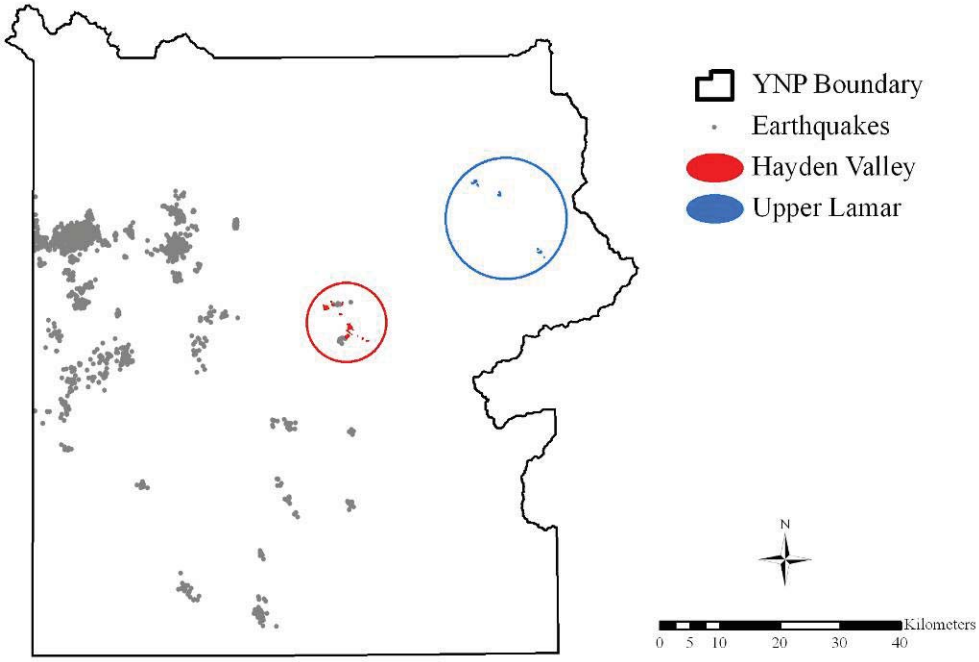

Figure 3.21: The Hayden Valley group and Upper Lamar group with earthquake swarms in Yellowstone National Park (YNP). Groups are circled. The Hayden Valley group was on average the closest to earthquake swarms at 1,412 m, while the Upper Lamar group was on average the furthest away from earthquake swarms at 3,023 m.

Eight swarm characteristics were used to choose one swarm per year for multitemporal linear regression analyses. The resulting R^2 values for the eight analyses ranged from 0.15 to 0.34 (Table 3.7). The best model, with an R^2 of 0.34, was based on the longest lag time between the last earthquake in a swarm and the image date (Figure 3.22).

Table 3.7: R^2 values of different combinations of "best" swarm per year (values are swarm ID #) (See Appendix A for details of swarm characteristics). The longest lag time had the highest R^2 value, explaining over one-third of the variation.

Year	Lag time long	Quakes per swarm	Max amp	Duration long	Mean amp	Duration short	Median amp	Lag time short
2007	33	1	32	32	32	1	32	1
2006	37	2	40	2	37	4	36	2
2005	43	46	44	44	5	5	5	5
2003	48	49	47	7	47	6	47	7
2002	53	54	55	9	50	52	50	10
2001	58	12	56	12	56	57	56	12
2000	64	14	62	14	62	13	62	13
1999	65	16	16	16	67	69	65	16
1998	70	70	70	18	19	19	19	18
1997	73	23	23	23	75	72	75	23
1996	78	26	25	25	24	24	24	24
1991	79	28	28	27	27	28	27	28
R^2	0.3402	0.2648	0.2571	0.2519	0.2093	0.1834	0.1617	0.1496

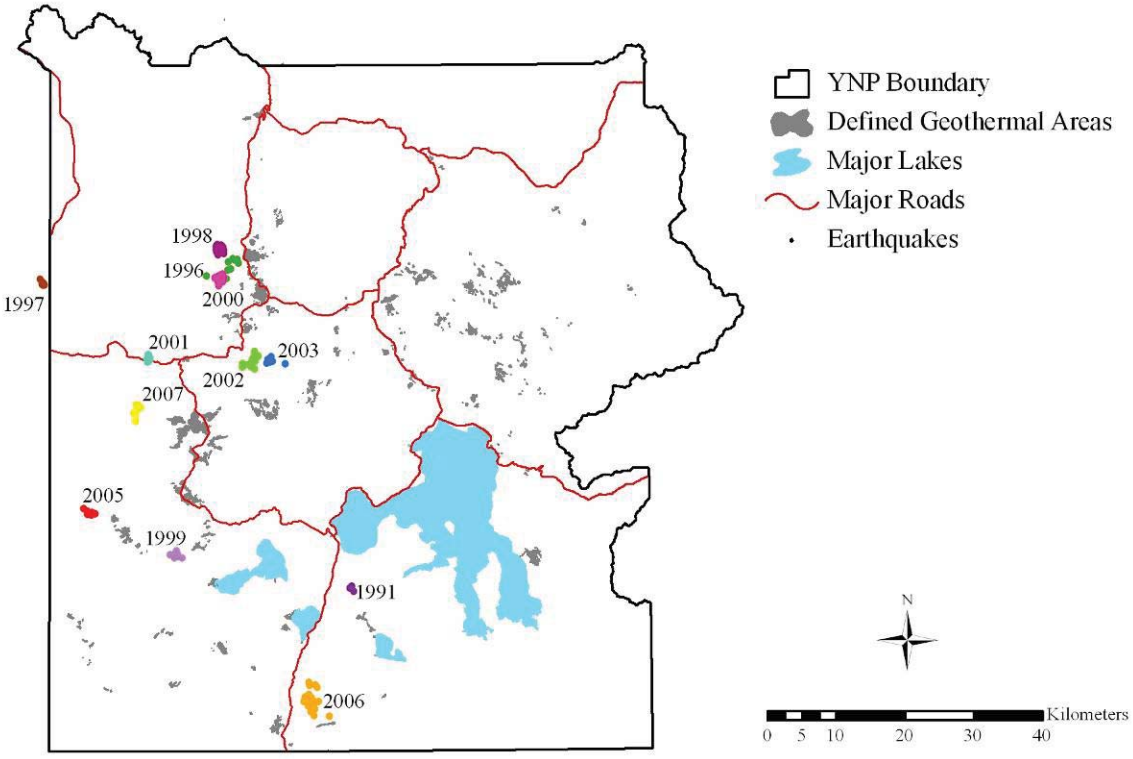

Figure 3.22: Earthquake swarms in and near Yellowstone National Park (YNP) used in a regression analysis based on longest lag time (see Table 3.7).

Discussion

Geothermal areas of YNP can range from highly stable to extremely dynamic. Landsat data were evaluated for their ability to detect change over a 21-year period in the defined geothermal areas of YNP. Trajectories of mean M_{terr} values were plotted across time and evaluated for spatial and temporal patterns of change. Locations where change had been observed were inspected in more detail. Spatial patterns of absolute change in M_{terr} were evaluated for correlations with distance to several natural features: geologic faults, large water bodies, and earthquake swarms.

Terrestrial Emittance

Reasonable estimates of terrestrial emittance that did not account for effects from solar radiation were produced from all 14 images, and change in M_{terr} was examined over these 14 dates. The same processes were completed for every image in this project. Even with solar radiation not taken into account, therefore, the M_{terr} values across time were comparable with this method because a change analysis on these data would indicate relative change rather than absolute change. In other words, the solar effects were expected to be similar across time, so observed differences should be due to geothermal change.

Image-to-image registration errors, however, might induce some errors in change analysis. For example, a feature with high M_{terr} might be at the edge of a pixel and thus change location due to registration error between two dates, resulting in a large, possibly false change at that pixel. Registration error might limit the utility of change analysis at the pixel level, but broader patterns of change are still apparent.

The general trend of all M_{terr} data was the same: increasing to 2000, with a subsequent decrease. This trend was demonstrated in every part of the defined geothermal areas. Although the study period might not have been long enough to observe a full cycle of terrestrial emittance change, the trend is consistent with an hypothesized cyclical pattern in terrestrial emittance in YNP, as is found in resurgent domes within the 640,000-year-old caldera (Brantley *et al.*, 2004). Thirty years of caldera measurements indicated a pattern of uplift from 1973 to 1985, subsidence to 1996, then uplift again to 2003 (Brantley *et al.*, 2004). This pattern is not the same as the

patterns observed in this study, but it does indicate cyclical tendencies in geothermal activity. Additionally, the "heavy breathing" of the caldera suggested by Pierce *et al*. (2007) supports the cyclical nature of geothermal activity in YNP.

It has been suggested that Norris Geyser Basin and Mammoth Hot Springs share "plumbing" to some degree (Bargar, 1978; White *et al.*, 1988). A comparison of M_{terr} trajectories of Mammoth Area, Norris Mammoth Corridor, and Gibbon Canyon (which includes Norris Geyser Basin) revealed that Gibbon Canyon and Norris Mammoth Corridor had almost identical trajectories, while the Mammoth Area trajectory had a very low correlation with the other two trajectories (Figure 3.12.a). Gibbon Canyon and Norris Mammoth Corridor are adjacent to one another (Figure 3.15) and both are associated with a river (Gibbon Canyon with Gibbon River and Norris Mammoth Corridor with Obsidian Creek). Mammoth Area, on the other hand, is over 13 km away from the bulk of Norris Mammoth Corridor and is not associated with a river.

Some have suggested that geothermal areas within the 640,000-year-old caldera boundary behave differently than geothermal areas outside of the boundary (Pierce and Morgan, 1992; Morgan *et al.*, 2003). When the Firehole River Drainage and Madison Plateau trajectories (within the caldera boundary) were compared to the Gibbon Canyon and Lewis Canyon trajectories (outside of the caldera boundary), few similarities in temporal patterns were observed (Figures 3.12.b, 3.12.c, and 3.15). This could support the idea that there are differences in geothermal behavior on either side of the caldera boundary.

The change analysis should detect change in geothermal areas of various sizes, so it was important to determine what the sensitivity to change was for Landsat thermal pixels. When the raw DN changes by 1, the M_{terr} values change on average by 1.14 Wm^{-2}. This means, for example, that a feature the size of Excelsior Geyser in Lower Geyser Basin (one of the largest features in YNP, at around 3000 m^2) would have to change by 5.47 Wm^{-2} (or 0.68 °C, assuming an initial temperature of 55.56 °C, the recorded temperature from the YNP Thermal Inventory Project) to see a change of 1 raw DN in the 120-m pixel in which it resides. Excelsior Geyser would be only 21% of a 120-m Landsat thermal pixel, so a larger feature, such as Grand Prismatic, the largest feature in YNP, at approximately 14,400 m^2, or a large area of geothermally active ground would need to change by 1.14 Wm^{-2} for the change to be detectable by Landsat. A small feature, such as Anemone Geyser near Old Faithful, which is approximately 1 m^2, or a small area of geothermally active ground would need to change by over 16,000 Wm^{-2} (assuming it is the only area within a pixel emitting heat). Temperature has a strong non-linear relationship to M_{terr}, thus the Landsat thermal pixel sensitivity to change will differ for every feature or location not only because of size but also because of inherent temperature.

Known Change Events

Institutional knowledge, although inconsistent and not uniform in coverage, is one way to learn about geothermal activity in YNP. Institutional knowledge, combined with more consistent and uniform Landsat data, allows scientists to study documented changes over time. Geothermal features are constantly changing, sometimes in small ways, such

as the periodicity of a geyser changing by one minute, and sometimes in spectacular ways, such as hydrothermal explosions. Some documented changes in geothermal areas during the study time period were observed in the change trajectories, while several were not detected with the Landsat data. The M_{terr} values of the feature near Narrow Gauge Geyser in Mammoth Hot Springs that appeared during the summer of 1998 showed a general increase from 1996 to 2000 with the biggest increase between 1996 and 1997 (Figure 3.13.a). The surrounding pixels had higher normalized M_{terr} values, indicating that the entire area was in an upward trend. Minerva Terrace, also in Mammoth Hot Springs, stopped flowing and emitting heat and steam in 1999, and its M_{terr} decreased from 1998 to 1999, although it increased again in 2000 (Figure 3.13.b). The trajectory for just the Minerva Terrace pixel is generally higher than the surrounding pixels trajectory, except in 1999, when they are almost exactly the same. This might be a representation of its change from flowing to not flowing, although the M_{terr} values increased again from 1999 to 2000, but Minerva Terrace did not begin to flow again.

Porkchop Geyser in Norris Geyser Basin showed a slight unexpected decrease in M_{terr} values from 2003 to 2005 (Figure 3.13.c), but it is unknown if M_{terr} actually increased or decreased in 2004. Thus no conclusion can be reached regarding whether the field-recorded increase in temperature in Norris Geyser Basin in 2003 can be sensed by Landsat data. The surrounding pixels had a slightly higher average normalized M_{terr} than the pixel that contained Porkchop Geyser and also increased between 2003 and 2005, possibly indicating a larger area of increased heat and/or a pixel registration error. The increase in M_{terr} from 2005 to 2006 was not observed by YNP scientists on the

ground and perhaps indicated the change seen in these trajectories was data noise rather than actual change in M_{terr}. The possible hydrothermal explosions near Jewel Geyser in Biscuit Basin in 2006 appeared to be sensed in M_{terr} since the values increased slightly after 2006 for the pixel that contained Jewel Geyser, but not for the surrounding pixels (Figure 3.13.d). A recent (May 2009) hydrothermal explosion in the same area is consistent with the increase in M_{terr} after 2006.

Brimstone Basin, close to the shore of the southeast arm of Yellowstone Lake, appears to be an extinct geothermal area, yet it is included in the defined geothermal areas. The waters running out of the basin are acidic and sulfuric, however, the waters are not hot and there has been no steam witnessed in the area since before YNP was established in 1872 (Langford, 1972; Nordstrom *et al.*, 2009). Very little change should have occurred in Brimstone Basin during the study period since it is a geothermally constant area emitting no heat. The M_{terr} trajectory graph for Brimstone Basin indicated year-to-year variability that might be more indicative of solar radiation issues rather than true increases and decreases in M_{terr} in the area (Figure 3.13.e). The degree of variability in M_{terr} at Brimstone Basin, however, was less than that of the features where true geothermal change was observed (Figure 3.13 and Table 3.6), supporting the conclusion that little to no M_{terr} change should be observed there since it has been inactive for over 100 years.

The GHF_{α} values in Brimstone Basin were noticeably different from the M_{terr} values of the same pixels (Figures 3.13.e and 3.13.f and Table 3.6). The GHF_{α} trajectory graph for Brimstone Basin showed large year-to-year variability and a wide range of

values, in addition to an obvious upward trend (Figure 3.13.f). This suggests that the solar and albedo corrections used in the GHF_{α} model were inadequate and the use of M_{terr} for this change analysis was preferred.

Spatial Patterns

There was no clear relationship between the temporal clusters and geologic faults even though part of Cluster 6 was intersected by faults (Figure 3.16). No clear relationship between temporal clusters and proximity to large water bodies was observed (Figure 3.18). Negligible relationships were observed between some spatial groupings and geologic faults and large water bodies. The Red Mountains spatial grouping had a relationship with intersecting geologic faults (Figure 3.17), while the Snake River and Firehole River Drainage spatial groupings were adjacent to and intersected by large water bodies (Figure 3.19). Finally, there was no relationship with precipitation data, indicating that the effects of drought on M_{terr} are not detectable with Landsat data.

Recorded earthquakes have had almost immediate effects on geysers in YNP, specifically on their periodicity (Rojstaczer *et al.*, 2003; Husen *et al.*, 2004). This behavior might indicate that the fluid movement beneath the surface is affected by earthquakes, and thus the heat emitted from some geothermal features might change with ground movement associated with earthquakes. In order to investigate the multitemporal spatial relationship of M_{terr} to earthquake swarms, one swarm was selected per year. The manner of choosing the swarms to include in the regression analyses is important. The nine regression models based on different swarm characteristics each explained over 10% of the between-date variation (Table 3.7), indicating that geothermal heat flux (as

opposed to terrestrial emittance) is actually an important part of the change analyses since earthquake swarms are unlikely to be correlated with solar inputs.

The regression model with the best predictive ability, based on longest lag time between last earthquake and image date, might be explained by the movement of fluid through the Earth's crust. Prior to an earthquake, the rock in the crust can be deformed and microscopic cracks spread. Water might fill in or escape through those cracks and water levels in wells might fluctuate (Roeloffs, 1988; Thompson and Turk, 2005). Earthquakes alter water levels in wells. As it takes time for geothermally-heated groundwater to flow to surface features, earthquake-mediated ground water changes might not be observed at the surface until as much as a year after the earthquake (Rojstaczer *et al.*, 1995). Thus, changes in hydrologic behavior from earthquakes might not be observable for some time after the earthquake. A relationship was observed between changes in M_{terr} and earthquake swarms that happened between 38 and 94 days prior to the image dates (Appendix A).

The lowest correlation found in this study between M_{terr} and earthquake swarms, on the other hand, was on the combination of swarms that had the *shortest* lag time between the last earthquake and the date of the imagery (1 to 2 days prior to the image dates) (Appendix A). If the hypothesis that the longest lag times have the strongest relationship because of hydrologic fluid movement is correct, it follows that a short lag time would not allow enough time for the fluid to move and create observable effects at the surface.

The remaining swarm characteristics explained additional variability in M_{terr} changes, with the number of earthquakes in each swarm showing the second best correlation at 0.265. This is not unexpected since the mean magnitude (see Appendix A) of all the earthquakes in the study was 1.58 (defined as "Micro" by the USGS and very rarely felt (USGS, 2009b; USGS, 2009a)), so 746 earthquakes with "Light" to "Micro" magnitudes might have greater effects than seven earthquakes with similar magnitudes. Magnitude (amplitude) and duration of swarm are, of course, important factors as well. When swarms were chosen based on maximum amplitude the correlation was 0.257, while the correlation was 0.252 when swarms were chosen for longest duration. These results also were not unexpected because higher amplitude earthquakes might be expected to cause more disturbance than lower amplitude earthquakes, and when swarms last for several days there might be accumulated effects on the Earth's crust.

Implications

Calculated terrestrial emittance over time using Landsat imagery could be a useful tool for monitoring geothermal areas at YNP and elsewhere. The values are calculated in a consistent manner and are comparable over time. Using the 2007 M_{terr} values as a base map, YNP scientists can continue looking at changes in terrestrial emittance over time with free Landsat data for the foreseeable future. The trajectory analysis of the spatial groupings provided insight into the spatial relationships (or lack thereof) of various defined geothermal areas within and outside of the 640,000-year-old caldera, as well as between Mammoth Hot Springs and Norris Geyser Basin. The trajectory analysis of the temporal clusters, on the other hand, found no spatial patterns related to known changes

in geothermal heat or vegetation. The effects of solar radiation might explain why the temporal cluster analysis was not as effective as hoped, and also might explain why Brimstone Basin registered as somewhat variable over time. Solar radiation remains a serious concern, as discussed in Chapter 2, and must be accounted for in future studies of this nature.

The results from this project indicate that spatial and temporal resolutions are important factors in calculating terrestrial emittance and analyzing change over time. This study focused on decadal change analysis and includes data that could be used for research with smaller temporal ranges. Since Landsat ETM+ thermal data are available as 60-m pixels, it would be of interest to study ETM+ images only to see if change is better detected at a finer spatial resolution (4 summer images are available from 1999 to 2002). The current dataset includes 7 consecutive anniversary dates (within 16 days in July) from 1996 to 2002. Focusing a study on these dates might remove the effects of the non-consecutive dates and missing data.

Earthquake swarms, as defined in this project, have a clear relationship with absolute changes in M_{terr}, with earthquake swarms explaining over one third of the variation in ΔM_{terr}. This relationship was studied without taking interactions between swarm characteristics into account (*e.g.*, how maximum amplitude relates to number of earthquakes in a swarm). These interactions might prove important in the M_{terr}/swarms relationship and could be investigated further to improve the understanding of these complex geological relationships.

Changes in the defined geothermal areas of YNP often are not visible with the naked eye or with ground-based field methods. The temporal trajectories developed for this project did not produce interpretable results that would aid YNP scientists in monitoring and multi-decadal change analysis of the defined geothermal areas. The proximity of geothermal areas to geologic faults and large water bodies had no detectable relationship to patterns of change measured by the Landsat sensors. Earthquake swarms as defined for this study, on the other hand, did have a significant correlation with the spatial patterns of change in geothermal areas. Further, more detailed studies of earthquake swarms and their affect on the behavior of geothermal areas and features might enable scientists at YNP to locate specific areas to study in more detail with on-the-ground field methods and/or higher spatial resolution airborne image analyses.

Literature Cited

Bargar, K.E. 1978. Geology and thermal history of Mammoth Hot Springs, Yellowstone National Park, Wyoming. Geological Survey Bulletin 1444, 55 pp.

Brantley, S.R., J.B. Lowenstern, R.L. Christiansen, R.B. Smith, H. Heasler, G. Waite, and C. Wicks. 2004. Tracking changes in Yellowstone's restless volcanic system. USGS Fact Sheet 100-03.

Brunsell, N.A. and R.R. Gillies. 2002. Incorporating surface emissivity into a thermal atmospheric correction. *Photogrammetric Engineering & Remote Sensing*, 68(12): 1263-1269.

Bryan, T.S. 2001. The Geysers of Yellowstone. University Press of Colorado, Boulder, Colorado, 472 pp.

Chavez, P.S.J. 1996. Image-based atmospheric corrections - revisited and revised. *Photogrammetric Engineering & Remote Sensing*, 62(9): 1025-1036.

Christiansen, R.L. and R.R. Wahl. 1999. Digital geologic map of Yellowstone National Park, Idaho, Montana, Wyoming and vicinity. U.S. Geological Survey, Open-File Report 99-174.

Custer, S.G., D.E. Michels, W. Sill, J.L. Sonderegger, W. Weight, and W. Woessner. 1993. Recommended Boundary for Controlled Groundwater Area in Montana Near Yellowstone Park, U.S. Department of the Interior National Park Service, Fort Collins, Colorado, 29 pp.

Dobson, P.F., T.J. Kneafsey, J. Hulen, and A. Simmons. 2003. Porosity, permeability, and fluid flow in the Yellowstone geothermal system, Wyoming. *Journal of Volcanology and Geothermal Research*, 123(3-4): 313-324.

Finn, C.A. and L.A. Morgan. 2002. High-resolution aeromagnetic mapping of volcanic terrain, Yellowstone National park. *Journal of Volcanology and Geothermal Research*, 115(1-2): 207-231.

Fournier, R.O., D.E. White, and A.H. Truesdell. 1975. Convective heat flow in Yellowstone National Park, Proceedings of the Second United Nations Symposium on the Development and Use of Geothermal Resources, San Francisco, California, USA, 731-739 pp.

Friedman, I. and D.R. Norton. 2007. Is Yellowstone losing its steam? - Chloride flux out of Yellowstone National Park. Chapter I in Professional Paper 1717, U.S. Geological Survey, pp. 272-297.

Hardy, C.C. 2005. "Characterizing thermal features from multi-spectral remote sensing data using dynamic calibration procedures", University of Montana, Missoula, Montana, 153 pp.

Harris, A.J.L., L.P. Flynn, L. Keszthelyi, P.J. Mouginis-Mark, S.K. Rowland, and J.A. Resing. 1998. Calculation of lava effusion rates from Landsat TM data. *Bulletin of Volcanology*, 60(1): 52-71.

Heasler, H., C. Jaworowski, and D. Susong. 2004. A geothermal monitoring plan for Yellowstone National Park, Yellowstone Center for Resources, Yellowstone National Park, Wyoming, 24 pp.

Husen, S., R. Taylor, R.B. Smith, and H. Heasler. 2004. Changes in geyser eruption behavior and remotely triggered seismicity in Yellowstone National Park produced by the 2002 M 7.9 Denali fault earthquake, Alaska. *Geology*, 32(6): 537-540.

Kennedy, R.E., W.B. Cohen, and T.A. Schroeder. 2007. Trajectory-based change detection for automated characterization of forest disturbance dynamics. *Remote Sensing of Environment*, 110(3): 370-386.

Langford, N.P. 1972. The Discovery of Yellowstone Park: Journal of the Washburn Expedition to the Yellowstone and Firehole Rivers in the Year 1870. University of Nebraska Press, Lincoln, Nebraska, 125 pp.

Lawrence, R.L. and W.J. Ripple. 1999. Calculating change curves for multitemporal satellite imagery: Mount St. Helens 1980-1995. *Remote Sensing of Environment*, 67(3): 309-319.

Lu, D., P. Mausel, E. Brondizio, and E. Moran. 2003. Change detection techniques. *International Journal of Remote Sensing*, 25(12): 2365-2407.

Morgan, L.A. *et al.* 2003. Exploration and discover in Yellowstone Lake: results from high-resolution sonar imaging, seismic reflection profiling, and submersible studies. *Journal of Volcanology and Geothermal Research*, 122(3-4): 221-242.

Neale, C. 2008. Personal Communication - Airborne remote sensing of geothermal heat flux in Upper Geyser Basin in Yellowstone National Park, Missoula, Montana.

Nordstrom, D.K., R.B. McCleskey, and J.W. Ball. 2009. Sulfur geochemistry of hydrothermal waters in Yellowstone National Park: IV Acid-sulfate waters. *Applied Geochemistry*, 24(2): 191-207.

Norton, D.R. and I. Friedman. 1985. Chloride flux out of Yellowstone National Park. *Journal of Volcanology and Geothermal Research*, 26(3-4): 231-250.

NRCS. 2009. SNOTEL Data & Products. Last accessed on 22 February 2009. http://www.wcc.nrcs.usda.gov/snow/.

Oechel, W.C., G.L. Vourlitis, S.J. Hastings, and S.A. Bochkarev. 1995. Change in arctic CO^2 flux over two decades: effects of climate change at Barrow, Alaska. *Ecological Applications*, 5(3): 846-855.

Oppenheimer, C., D.A. Rothery, and P.W. Francis. 1993. Thermal distributions at fumarole fields: implications for infrared remote sensing of active volcanoes. *Journal of Volcanology and Geothermal Research*, 55(1-2): 97-115.

Pierce, K.L. and L.A. Morgan. 1992. The track of the Yellowstone hot spot: Volcanism, faulting, and uplift. In: K. Link, M.A. Kuntz and L.B. Platt (Editors), Regional Geology of Eastern Idaho and Western Wyoming. Geological Society of America, 53 pp.

Pierce, K.L., K.P. Cannon, G.A. Meyer, M.J. Trebesch, and R.D. Watts. 2007. Postglacial inflation-deflation cycles, tilting, and faulting in the Yellowstone caldera based on Yellowstone Lake Shorelines. Chapter E in Professional Paper 1717, U.S. Geological Survey, pp. 128-168.

Roeloffs, E.A. 1988. Hydrologic precursors to earthquakes: A review. *Pageoph*, 126(2-4): 134-139.

Rojstaczer, S. and S. Wolf. 1992. Permeability changes associated with large earthquakes: An example from Loma Prieta, California. *Geology*, 20(3): 211-214.

Rojstaczer, S., D.L. Galloway, S.E. Ingebritsen, and D.M. Rubin. 2003. Variability in geyser eruptive timing and its causes: Yellowstone National Park. *Geophysical Research Letters*, 30(18): 2-1 to 2-4.

Rojstaczer, S., S. Wolf, and R. Michel. 1995. Permeability enhancement in the shallow crust as a cause of earthquake-induced hydrological changes. *Nature*, 373(6511): 237-239.

Seielstad, C. and L. Queen. 2009. Thermal remote monitoring of the Norris Geyser Basin, Yellowstone National Park. Final Report for the National Park Service Cooperative Ecosystem Studies Unit, Agreement No. H1200040001, 38 pp.

Sorey, M.L. 1991. Effects of potential geothermal development in the Corwin Springs known geothermal resources area, Montana, on the thermal features of Yellowstone National Park. Water-Resources Investigations Report 91-4052, U.S. Geological Survey, Menlo Park, CA, 204 pp.

Spatial Analysis Center. 1998. 30-meter elevation data for Yellowstone National Park, Wyoming, Montana, Idaho. Digital Spatial Data, Yellowstone Center for Resources, Yellowstone National Park, Wyoming.

Spatial Analysis Center. 2000. Precipitation in Yellowstone National Park, Wyoming, Montana, Idaho. Digital Spatial Data, Yellowstone Center for Resources, Yellowstone National Park, Wyoming.

Spatial Analysis Center. 2005. Hydrogeothermal Areas of Yellowstone National Park, Wyoming, Montana, Idaho. Digital Spatial Data, Yellowstone Center for Resources, Yellowstone National Park, Wyoming.

Spatial Analysis Center. 2008. Thermal Inventory point data for Yellowstone National Park, 1998 - 2008. Digital Spatial Data, Yellowstone Center for Resources, Yellowstone National Park, Wyoming.

Spicak, A. 2000. Earthquake swarms and accompanying phenomena in intraplate regions: a review. *Studia Geophysica et Geodaetica*, 44(2): 89-106.

Thompson, G.R. and J. Turk. 2005. Earth Science and the Environment. Brooks/Cole - Thomson Learning, Belmont, California, 601 pp.

University of Utah. 2009. Yellowstone National Park Region Earthquake Listings. Last accessed on 15 March 2009. http://www.quake.utah.edu/EQCENTER/LISTINGS/OTHER/yellowregion.htm.

USGS. 2008. National Hydrography Dataset. Last accessed on 13 August 2008. http://nhd.usgs.gov/.

USGS. 2009a. Magnitude/Intensity Comparison. Last accessed on 17 March 2009. http://earthquake.usgs.gov/learning/topics/mag_vs_int.php.

USGS. 2009b. What are the earthquake magnitude classes? Last accessed on 17 March 2009. http://earthquake.usgs.gov/learning/faq.php?categoryID=2&faqID=24.

Utah State University. 2008. Image Standardization: At-sensor Reflectance and COST Correction. Last accessed on 8 April 2009. http://earth.gis.usu.edu/imagestd/.

Waring, G.A., R.R. Blankenship, and R. Bentall. 1983. Thermal springs of the United States and other countries of the world - a summary. U.S.G.S. Professional Paper 492, U.S. Geological Survey, Alexandria, Virginia, 401 pp.

Watson, F.G.R., R.E. Lockwood, W.B. Newman, T.N. Anderson, and R.A. Garrott. 2008. Development and comparison of Landsat radiometric and snowpack model inversion techniques for estimating geothermal heat flux. *Remote Sensing of Environment*, 112(2): 471-481.

Western Regional Climate Center. 2005. Period of record monthly climate summary - Yellowstone Park, Wyoming (489905). Last accessed on 6 April 2009. http://www.wrcc.dri.edu/cgi-bin/cliRECtM.pl?wyyell.

White, D.E., R.A. Hutchinson, and T.E.C. Keith. 1988. The geology and remarkable thermal activity of Norris Geyser Basin, Yellowstone National Park, Wyoming. U.S. Geological Survey, Professional Paper 1456, 84 pp.

CHAPTER 4

CLASSIFYING GEOTHERMALLY ACTIVE AREAS IN YELLOWSTONE AND SURROUNDING AREAS WITH LANDSAT TM IMAGERY

Introduction

Yellowstone National Park (YNP), located in Wyoming, Montana, and Idaho, USA, is home to thousands of geothermal features and contains the highest concentration of geysers, hot springs, fumaroles, and mud pots in the world (Waring *et al.*, 1983). Nearly 13,000 individual geothermal features have been identified within the defined geothermal areas in YNP via the Thermal Inventory Project, a multi-year National Park Service-sponsored project with the goal of collecting precise GPS measurements of every geothermal feature in YNP (Spatial Analysis Center, 2008). The defined geothermal areas were delineated from historical data, field observations, data from the Thermal Inventory Project, and heads-up digitizing using one-meter resolution digital orthophoto quarter quadrangles (DOQQs) (Spatial Analysis Center, 2005). The defined geothermal areas include locations that are geothermally inactive, such as Brimstone Basin, near the southeastern arm of Yellowstone Lake. Geothermal activity has never been observed at Brimstone Basin, but the area appears geothermally influenced (Langford, 1972; Nordstrom *et al.*, 2009).

The National Park Service (NPS) is legally mandated to monitor and protect geothermal features within its units (Geothermal Steam Act, 1970 as amended in 1988). Monitoring geothermal features requires an accepted base map of the area, and while the

defined geothermal areas are reasonably accurate, they need to be refined so that inactive geothermal barrens (*e.g.*, Brimstone Basin; ground that is not geothermally active but appears geothermally influenced) are not included as active geothermal barrens (*e.g.*, white ground with little to no live vegetation and emitted geothermal heat), and active areas that do not appear geothermally influenced are included as geothermally active areas (GAA). For the purposes of this project, a GAA is defined as an area that has hot springs, geysers, fumaroles, and/or mudpots, and/or is emitting geothermal heat. An accurate, refined base map of GAA could provide YNP scientists a starting point for monitoring for changes in the presence or absence of geothermal features.

YNP covers a large area (approximately 890,000 ha), and the current defined geothermal areas cover less than 1% of that area. The size of YNP prevents personnel from being able to visit and monitor all of the geothermal areas each year as part of a monitoring program. Many geothermal areas are in remote backcountry areas not easily accessible on a day-hike, thus requiring multi-day excursions in order to monitor changes at these areas. Not only is this time-consuming, it is expensive, and not practical.

Remote sensing offers a possible alternative to endless field work for monitoring YNP's geothermal areas. Landsat Thematic Mapper (TM) multispectral satellite imagery covers the entirety of YNP and collects information from the visible (0.452–0.518 μm, 0.528–0.609 μm, and 0.626–0.693 μm), near infrared (NIR; 0.776–0.904 μm), middle infrared (MIR; 1.57–1.78 μm, and 2.1–2.35 μm), and thermal infrared (TIR; 10.45–12.42 μm) portions of the electromagnetic spectrum (EMS) (Chander *et al.*, 2009). All but the TIR band have 30-m spatial resolution (30 m on a pixel side, or 900 m^2), while the TIR

band has 120-m spatial resolution (14,400 m^2). The current TM sensor on Landsat 5 has been in orbit since 1984 and a new TM sensor with a similar spectral range, including TIR, is expected to be sent into orbit on Landsat 8 in 2012 (NASA, 2009). Landsat TM images are collected over YNP every 16 days, allowing annual or seasonal classification of the GAAs.

Use of Landsat Data for Classification

One of the primary applications of remote sensing, and Landsat data in particular, is classifications of features on the landscape, often land cover/vegetation, but also minerals, water, human impacts, and geothermally influenced ground. Classifications of landscape features produce maps that can be compared over time to assess change. Thermal and terrestrial emittance anomalies, for example, have been identified successfully with Landsat data. Three Landsat TM scenes recorded high-temperature thermal anomalies, such as vertical ash eruptions and an active basaltic lava flow, from 1986 to 1988 over Santiaguito Dome and Pacaya Volcano in Guatemala (Andres and Rose, 1995). A method of quantifying the intensity of surficial geothermal activity in YNP was developed with 2004 Landsat ETM+ imagery (Watson *et al.*, 2008). This method utilized thermal radiance data to create a map of terrestrial emittance anomalies, proxies for geothermal heat flux (GHF).

Classification Methods

Decision tree classification methods are recent additions to the image classification arsenal that allow analysts to utilize original imagery along with ancillary

data without requiring expert knowledge to conduct highly accurate image classifications (Lawrence and Wright, 2001; Lawrence *et al.*, 2004). Random Forest (RF) is a decision tree classification method that grows hundreds of decision trees, where each tree is grown using a different bootstrapped (resampled with replacement) random subset of training data, and each split within each tree is based on a different random subset of predictor variables (Breiman, 2001; Lawrence *et al.*, 2006). The "forest" of trees then votes to assign a class to each input data point (Breiman, 2001; Prasad *et al.*, 2006). RF classifications have been shown to have accuracy rates as good as or better than any other classification method used for remote sensing, while being less sensitive to noise and uneven classes in training sets (Pal, 2005; Gislason *et al.*, 2006; Lawrence *et al.*, 2006). Internal accuracies of RF datasets are calculated with out-of-bag (OOB) samples, that is, those training data excluded from the bootstrapped random subsets, potentially reducing the need for independent accuracy assessments (Liaw and Wiener, 2002; Gislason *et al.*, 2006; Lawrence *et al.*, 2006; Prasad *et al.*, 2006). When the reference data are biased, however, the OOB estimation might not be reliable (Lawrence *et al.*, 2006). RF has been applied to Landsat ETM+ data to classify agricultural land cover in Littleport, Cambridgeshire, UK (Pal, 2005) and to Landsat Multispectral Scanner (MSS) data to classify forest types in a mountainous area in Colorado (Gislason *et al.*, 2006) with 88% and 83% accuracy respectively. RF can handle high dimensional data, easily accommodates ancillary data, avoids overfitting, does not make assumptions about the distribution of data, and is particularly well suited to predictive mapping. It is, however, somewhat of a "black box" method since the resulting statistical model consisting of a

forest of decision trees is not subject to easy interpretation of the relationship of predictor and response variables other than the relative importance of predictors (Friedl and Brodley, 1997; Liaw and Wiener, 2002; Gislason *et al.*, 2006; Prasad *et al.*, 2006). RF should be a reasonable classification technique for determining whether Landsat imagery is able to map the distribution of GAA in the defined geothermal areas of YNP since GAA have not yet been classified in YNP and there is no reported study of any other statistical method substantially outperforming RF for classification purposes.

The constrained energy minimization (CEM) method is a target detection classification technique, developed primarily for hyperspectral data and often used to identify minerals or very rare targets. The method only requires prior knowledge of the distinct target of interest and eliminates unidentified spectral signature sources and suppresses noise in the data (Du *et al.*, 2003). The distribution of mine tailings in Coeur d'Alene River Valley, Idaho in 1993 was mapped using CEM (Farrand and Harsanyi, 1997). Twelve false-alarm pixels were found out of 484 pixels determined to be rich in ferruginous sediments. Although designed for hyperspectral imagery, an empirical study showed that CEM can be used with SPOT imagery (multispectral imagery with spectral similarities to Landsat imagery) and correlated derivatives of these data for classification of individual targets (Chang *et al.*, 2000). Since GAA are rare targets of interest outside defined geothermal areas at YNP, and non-GAA information is highly variable and difficult to collect due to the size of and diversity of landcover types within YNP, the CEM target detection algorithm is an appropriate tool for classifications of GAA outside the defined geothermal areas.

The main purpose of this project was to assess the ability of Landsat TM data combined with RF and CEM classifiers to classify GAA accurately. An effective method would enable the classification of GAA in and outside YNP that could be applied to additional Landsat images for use in monitoring and change analysis. A successful classification method would provide scientists with information on where to check for new geothermal areas in YNP and where to focus on ground-work or aerial flights to best assess change. This strategy would reduce the amount of time-consuming and expensive field monitoring or aerial image acquisition, especially in the backcountry.

Methods

Study Area

A 30-km buffer was delineated around YNP so that the Corwin Springs, Montana, and Island Park, Idaho, Known Geothermal Resource Areas (KGRAs) (Long *et al.*, 1976; Sorey, 1991) would be included in the classification. The 30-km-buffered study area encompasses approximately 2,400,000 ha in Wyoming, Montana, and Idaho, USA (Figure 4.1). Elevation ranges from 1,495 m to 3,886 m (Spatial Analysis Center, 1998). Vegetation includes grassland, brushland, agricultural land, and forest, with bare ground interspersed. Average precipitation ranges from 25-30 cm in the lower elevations and up to 203 cm in the higher elevations (Spatial Analysis Center, 2000), with warm, dry summers and cold, wet winters (Western Regional Climate Center, 2005).

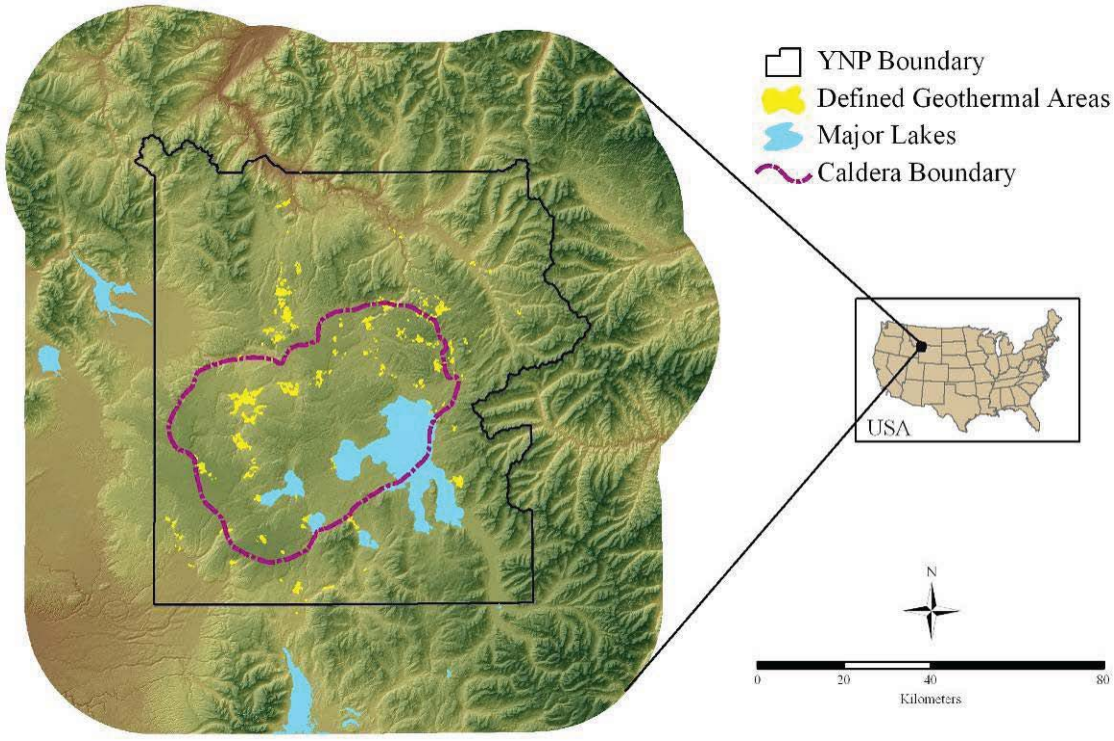

Figure 4.1: Location map for Yellowstone National Park, its 30-km buffer, and the currently defined geothermal areas displayed with a shaded relief background.

The currently defined geothermal areas, at 6,343 ha, comprise less than 0.5% of the entire study area (Figure 4.1). More than 60% of the defined geothermal areas are within the 640,000-year-old caldera boundary. Elevation in these areas ranges from 1,728 m to 2,775 m (Spatial Analysis Center, 1998). The majority of the vegetation within geothermal areas is grassland, however, brushland, and forest are also found. Average precipitation in the geothermal areas ranges from 35-203 cm (Spatial Analysis Center, 2000).

Data Acquisition

YNP is centered within one Landsat scene at Path 38 Row 29. A TM scene from 25 June 2007 was acquired from the USGS Earth Resources Observation and Science (EROS) Data Center. This scene was chosen because it was the most recent, complete, and mostly cloud-free (less than 5%) summer scene available at the time the study took place.

Several ancillary data sets were required for analysis. A 30-m digital elevation model (DEM), digital spatial polygon data of the defined geothermal areas, and digital spatial point data of the Thermal Inventory Project data were provided by YNP. The defined geothermal area polygons include nearly all known geothermally active areas in YNP as well as some inactive areas. These data were provided as the starting point for classification with the aim of refining the boundaries so inactive areas would not be included. The Thermal Inventory Project includes nearly 13,000 precise (sub-meter accuracy) GPS locations of individual geothermal features. If a GPS point was collected at the edge of a feature, the distance and azimuth to the center was estimated and the point was moved to that center location. The Thermal Inventory Project points represent the most complete collection of all geothermal features within YNP, but do not include areas of hot ground with no geothermal features. These ancillary data were utilized as reference data for the classification process.

Slope and aspect were derived from the DEM, with slope in degrees and aspect as categorical data with 9 categories (N, S, E, W, NE, SE, SW, NW, and flat). These topographic data were utilized in subsequent calculations (see below) as well as in the

classification process as additional predictor variables. Slope and aspect by themselves would not be able to classify GAA, but their interactions with other predictor variables might help the classification process.

Image Preprocessing

The TM image and all ancillary data were clipped to the full study area. Clouds and cloud shadows were masked by on-screen digitizing, and elevations greater than 2,700 m were masked to remove snow from the study area as no records of geothermal features have been found for these areas and deep snow conceals thermal signatures (if they exist). The methods described in Chapter 2 to calculate the Normalized Difference Vegetation Index (NDVI) and terrestrial emittance (M_{terr}) (Watson *et al.*, 2008) from the red, NIR, and TIR Landsat bands were followed (Equations 2.1 – 2.2, and 2.5 – 2.8). Potential annual direct incident solar radiation (SR) was calculated from latitude, slope, and aspect (Equation 2.3) (McCune and Keon, 2002), albedo was calculated from five of the six reflective bands (Equation 2.4) (Liang, 2000), and GHF_{α} was calculated from M_{terr}, SR, and albedo following the methods from Chapter 2 (Equation 2.11). NDVI, albedo, SR, and GHF_{α} were included in the classification process along with the original reflective spectral bands and M_{terr} in order to provide the classification algorithm with many possible predictors and predictor interactions that might improve the final outcome.

Transformed datasets were derived from the original Landsat bands to potentially improve the classification process by adding additional predictors that can detect diverse landscape features. Principal components analysis (PCA) reduces the amount of data to be analyzed and accounts for the most variance in the original image (Singh, 1989).

Correlations between the components and the input bands can be calculated and each PC can be interpreted as representing certain combinations of Landsat bands and/or features on the ground (Jensen, 2005). A standardized PCA was performed on the original reflective bands and M_{terr} resulting in 7 new components where the majority of the original variance can be found in the first 3 components.

A tasseled cap (TC) transformation was performed on the six reflective bands, resulting in 3 additional transformed components for the classification process. This is a physically based identification process similar to PCA in that it reduces the amount of information to be analyzed into the first three components. These components represent brightness (TCB) (soil brightness or total reflectance), greenness (TCG) (relative amounts of leafy green vegetation), and wetness (TCW) (soil moisture) (Crist and Cicone, 1984).

The six original reflective Landsat bands and 17 derived and ancillary data components were stacked to create one 23-component image for the study area (Table 4.1). This 23-component image was clipped to the defined geothermal area boundaries for use in an initial classification. The final images used in the classification processes had 30-m spatial resolution.

Table 4.1: Components used in the random forest and constrained energy minimization classification processes. Components 1 through 5 and 7 were original Landsat bands. Components 6, 8 through 18, 20, and 23 were derived from the original Landsat bands. Components 19, 21, and 22 were derived from topographic information.

#	Component Name	#	Component Name
1	Band 1 – Blue	**13**	Principal Component 6 (PCA6)
2	Band 2 – Green	**14**	Principal Component 7 (PCA7)
3	Band 3 – Red	**15**	Tasseled Cap Brightness (TCB)
4	Band 4 – Near Infrared (NIR)	**16**	Tasseled Cap Greenness (TCG)
5	Band 5 – Middle Infrared (MIR1)	**17**	Tasseled Cap Wetness (TCW)
6	Terrestrial Emmitance (M_{terr})	**18**	Normalized Difference Vegetation Index (NDVI)
7	Band 7 – Middle Infrared (MIR2)	**19**	Potential Annual Direct Incident Solar Radiation (SR)
8	Principal Component 1 (PCA1)	**20**	Albedo
9	Principal Component 2 (PCA2)	**21**	Aspect
10	Principal Component 3 (PCA3)	**22**	Slope in degrees
11	Principal Component 4 (PCA4)	**23**	Estimated Geothermal Heat Flux (GHF_{α})
12	Principal Component 5 (PCA5)		

Random Forest Classification Procedures

The classifications developed for this study had two classes: (1) GAA – anywhere that was geothermally active, and (2) non-GAA – anywhere that was not geothermally active. The RF classification was designed to refine the currently defined geothermal areas by distinguishing the non-GAA contained within the defined geothermal areas.

The GAA reference data for the RF classification processes were collected as a random selection of Thermal Inventory data points (Table 4.2) (Spatial Analysis Center, 2008). The Thermal Inventory Project began in 1998 and was completed in 2008. Over 12,000 GPS-located points were collected along with pH, conductivity, temperature, and a description of each geothermal feature. The data from the Thermal Inventory were the most accurate available data for representing GAA, since the points are locations of active geothermal features and were collected with a sub-meter precision GPS unit. An inherent bias to these data is that the Thermal Inventory Project focused on *features*, not

areas, so active geothermal barrens were not identified in this dataset, and therefore are absent from the reference data.

Non-GAA reference data were impossible to collect in the field due to the lack of time, money, and permission to place thousands of temperature loggers throughout the defined geothermal areas that would be necessary to indentify a large number of 900 m^2 locations known to not be emitting geothermal energy. Thus, the non-GAA training and validation data were collected with digital spatial data in three different ways and three RF classifications were performed with each of the non-GAA reference datasets. The first method (Inventory Buffer) was likely the least biased. The Thermal Inventory Project points were buffered with a 60-m radius (in order to exclude the 30-m pixel in which the points reside and the 8 surrounding 30-m pixels) and random points were generated in the areas outside those buffer zones but within the defined geothermal areas (Table 4.2). The second method (Photo Interp) incorporated greater expert knowledge, but also thereby increased the potential for bias. Randomly placed points within the defined geothermal areas were photo interpreted using National Agriculture Imagery Program (NAIP) imagery, proximity to Thermal Inventory Project points, and my knowledge of geothermal areas in YNP. Those points that were located on what appeared to be a geothermal barren but not within 60 m of any Thermal Inventory Project point were rejected from the sample data set because I could not determine whether they were actually hot (except in Brimstone Basin, where no geothermal heat is being emitted from the geothermal barrens), introducing potential bias in the interpretation. Three hundred points were interpreted as either GAA or non-GAA, where GAA points were

within 60 m of a Thermal Inventory Project point and not vegetated, while non-GAA points were at least 60 m away from Thermal Inventory Project points and vegetated (except Brimstone Basin as mentioned above). Fifty of each of the two classes were set aside for accuracy assessment and 29 points were rejected for reasons explained above, leaving 171 points for training data (Table 4.2). The third method (M_{terr} Threshold) had the greatest potential for bias as the non-GAA points were selected randomly from pixels that had M_{terr} values less than the study area mean M_{terr} value (351.1 Wm^{-2}). Locations that had a high M_{terr} value because of solar effects, but are not emitting geothermal heat and should be considered non-GAA were consequently excluded from that class (Table 4.2).

The number of reference points varies between the three methods. Over 3,500 reference points each were collected for the Inventory Buffer and M_{terr} Threshold methods, while less than 300 reference points were used for the Photo Interp method. More points were collected for the Inventory Buffer and M_{terr} Threshold methods because they were automatically generated with little analyst contribution.

Table 4.2: Geothermally active area (GAA) and non-geothermally active area (non-GAA) reference data used in three random forest classifications of defined geothermal areas. All GAA reference data were based on Thermal Inventory points. Inventory Buffer non-GAA reference data were randomly generated in areas at least 60 meters away from Thermal Inventory points. Photo Interp non-GAA reference data were randomly generated in the defined geothermal areas and manually interpreted with local knowledge. Terrestrial emittance (M_{terr}) Threshold non-GAA reference data were randomly generated within the defined geothermal areas with M_{terr} values less than 351.08 Wm^{-2}.

Method	GAA Training	Non-GAA Training	GAA Validation	Non-GAA Validation
Inventory Buffer	1,366	1,914	300	300
Photo Interp	89	82	50	50
M_{terr} Threshold	1,366	1,708	300	300

The classifications were performed with the ModelMap package within R statistical software (Freeman and Frescino, 2009). ModelMap contains the randomForest function and in addition to producing an out-of-bag (OOB) error estimate and a graph of predictor importance, creates a text file that can be converted to a raster image. The three training data sets were used to create three RF classifications. All 23 image components (listed in Table 4.1) were utilized as predictor variables for all three classification methods. Each output text file was converted to a classified raster image based on the probability threshold of 0.5. In other words, any value greater than 0.5 was classified as GAA, while the rest were classified as non-GAA. The classified raster image was subsequently converted to polygon data for use as training data for classifications of study area locations outside the defined thermal areas.

Three error matrices based on data withheld from the reference data were constructed to calculate the overall and class accuracies of each classification method. Class accuracies are shown with user's accuracy (errors of commission) and producer's accuracy (errors of omission) (Congalton, 2001). Kappa statistics were calculated for each classification method. The Kappa statistic measures how much better (or worse) the classification is from a randomly generated classification and is more conservative than overall accuracy (Congalton and Green, 1999; Congalton, 2001). Kappa values range from -1 to 1 and the closer the value to 1, the more accurate the classification. The maps were visually inspected for similarities to Thermal Inventory Project points and landscape features on NAIP imagery.

Cross-validations of these three methods to one another with independent validation data might indicate the best method to use for classification of GAAs in YNP. Two independent error matrices were constructed for each classification method with validation data collected for the other two methods for a total of six additional error matrices (*e.g.*, the validation data from the Inventory Buffer method were used to create error matrices of the Photo Interp and M_{terr} Threshold methods). Kappa and Z statistics and *p*-values were calculated for all error matrices, and pairwise comparisons were performed between different methods to determine whether the sample data could detect significant differences from one another (Congalton and Green, 1999). If no differences are detected, no method can be deemed better than the others, while a statistically significant difference between any pair of methods should provide statistical justification for choosing one method over the other.

Target Detection Classification Procedures

The target detection classification was designed to classify GAA outside of the defined geothermal areas, perhaps identifying previously unknown areas of geothermal activity. The training data for these classifications were taken from the final RF classified shapefiles of the defined geothermal areas. All GAA polygons greater than 900 m^2 were selected for each RF classification method and used as training for target detection classifications of the full study area. The CEM algorithm was utilized for target detection. CEM outputs an image containing continuous values on an arbitrary scale with higher values indicating pixels more similar to the training data. The resulting continuous data were converted to binary classified images based on a threshold set by

the CEM process (a value of 2), then merged with the defined geothermal area classifications to create final classified images of the entire study area.

Complete error matrices could not be constructed since there were no non-GAA validation data available outside of the defined geothermal areas. 174 Thermal Inventory points were identified outside of the defined geothermal areas, however, and were used to evaluate the ability of CEM to identify GAA for each of the three training sets. The maps were displayed over NAIP imagery and visually inspected for similarities to Thermal Inventory Project points and landscape features.

Results

Random Forest Classification of Defined Geothermal Areas

Three classified maps of the defined geothermal areas were produced with low to potentially artificially high accuracies. Semi-independent overall accuracies ranged from 66.17% to 96.33% with Kappa statistics ranging from 0.32 to 0.93 (Table 4.3).

Table 4.3: Random forest out-of-bag accuracies, semi-independent overall accuracies, and Kappa statistics for the three random forest classifications of the defined geothermal areas.

Method	Random Forest OOB Accuracy	Semi-independent Overall Accuracy	Semi-independent Kappa Statistic
Inventory Buffer	57.56%	66.17%	0.32
Photo Interp	71.93%	73.00%	0.46
M_{terr} Threshold	93.14%	96.33%	0.93

Inventory Buffer Method: 16.67% of the defined geothermal areas were classified as GAA with the Inventory Buffer method. Class accuracies ranged from 60.00% to 72.33% (Table 4.4). Variable importance plots illustrate each predictor variable's contribution to the mean decrease in the OOB error rate (Sesnie *et al.*, 2008),

Table 4.4: Semi-independent error matrix for the Inventory Buffer classification of the defined geothermal areas. Class accuracies are represented by user's accuracy (errors of commission) and producer's accuracy (errors of omission). The Kappa statistic is a measure of classification accuracy that is more conservative than overall accuracy.

		Reference Data		
	Class	GAA	Non-GAA	User's Accuracy
Classified Data	GAA	180	83	68.44%
	Non-GAA	120	217	64.39%
	Producer's Accuracy	60.00%	72.33%	
		Overall Accuracy = 66.17% Kappa = 0.3233		

where those variables closer to the top of the plot are the most influential to the accuracy of the classification and those closer to the bottom are the least important to the accuracy. The RF variable importance plot for the Inventory Buffer method indicated that 11 of the top 12 variables were dominated by reflective spectral information (Figure 4.2). All of the original Landsat reflective bands were in the top 12. PCA3 was interpreted from the eigenvector weightings as representing primarily the NIR band with additional influence from the MIR2 band (Table 4.5), PCA1 was interpreted as representing all of the reflective spectral bands almost equally (in other words, the pixel brightness), and TCW, TCB, and albedo were derived from the reflective bands. These 5 components were in the top 12. The only non-reflective spectral information in the top 12 was topographic information (slope). Three of the 4 geothermal components, PCA4 (interpreted as representing primarily M_{terr}), M_{terr}, and GHF_{α}, on the other hand, were among the bottom 6 variables and were of lesser importance than the majority of the included predictor variables (Figure 4.2). Aspect, a topographic variable, was one of the

least influential predictor variables along with PCA5 and PCA6 (interpreted as representing primarily the visible bands).

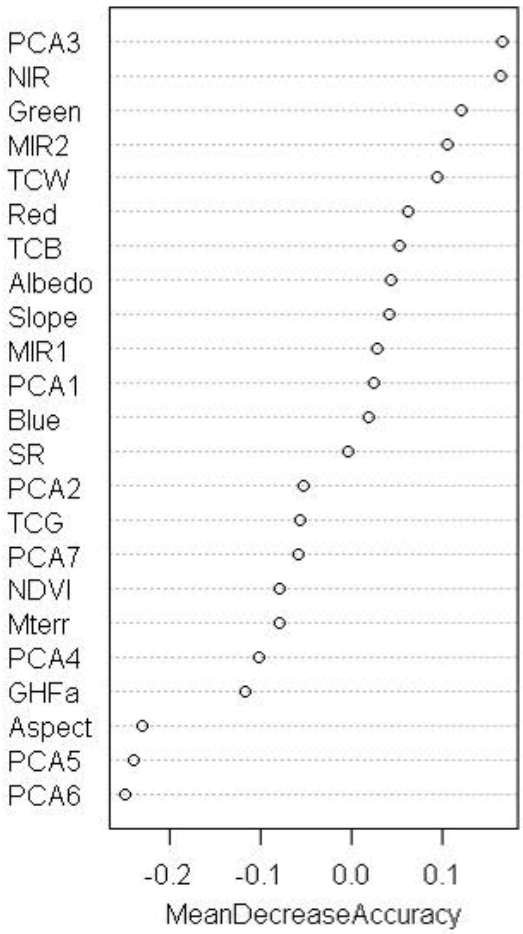

Figure 4.2: Predictor variable importance plot for the Inventory Buffer classification of the defined geothermal areas. Variables at the top of the plot were more influential to the accuracy of the classification than variables at the bottom.

Table 4.5: Principal component eigenvectors that show the weightings of each input band on each principal component (PCA). PCA1 is highly weighted in visible bands and the NIR and MIR bands. PCA2 and PCA4 are weighted high in M_{terr} and MIR. PCA3 is weighted mostly in the NIR. PCA5 is highly weighted in blue and green, and PCA6 is highly weighted in green and red. PCA7 is mostly weighted in MIR, with some influence from red.

	PCA1	PCA2	PCA3	PCA4	PCA5	PCA6	PCA7
Blue	0.443	-0.307	0.191	-0.093	-0.791	0.190	0.052
Green	0.450	-0.302	0.116	-0.125	0.560	0.542	0.263
Red	0.463	-0.260	0.205	-0.108	0.242	-0.621	-0.470
NIR	0.372	-0.011	-0.900	0.037	-0.036	-0.161	0.170
MIR	0.326	0.496	-0.035	0.391	-0.007	0.394	-0.582
M_{terr}	0.148	0.550	0.021	-0.821	-0.026	0.013	0.008
MIR	0.345	0.445	0.320	0.369	0.016	-0.321	0.583

The Inventory Buffer method classified only a small portion of the largest geothermal feature in YNP, Grand Prismatic in Midway Geyser Basin, as GAA, but classified all of Excelsior Geyser, a large feature adjacent to Grand Prismatic, as GAA (Figure 4.3). Much of the geothermal barrens were classified as GAA. The Firehole River was generally classified as non-GAA, with a few exceptions that might be related to pixel geometric registration. For example, a feature with high M_{terr} might be located at the edge of a pixel, but with geometric registration errors might fall in a different pixel and be classified incorrectly.

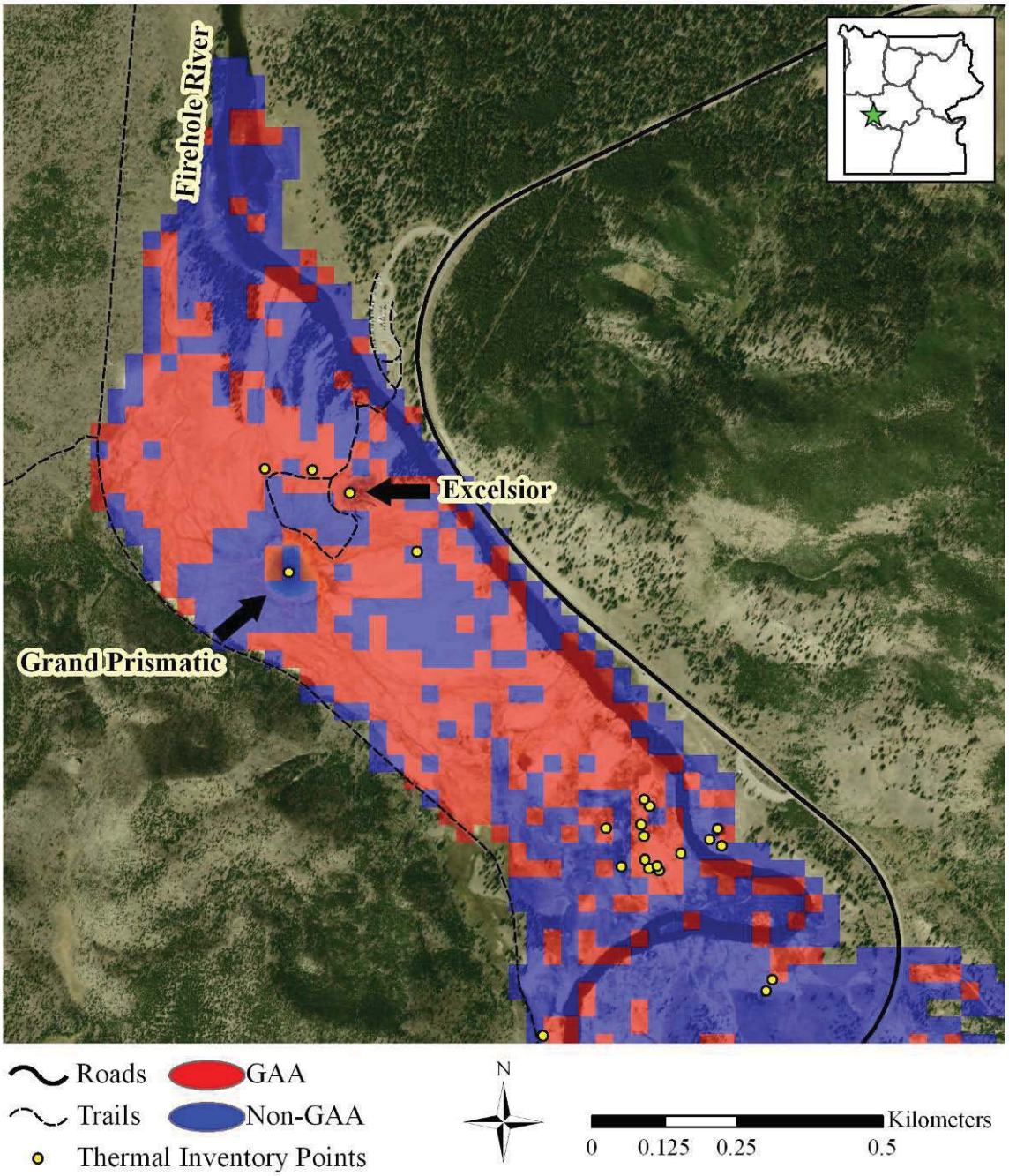

Figure 4.3: Buffer Inventory classified map of Grand Prismatic Spring and Excelsior Geyser in Midway Geyser Basin. Thermal Inventory points are displayed over the classification, with National Agriculture Imagery Program (NAIP) imagery in the background. Excelsior Geyser was successfully classified as a geothermally active area (GAA), but much of Grand Prismatic Spring was misclassified as a non-geothermally active area (non-GAA). Geothermal barrens were classified as both GAA and non-GAA throughout the area. The majority of the Firehole River was classified as non-GAA.

Photo Interp Method: 45.9% of the defined geothermal areas were classified as GAA with the Photo Interp method. Class accuracies ranged from 66.00% to 80.00% (Table 4.6). The RF variable importance plot for the Photo Interp method indicated that the top 14 variables were dominated by reflective spectral information. PCA7 was interpreted as representing primarily the MIR bands (Table 4.5), and TCG and NDVI were derived from reflective data and represent green vegetation (Figure 4.4). These 3 components, along with the 11 other components described above, were in the top 14 variables. Again, 3 of the 4 geothermal components, PCA4, Mterr, and GHFα, were among the bottom 6 variables and were of lesser importance than the majority of the included predictor variables, with GHFα the least important variable (Figure 4.4). Again, aspect was one of the least influential predictor variables, along with SR, a combination of latitude, aspect, and slope.

Table 4.6: Semi-independent error matrix for the Photo Interp classification of the defined geothermal areas. Class accuracies are represented by user's accuracy (errors of commission) and producer's accuracy (errors of omission). The Kappa statistic is a measure of classification accuracy that is more conservative than overall accuracy.

		Reference Data		
	Class	GAA	Non-GAA	User's Accuracy
Classified Data	GAA	40	17	70.18%
	Non-GAA	10	33	76.74%
	Producer's Accuracy	80.00%	66.00%	
		Overall Accuracy = 73.00% Kappa = 0.4600		

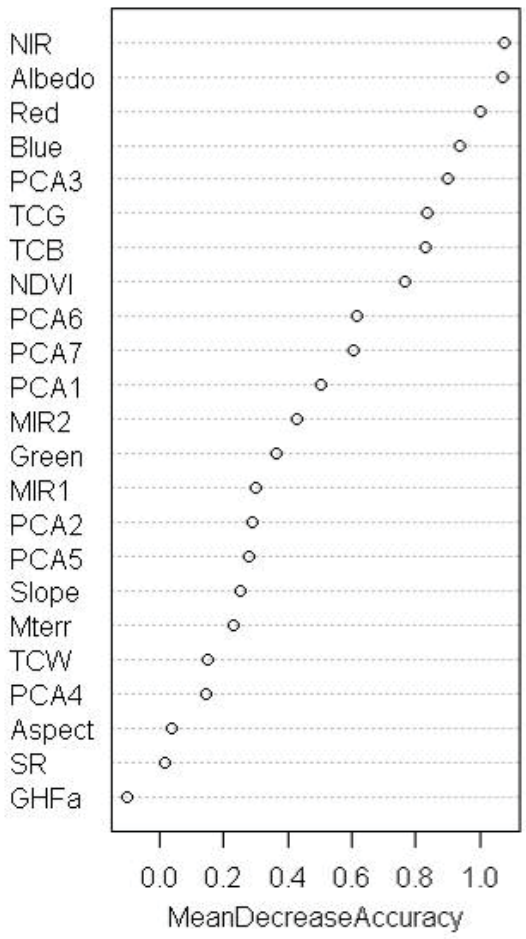

Figure 4.4: Predictor variable importance plot for the Photo Interp classification of the defined geothermal areas. Variables at the top of the plot were more influential to the accuracy of the classification than variables at the bottom.

The Photo Interp classification method successfully classified pixels that included Old Faithful and many of the geothermal features in Upper Geyser Basin as GAA (Figure 4.5). The outer edges of the defined geothermal areas, grassy fields, and buildings were generally classified as non-GAA, while much of the geothermal barrens and some of the Firehole River were classified as GAA.

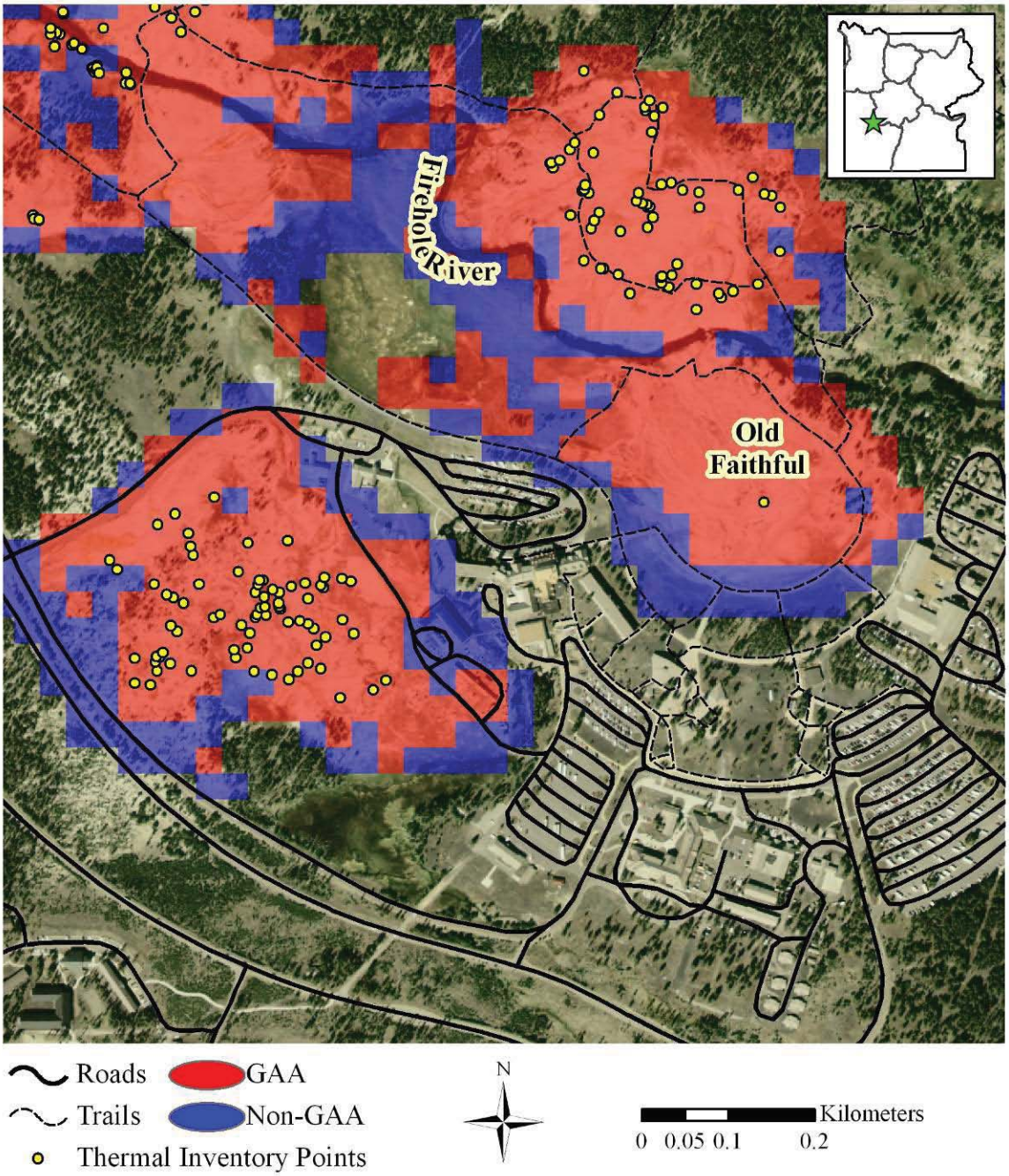

Figure 4.5: Photo Interp classified map of the Old Faithful area in Upper Geyser Basin. Thermal Inventory points are displayed over the classification, with National Agriculture Imagery Program (NAIP) imagery in the background. Old Faithful Geyser was successfully classified as a geothermally active area (GAA). Roads, buildings, and grassy expanses were correctly classified as non-geothermally active areas (non-GAA). Geothermal barrens might have been over-classified as GAA.

Mterr Threshold Method: 80.93% of the defined geothermal areas were classified as GAA with the Mterr Threshold method. Class accuracies ranged from 94.00% to 98.67% (Table 4.7). The RF variable importance plot for the M_{terr} Threshold method indicated that the 4 geothermally influenced components, PCA2 (interpreted as representing a combination of M_{terr} and the MIR bands (Table 4.5)), PCA4, M_{terr}, and GHF_{α}, were among the top 6 most important variables (Figure 4.6). Slope was very important, as was TCW. Similar to the Inventory Buffer method, aspect and PCA6 were the least influential predictor variables.

Table 4.7: Semi-independent error matrix for the M_{terr} Threshold classification of the defined geothermal areas. Class accuracies are represented by user's accuracy (errors of commission) and producer's accuracy (errors of omission). The Kappa statistic is a measure of classification accuracy that is more conservative than overall accuracy.

		Reference Data		
	Class	GAA	Non-GAA	User's Accuracy
Classified Data	GAA	282	4	98.60%
	Non-GAA	18	296	94.27%
	Producer's Accuracy	94.00%	98.67%	
		Overall Accuracy = 96.33% Kappa = 0.9267		

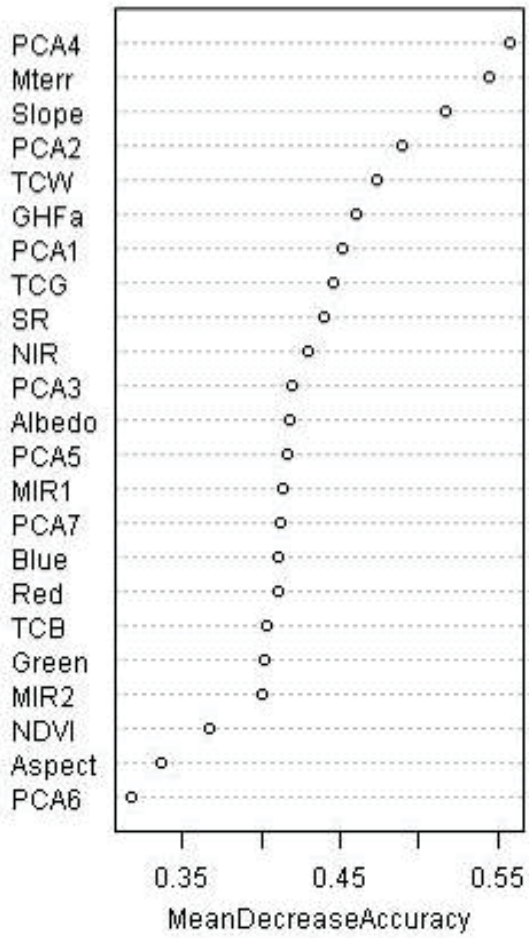

Figure 4.6: Predictor variable importance plot for the M_{terr} Threshold classification of the defined geothermal areas. Variables at the top of the plot were more influential to the accuracy of the classification than variables at the bottom.

The M_{terr} Threshold method classified nearly all of Mammoth Hot Springs as GAA (Figure 4.7). The few pixels classified as non-GAA appeared to be forested, thus all geothermal barrens were classified as GAA. GAA in this area was likely very over-classified, although the accuracy assessment indicated very high overall and class accuracies (Table 4.7).

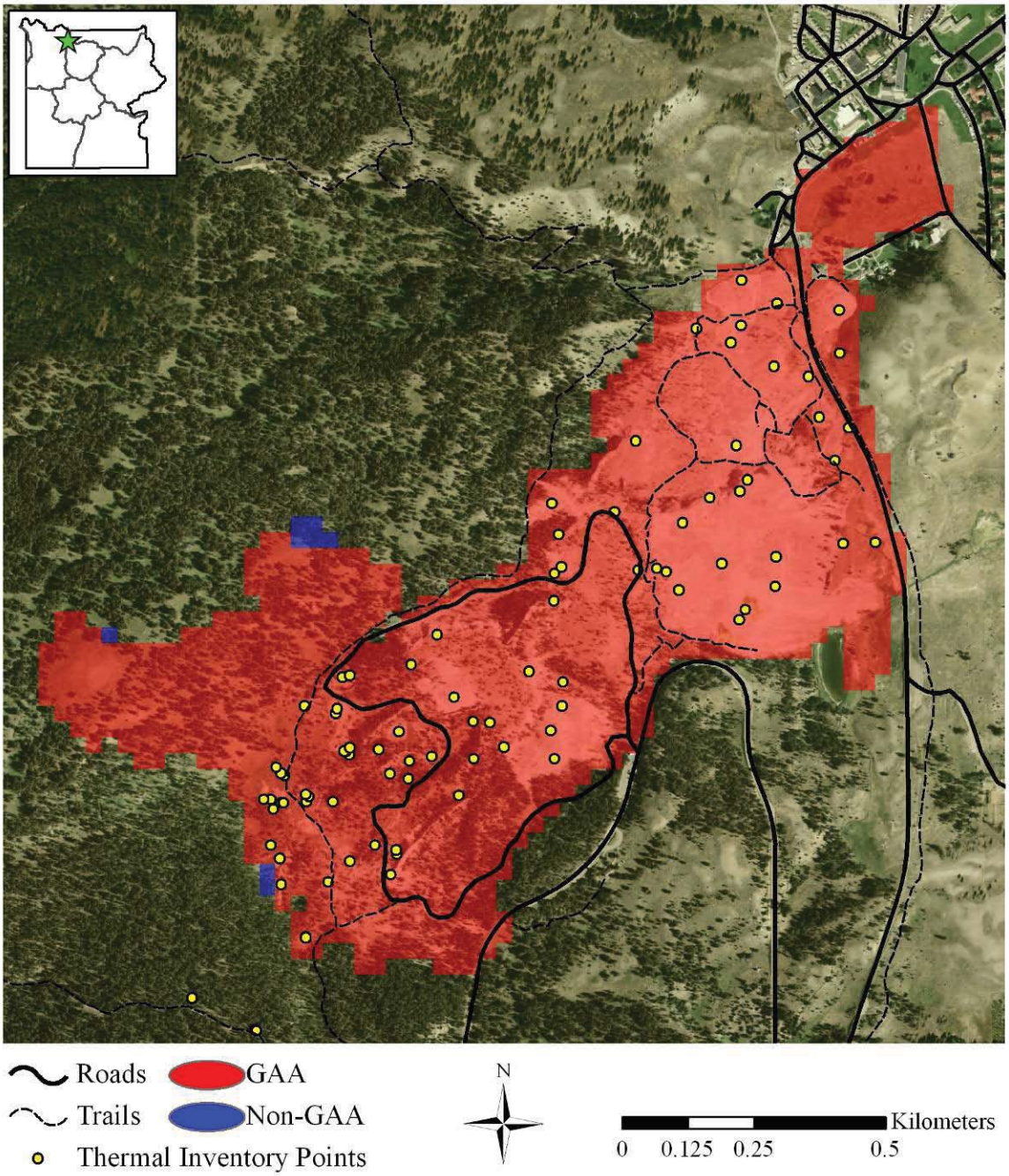

Figure 4.7: M_{terr} Threshold classified map of Mammoth Hot Springs. Thermal Inventory points are displayed over the classification, with National Agriculture Imagery Program (NAIP) imagery in the background. Nearly the entire area was classified as geothermally active areas (GAA), most likely an over-classification. Only forested areas were classified as non-geothermally active areas (non-GAA).

Pairwise Comparisons: Four of the six Z statistics and *p*-values for the independent accuracy assessments indicated the classifications were better than random (Table 4.8). The Mterr Threshold classifications cross-validated with independent reference data had Z statistics less than the critical value of 1.96 and *p*-values greater than 0.025, indicating this classification was no better than random. A statistically significant difference was detected between the Photo Interp and the Inventory Buffer methods, but the sample data did not detect differences among the other method pairs (Table 4.9).

Table 4.8: Kappa and Z statistics and p-values for independent accuracy assessments. Each classification method was tested with validation data from the other 2 classification methods. Z statistic values greater than 1.96 indicate statistical significance at the 95% confidence level; *p*-values less than 0.025 indicate statistical significance. The M_{terr} Threshold method was no better than random with both sets of validation data.

Classification Method	**Validation Method**	**Kappa**	**Z**	***p*-value**
Inventory Buffer	Photo Interp	0.24	2.27	0.013
Inventory Buffer	M_{terr} Threshold	0.56	16.65	<0.001
Photo Interp	M_{terr} Threshold	0.44	11.86	<0.001
Photo Interp	Inventory Buffer	0.18	2.63	0.004
M_{terr} Threshold	Inventory Buffer	0.11	1.81	0.035
M_{terr} Threshold	Photo Interp	0.06	0.41	0.339

Table 4.9: Pairwise comparisons of independent accuracy assessments. Pairs of classification methods were compared to determine if they were statistically different. Z statistic values greater than 1.96 indicate statistical significance at the 95% confidence level; *p*-values less than 0.025 indicate statistical significance. The Photo Interp and Inventory Buffer methods were found to be statistically significantly different when the M_{terr} Threshold data were used for validation.

Pairwise Comparison	**Validation Method**	**Z statistic**	***p*-value**
Inventory Buffer vs. M_{terr} Threshold	Photo Interp	1.00	0.159
M_{terr} Threshold vs. Photo Interp	Inventory Buffer	0.08	0.465
Photo Interp vs. Inventory Buffer	M_{terr} Threshold	2.53	0.006

Target Detection Classification

Continuous output values for each target detection classification ranged from -1 to 2. Pixels with a value of 2 were classified as GAA. All other pixels were classified as non-GAA. The percentage of known GAA locations outside the defined geothermal areas (located during the Thermal Inventory Project, but not found within the boundaries of the defined geothermal areas) that each classification method was able to detect ranged from 6.3% to 30.5% (Table 4.10).

Table 4.10: Percent of known geothermally active area (GAA) locations outside the defined geothermal areas detected by each classification method. The GAA reference data were collected from the Thermal Inventory points.

Classification Method	Reference Totals	Classified Totals	Percent Detected
Inventory Buffer	174	11	6.32%
Photo Interp	174	48	27.59%
Mterr Threshold	174	53	30.46%

Only 0.07% of the study area was classified as GAA with the Inventory Buffer method. 0.42%, of the study area was classified as GAA with the Photo Interp method. 0.29% of the study area was classified as GAA with the Mterr Threshold method. The map of the Inventory Buffer classification of the area near La Duke Hot Springs in Montana (just outside of YNP) showed very little area classified as GAA (Figure 4.8.b), however, two of the three geothermal features at La Duke Hot Springs fall on one pixel that was successfully classified as GAA (Figure 4.8.b inset). The Photo Interp and M_{terr} Threshold classifications show considerably more area classified as GAA, including over-classification of the gravel quarry and Devil's Slide, a south-facing, steep, linear,

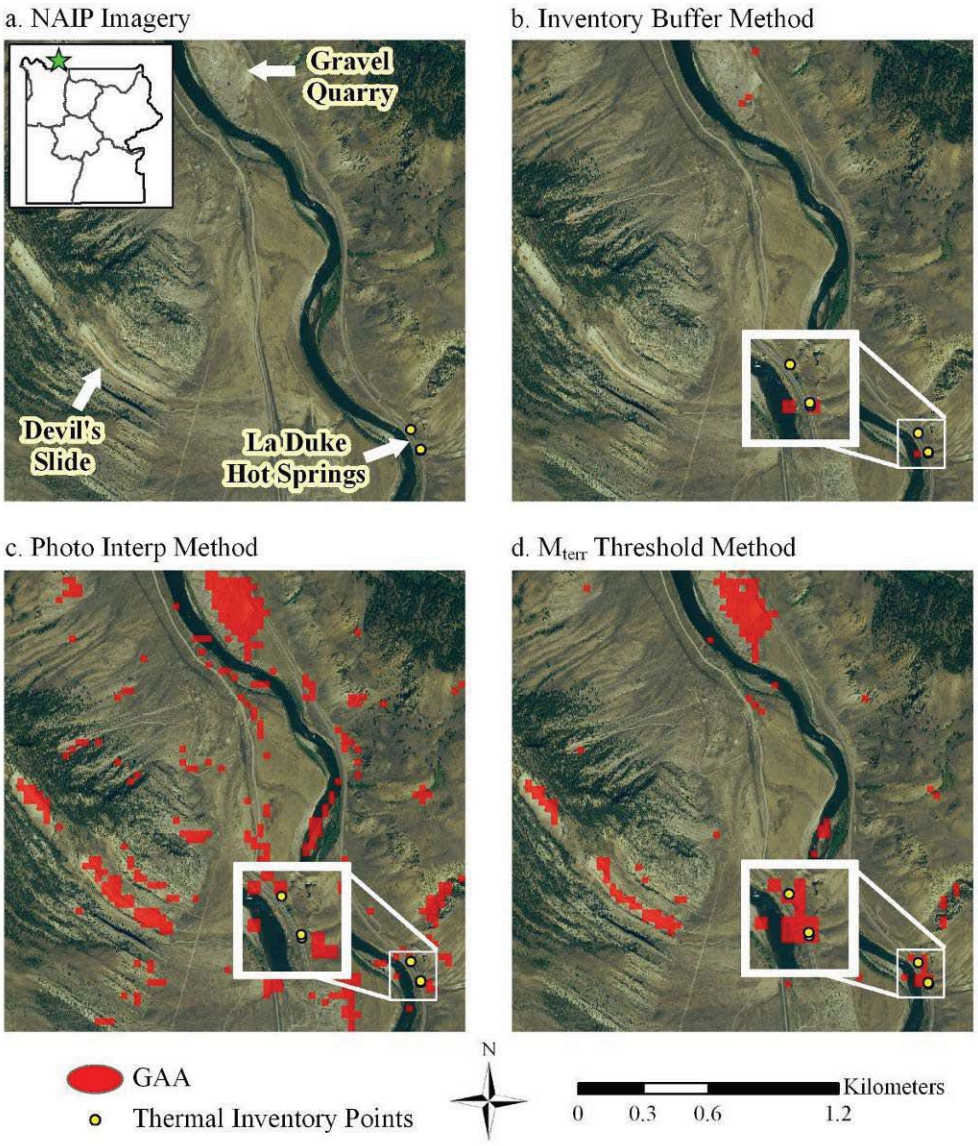

Figure 4.8: Classified maps of a portion of the Corwin Springs, Montana Known Geothermal Resource Area. Thermal Inventory points are displayed over the classification, with National Agriculture Imagery Program (NAIP) imagery in the background. Devil's Slide, a geological feature, and the gravel quarry were over-classified by the Photo Interp and M_{terr} Threshold methods. One of the two pixels with Thermal Inventory points was classified as a geothermally active area (GAA) by the Inventory Buffer method, while neither were by the Photo Interp method and both were by the M_{terr} Threshold method.

geologic feature with no vegetation or geothermal activity (Figures 4.8.c and 4.8.d). The pixels that cover the area of the three geothermal features at La Duke Hot Springs were

classified as GAA with the M_{terr} Threshold method (Figure 4.8.d inset), but not with the Photo Interp method (Figure 4.8.c inset).

Discussion

Classification of Defined Geothermal Areas

Three different RF classifications were performed with three different sets of reference data. The OOB accuracies reported by the RF algorithm were considerably different from one another, with a 35% difference between the lowest and highest accuracies (Table 4.3). When the methods of collecting non-GAA reference data were considered (since all GAA reference data were based on Thermal Inventory points), these results were expected. The Inventory Buffer method was the least biased as the reference points were randomly generated, while the M_{terr} Threshold method was the most biased because its randomly selected non-GAA points were actually stratified by M_{terr} values less than the established threshold. The reported accuracies for the M_{terr} Threshold method were, therefore, artificially high due to the bias introduced by the training data selection process, however, the OOB accuracies were representative of how well the classification method worked with those specific data.

The semi-independent overall accuracies were within approximately 3% of the OOB accuracies for the Photo Interp and M_{terr} Threshold methods (Table 4.3), as expected (Lawrence *et al.*, 2006). The semi-independent overall accuracy for the Inventory Buffer method, on the other hand, was nearly 9% higher than the OOB accuracy (Table 4.3). This substantial difference was likely because of the variability

within the reference data as the randomly generated points covered a diverse and highly variable landscape. The kappa statistics were all positive values and indicated that all three methods were better than random.

The variables of importance in the RF classifications (Figures 4.2, 4.4, and 4.6) indicated additional biases in the classifications. M_{terr}, PCA4, and GHF_{α}, derivatives of the Landsat TIR band, were among the least important predictor variables for the Inventory Buffer and Photo Interp methods. Reflective data, however, were significantly more important than TIR derivatives in these two methods. PCA3, mostly influenced by the NIR, PCA1, a representation of brightness mostly influenced by the visible bands, and the NIR band were among the top half of the important variables in all three variable importance plots. This indicated a bias for reflective rather than emitted (geothermal) information and was evident in the mapped data, especially for the Photo Interp classification method. In essence, the Inventory Buffer and Photo Interp classification methods were relying heavily on reflected information (bright white geothermal barrens that might or might not be geothermally active, dark cinder, etc.) associated with geothermal areas more than on thermal information from geothermal emittance. Slope was an important variable for the Inventory Buffer method, but one of the least important variables for the Photo Interp method, suggesting the Inventory Buffer method had a bias towards slope. Aspect was unimportant for both methods and although its interactions with other variables might be important, on its own it has little influence on these classifications.

The M_{terr} Threshold method was biased in its preference for the 4 TIR-derived predictor variables, M_{terr}, PCA2, PCA4, and GHF_{α}. This was expected as the non-GAA reference data were based on the emittance of heat from the ground as opposed to reflective properties of geothermally active ground. The top 6 most important variables for the M_{terr} Threshold method were among the bottom 7 least important variables for the Photo Interp method, suggesting biases in both methods and serious differences among the two methods. Aspect was, once again, one of the least important variables even though it is a portion of GHF_{α} (in the calculation for SR that is included in the calculation for GHF_{α}), leading to the conclusion that even with interactions with other variables, aspect was not a useful predictor variable in these classifications.

The pairwise comparisons of two classification accuracies based on independent validation data from the third method indicated that the Inventory Buffer and Photo Interp methods were better than random and significantly different from one another when the M_{terr} Threshold data were used for cross-validation (Tables 4.8 and 4.9). The statistical difference between these two methods was likely due to the substantial difference in numbers in the training datasets (3,280 points for the Inventory Buffer method compared to 171 points for the Photo Interp method) as well as the differences in nature of the non-GAA reference data. The Inventory Buffer non-GAA reference data were highly variable as opposed to both the non-GAA reference datasets for the Photo Interp and M_{terr} Threshold methods that were less variable because of inherent biases. The M_{terr} Threshold method was found to be no better than random based on both sets of independent data (Table 4.8) and the sample data were unable to detect any significant

differences between the Mterr Threshold method and the other two classification methods (Table 4.9).

Less than 20% of the defined geothermal areas were classified as GAA with the Inventory Buffer method, most likely an under-prediction based on locations of Thermal Inventory points (see Figure 4.3), but perhaps more realistic than the M_{terr} Threshold method that classified more than 80% of the defined geothermal areas as GAA, most likely a serious over-prediction (see Figure 4.7). The Photo Interp method classified 46% of the defined geothermal areas as GAA and appeared to classify most of the Thermal Inventory points while not over-classifying the GAA as substantially as the M_{terr} Threshold method (see Figure 4.5).

Visual inspections of the classified maps showed that the classifications were successful in some locations and not in others (Figures 4.3, 4.5, and 4.7). Further comparisons of the three methods are of interest. Grand Prismatic Spring and Excelsior Geyser in Midway Geyser Basin are two of the largest geothermal features in YNP, yet both features were missed by the Photo Interp method, most of Grand Prismatic was missed by the Inventory Buffer method, and one pixel of Grand Prismatic was missed by the M_{terr} Threshold method (Figure 4.9). The Inventory Buffer method appeared to under-classify GAA as many of the pixels with Thermal Inventory points, including Grand Prismatic, were classified as non-GAA (Figure 4.9.b). The Photo Interp method appeared to successfully classify most of the pixels with Thermal Inventory points as GAA (except portions of Grand Prismatic and Excelsior) and most of the river pixels as non-GAA, but possibly over-classified the geothermal barrens as GAA (Figure 4.9.c).

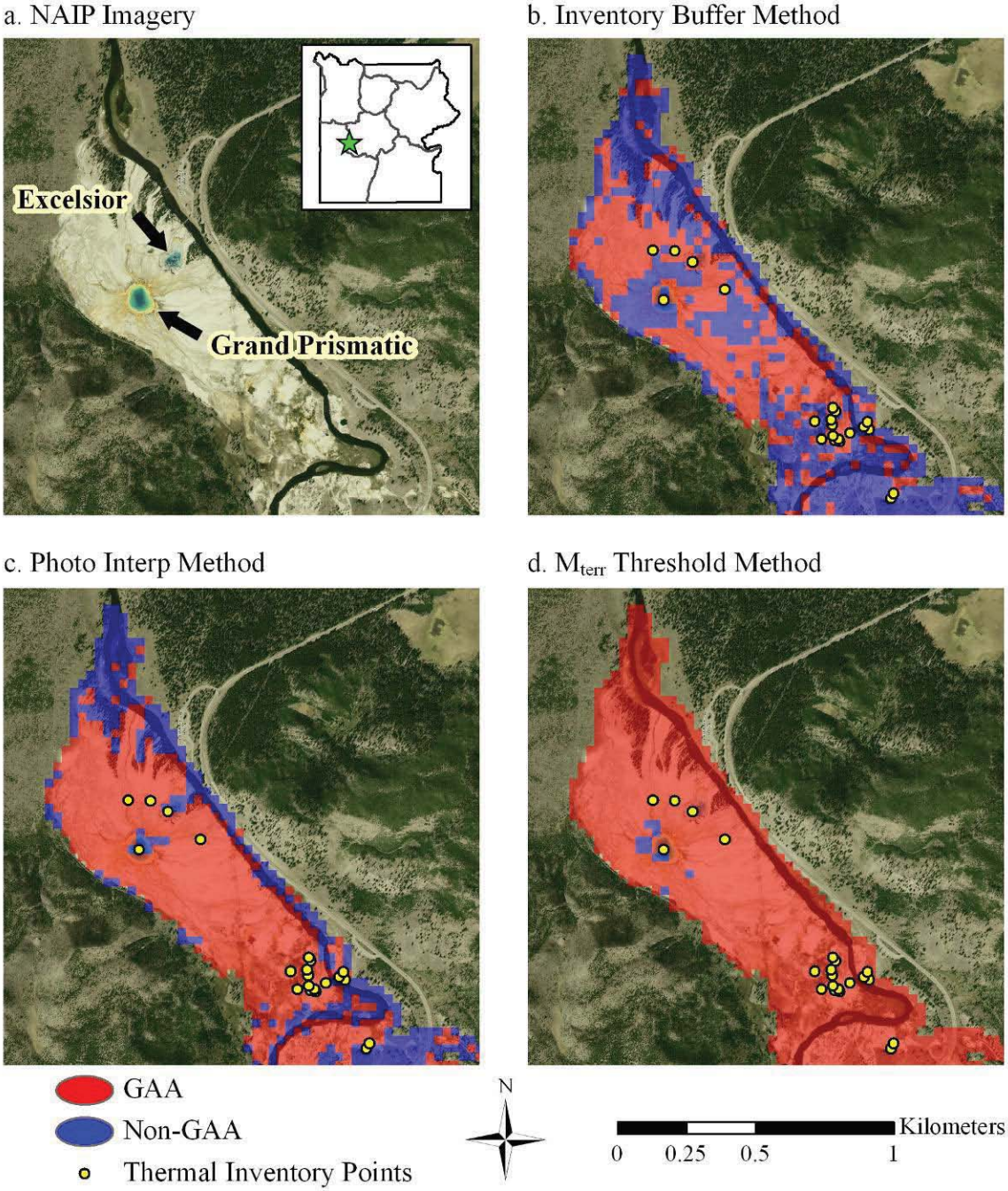

Figure 4.9: Classified maps of Grand Prismatic Spring and Excelsior Geyser in Midway Geyser Basin. Thermal Inventory points are displayed over the classification, with National Agriculture Imagery Program (NAIP) imagery in the background. The Inventory Buffer method appears to slightly under-classify the geothermally active areas (GAA), while the Photo Interp method slightly over-classified GAA and the M_{terr} Threshold method seriously over-classified GAA. Only the M_{terr} Threshold method successfully classified both Grand Prismatic Spring and Excelsior Geyser. The Photo Interp classified both features as non-geothermally active areas (non-GAA), and the Inventory Buffer classified Excelsior Geyser as GAA, but misclassified most of Grand Prismatic Spring as non-GAA.

The M_{terr} Threshold method seriously over-classified nearly the entire area as GAA, successfully classifying pixels with Thermal Inventory points as GAA, but also classifying all forest and water pixels as GAA as well (Figure 4.9.d). Based on visual inspection alone, in Midway Geyser Basin the Inventory Buffer method appeared to perform the best, even though part of Grand Prismatic was misclassified and GAA might have been slightly under-classified.

Old Faithful Geyser in Upper Geyser Basin is well-known due to its regular eruptions. All three classification methods classified Old Faithful as GAA, (Figure 4.10). Many of the pixels with Thermal Inventory points were classified by the Inventory Buffer method as non-GAA (Figure 4.10.b), however, the Photo Interp method classified nearly all of the pixels with Thermal Inventory points as GAA (Figure 4.10.c). The Photo Interp method, additionally, appeared to do a good job of classifying the grasslands, buildings, roads, and parking lots as non-GAA (Figure 4.10.c), but the M_{terr} Threshold method seriously over-classified the entire area as GAA (Figure 4.10.d). Based on visual inspection alone, in Upper Geyser Basin the Photo Interp method appeared to perform the best, although GAA might have been slightly over-classified.

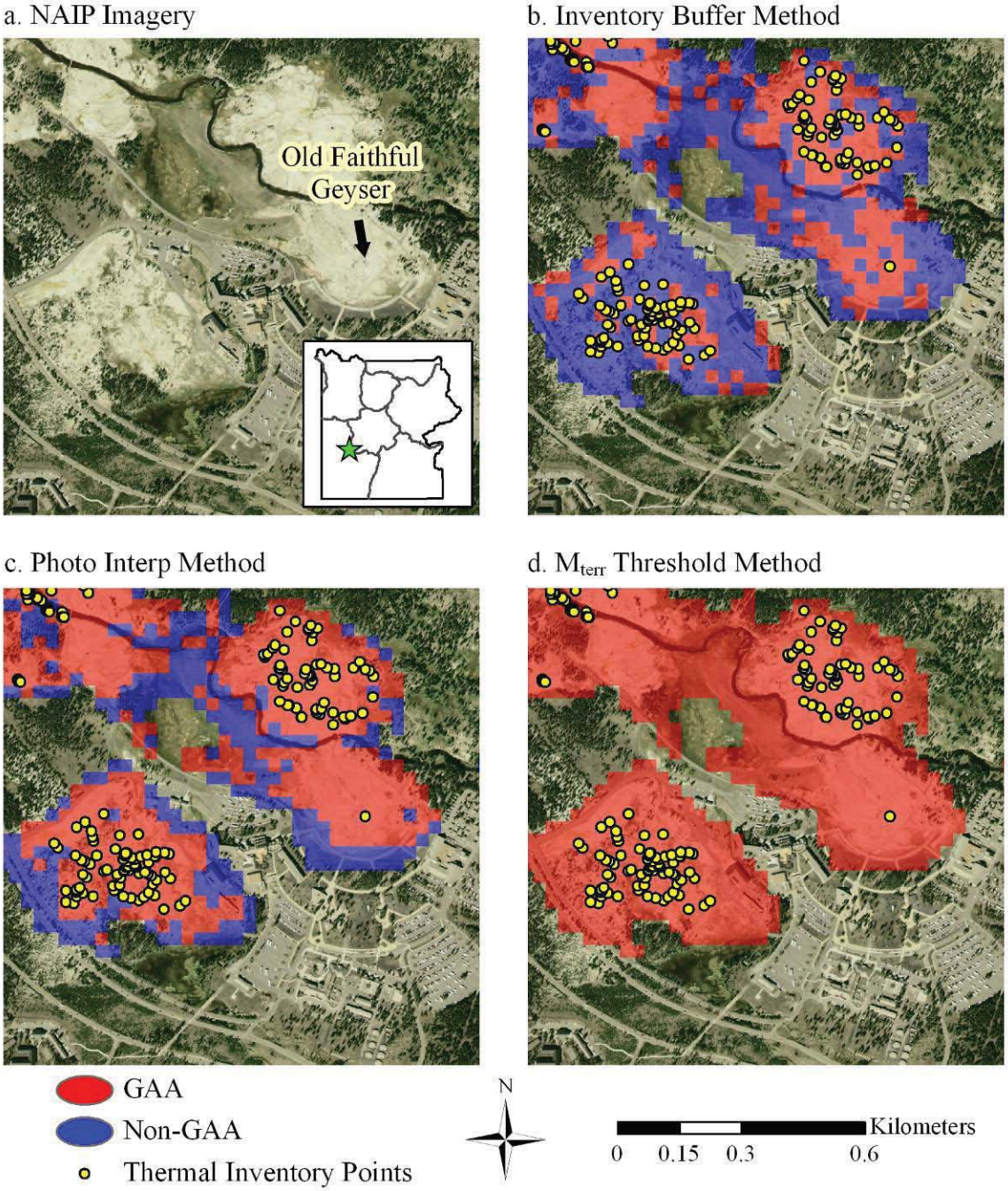

Figure 4.10: Classified maps of the Old Faithful area in Upper Geyser Basin. Thermal Inventory points are displayed over the classification, with National Agriculture Imagery Program (NAIP) imagery in the background. Old Faithful Geyser was accurately classified as a geothermally active area (GAA) by all three methods.The Inventory Buffer method appears to slightly under-classify GAA, while the Photo Interp method possibly slightly over-classified GAA and the M_{terr} Threshold method seriously over-classified GAA as nothing was classified as a non-geothermally active area (non-GAA).

Mammoth Hot Springs near the north entrance to YNP is an active geothermal area and has many constantly changing geothermal features including an unnamed feature that appeared next to Narrow Gauge Spring during the summer of 1998, another feature that was mostly inactive for many years prior to overtaking the boardwalk in 2005 (Palette Spring), and a feature that has stopped and started flowing again multiple times over the last several decades (Canary Spring) (personal observations). The Inventory Buffer method classified nearly all of the Mammoth area as non-GAA, including most of the pixels that include Thermal Inventory points, seriously under-classifying GAA in the area (Figure 4.11.b). The Photo Interp method classified many large solid areas of GAA and successfully classified many of the pixels with Thermal Inventory points as GAA (Figure 4.11.c), while the M_{terr} Threshold method seriously over-classified nearly the entire area as GAA (Figure 4.11.d). Once again, based on visual inspection alone, in Mammoth Hot Springs the Photo Interp method appeared to perform the best, although GAA was possibly slightly over-classified.

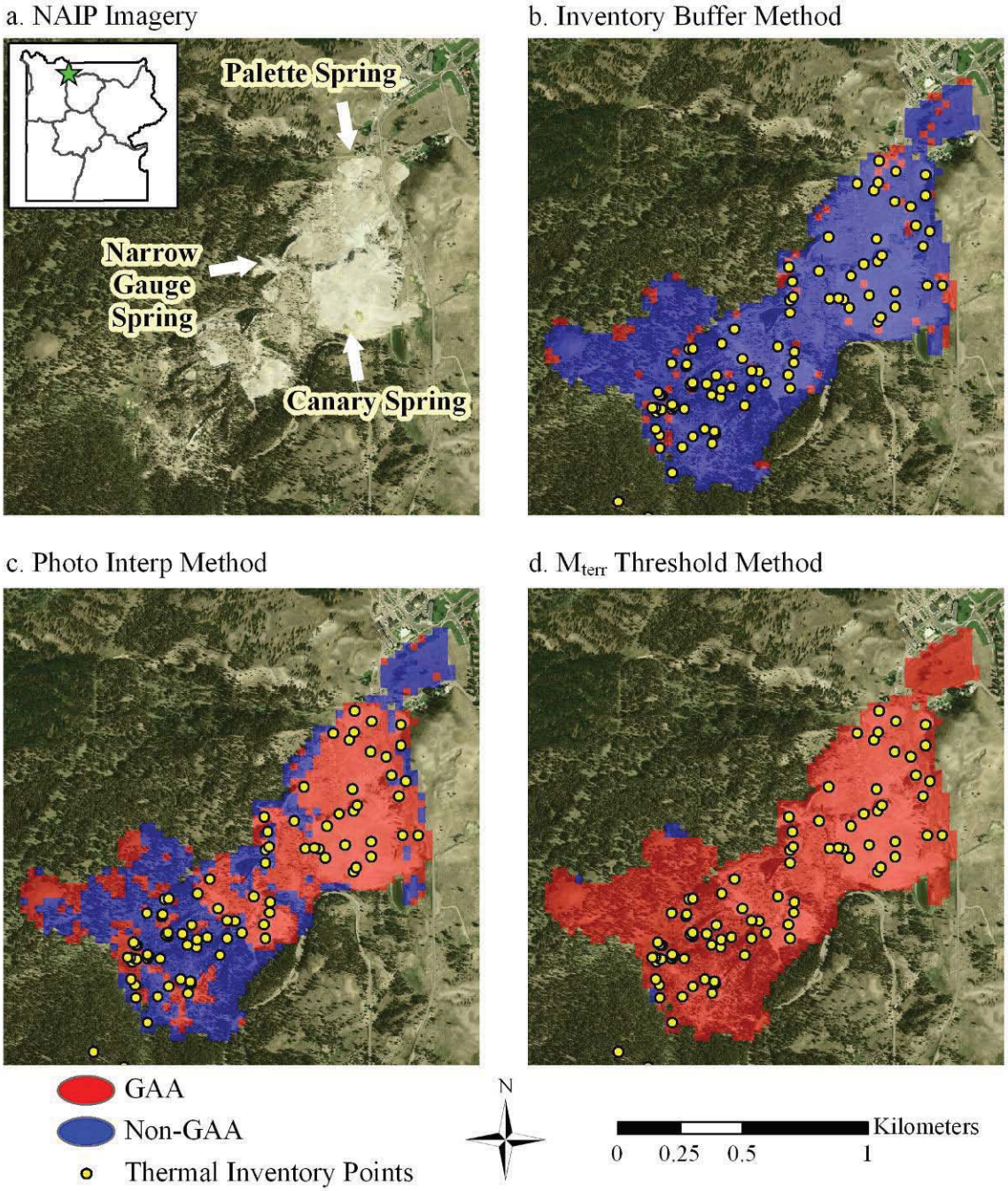

Figure 4.11: Classified maps of Mammoth Terraces in Mammoth Hot Springs. Thermal Inventory points are displayed over the classification, with National Agriculture Imagery Program (NAIP) imagery in the background. The Inventory Buffer method appears to seriously under-classify the geothermally active areas (GAA) as the majority of the pixels were classified as non-geothermally active areas (non-GAA). The Photo Interp method possibly slightly over-classified GAA and the M_{terr} Threshold method seriously over-classified GAA.

Classification of Entire Study Area

There are recognized potential threats to geothermal features in YNP, including possible geothermal development in the Corwin Springs, Montana, and Island Park, Idaho KGRAs (Sorey, 1991; Heasler *et al.*, 2004), that make accurate maps of GAA outside of YNP increasingly important. The classified data from the defined geothermal area were used as training data to classify all of the study area with a CEM target detection algorithm. A small percentage of known geothermal locations were detected with these methods (Table 4.10), with the M_{terr} Threshold method successfully classifying just over 30% of the known geothermal locations outside the defined geothermal areas. Visual inspection of the data in a portion of the Corwin Springs KGRA (Figure 4.8) showed that the Inventory Buffer method classified very little GAA in the area and the other two methods classified considerably more. Many of the areas classified with the Photo Interp and M_{terr} Threshold methods were south-facing rocky slopes (*e.g.*, Devil's Slide), flat grasslands, or the gravel quarry. The M_{terr} Threshold method successfully classified the features at La Duke Hot Springs as GAA, while the Inventory Buffer method classified only one pixel there as GAA and the Photo Interp method did not classify any of the features at La Duke Hot Springs as GAA. The visual inspection supported the very low GAA class accuracies, suggesting the Inventory Buffer method under-classified and the Photo Interp and M_{terr} Threshold methods over-classified, but no one method was appreciably better than the others in classifying the entire study area.

Implications

At first glance, the accuracies of the three different RF classification methods appeared to indicate that the M_{terr} Threshold method was the best overall (Table 4.3). The nature of the validation data for the Photo Interp and M_{terr} Threshold methods, however, would not allow for the detection of any errors that resulted from the acknowledged bias in the training data, thus suggesting the accuracies for these two methods are artificially inflated. The Inventory Buffer method had the least biased non-GAA reference data and when these validation data were utilized for accuracy assessment of each of the three methods, the Inventory Buffer method appeared to perform the best (Kappa values = 0.32 for Inventory Buffer, 0.18 for Photo Interp, and 0.11 for M_{terr} Threshold)(Tables 4.3 and 4.8). The Inventory Buffer classification was better than random, but accuracies were low. The area where the reference data for the Inventory Buffer method were randomly generated was a highly variable landscape, and it is likely that many of the non-GAA training and validation points were in areas of high M_{terr} that had no geothermal activity, such as inactive geothermal barrens, and were thus confused with areas of high M_{terr} that *were* geothermally active, such as active geothermal barrens. The Inventory Buffer method was not robust enough, or more likely the geothermal landscape was too variable, to produce an acceptable GAA classification, although the reference data for this method were the least biased of the three methods.

Inherent geothermal characteristics such as biological and steam spectral signatures might affect classification of GAA in different ways. Grand Prismatic Spring, as seen in Figure 4.12, is brilliantly colorful and very different from the surrounding

landscape. The colors are produced by different microbes within the hot water that survive (and thrive) in various chemical and temperature gradients (Brock, 1967; Brock, 1978), each of which are expressed as distinctive bands of color: Archaea in the blue/green center of the pool at the hottest temperature (75° C), the cyanobacterium, *Synechococcus*, at the pool's yellow edge (59° C to 70° C), a rusty-brown microbial mat produced by the cyanobacterium, *Phormidium*, outside the pool between 30° C and 59° C, and furthest away from the heat source in the center of the pool, the cyanobacterium, *Calthrix*, produces a dull-brown microbial mat (Kaplan and Bartley, 2000). Various photopigments are found in the different microbes in the geothermal features of YNP, including carotenoids (absoption peaks at 0.45 – 0.55 μm), chlorophyll *a* (absorption peaks at 0.43 μm and 0.67 μm), phycocyanin (absorption peak at 0.62 μm), and bacterioclorophylls *a* and *c* (absorption peaks at 0.80 – 0.90 μm and 0.73 μm, respectively) (Jorgensen and DeMarais, 1988; Ward *et al*., 1989). The absorption peaks for these photopigments might be related to the three consistent components for all three classification methods: PCA1, PCA3, and NIR and thus detectable with the reflective Landsat bands, however, the Landsat bandwidths are most likely too wide to distinguish different microbial communities from one another and from vegetation. Only the M_{terr} Threshold classification method was successful at classifying Grand Prismatic Spring as GAA, suggesting that thermal signatures were more important for classification at Grand Prismatic. It is also often covered by a thick layer of steam as the average temperature in the middle of the pool is approximately 75° C (Kaplan and Bartley, 2000). Excelsior Geyser, whose average temperature is approximately 93° C (Thompson and Yadav, 1979;

Brody and Tomkiewicz, 2002) is rarely seen without steam (behind Grand Prismatic in Figure 4.12). Steam has a distinctive spectral signature and is lower in temperature than the water that is producing it, likely obscuring geothermal signatures and causing confusion in the GAA classification with Landsat data as seen in the Photo Interp classification method.

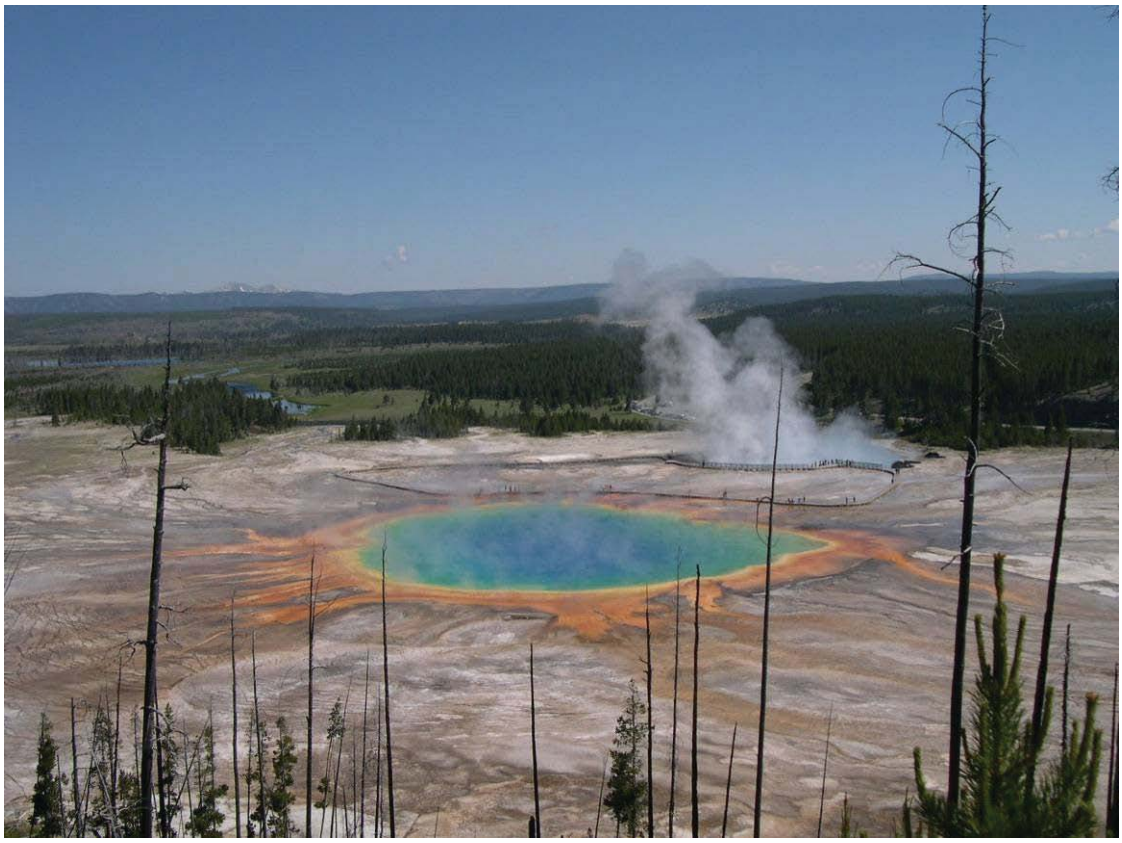

Figure 4.12: Grand Prismatic Spring in Midway Geyser Basin, with Excelsior Geyser steaming in the background, demonstrating the extraordinary variability of geothermal areas in Yellowstone National Park. Photograph by Shannon Savage, taken on 22 June 2006.

The combination of statistical accuracies, variable importance plots, pairwise comparisons, and visual inspections of the Buffer Inventory, Photo Interp, and M_{terr} Threshold RF classification methods was unable to identify any one method of the three

that consistently out-performed the others. After considering the inherent biases in much of the reference data, the higher accuracies of the Photo Interp and M_{terr} Threshold methods were deemed inflated and thus no better than the Inventory Buffer method, if not worse. The Inventory Buffer and Photo Interp random forest classifications were dominated by reflective spectral information, while the M_{terr} Threshold random forest classification was strongly influenced by TIR-derived information. The pairwise cross-validations suggested that the M_{terr} Threshold method was no better than random and that there was a significant difference between the Inventory Buffer and Photo Interp methods. The Inventory Buffer method under-classified GAA, the Photo Interp method over-classified GAA, and the M_{terr} Threshold method seriously over-classified GAA. These results suggest that the M_{terr} Threshold method was in fact a poor method and that something in between the Inventory Buffer and Photo Interp methods might ultimately be the best method for classifying GAA in YNP with Landsat data.

Good training and validation data are fundamental to the success of remotely sensed classifications. The reference data used for this study were not ideal due to both the lack of resources and the lack of ability to collect proper information at a 30-m spatial resolution. Given much additional time and money (and permission from YNP), appropriate sample data could possibly be collected by placing thousands of temperature probes (based on common sampling approaches) across the defined geothermal areas at the same time the Landsat satellite collects data over YNP and interpolating the temperatures to fit 30-m pixels. By using ground probes, the influences of solar radiation and albedo can be better modeled and minimized, allowing the Landsat TIR band to be

properly calibrated to ground temperature, and GAA could then be distinguished from non-GAA. Unfortunately, placing that many probes to get adequate training data is simply not practical, especially for an ongoing monitoring program.

It is possible that Landsat imagery can be an effective tool for monitoring geothermal landscapes. GAA have been difficult to accurately classify with Landsat data in this study, although the classifications were better than random. The difficulty in GAA classification with Landsat lies in the inherent issues with geothermal features and areas and the inherent limitations of Landsat thermal data. Surface reflectance is similar for both active and formerly active geothermally influenced ground, causing confusion between GAA and non-GAA pixels. Steam and snow (if not masked out of image) obscure thermal responses. The thermal response is highly variable not only from different landscape features, but from solar effects. Geothermal features are generally a very small portion of that variability and are often lost in the 120-m thermal pixels. Finally, collecting adequate reference data is impractical.

Scientists will better be able to monitor and protect the geothermal features of YNP as mandated with an accurate refined map of the geothermally active areas within the defined geothermal areas. High spatial resolution (nighttime) thermal imagery might be more useful than Landsat imagery for this purpose, however, there are no known plans for acquiring high spatial resolution imagery covering the entirety of YNP on an annual or seasonal basis. Along with higher spatial resolution, increased spectral resolution should aid in the detection of differing biological influence from microbial communities and might improve the accuracy of geothermal maps of YNP. Despite its limitations,

however, Landsat is the only available thermal data for historical analysis and long-term monitoring of geothermal areas in YNP from 1978 to the foreseeable future (NASA, 2009). Improved reference data collection and ground calibration will be required for future studies of geothermal areas in YNP conducted using Landsat data.

Literature Cited

Andres, R.J. and W.I. Rose. 1995. Description of thermal anomalies on two active Guatemalan volcanoes using Landsat Thematic Mapper imagery. *Photogrammetric Engineering & Remote Sensing*, 61(6): 775-782.

Breiman, L. 2001. Random forests. *Machine Learning*, 45(1): 5-32.

Brock, T.D. 1967. Life at high temperatures. *Science*, 158(3804): 1012-1019.

Brock, T.D. 1978. Thermophilic Microorganisms and Life at High Temperatures. Springer-Verlag, New York, New York, 465 pp.

Brody, M. and W. Tomkiewicz. 2002. Park visitors' understandings, values and beliefs related to their experience at Midway Geyser Basin, Yellowstone National Park, USA. *International Journal of Science Education*, 24(11): 1119-1141.

Chander, G., B.L. Markham, and D.L. Helder. 2009. Summary of current radiometric calibration coefficients for Landsat MSS, TM, ETM+, and EO-1 ALI sensors. *Remote Sensing of Environment*, 113(5): 893-903.

Chang, C.-I., J.-M. Liu, B.-C. Chieu, H. Ren, C.-M. Wang, C.-S. Lo, P.-C. Chung, C.-W. Yang, and D.-J. Ma. 2000. Generalized constrained energy minimization approach to subpixel target detection for multispectral imagery. *Optical Engineering*, 39(5): 1275-1281.

Congalton, R.G. 2001. Accuracy assessment and validation of remotely sensed and other spatial information. *International Journal of Wildland Fire*, 10(4): 321-328.

Congalton, R.G. and K. Green. 1999. Assessing the Accuracy of Remotely Sensed Data: Principles and Practices. Lewis Publishers, Boca Raton, Florida, 137 pp.

Crist, E.P. and R.C. Cicone. 1984. A physically-based transformation of Thematic Mapper data - the TM tasseled cap. *IEEE Transactions on Geoscience and Remote Sensing*, GE-22(23): 256-263.

Du, Q., H. Ren, and C.-I. Chang. 2003. A comparative study for orthogonal subspace projection and constrained energy minimization. *IEEE Transactions on Geoscience and Remote Sensing*, 41(6): 1525-1529.

Farrand, W.H. and J.C. Harsanyi. 1997. Mapping the distribution of mine tailings in the Coeur d'Alene River Valley, Idaho, through the use of a constrained energy minimization technique. *Remote Sensing of Environment*, 59(1): 64-76.

Freeman, E. and T. Frescino. 2009. ModelMap: Modeling and map production using random forest and stochastic gradient boosting. USDA Forest Service, Rocky Mountain Research Station, Ogden, Utah. Last accessed on 9 June 2009. http://cran.r-project.org/web/packages/ModelMap/index.html.

Friedl, M.A. and C.E. Brodley. 1997. Decision tree classification of land cover from remotely sensed data. *Remote Sensing of Environment*, 61(3): 399-409.

Gislason, P.O., J.A. Benediktsson, and J.R. Sveinsson. 2006. Random forests for land cover classification. *Pattern Recognition Letters*, 27(4): 294-300.

Heasler, H., C. Jaworowski, and D. Susong. 2004. A geothermal monitoring plan for Yellowstone National Park, Yellowstone Center for Resources, Yellowstone National Park, Wyoming, 24 pp.

Jensen, J.R. 2005. Introductory Digital Image Processing - A Remote Sensing Perspective. Prentice Hall, Upper Saddle River, NJ, 526 pp.

Jorgensen, B.B. and D.J. Des Marais. 1988. Optical properties of benthic photosynthetic communities: Fiber-optic studies of cyanobacterial mats. *Limnology and Oceonography*, 33(1): 99-113.

Kaplan, I.R. and J.K. Bartley. 2000. Global Biogeochemical Cycles: Carbon, Sulfur, and Nitrogen. In: W.G. Ernst (Editor), Earth Systems: Processes and Issues. Cambridge University Press, London, UK, 566 pp.

Langford, N.P. 1972. The Discovery of Yellowstone Park: Journal of the Washburn Expedition to the Yellowstone and Firehole Rivers in the Year 1870. University of Nebraska Press, Lincoln, Nebraska, 125 pp.

Lawrence, R., A. Bunn, S. Powell, and M. Zambon. 2004. Classification of remotely sensed imagery using stochastic gradient boosting as a refinement of classification tree analysis. *Remote Sensing of Environment*, 90(3): 331-336.

Lawrence, R.L., S.D. Wood, and R.L. Sheley. 2006. Mapping invasive plants using hyperspectral imagery and Breiman Cutler classifications (RandomForest). *Remote Sensing of Environment*, 100(3): 356-362.

Lawrence, R.L. and A. Wright. 2001. Rule-based classification systems using classification and regression tree (CART) analysis. *Photogrammetric Engineering & Remote Sensing*, 67(10): 1137-1142.

Liang, S. 2000. Narrowband to broadband conversions of land surface albedo: I Algorithms. *Remote Sensing of Environment*, 76(2): 213-238.

Liaw, A. and M. Wiener. 2002. Classification and regression by randomForest. *R News*, 2(3): 18-22.

Long, C.L., D.B. Hoover, and C.L. Tippens. 1976. Audio-magnetotelluric station location map Island Park Known Geothermal Resource Area, Idaho. Open-File Report No. 76-700E, U.S. Geological Survey, 19 pp.

Lu, D., P. Mausel, E. Brondizio, and E. Moran. 2003. Change detection techniques. *International Journal of Remote Sensing*, 25(12): 2365-2407.

McCune, B. and D. Keon. 2002. Equations for potential annual direct incident radiation and heat load. *Journal of Vegetation Science*, 13(4): 603-606.

NASA. 2009. The Landsat Data Continuity Mission. Last accessed on 28 March 2009. http://ldcm.nasa.gov/about.html.

Nordstrom, D.K., R.B. McCleskey, and J.W. Ball. 2009. Sulfur geochemistry of hydrothermal waters in Yellowstone National Park: IV Acid-sulfate waters. *Applied Geochemistry*, 24(2): 191-207.

Pal, M. 2005. Random forest classifier for remote sensing classification. *International Journal of Remote Sensing*, 26(1): 217-222.

Prasad, A.M., L.R. Iverson, and A. Liaw. 2006. Newer classification and regression tree techniques: Bagging and random forests for ecological prediction. *Ecosystems*, 9(2): 181-199.

Sesnie, S.E., P.E. Gessler, B. Finegan, and S. Thessler. 2008. Integrating Landsat TM and SRTM-DEM derived variables with decision trees for habitat classification and change detection in complex neotropical environments. *Remote Sensing of Environment*, 112(5): 2145-2159.

Sorey, M.L. 1991. Effects of potential geothermal development in the Corwin Springs known geothermal resources area, Montana, on the thermal features of Yellowstone National Park. Water-Resources Investigations Report 91-4052, U.S. Geological Survey, Menlo Park, California, 204 pp.

Spatial Analysis Center. 1998. 30-meter elevation data for Yellowstone National Park, Wyoming, Montana, Idaho. Digital Spatial Data, Yellowstone Center for Resources, Yellowstone National Park, Wyoming.

Spatial Analysis Center. 2000. Precipitation in Yellowstone National Park, Wyoming, Montana, Idaho. Digital Spatial Data, Yellowstone Center for Resources, Yellowstone National Park, Wyoming.

Spatial Analysis Center. 2005. Hydrogeothermal Areas of Yellowstone National Park, Wyoming, Montana, Idaho. Digital Spatial Data, Yellowstone Center for Resources, Yellowstone National Park, Wyoming.

Spatial Analysis Center. 2008. Thermal Inventory point data for Yellowstone National Park, 1998 - 2008. Digital Spatial Data, Yellowstone Center for Resources, Yellowstone National Park, Wyoming.

Thompson, J.M. and S. Yadav. 1979. Chemical analyses of waters from geysers, hot springs, and pools in Yellowstone National Park, Wyoming from 1974 to 1978. Open-File Report 79-704, United States Geological Survey, Menlo Park, California, 51 pp.

Ward, D.M., R. Weller, J. Shiea, R.W. Castenholz, and Y. Cohen. 1989. Hot spring microbial mats: anoxygenic and oxygenic mats of possible evolutionary significance. In: Y. Cohen and E. Rosenburg (Editors), Microbial Mats: Physiological Ecology of Benthic Microbial Communities. American Society for Microbiology, Washington, D.C., 494 pp.

Waring, G.A., R.R. Blankenship, and R. Bentall. 1983. Thermal springs of the United States and other countries of the world - a summary. U.S.G.S. Professional Paper 492, U.S. Geological Survey, Alexandria, Virginia, 401 pp.

Watson, F.G.R., R.E. Lockwood, W.B. Newman, T.N. Anderson, and R.A. Garrott. 2008. Development and comparison of Landsat radiometric and snowpack model inversion techniques for estimating geothermal heat flux. *Remote Sensing of Environment*, 112(2): 471-481.

Western Regional Climate Center. 2005. Period of record monthly climate summary - Yellowstone Park, Wyoming (489905). Last accessed on 6 April 2009. http://www.wrcc.dri.edu/cgi-bin/cliRECtM.pl?wyyell.

CHAPTER 5

CONCLUSION

Landsat data include information from the thermal infrared portion of the electromagnetic spectrum and were assessed for their ability to successfully map geothermally active areas and geothermal heat flux in geothermally influenced Yellowstone National Park (YNP). Landsat thermal data from 1978 to present and into the foreseeable future are freely available from the United States Geological Survey, effectively providing an opportunity to study geothermal ground over the entirety of YNP for 30 years and beyond. An accurate, inexpensive, and reproducible method for mapping geothermal ground at YNP might be possible with Landsat data, but the results of this study indicate there are inherent limitations to Landsat data and issues with the nature of geothermal features that, combined, make accurately mapping geothermally active areas and geothermal heat flux difficult with the methods tested herein.

Terrestrial emittance represents all heat being emitted from the ground, including effects from direct and indirect solar radiation, as opposed to geothermal heat flux, which represents only geothermal heat emitted from below ground. The Landsat thermal band, with assistance from the red and near infrared bands, was able to detect terrestrial emittance, but without rigorous solar radiation field data, was unable to accurately estimate geothermal heat flux. Incorporating estimates of potential direct incident solar radiation and surface albedo into the terrestrial emittance calculation produced a moderately acceptable estimation of geothermal heat flux covering all of YNP that,

although unable to account for all inherent variability such as conductance of non-geothermal heat through the soil or diurnal, seasonal, or annual temperature oscillations, might help YNP scientists identify areas of interest for further study.

Change analysis for the currently defined geothermal areas was performed with the terrestrial emittance data because it was created with an established method, it did not have data artifacts and artificially high values on north-facing slopes, and solar effects appeared to be relatively constant over time. In addition, comparison of terrestrial emittance to the solar radiation and albedo adjusted geothermal heat flux in the Brimstone Basin area illustrated that terrestrial emittance was better for the change analysis performed for this study because it was considerably less variable than the estimated geothermal heat flux in an area where very little, if any, geothermal change should have been detected.

Change trajectories did not allow for the detection of spatio-temporal relationships between absolute change in terrestrial emittance and temporal clusters and spatial groupings. Known change events, however, were detected within trajectories for the most part. No relationships were detected between the temporal clusters and spatial groupings and distance to geologic faults or distance to large water bodies. A clear relationship between earthquake swarms and absolute changes in terrestrial emittance was observed, and further investigations of interactions between earthquake swarm characteristics might prove important in studies of terrestrial emittance and earthquake swarm relationships.

The random forest classification method was unable to produce an acceptably accurate classification of geothermally active areas in the currently defined geothermal areas at YNP, however, the classifications developed were better than random. The inherent limitations of Landsat data, the inherent nature of geothermal features and areas, and acknowledged biases within the reference data used were probable reasons for the unacceptable classifications. Appropriate reference data, however, are impractical to collect, and even with excellent reference data, the technological limitations of Landsat imagery might preclude producing highly accurate geothermally active area classifications. The target detection training data were based on the poor random forest classifications and did not perform well. Given a highly accurate classification of the defined geothermal areas, however, the constrained energy minimization target detection classification method might prove to be the appropriate tool to classify geothermally active areas in and around YNP.

The primary lesson learned through this study was that while Landsat data are excellent resources for mapping many landscape features, the inherent technological limitations of Landsat data, in particular the thermal band, impede accurate mapping of geothermal heat flux and geothermally active areas. The Landsat thermal band has relatively low spatial resolution and is not sensitive enough to variations in terrestrial emittance that might be caused by individual geothermal features or areas of geothermally active ground, thus geothermal heat flux and geothermally active areas are difficult to detect accurately even when Landsat thermal data are combined with the reflective data. Geothermal barrens, for example, include both geothermally active and

inactive areas that have very similar reflective properties, resulting in confusion when attempting to classify geothermally active areas or improve estimations of geothermal heat flux with a combination of thermal and reflective bands. Until a high spatial resolution thermal scanner is developed that images the entirety of YNP on a regular basis, Landsat data will remain the only available thermal data for historical and continuous monitoring of geothermal areas in YNP. The results of this study suggest that future studies of geothermal areas at YNP with Landsat data will be unsuccessful until Landsat data can be more accurately calibrated to geothermal heat flux and solar effects.

APPENDICES

APPENDIX A

USGS DEFINITION OF MAGNITUDE CLASSES AND EARTHQUAKE SWARMS INVESTIGATED IN SPATIAL ANALYSIS OF SPATIAL GROUPINGS

To calculate magnitude from amplitude, take LOG_{10} of amplitude.

There were 2,535 total earthquakes during the study period.
Magnitudes ranged from -1.06 to 4.69 with a mean of 1.58.

From the USGS Earthquake Hazards Program (USGS, 2009b):
Earthquake Magnitude Classes

Great: M >= 8
Major: 7 <= M < 7.9
Strong: 6 <= M < 6.9
Moderate: 5 <= M < 5.9
Light: 4 <= M < 4.9
Minor: 3 <= M < 3.9
Micro: M < 3

Year	Swarm ID #	Maximum amplitude	Mean amplitude	Median amplitude	Number of earthquakes	Duration (days)	Lag time (days)
2007	1	22.909	3.226	2.09	26	1	5
2007	32	43.652	17.923	12.171	16	28	29
2007	33	15.136	7.073	5.495	9	18	79
2007	34	19.953	5.344	2.57	7	14	65
2007	35	16.982	9.839	8.622	4	1	32
2006	2	131.826	8.633	2.851	76	23	5
2006	3	181.97	11.856	6.31	61	8	12
2006	4	12.303	4.859	4.501	8	1	13
2006	36	31.623	12.267	7.853	8	1	46
2006	37	269.153	23.785	5.821	76	2	94
2006	38	21.878	7.164	3.715	9	4	59
2006	40	316.228	13.575	1.38	45	22	36
2006	41	18.621	6.558	5.888	9	1	67
2005	5	269.153	79.849	31.623	5	1	5
2005	42	389.045	73.534	23.748	10	2	51
2005	43	35.481	15.767	13.602	7	1	91
2005	44	812.831	46.053	7.01	26	16	67
2005	45	61.66	19.399	19.953	13	2	57
2005	46	120.226	12.513	2.188	49	10	54
2003	6	28.84	10.931	6.941	5	1	26
2003	7	21.878	4.904	2.256	13	22	8
2003	8	20.893	10.724	9.227	4	2	8

Year	Swarm ID #	Maximum amplitude	Mean amplitude	Median amplitude	Number of earthquakes	Duration (days)	Lag time (days)
2003	47	25.119	14.843	14.125	11	1	71
2003	48	5.888	3.664	4.365	8	9	81
2003	49	24.547	7.174	3.388	14	12	58
2002	9	12.589	4.908	3.467	14	16	5
2002	10	6.607	2.952	2.239	7	4	4
2002	50	33.113	18.953	20.417	7	2	61
2002	51	14.454	2.922	1	8	4	40
2002	52	27.542	5.885	3.719	16	1	59
2002	53	7.943	3.464	2.786	15	1	98
2002	54	32.359	5.52	2.63	31	9	59
2002	55	34.674	5.943	1.842	18	13	42
2001	11	165.959	61.093	46.61	22	1	3
2001	12	104.713	24.654	22.909	39	24	2
2001	56	301.995	243.11	234.423	7	1	38
2001	57	87.096	34.33	24.281	10	1	33
2001	58	58.884	39.904	45.429	10	2	73
2001	59	97.724	37.919	32.465	8	1	68
2001	60	173.78	38.188	11.955	12	5	41
2001	61	102.329	27.822	21.38	36	5	9
2000	13	380.189	147.232	134.896	7	1	3
2000	14	165.959	22.081	14.458	30	20	7
2000	62	9549.926	1121.52	138.038	11	3	50
2000	63	114.815	16.37	7.097	18	1	47
2000	64	741.31	49.728	18.438	26	14	51
1999	15	281.838	52.943	24.846	34	13	1
1999	16	8709.636	128.465	27.542	746	30	1
1999	17	1513.561	88.845	22.133	176	30	1
1999	65	1174.898	298.32	251.189	16	4	82
1999	66	2691.535	165.783	64.565	63	21	44
1999	67	17782.79	1670.222	232.124	18	1	52
1999	69	316.228	112.9	72.444	17	1	34
1998	18	125.893	41.067	27.908	22	15	2
1998	19	758.578	284.322	269.153	9	1	3
1998	70	691.831	66.067	43.652	39	14	38
1997	21	144.544	51.694	29.116	8	6	1
1997	23	48977.88	420.197	22.387	356	37	1
1997	71	69.183	28.377	26.303	23	11	66
1997	72	120.226	33.644	20.893	9	1	33

Year	Swarm ID #	Maximum amplitude	Mean amplitude	Median amplitude	Number of earthquakes	Duration (days)	Lag time (days)
1997	73	467.735	114.212	31.512	6	1	68
1997	74	2238.721	556.195	173.78	13	17	3
1997	75	2818.383	1087.118	691.831	7	10	3
1996	24	6918.31	1928.031	758.578	5	1	1
1996	25	4786.301	525.795	334.988	24	21	6
1996	26	186.209	35.229	15.849	25	2	14
1996	77	2290.868	569.615	281.838	23	14	44
1996	78	1905.461	263.322	81.283	11	1	47
1991	27	630.957	385.767	338.844	4	2	29
1991	28	1023.293	462.05	239.883	7	1	5
1991	79	346.737	333.821	331.131	3	1	72

APPENDIX B

IMAGES OF M_{terr} FOR ALL 14 DATES

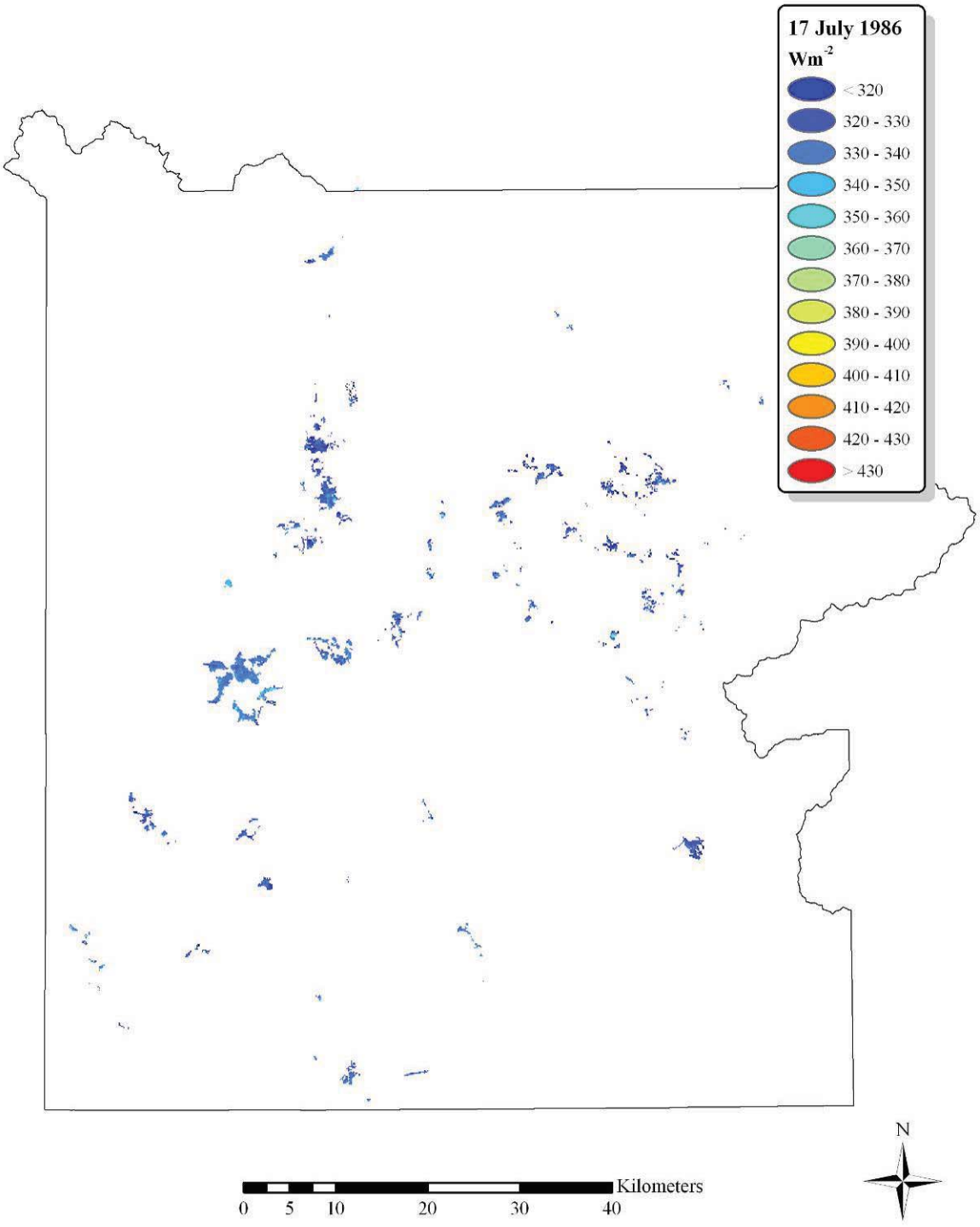
17 July 1986
Wm-2
< 320
320 - 330
330 - 340
340 - 350
350 - 360
360 - 370
370 - 380
380 - 390
390 - 400
400 - 410
410 - 420
420 - 430
> 430
N
Kilometers
0 5 10 20 30 40

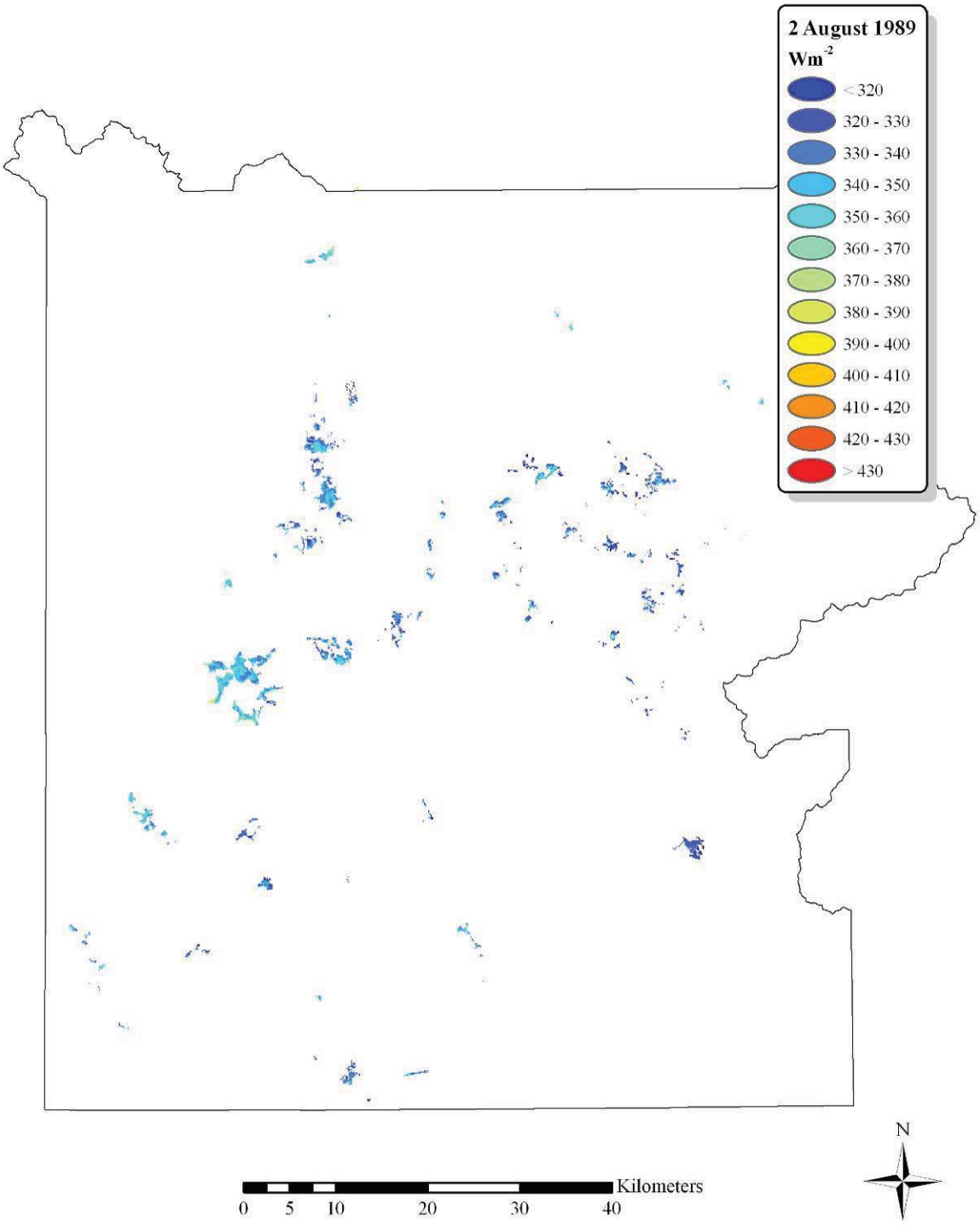
2 August 1989
Wm-2
< 320
320 - 330
330 - 340
340 - 350
350 - 360
360 - 370
370 - 380
380 - 390
390 - 400
400 - 410
410 - 420
420 - 430
> 430
N
Kilometers
0 5 10 20 30 40

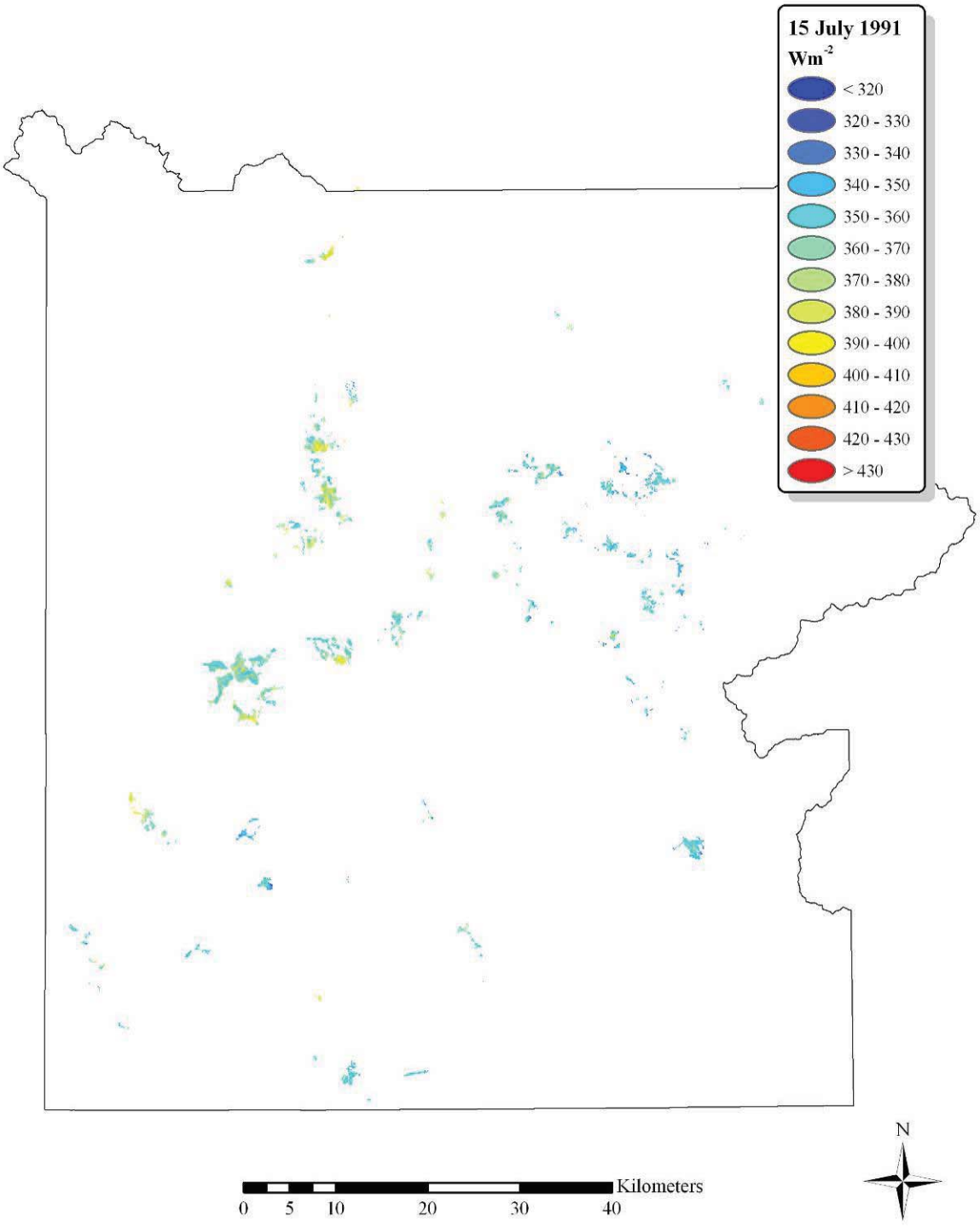
15 July 1991
Wm-2
< 320
320 - 330
330 - 340
340 - 350
350 - 360
360 - 370
370 - 380
380 - 390
390 - 400
400 - 410
410 - 420
420 - 430
> 430
N
Kilometers
0 5 10 20 30 40

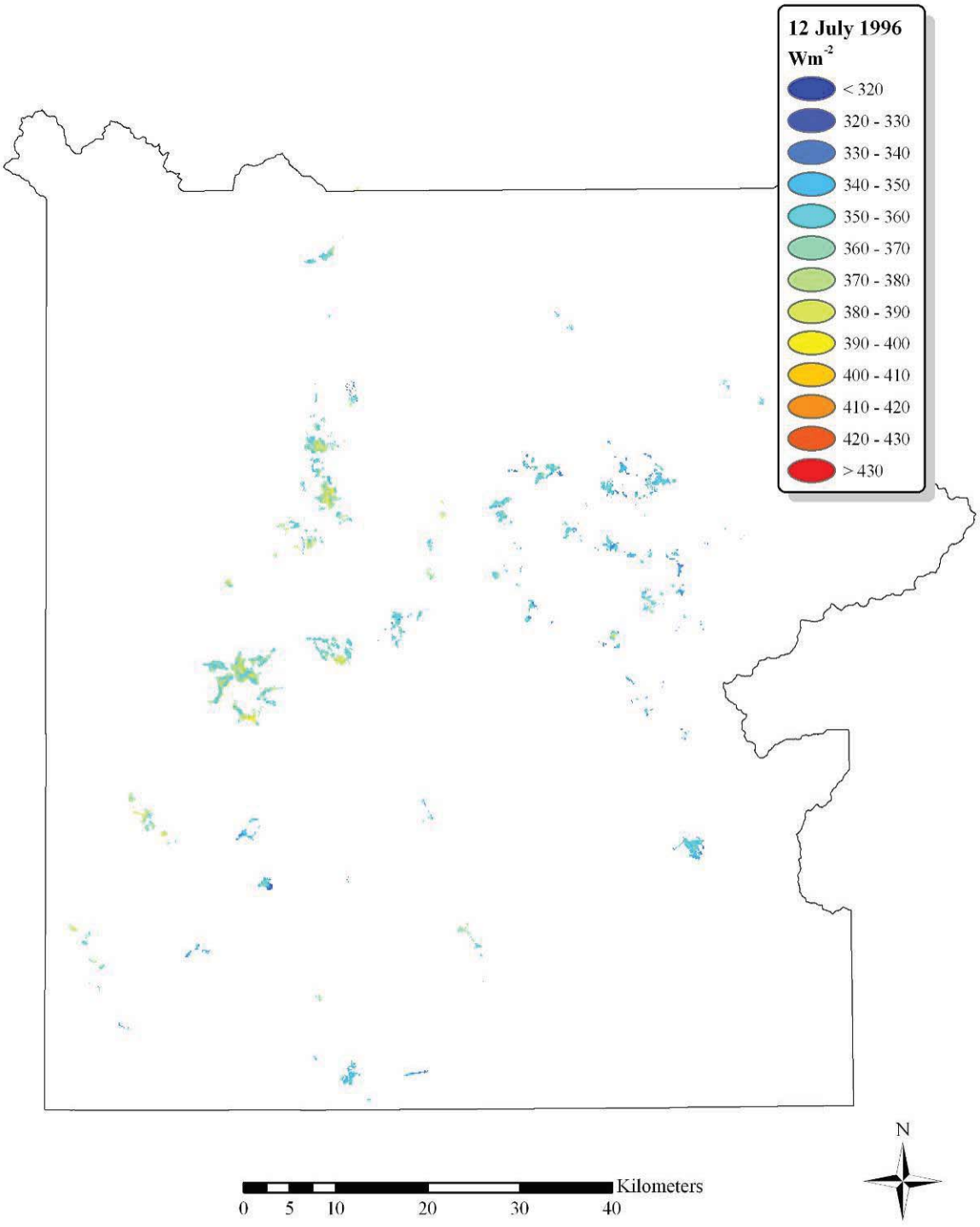
12 July 1996
Wm-2
< 320
320 - 330
330 - 340
340 - 350
350 - 360
360 - 370
370 - 380
380 - 390
390 - 400
400 - 410
410 - 420
420 - 430
> 430
N
Kilometers
0 5 10 20 30 40

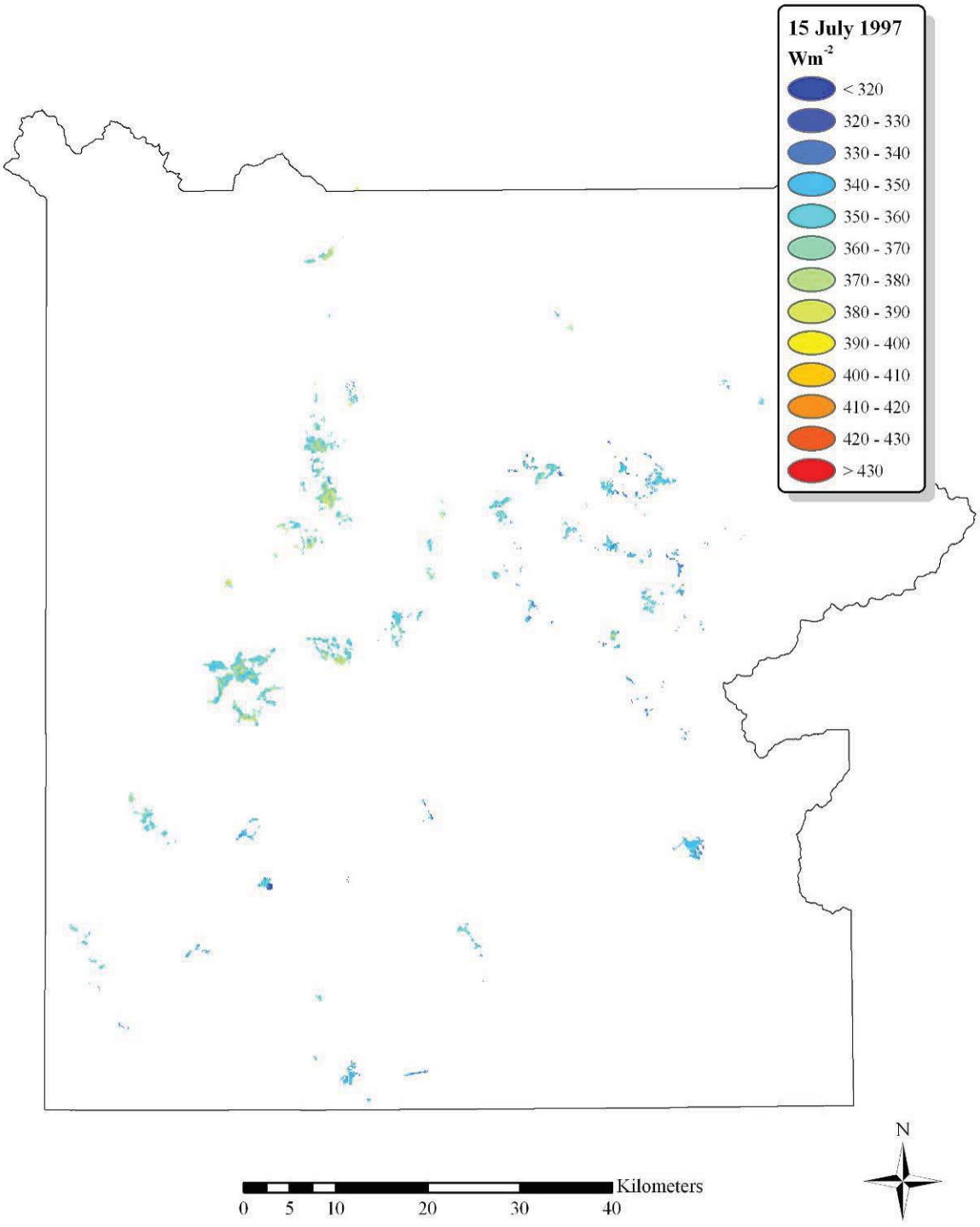
15 July 1997
Wm-2
< 320
320 - 330
330 - 340
340 - 350
350 - 360
360 - 370
370 - 380
380 - 390
390 - 400
400 - 410
410 - 420
420 - 430
> 430
N
Kilometers
0 5 10 20 30 40

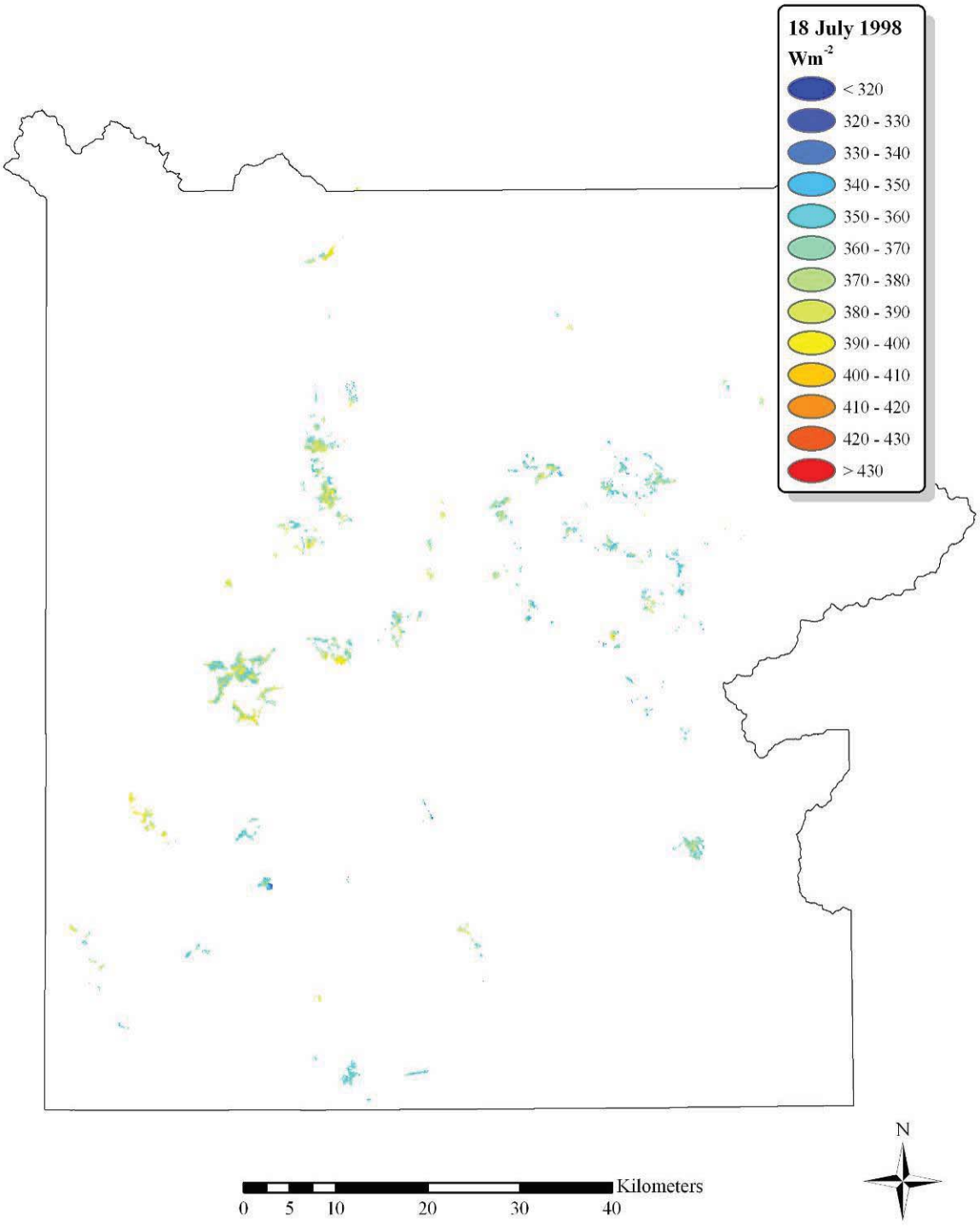
18 July 1998
Wm-2
< 320
320 - 330
330 - 340
340 - 350
350 - 360
360 - 370
370 - 380
380 - 390
390 - 400
400 - 410
410 - 420
420 - 430
> 430
N
Kilometers
0 5 10 20 30 40

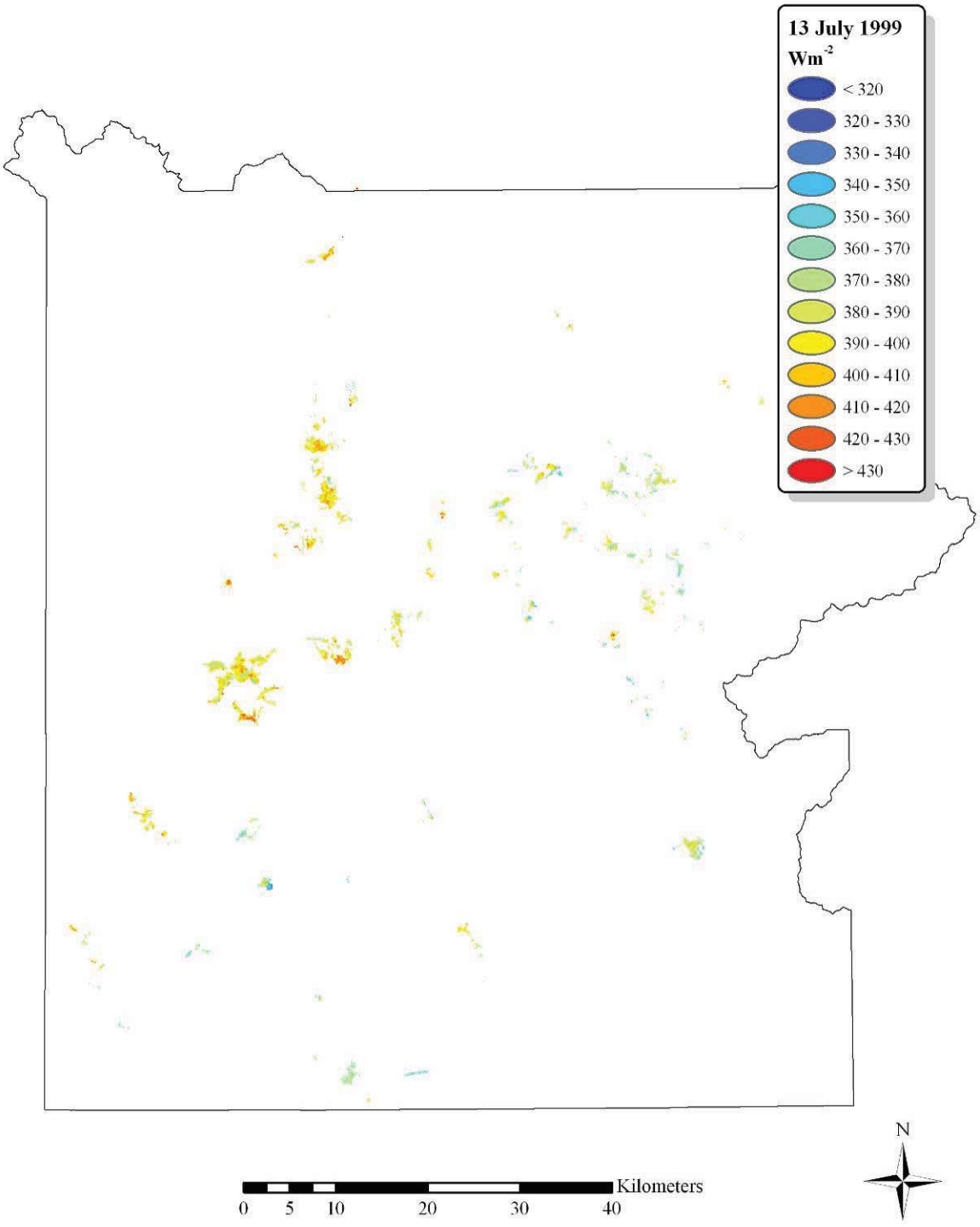
13 July 1999
Wm-2
< 320
320 - 330
330 - 340
340 - 350
350 - 360
360 - 370
370 - 380
380 - 390
390 - 400
400 - 410
410 - 420
420 - 430
> 430
N
Kilometers
0 5 10 20 30 40

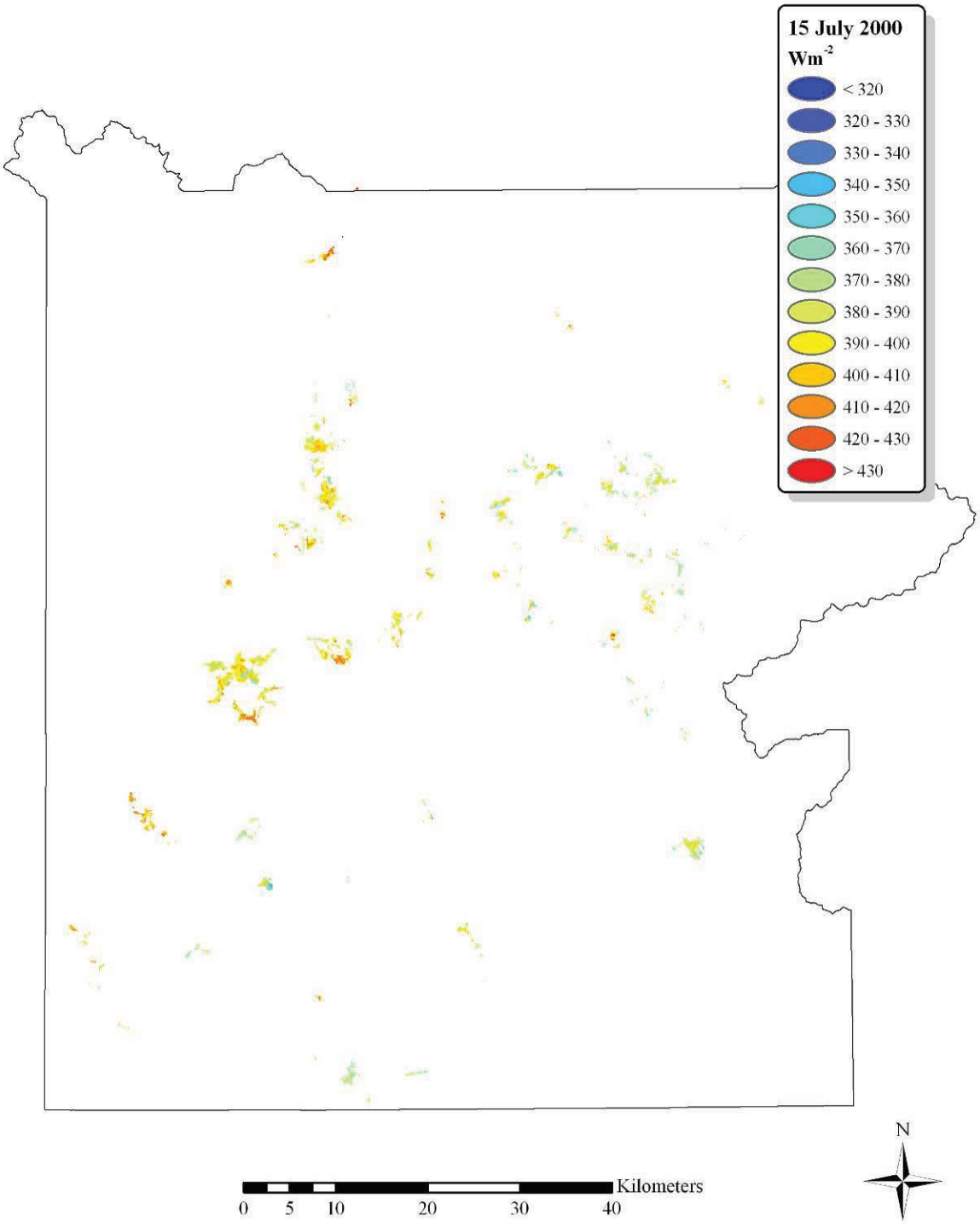
15 July 2000
Wm-2
< 320
320 - 330
330 - 340
340 - 350
350 - 360
360 - 370
370 - 380
380 - 390
390 - 400
400 - 410
410 - 420
420 - 430
> 430
N
Kilometers
0 5 10 20 30 40

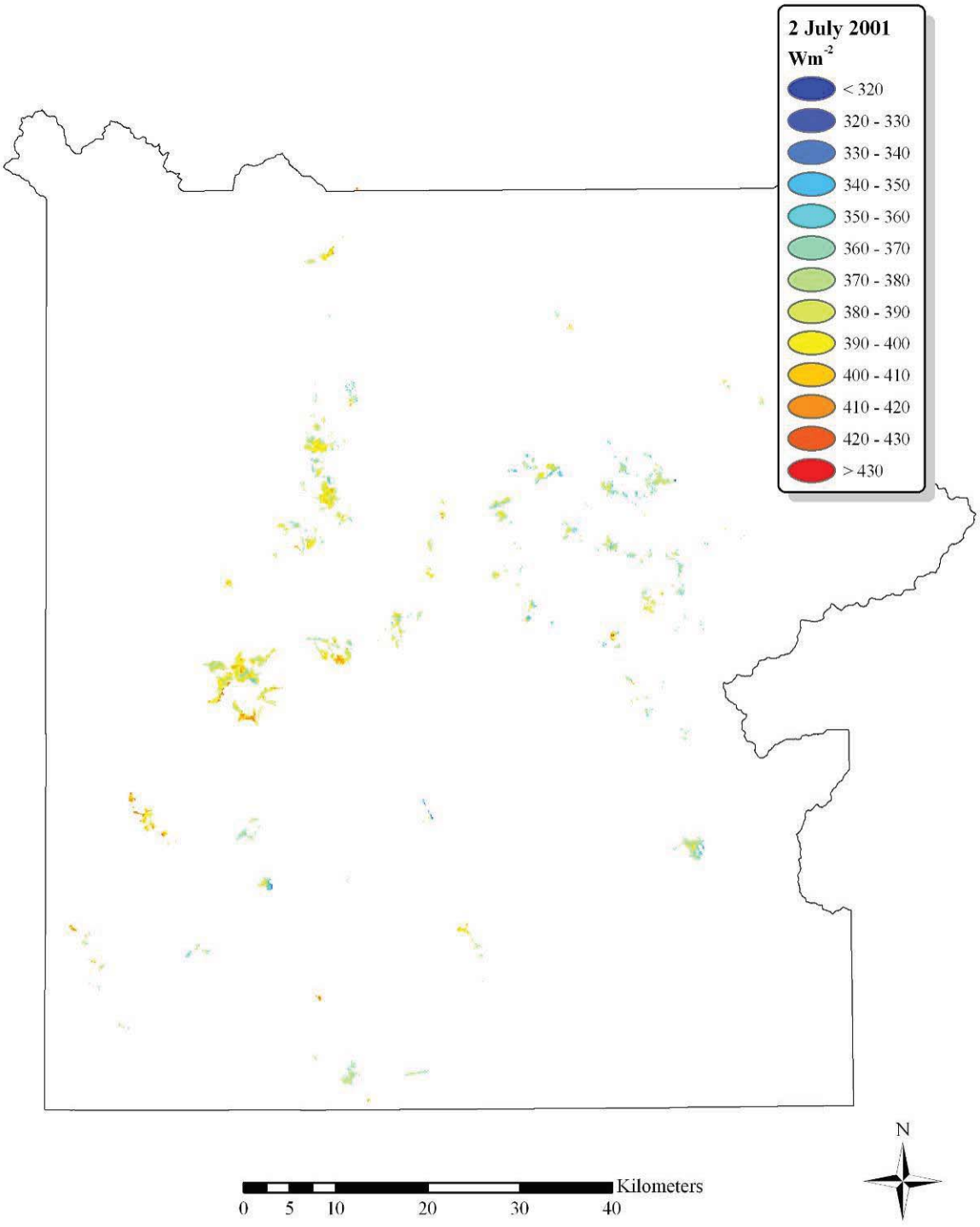
2 July 2001
Wm-2
< 320
320 - 330
330 - 340
340 - 350
350 - 360
360 - 370
370 - 380
380 - 390
390 - 400
400 - 410
410 - 420
420 - 430
> 430
N
Kilometers
0 5 10 20 30 40

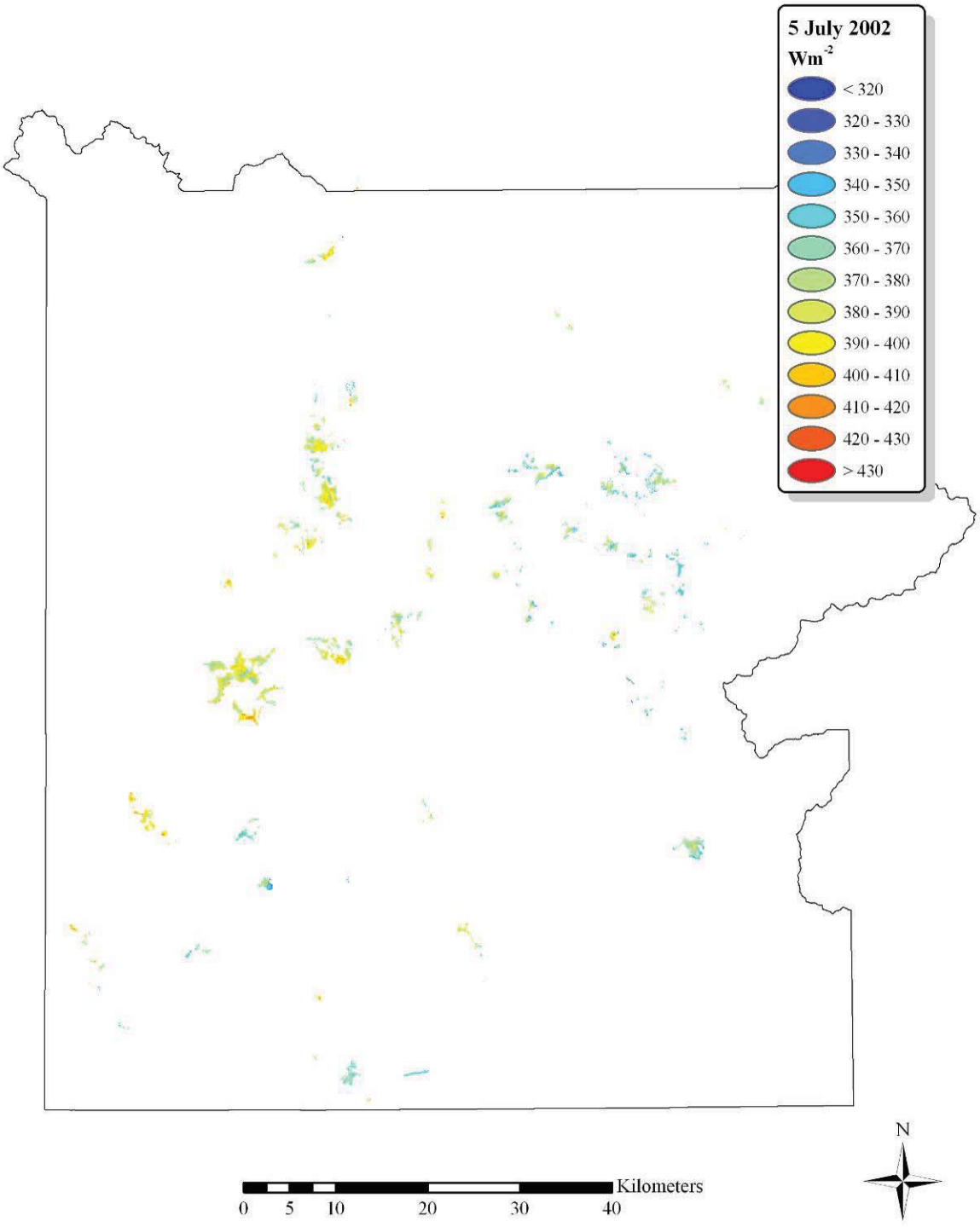
5 July 2002
Wm-2
< 320
320 - 330
330 - 340
340 - 350
350 - 360
360 - 370
370 - 380
380 - 390
390 - 400
400 - 410
410 - 420
420 - 430
> 430
N
Kilometers
0 5 10 20 30 40

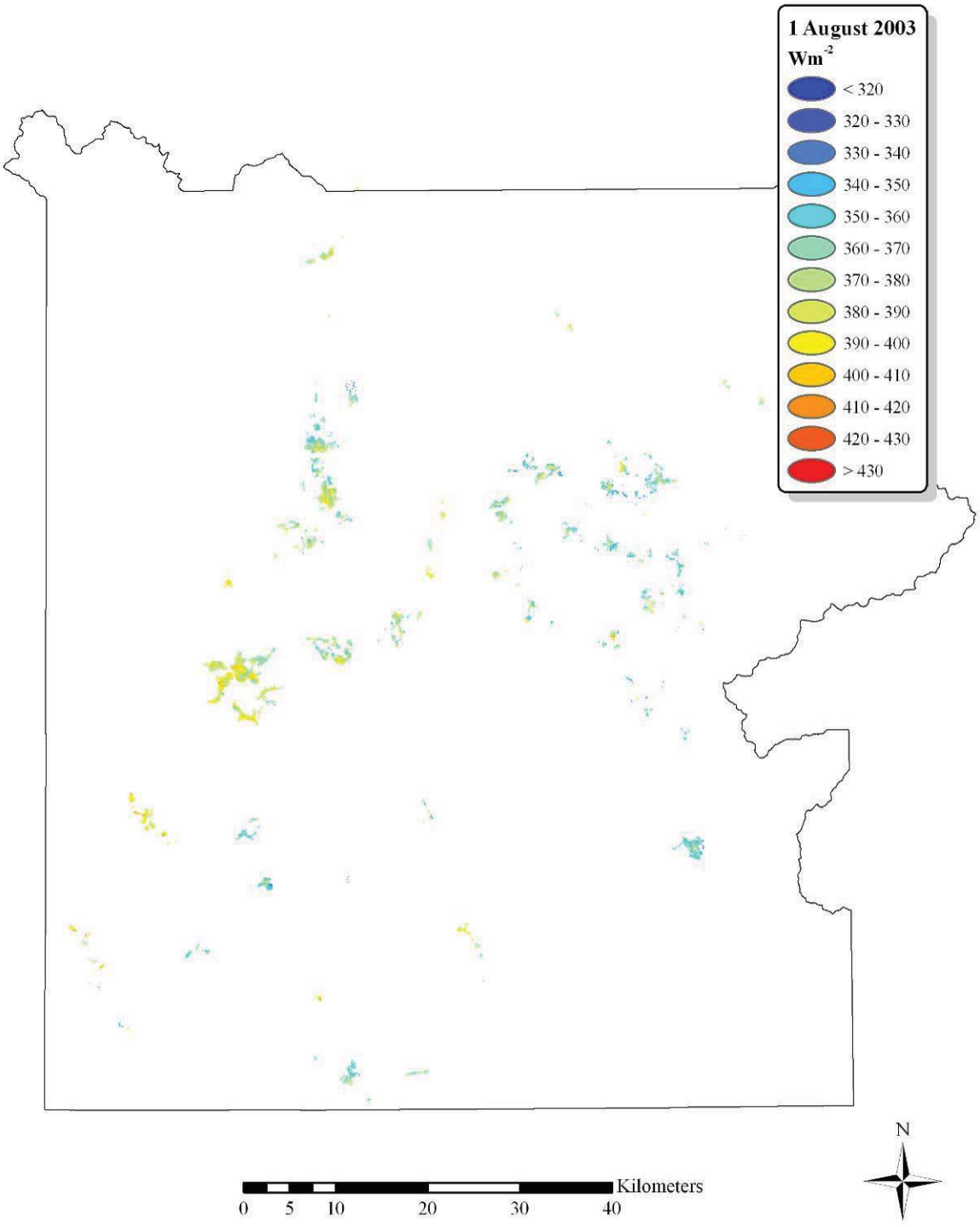
1 August 2003
Wm-2
< 320
320 - 330
330 - 340
340 - 350
350 - 360
360 - 370
370 - 380
380 - 390
390 - 400
400 - 410
410 - 420
420 - 430
> 430
N
Kilometers
0 5 10 20 30 40

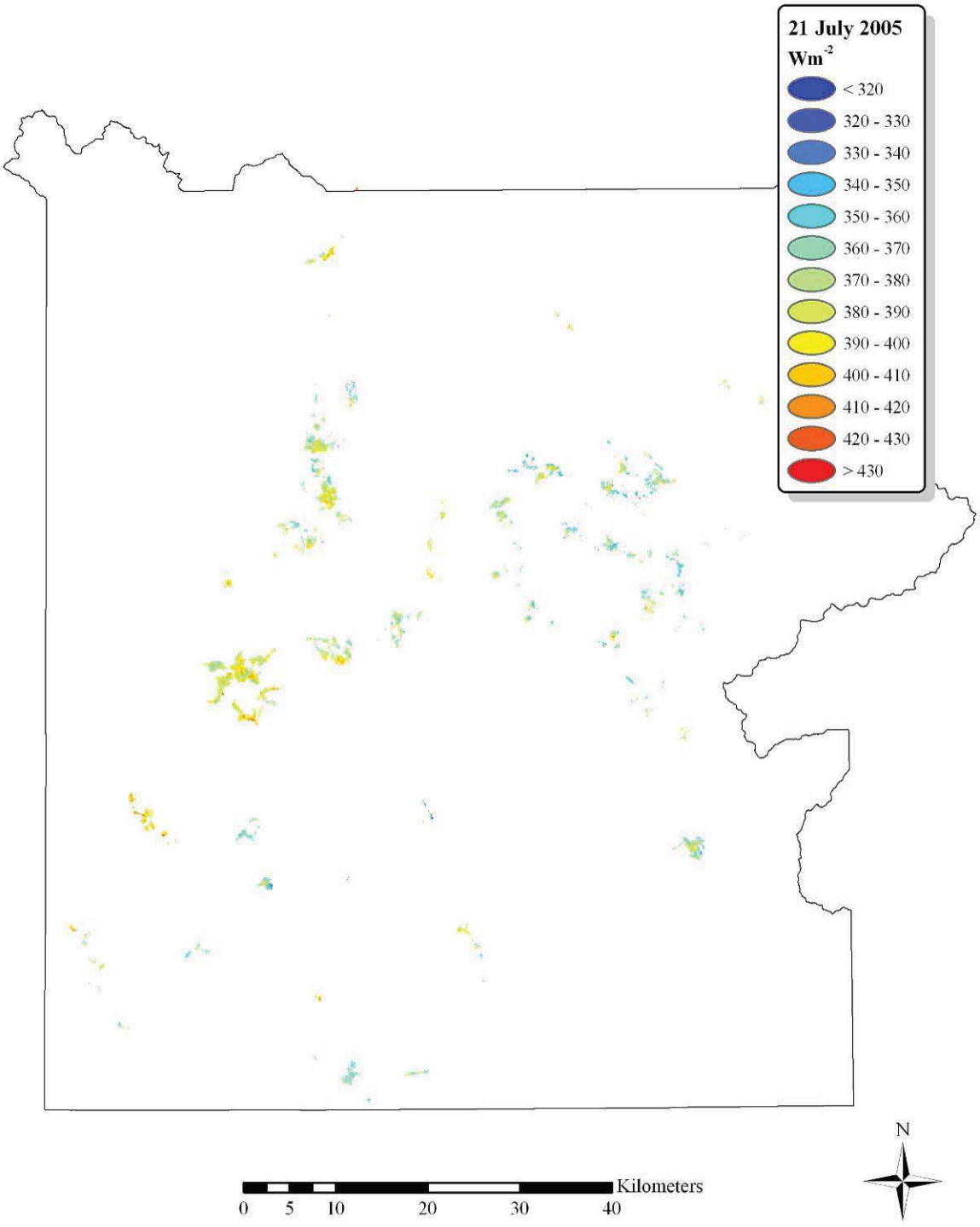
21 July 2005
Wm-2
< 320
320 - 330
330 - 340
340 - 350
350 - 360
360 - 370
370 - 380
380 - 390
390 - 400
400 - 410
410 - 420
420 - 430
> 430
N
Kilometers
0 5 10 20 30 40

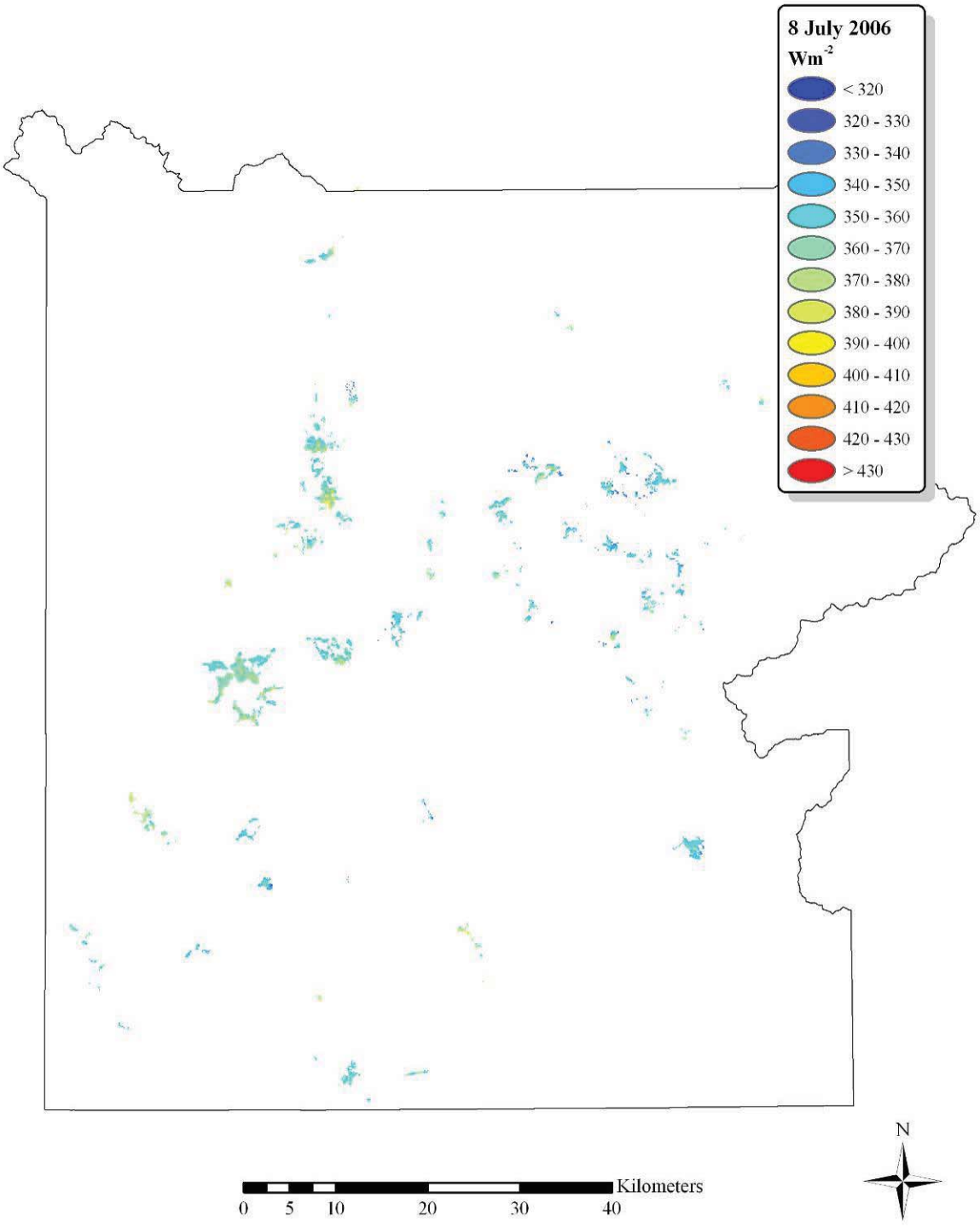
8 July 2006
Wm-2
< 320
320 - 330
330 - 340
340 - 350
350 - 360
360 - 370
370 - 380
380 - 390
390 - 400
400 - 410
410 - 420
420 - 430
> 430
N
Kilometers
0 5 10 20 30 40

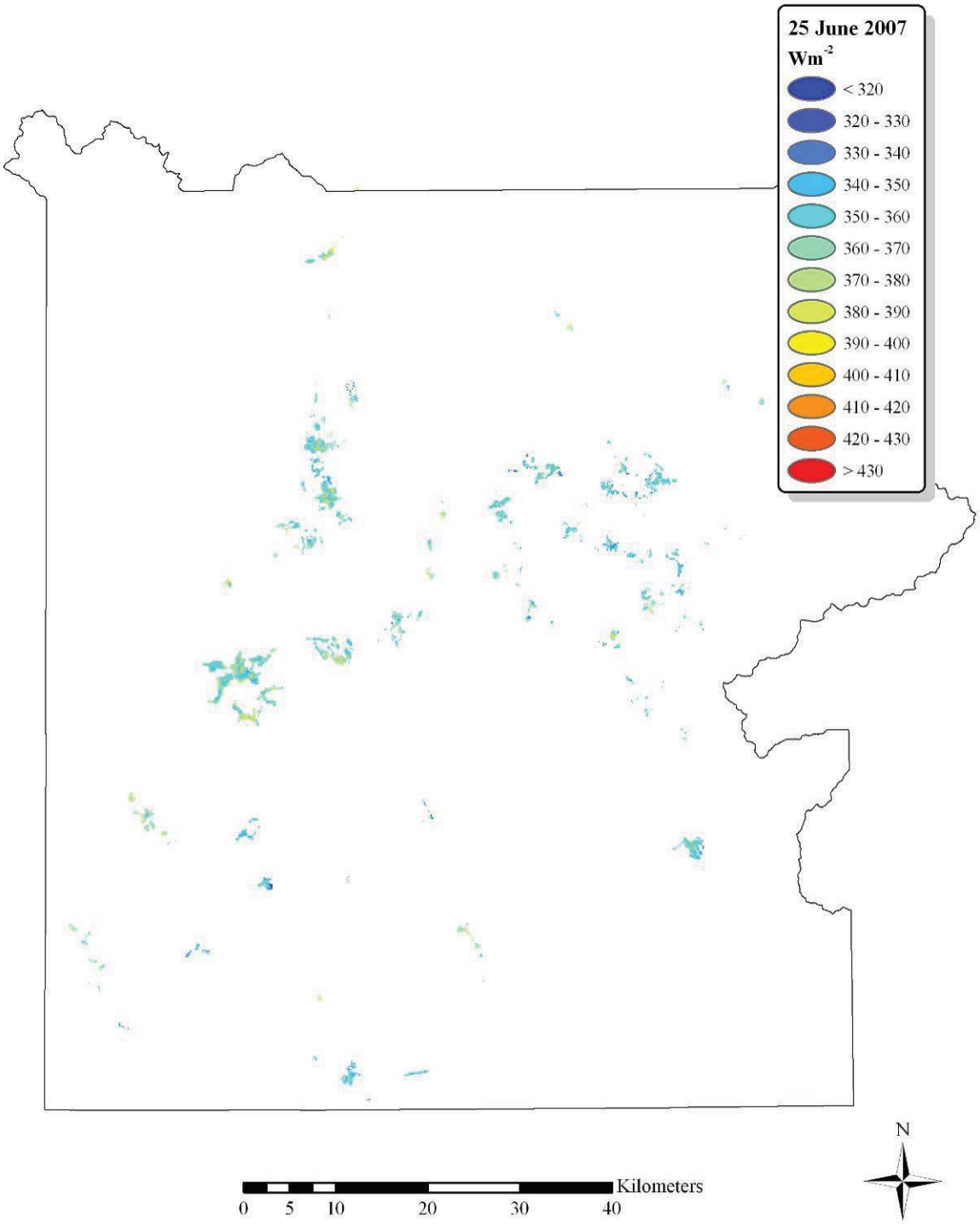
25 June 2007
Wm-2
< 320
320 - 330
330 - 340
340 - 350
350 - 360
360 - 370
370 - 380
380 - 390
390 - 400
400 - 410
410 - 420
420 - 430
> 430
N
Kilometers
0 5 10 20 30 40

APPENDIX C

M_{terr} TRAJECTORY GRAPHS FOR 24 TEMPORAL CLUSTERS
(Y-axis Values in Wm^{-2})

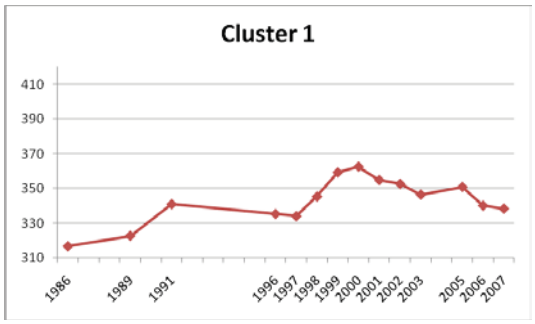
Cluster 1
410
390
370
350
330
310
1986
1989
1991
1996
1997
1998
1999
2000
2001
2002
2003
2005
2006
2007

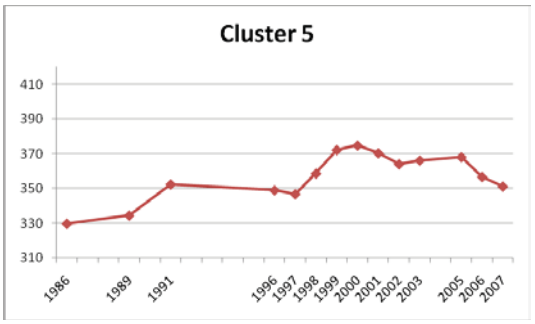
Cluster 5
410
390
370
350
330
310
1986
1989
1991
1996
1997
1998
1999
2000
2001
2002
2003
2005
2006
2007

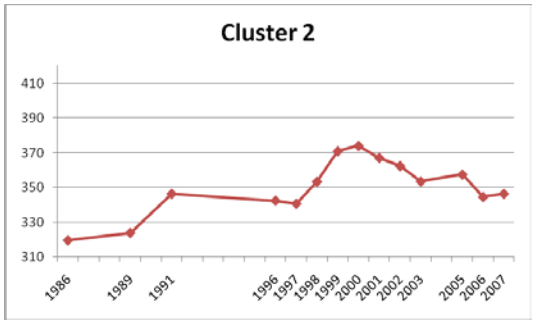
Cluster 2
410
390
370
350
330
310
1986
1989
1991
1996
1997
1998
1999
2000
2001
2002
2003
2005
2006
2007

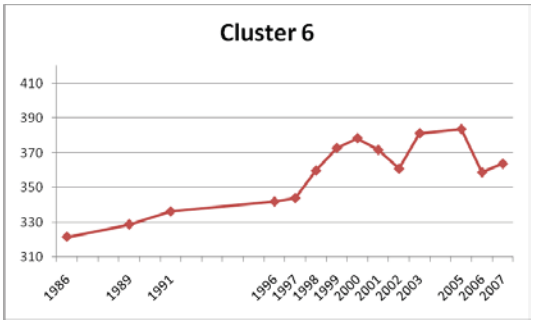
Cluster 6
410
390
370
350
330
310
1986
1989
1991
1996
1997
1998
1999
2000
2001
2002
2003
2005
2006
2007

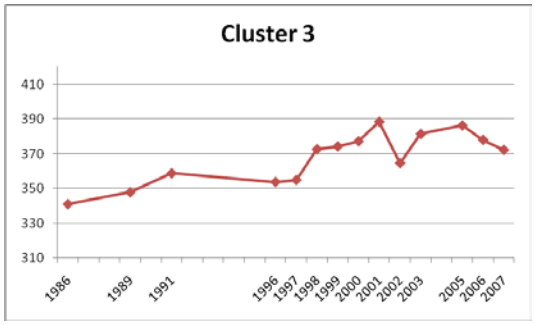
Cluster 3
410
390
370
350
330
310
1986
1989
1991
1996
1997
1998
1999
2000
2001
2002
2003
2005
2006
2007

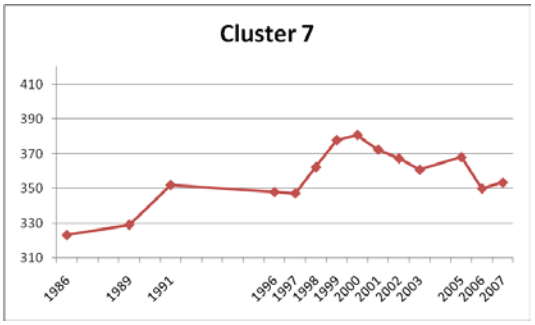
Cluster 7
410
390
370
350
330
310
1986
1989
1991
1996
1997
1998
1999
2000
2001
2002
2003
2005
2006
2007

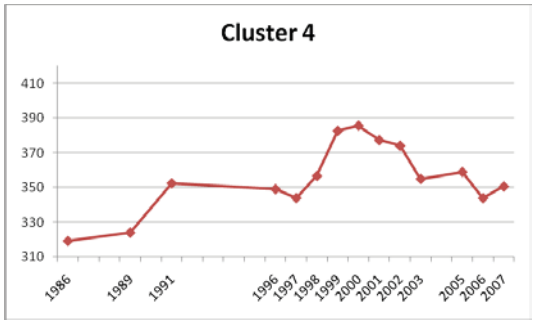
Cluster 4
410
390
370
350
330
310
1986
1989
1991
1996
1997
1998
1999
2000
2001
2002
2003
2005
2006
2007

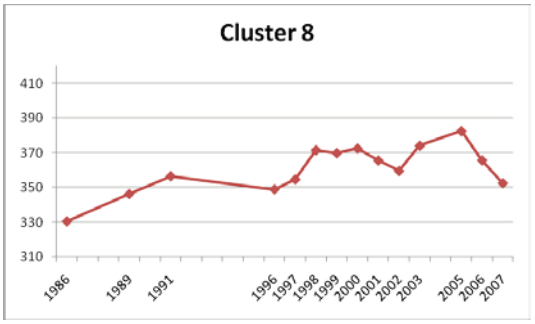
Cluster 8
410
390
370
350
330
310
1986
1989
1991
1996
1997
1998
1999
2000
2001
2002
2003
2005
2006
2007

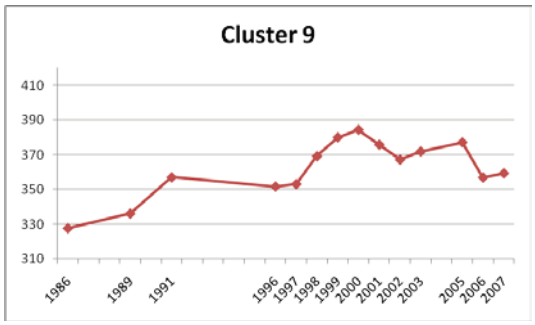
Cluster 9
410
390
370
350
330
310
1986
1989
1991
1996
1997
1998
1999
2000
2001
2002
2003
2005
2006
2007

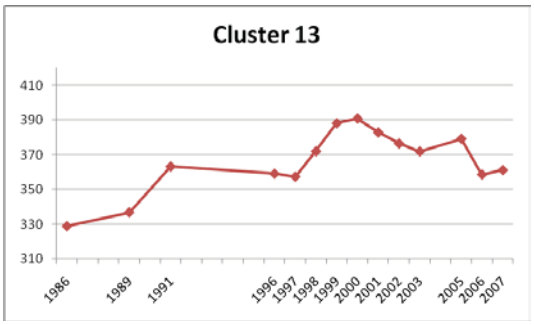
Cluster 13
410
390
370
350
330
310
1986
1989
1991
1996
1997
1998
1999
2000
2001
2002
2003
2005
2006
2007

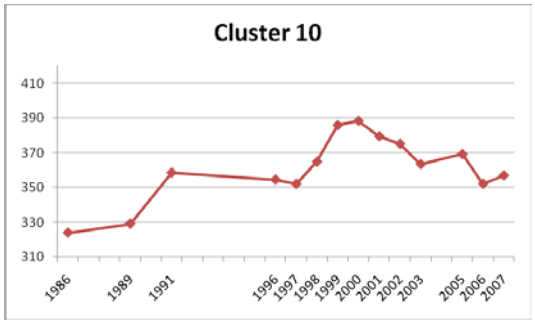
Cluster 10
410
390
370
350
330
310
1986
1989
1991
1996
1997
1998
1999
2000
2001
2002
2003
2005
2006
2007

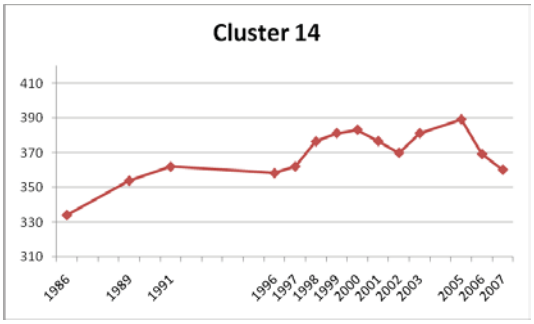
Cluster 14
410
390
370
350
330
310
1986
1989
1991
1996
1997
1998
1999
2000
2001
2002
2003
2005
2006
2007

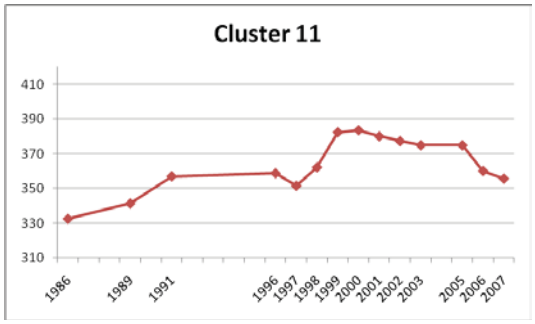
Cluster 11
410
390
370
350
330
310
1986
1989
1991
1996
1997
1998
1999
2000
2001
2002
2003
2005
2006
2007

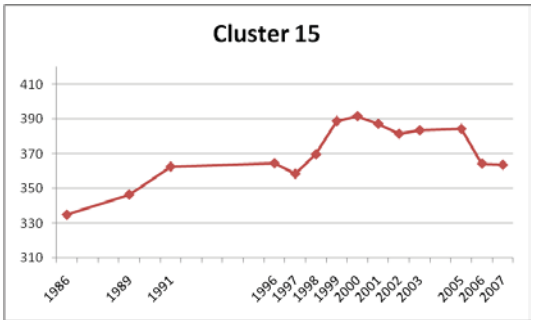
Cluster 15
410
390
370
350
330
310
1986
1989
1991
1996
1997
1998
1999
2000
2001
2002
2003
2005
2006
2007

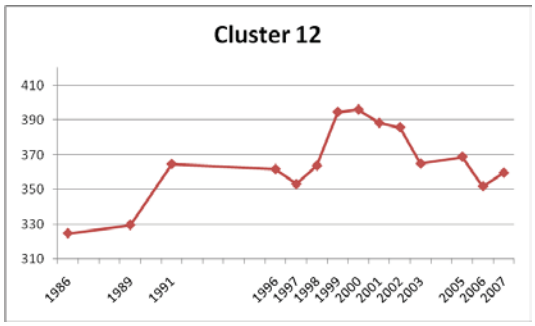
Cluster 12
410
390
370
350
330
310
1986
1989
1991
1996
1997
1998
1999
2000
2001
2002
2003
2005
2006
2007

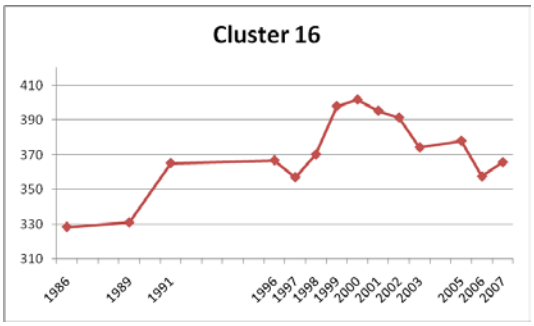
Cluster 16
410
390
370
350
330
310
1986
1989
1991
1996
1997
1998
1999
2000
2001
2002
2003
2005
2006
2007

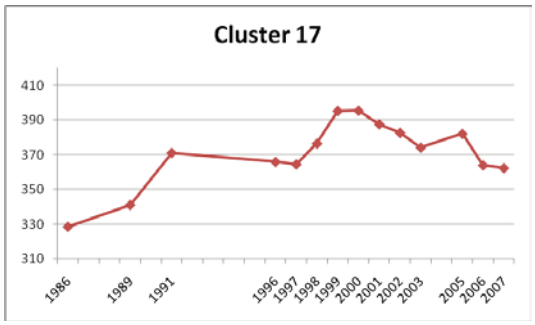
Cluster 17
410
390
370
350
330
310
1986
1989
1991
1996
1997
1998
1999
2000
2001
2002
2003
2005
2006
2007

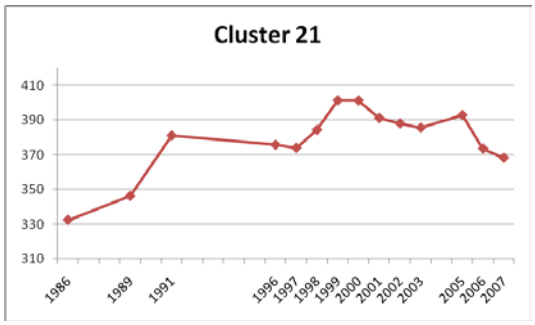
Cluster 21
410
390
370
350
330
310
1986
1989
1991
1996
1997
1998
1999
2000
2001
2002
2003
2005
2006
2007

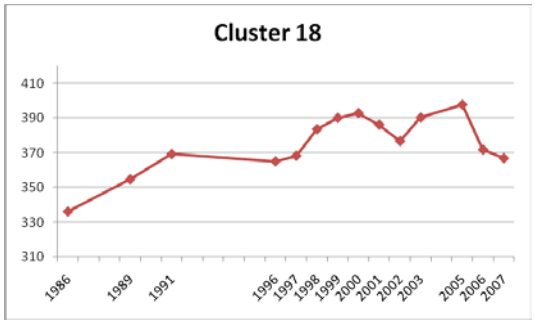
Cluster 18
410
390
370
350
330
310
1986
1989
1991
1996
1997
1998
1999
2000
2001
2002
2003
2005
2006
2007

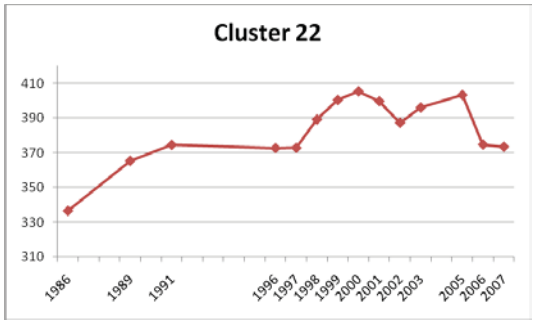
Cluster 22
410
390
370
350
330
310
1986
1989
1991
1996
1997
1998
1999
2000
2001
2002
2003
2005
2006
2007

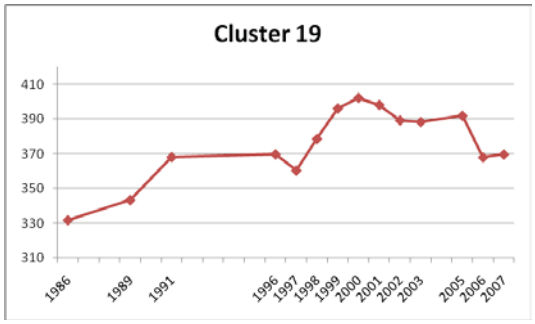
Cluster 19
410
390
370
350
330
310
1986
1989
1991
1996
1997
1998
1999
2000
2001
2002
2003
2005
2006
2007

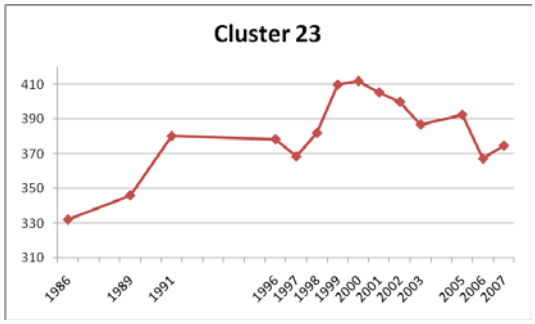
Cluster 23
410
390
370
350
330
310
1986
1989
1991
1996
1997
1998
1999
2000
2001
2002
2003
2005
2006
2007

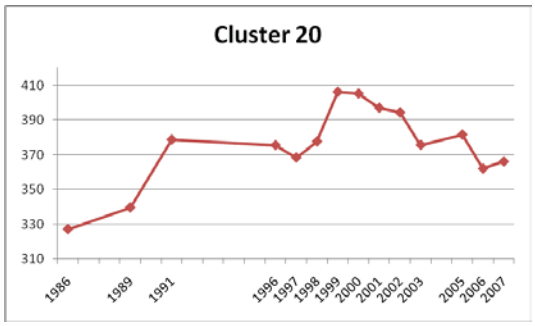
Cluster 20
410
390
370
350
330
310
1986
1989
1991
1996
1997
1998
1999
2000
2001
2002
2003
2005
2006
2007

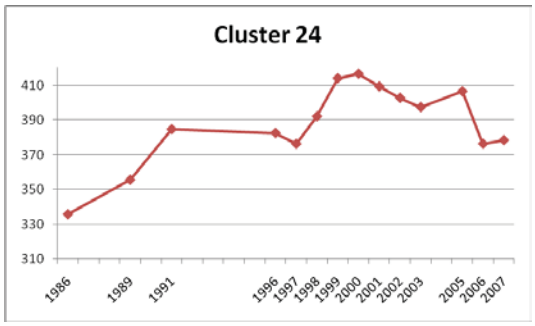
Cluster 24
410
390
370
350
330
310
1986
1989
1991
1996
1997
1998
1999
2000
2001
2002
2003
2005
2006
2007

APPENDIX D

M_{terr} TRAJECTORY GRAPHS FOR 20 SPATIAL GROUPINGS
(Y-axis Values in Wm^{-2})

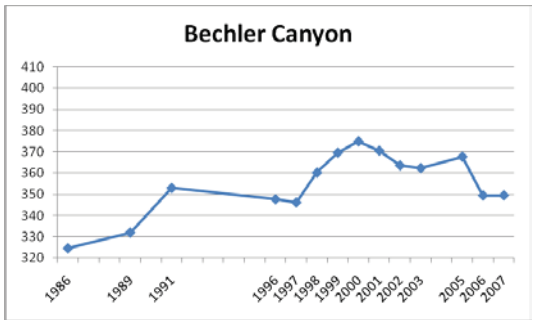
Bechler Canyon
410
400
390
380
370
360
350
340
330
320
1986
1989
1991
1996
1997
1998
1999
2000
2001
2002
2003
2005
2006
2007

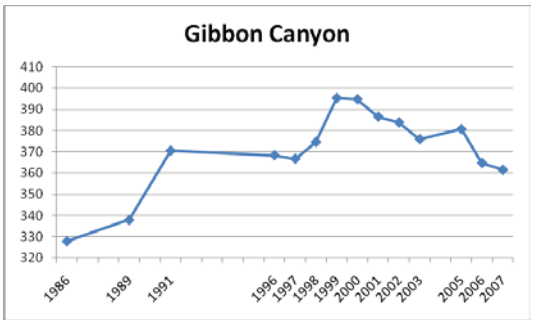
Gibbon Canyon
410
400
390
380
370
360
350
340
330
320
1986
1989
1991
1996
1997
1998
1999
2000
2001
2002
2003
2005
2006
2007

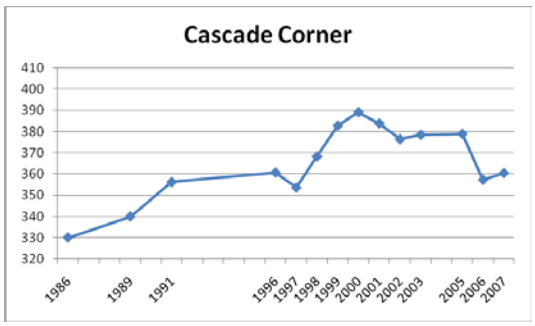
Cascade Corner
410
400
390
380
370
360
350
340
330
320
1986
1989
1991
1996
1997
1998
1999
2000
2001
2002
2003
2005
2006
2007

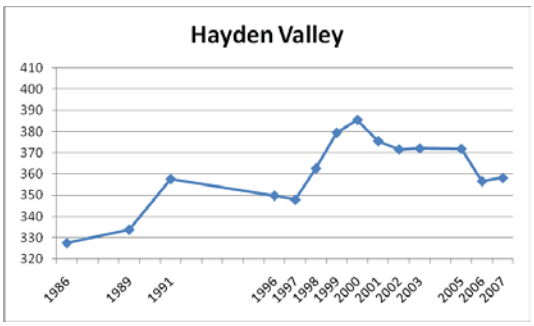
Hayden Valley
410
400
390
380
370
360
350
340
330
320
1986
1989
1991
1996
1997
1998
1999
2000
2001
2002
2003
2005
2006
2007

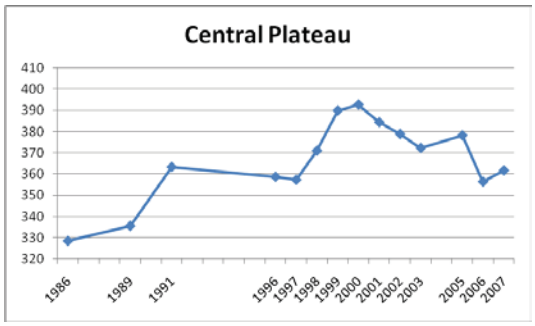
Central Plateau
410
400
390
380
370
360
350
340
330
320
1986
1989
1991
1996
1997
1998
1999
2000
2001
2002
2003
2005
2006
2007

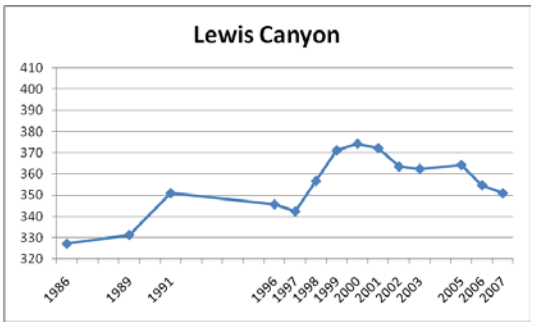
Lewis Canyon
410
400
390
380
370
360
350
340
330
320
1986
1989
1991
1996
1997
1998
1999
2000
2001
2002
2003
2005
2006
2007

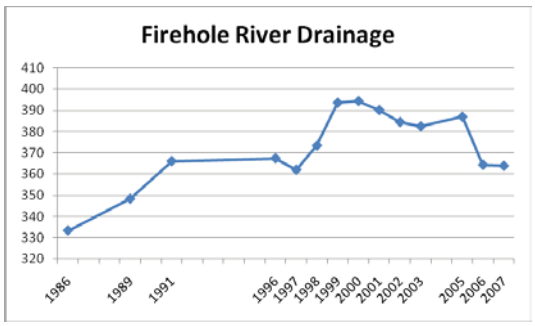
Firehole River Drainage
410
400
390
380
370
360
350
340
330
320
1986
1989
1991
1996
1997
1998
1999
2000
2001
2002
2003
2005
2006
2007

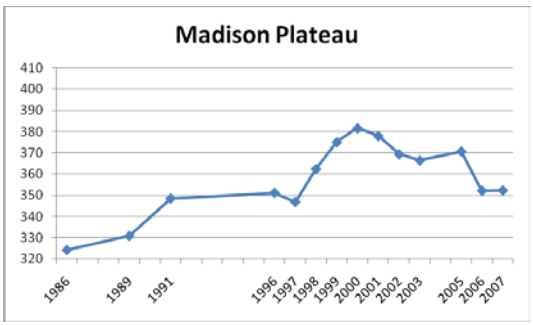
Madison Plateau
410
400
390
380
370
360
350
340
330
320
1986
1989
1991
1996
1997
1998
1999
2000
2001
2002
2003
2005
2006
2007

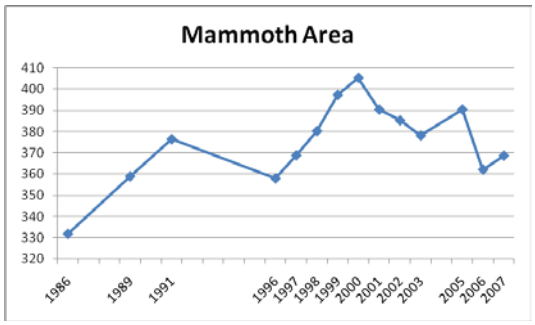
Mammoth Area
410
400
390
380
370
360
350
340
330
320
1986
1989
1991
1996
1997
1998
1999
2000
2001
2002
2003
2005
2006
2007

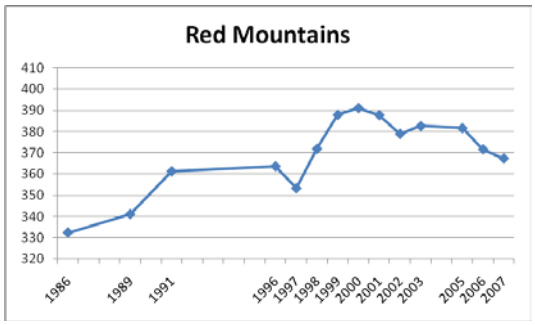
Red Mountains
410
400
390
380
370
360
350
340
330
320
1986
1989
1991
1996
1997
1998
1999
2000
2001
2002
2003
2005
2006
2007

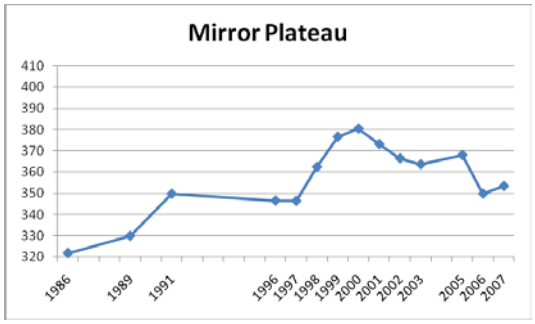
Mirror Plateau
410
400
390
380
370
360
350
340
330
320
1986
1989
1991
1996
1997
1998
1999
2000
2001
2002
2003
2005
2006
2007

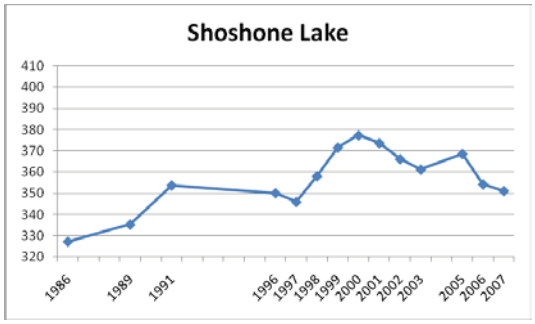
Shoshone Lake
410
400
390
380
370
360
350
340
330
320
1986
1989
1991
1996
1997
1998
1999
2000
2001
2002
2003
2005
2006
2007

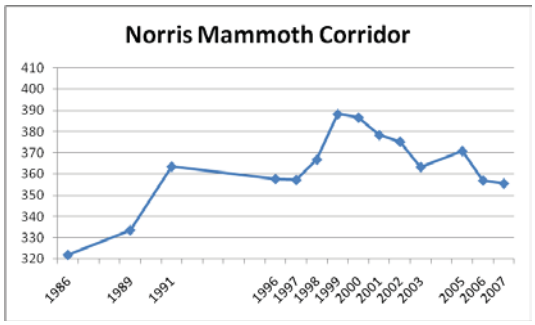
Norris Mammoth Corridor
410
400
390
380
370
360
350
340
330
320
1986
1989
1991
1996
1997
1998
1999
2000
2001
2002
2003
2005
2006
2007

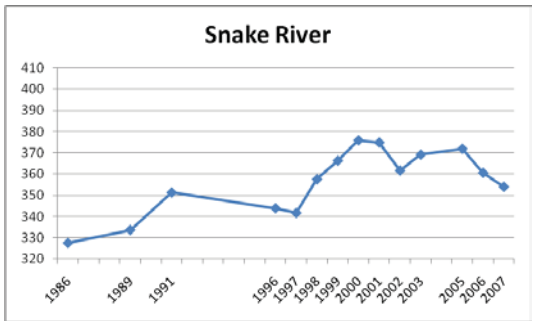
Snake River
410
400
390
380
370
360
350
340
330
320
1986
1989
1991
1996
1997
1998
1999
2000
2001
2002
2003
2005
2006
2007

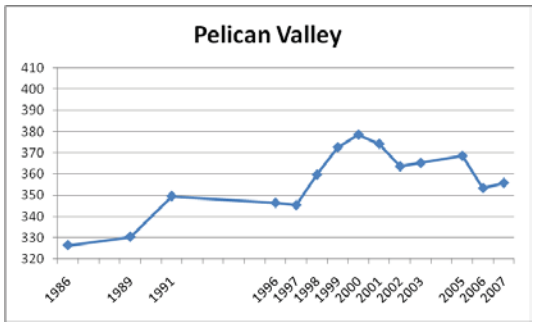
Pelican Valley
410
400
390
380
370
360
350
340
330
320
1986
1989
1991
1996
1997
1998
1999
2000
2001
2002
2003
2005
2006
2007

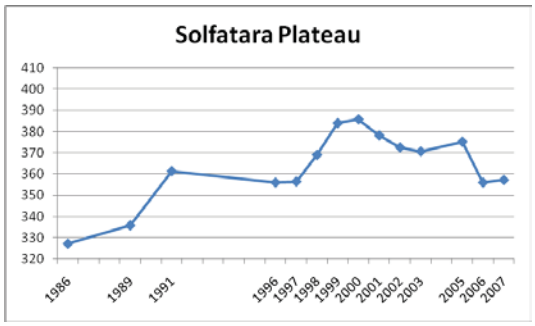
Solfatara Plateau
410
400
390
380
370
360
350
340
330
320
1986
1989
1991
1996
1997
1998
1999
2000
2001
2002
2003
2005
2006
2007

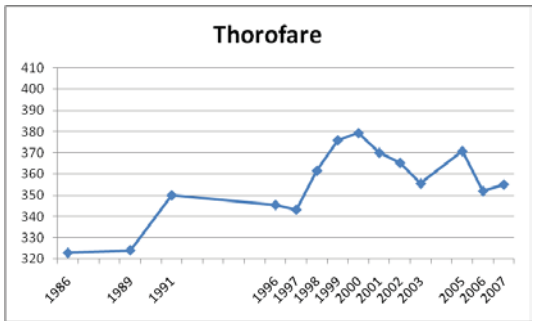
Thorofare
410
400
390
380
370
360
350
340
330
320
1986
1989
1991
1996
1997
1998
1999
2000
2001
2002
2003
2005
2006
2007

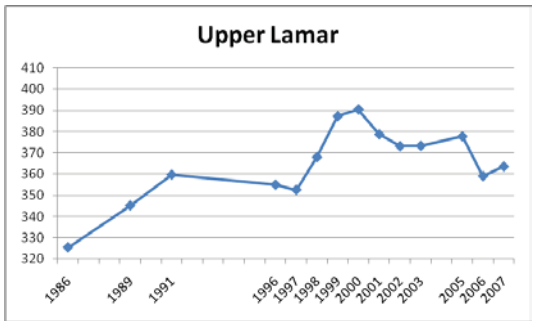
Upper Lamar
410
400
390
380
370
360
350
340
330
320
1986
1989
1991
1996
1997
1998
1999
2000
2001
2002
2003
2005
2006
2007

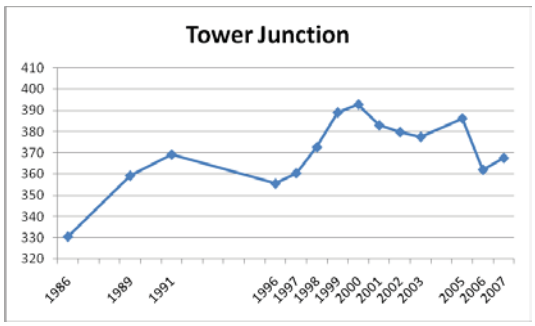
Tower Junction
410
400
390
380
370
360
350
340
330
320
1986
1989
1991
1996
1997
1998
1999
2000
2001
2002
2003
2005
2006
2007

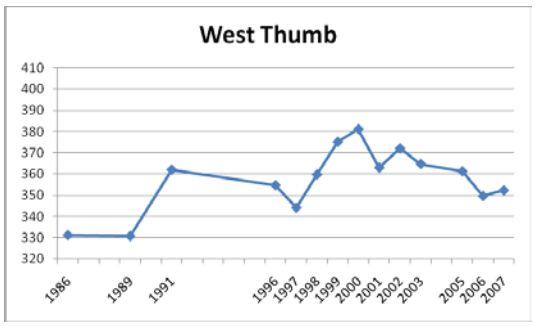
West Thumb
410
400
390
380
370
360
350
340
330
320
1986
1989
1991
1996
1997
1998
1999
2000
2001
2002
2003
2005
2006
2007

APPENDIX E

NORMALIZED M_{terr} TRAJECTORY GRAPHS FOR 24 TEMPORAL CLUSTERS
(Y-axis is difference from the date mean in Wm^{-2})

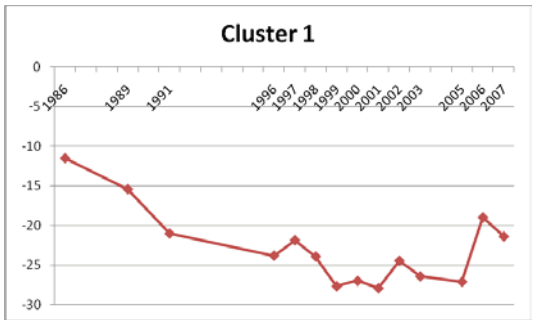
Cluster 1
0
-5
-10
-15
-20
-25
-30
1986
1989
1991
1996
1997
1998
1999
2000
2001
2002
2003
2005
2006
2007

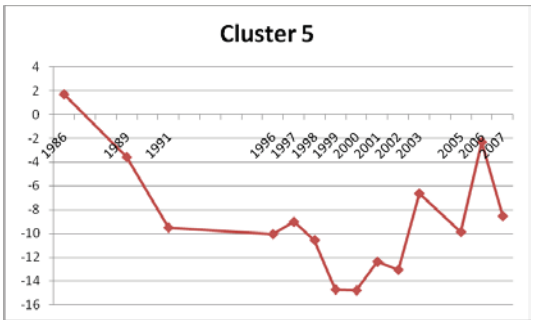
Cluster 5
4
2
0
-2
-4
-6
-8
-10
-12
-14
-16
1986
1989
1991
1996
1997
1998
1999
2000
2001
2002
2003
2005
2006
2007

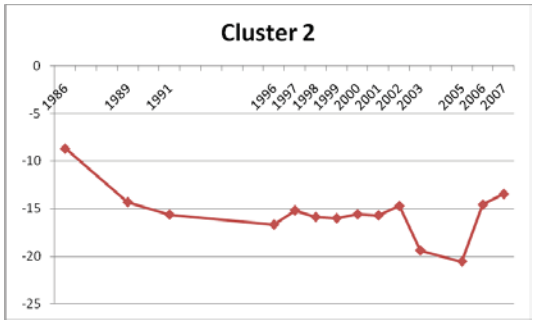
Cluster 2
0
-5
-10
-15
-20
-25
1986
1989
1991
1996
1997
1998
1999
2000
2001
2002
2003
2005
2006
2007

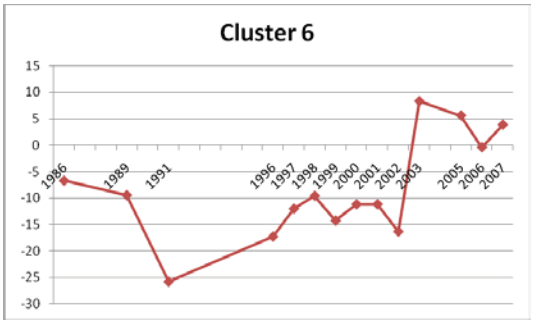
Cluster 6
15
10
5
0
-5
-10
-15
-20
-25
-30
1986
1989
1991
1996
1997
1998
1999
2000
2001
2002
2003
2005
2006
2007

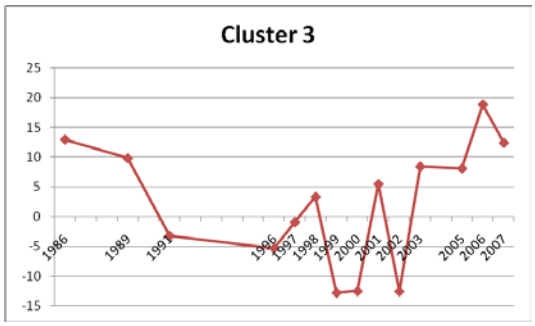
Cluster 3
25
20
15
10
5
0
-5
-10
-15
1986
1989
1991
1996
1997
1998
1999
2000
2001
2002
2003
2005
2006
2007

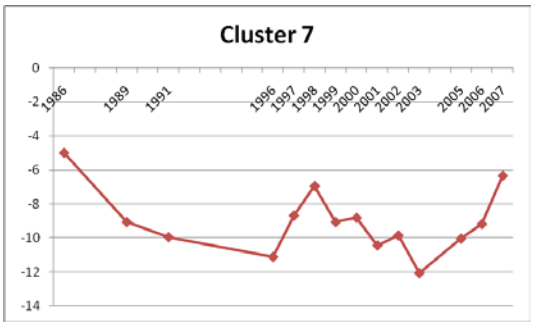
Cluster 7
0
-2
-4
-6
-8
-10
-12
-14
1986
1989
1991
1996
1997
1998
1999
2000
2001
2002
2003
2005
2006
2007

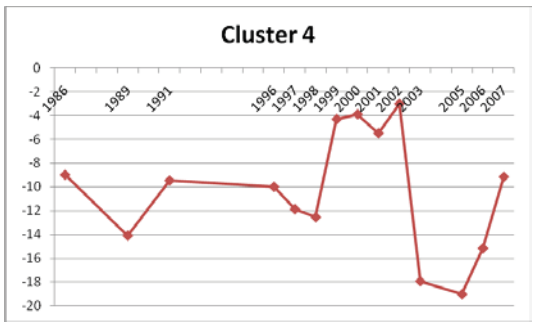
Cluster 4
0
-2
-4
-6
-8
-10
-12
-14
-16
-18
-20
1986
1989
1991
1996
1997
1998
1999
2000
2001
2002
2003
2005
2006
2007

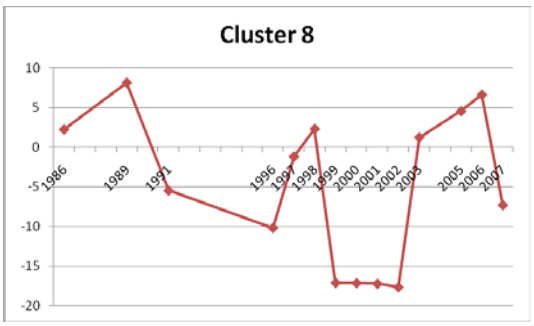
Cluster 8
10
5
0
-5
-10
-15
-20
1986
1989
1991
1996
1997
1998
1999
2000
2001
2002
2003
2005
2006
2007

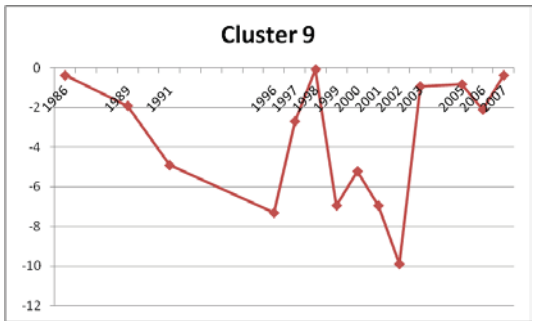
Cluster 9
0
-2
-4
-6
-8
-10
-12
1986
1989
1991
1996
1997
1998
1999
2000
2001
2002
2003
2005
2006
2007

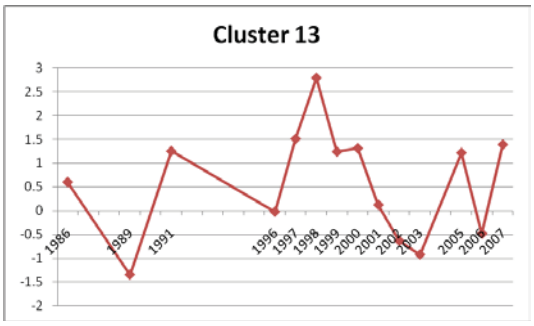
Cluster 13
3
2.5
2
1.5
1
0.5
0
-0.5
-1
-1.5
-2
1986
1989
1991
1996
1997
1998
1999
2000
2001
2002
2003
2005
2006
2007

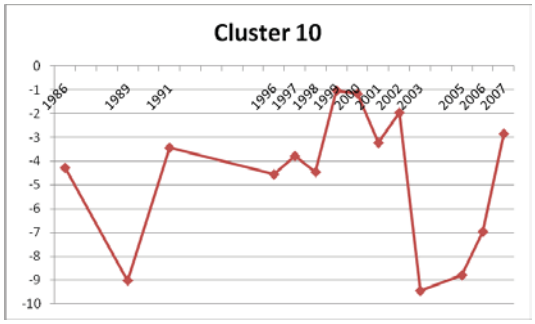
Cluster 10
0
-1
-2
-3
-4
-5
-6
-7
-8
-9
-10
1986
1989
1991
1996
1997
1998
1999
2000
2001
2002
2003
2005
2006
2007

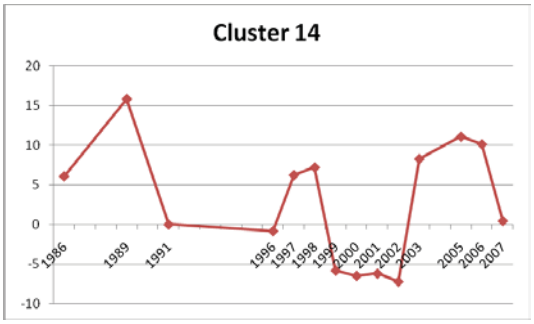
Cluster 14
20
15
10
5
0
-5
-10
1986
1989
1991
1996
1997
1998
1999
2000
2001
2002
2003
2005
2006
2007

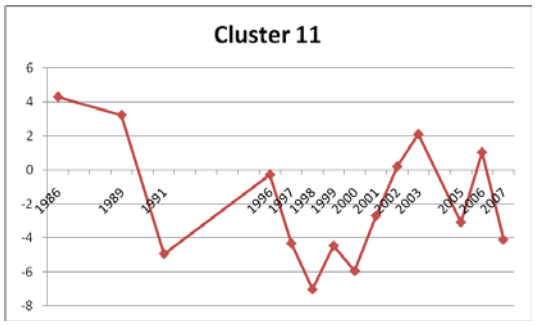
Cluster 11
6
4
2
0
-2
-4
-6
-8
1986
1989
1991
1996
1997
1998
1999
2000
2001
2002
2003
2005
2006
2007

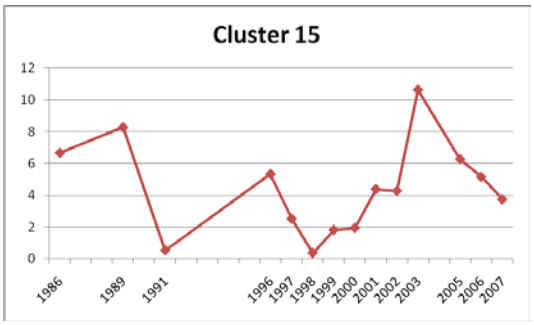
Cluster 15
12
10
8
6
4
2
0
1986
1989
1991
1996
1997
1998
1999
2000
2001
2002
2003
2005
2006
2007

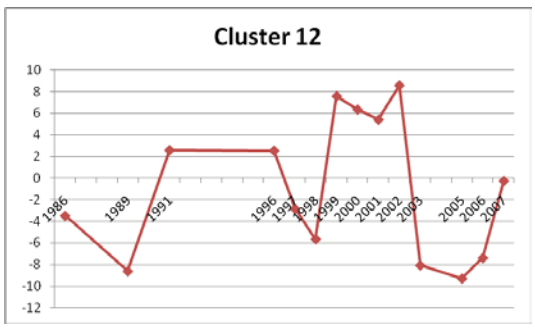
Cluster 12
10
8
6
4
2
0
-2
-4
-6
-8
-10
-12
1986
1989
1991
1996
1998
1999
2000
2001
2002
2003
2005
2006
2007

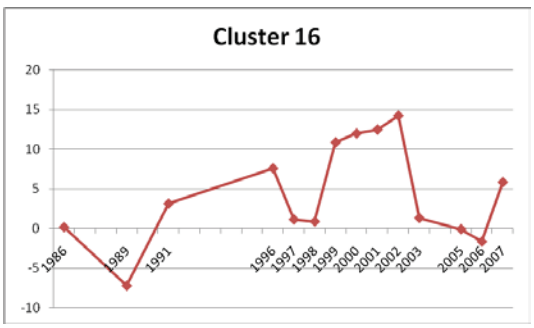
Cluster 16
20
15
10
5
0
-5
-10
1986
1989
1991
1996
1997
1998
1999
2000
2001
2002
2003
2005
2006
2007

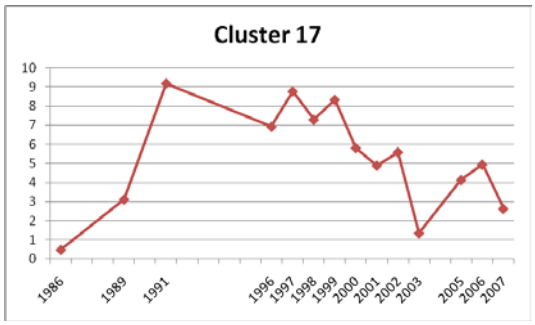
Cluster 17
10
9
8
7
6
5
4
3
2
1
0
1986
1989
1991
1996
1997
1998
1999
2000
2001
2002
2003
2005
2006
2007

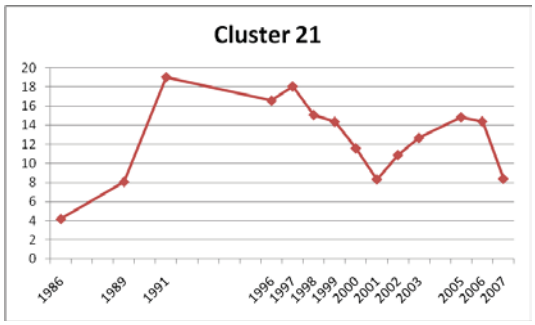
Cluster 21
20
18
16
14
12
10
8
6
4
2
0
1986
1989
1991
1996
1997
1998
1999
2000
2001
2002
2003
2005
2006
2007

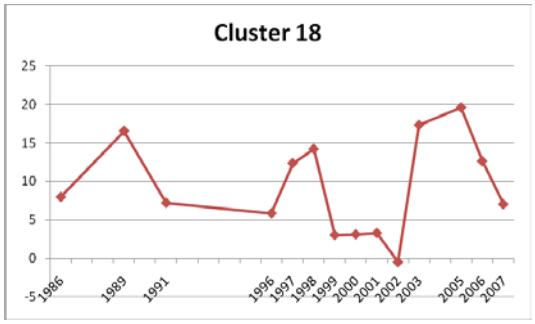
Cluster 18
25
20
15
10
5
0
-5
1986
1989
1991
1996
1997
1998
1999
2000
2001
2002
2003
2005
2006
2007

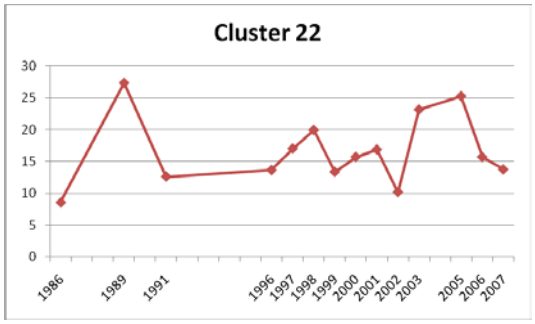
Cluster 22
30
25
20
15
10
5
0
1986
1989
1991
1996
1997
1998
1999
2000
2001
2002
2003
2005
2006
2007

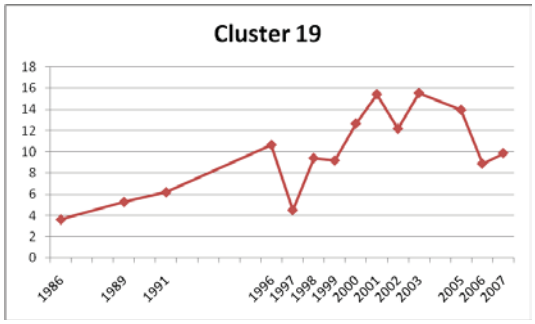
Cluster 19
18
16
14
12
10
8
6
4
2
0
1986
1989
1991
1996
1997
1998
1999
2000
2001
2002
2003
2005
2006
2007

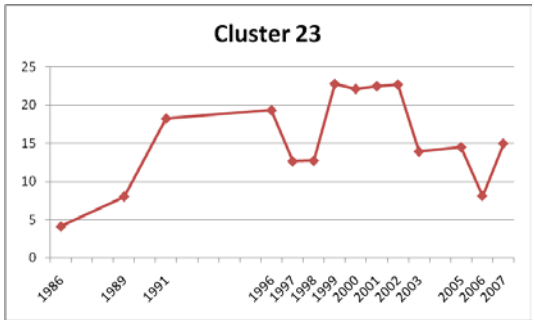
Cluster 23
25
20
15
10
5
0
1986
1989
1991
1996
1997
1998
1999
2000
2001
2002
2003
2005
2006
2007

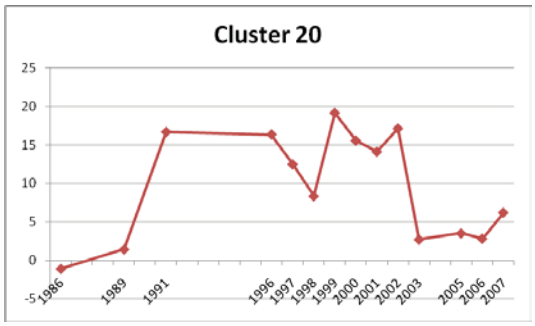
Cluster 20
25
20
15
10
5
0
-5
1986
1989
1991
1996
1997
1998
1999
2000
2001
2002
2003
2005
2006
2007

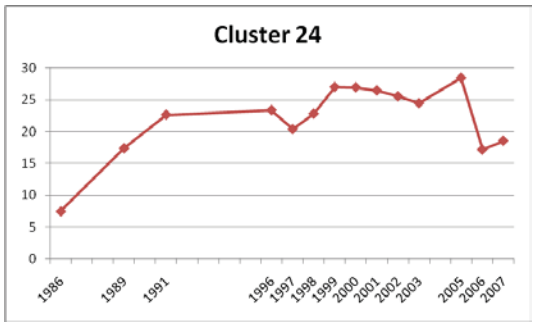
Cluster 24
30
25
20
15
10
5
0
1986
1989
1991
1996
1997
1998
1999
2000
2001
2002
2003
2005
2006
2007

APPENDIX F

NORMALIZED M_{terr} TRAJECTORY GRAPHS FOR 20 SPATIAL GROUPINGS
(Y-axis is difference from the date mean in Wm^{-2})

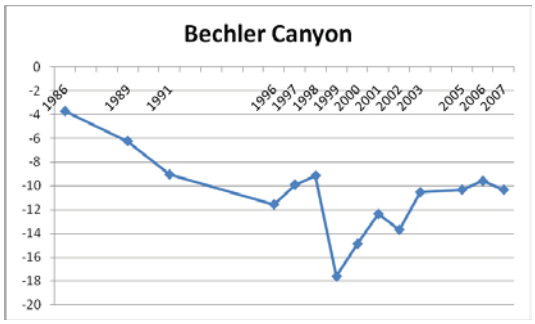
Bechler Canyon
0
-2
-4
-6
-8
-10
-12
-14
-16
-18
-20
1986
1989
1991
1996
1997
1998
1999
2000
2001
2002
2003
2005
2006
2007

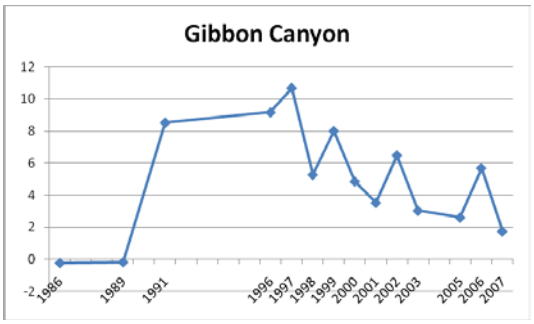
Gibbon Canyon
12
10
8
6
4
2
0
-2
1986
1989
1991
1996
1997
1998
1999
2000
2001
2002
2003
2005
2006
2007

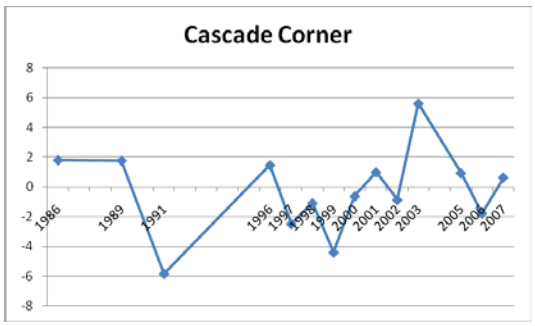
Cascade Corner
8
6
4
2
0
-2
-4
-6
-8
1986
1989
1991
1996
1997
1998
1999
2000
2001
2002
2003
2005
2006
2007

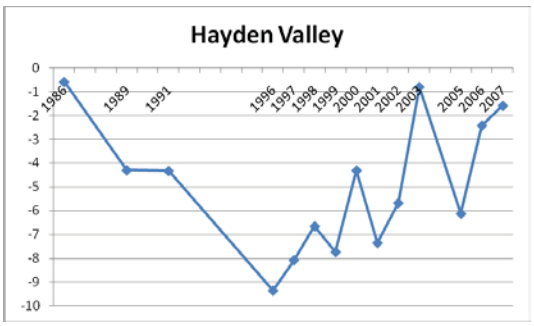
Hayden Valley
0
-1
-2
-3
-4
-5
-6
-7
-8
-9
-10
1986
1989
1991
1996
1997
1998
1999
2000
2001
2002
2003
2005
2006
2007

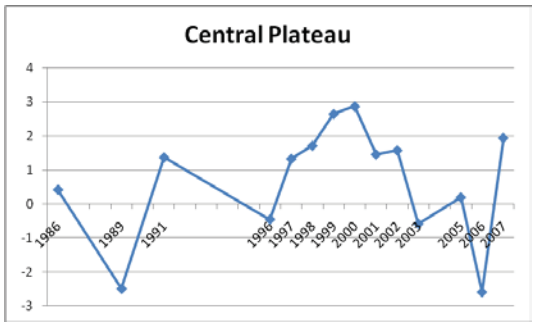
Central Plateau
4
3
2
1
0
-1
-2
-3
1986
1989
1991
1996
1997
1998
1999
2000
2001
2002
2003
2005
2006
2007

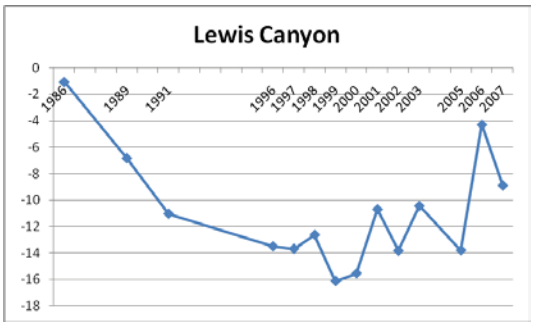
Lewis Canyon
0
-2
-4
-6
-8
-10
-12
-14
-16
-18
1986
1989
1991
1996
1997
1998
1999
2000
2001
2002
2003
2005
2006
2007

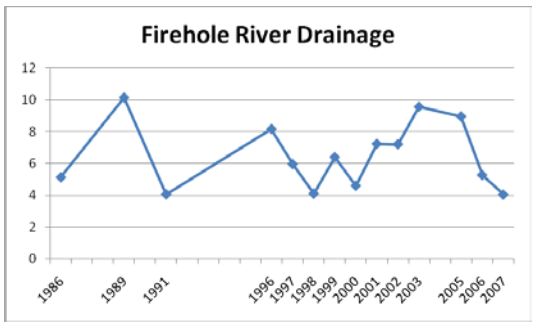
Firehole River Drainage
12
10
8
6
4
2
0
1986
1989
1991
1996
1997
1998
1999
2000
2001
2002
2003
2005
2006
2007

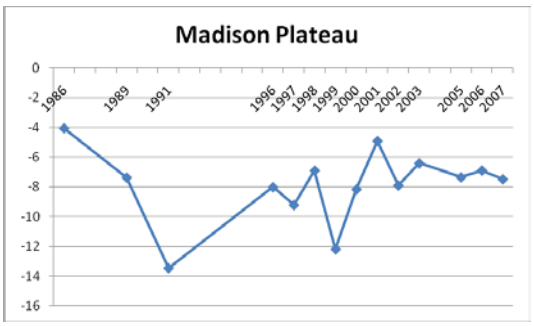
Madison Plateau
0
-2
-4
-6
-8
-10
-12
-14
-16
1986
1989
1991
1996
1997
1998
1999
2000
2001
2002
2003
2005
2006
2007

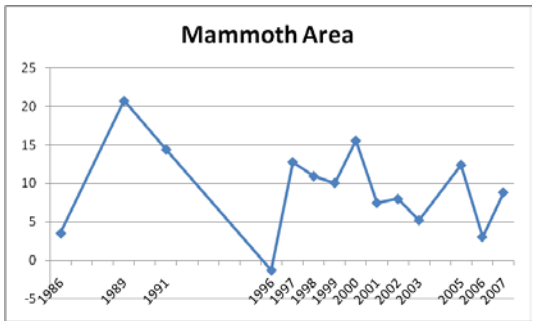
Mammoth Area
25
20
15
10
5
0
-5
1986
1989
1991
1996
1997
1998
1999
2000
2001
2002
2003
2005
2006
2007

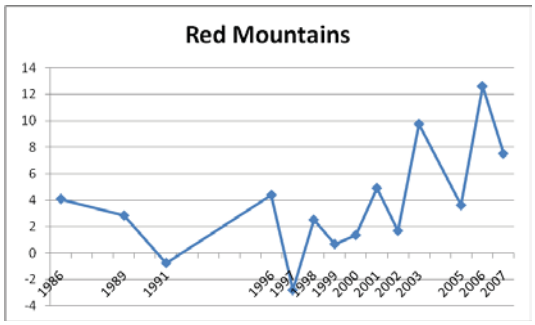
Red Mountains
14
12
10
8
6
4
2
0
-2
-4
1986
1989
1991
1996
1997
1998
1999
2000
2001
2002
2003
2005
2006
2007

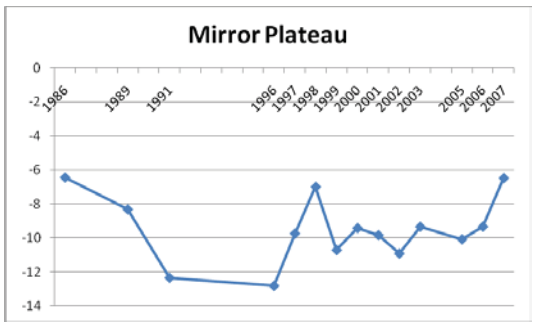
Mirror Plateau
0
-2
-4
-6
-8
-10
-12
-14
1986
1989
1991
1996
1997
1998
1999
2000
2001
2002
2003
2005
2006
2007

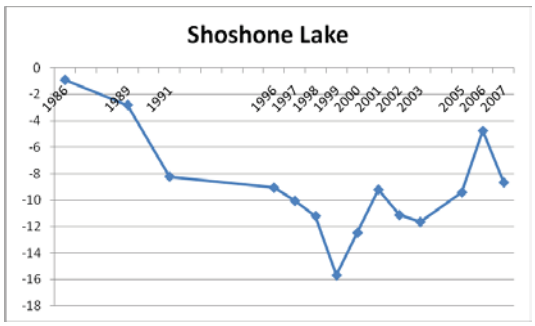
Shoshone Lake
0
-2
-4
-6
-8
-10
-12
-14
-16
-18
1986
1989
1991
1996
1997
1998
1999
2000
2001
2002
2003
2005
2006
2007

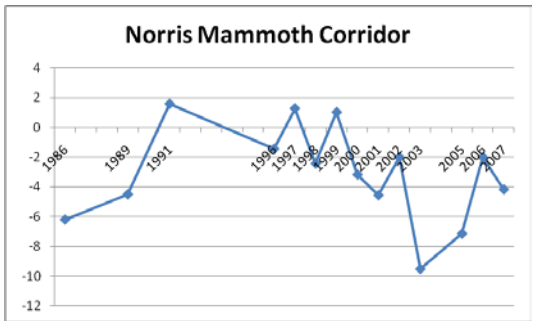
Norris Mammoth Corridor
4
2
0
-2
-4
-6
-8
-10
-12
1986
1989
1991
1996
1997
1998
1999
2000
2001
2002
2003
2005
2006
2007

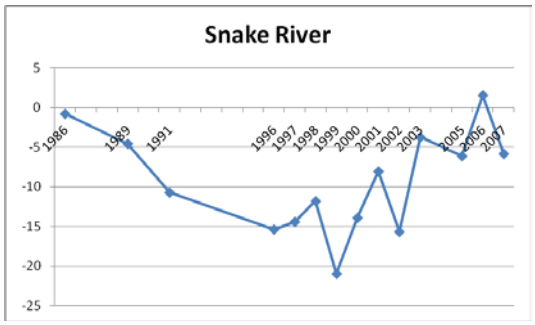
Snake River
5
0
-5
-10
-15
-20
-25
1986
1989
1991
1996
1997
1998
1999
2000
2001
2002
2003
2005
2006
2007

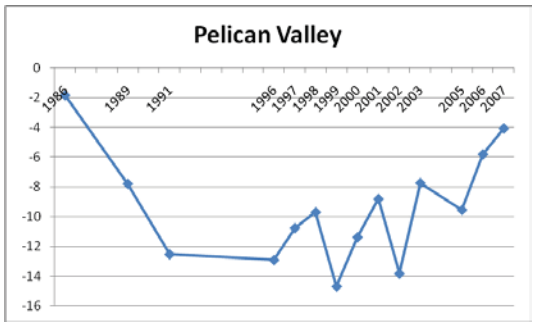
Pelican Valley
0
-2
-4
-6
-8
-10
-12
-14
-16
1986
1989
1991
1996
1997
1998
1999
2000
2001
2002
2003
2005
2006
2007

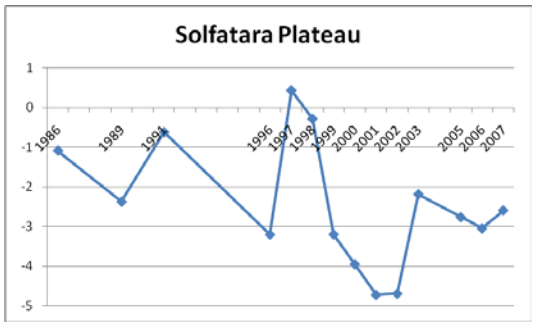
Solfatara Plateau
1
0
-1
-2
-3
-4
-5
1986
1989
1994
1996
1997
1998
1999
2000
2001
2002
2003
2005
2006
2007

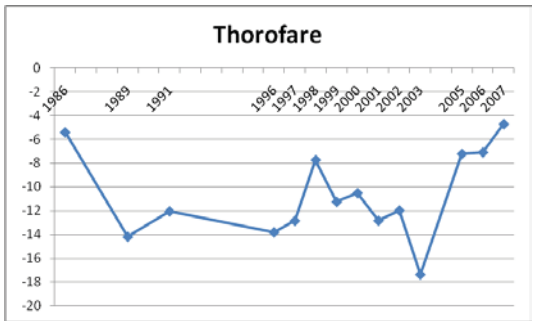
Thorofare
0
-2
-4
-6
-8
-10
-12
-14
-16
-18
-20
1986
1989
1991
1996
1997
1998
1999
2000
2001
2002
2003
2005
2006
2007

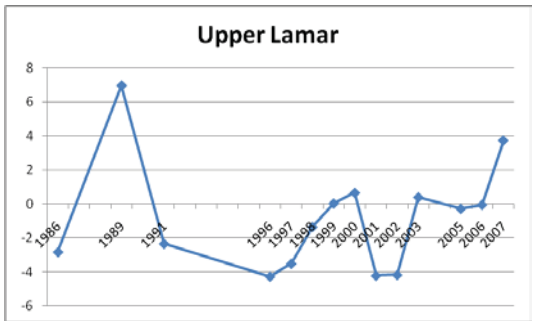
Upper Lamar
8
6
4
2
0
-2
-4
-6
1986
1989
1991
1996
1997
1998
1999
2000
2001
2002
2003
2005
2006
2007

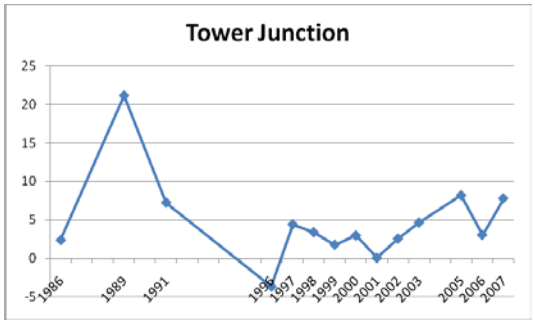
Tower Junction
25
20
15
10
5
0
-5
1986
1989
1991
1996
1997
1998
1999
2000
2001
2002
2003
2005
2006
2007

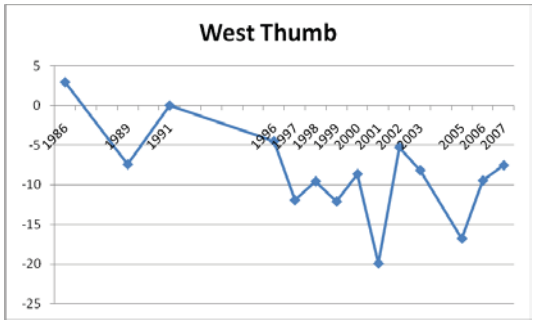
West Thumb
5
0
-5
-10
-15
-20
-25
1986
1989
1991
1996
1997
1998
1999
2000
2001
2002
2003
2005
2006
2007

APPENDIX G

CALCULATED DISTANCES FROM GEOLOGIC FAULTS, LARGE WATER BODIES, AND EARTHQUAKE SWARMS

Table G.1.a: Distance to geologic faults in meters, by temporal cluster (**maximum mean bolded**, *minimum mean italicized*)

Cluster	Maximum	Minimum	Mean	Median	Mode	Standard deviation
1	5,400	0	2,314	1,560	0	2,269
2	10,680	0	1,840	600	120	2,614
3	13,440	0	2,121	600	120	2,679
4	9,960	0	1,944	720	120	2,833
5	13,800	0	2,733	1,080	120	2,890
6	**11,880**	**0**	**772**	**360**	**120**	**1,170**
7	13,680	0	1,854	480	120	2,652
8	10,200	120	2,472	2,280	120	2,410
9	7,800	0	3,234	2,040	120	3,402
10	12,120	0	2,532	1,080	120	3,082
11	*13,920*	*0*	*4,965*	*4,920*	*4,560*	*2,764*
12	14,040	0	3,111	1,440	120	3,319
13	14,160	0	3,307	2,040	120	3,222
14	14,040	0	3,250	2,760	120	2,723
15	13,560	0	4,302	4,560	4,920	2,530
16	10,440	0	4,275	3,600	120	3,644
17	12,240	0	2,112	1,080	480	2,419
18	14,760	0	3,616	3,240	720	2,901
19	14,640	0	4,878	4,680	120	3,448
20	13,440	0	2,278	1,320	1,320	2,376
21	14,640	0	1,937	1,080	960	2,119
22	14,760	0	4,523	4,320	4,920	3,657
23	14,880	0	4,070	2,880	1,080	3,707
24	13,920	0	4,337	3,480	1,080	4,083

Table G.1.b: Distance to geologic faults in meters, by spatial grouping (**maximum mean bolded**, *minimum mean italicized*)

Group	Minimum	Maximum	Mean	Median	Mode	Standard deviation
Bechler Canyon	3,360	5,640	4,264	3,960	3,720	685
Cascade Corner	**4,800**	**14,880**	**11,845**	**13,080**	**13,680**	**3,141**
Central Plateau	4,680	10,680	8,057	7,920	6,840	1,402
Firehole River Drainage	0	7,800	3,864	4,440	5,040	1,902
Gibbon Canyon	0	2,520	838	840	1,080	474
Hayden Valley	0	4,440	1,594	840	120	1,586
Lewis Canyon	0	5,640	814	480	120	1,242
Madison Plateau	4,920	12,960	8,515	8,640	7,080	2,125
Mammoth Area	0	2,160	784	840	960	409
Mirror Plateau	0	3,720	878	480	120	864
Norris Mammoth Corridor	0	2,160	761	720	480	510
Pelican Valley	120	6,000	2,213	2,040	2,520	1,482
Red Mountains	*0*	*1,080*	*309*	*240*	*120*	*267*
Shoshone Lake	3,000	6,000	5,068	5,280	5,400	675
Snake River	0	960	330	240	120	271
Solfatara Plateau	0	4,200	2,147	2,520	120	1,325
Thorofare	0	2,760	467	120	120	704
Tower Junction	480	960	695	720	720	150
Upper Lamar	0	7,320	3,149	4,080	120	2,840
West Thumb	6,000	7,800	7,010	7,080	7,560	574

Table G.2.a: Distance to large water bodies in meters, by temporal cluster (**maximum mean bolded**, *minimum mean italicized*)

Cluster	Maximum	Minimum	Mean	Median	Mode	Standard deviation
1	5,880	0	1,379	600	0	1,537
2	6,240	0	2,139	1,920	120	1,568
3	6,360	0	1,980	1,920	0	1,787
4	5,520	0	1,734	1,560	120	1,240
5	5,760	0	1,517	1,080	120	1,481
6	**5,160**	**0**	**3,125**	**4,560**	**0**	**2,156**
7	6,000	0	1,900	1,680	1,920	1,359
8	5,760	0	1,167	600	0	1,489
9	6,000	0	1,859	1,680	1,920	1,446
10	5,880	0	1,564	1,440	1,440	1,063
11	5,280	0	1,314	1,320	1,680	943
12	4,560	0	1,457	1,440	1,320	927
13	5,280	0	1,471	1,440	1,320	934
14	4,080	0	1,179	960	0	1,108
15	*5,040*	*0*	*1,046*	*1,080*	*0*	*930*
16	5,880	0	1,507	1,560	1,560	1,032
17	4,200	0	1,248	1,200	480	850
18	4,920	0	1,198	1,080	120	1,110
19	6,120	0	1,510	1,440	1,560	1,134
20	3,600	120	1,326	1,200	1,080	782
21	3,360	0	1,373	1,320	1,560	708
22	5,760	0	1,350	1,200	120	1,188
23	5,760	0	1,363	1,200	1,080	994
24	5,880	0	1,577	1,440	240	1,153

Table G.2.b: Distance to large water bodies in meters, by spatial grouping (**maximum mean bolded**, *minimum mean italicized*)

Group	Minimum	Maximum	Mean	Median	Mode	Standard deviation
Bechler Canyon	**4,080**	**6,480**	**5,458**	**5,640**	**6,000**	**573**
Cascade Corner	0	4,920	2,843	3,600	4,080	1,522
Central Plateau	240	4,680	1,932	1,920	2,160	782
Firehole River Drainage	0	3,000	993	960	120	679
Gibbon Canyon	0	3,960	1,271	1,080	1,080	927
Hayden Valley	0	1,800	554	360	120	558
Lewis Canyon	840	6,120	2,294	2,040	1,560	1,103
Madison Plateau	600	6,000	2,947	2,520	1,320	1,677
Mammoth Area	0	4,320	2,447	2,400	1,560	1,157
Mirror Plateau	0	5,400	2,276	2,160	2,040	1,224
Norris Mammoth Corridor	0	2,400	896	840	720	563
Pelican Valley	0	2,520	670	480	0	660
Red Mountains	0	3,240	1,750	1,920	2,640	877
Shoshone Lake	0	840	235	120	0	252
Snake River	*0*	*360*	*78*	*0*	*0*	*0*
Solfatara Plateau	0	3,360	940	360	120	1,076
Thorofare	0	2,880	1,543	1,560	1,560	694
Tower Junction	0	240	81	120	0	87
Upper Lamar	0	4,920	1,910	1,920	0	1,749
West Thumb	0	600	137	120	0	161

Table G.3.a: Distance to earthquake swarms in meters, by temporal cluster (**maximum mean bolded**, *minimum mean italicized*)

Cluster	Maximum	Minimum	Mean	Median	Mode	Standard deviation
1	33,000	480	9,917	10,134	10,388	5,226
2	19,200	480	9,400	9,000	4,440	5,646
3	32,400	240	9,929	9,536	3,255	6,211
4	19,320	480	9,578	9,000	17,280	5,368
5	30,480	240	6,524	5,280	5,040	5,120
6	**18,960**	**120**	**12,506**	**14,400**	**14,520**	**5,565**
7	32,760	480	10,857	11,450	16,872	6,403
8	22,680	720	7,789	6,840	6,840	4,672
9	32,520	240	8,953	6,923	5,158	6,332
10	32,760	480	7,664	4,521	2,756	6,213
11	28,680	480	4,783	4,200	3,960	4,078
12	28,560	360	6,007	4,560	2,760	4,626
13	32,520	960	7,224	4,905	5,398	6,633
14	30,720	120	7,190	4,800	3,360	6,245
15	30,600	240	5,041	4,200	4,200	3,639
16	28,800	240	6,434	4,800	2,640	4,755
17	30,600	480	5,143	3,360	3,360	5,092
18	30,600	0	6,865	4,920	4,560	5,495
19	28,800	120	6,221	4,920	3,720	4,125
20	16,440	840	3,698	3,000	3,000	2,363
21	*16,080*	*1,080*	*3,654*	*3,120*	*3,000*	*2,148*
22	30,840	1,320	7,423	4,920	4,800	5,402
23	26,040	1,320	5,427	4,320	2,880	3,868
24	25,920	1,320	6,514	4,800	4,800	4,704

Table G.3.b: Distance to earthquake swarms in meters, by spatial grouping (**maximum mean bolded**, *minimum mean italicized*)

Group	Minimum	Maximum	Mean	Median	Mode	Standard deviation
Bechler Canyon	7,440	9,840	8,734	8,880	9,600	802
Cascade Corner	14,640	19,680	16,409	16,200	15,120	1,236
Central Plateau	360	9,120	4,475	4,320	4,200	2,143
Firehole River Drainage	720	8,280	4,474	4,440	4,320	1,476
Gibbon Canyon	480	5,760	2,965	3,000	3,000	1,193
Hayden Valley	*0*	*3,480*	*1,412*	*1,440*	*1,680*	*782*
Lewis Canyon	2,520	6,360	4,958	5,040	4,800	852
Madison Plateau	1,920	6,240	4,331	4,680	4,800	1,167
Mammoth Area	15,000	24,480	16,791	16,320	15,960	2,190
Mirror Plateau	1,920	23,160	12,470	13,200	15,720	4,064
Norris Mammoth Corridor	840	10,680	2,894	2,640	3,000	1,268
Pelican Valley	8,040	19,800	12,339	12,240	12,840	3,108
Red Mountains	3,360	9,360	5,086	4,440	3,840	1,477
Shoshone Lake	5,280	8,880	6,140	5,880	6,000	899
Snake River	840	5,640	2,130	1,320	1,080	1,678
Solfatara Plateau	6,720	12,120	9,517	9,960	10,800	1,580
Thorofare	15,000	18,360	17,071	17,160	17,640	722
Tower Junction	25,200	26,160	25,691	25,680	25,320	333
Upper Lamar	**28,080**	**33,000**	**30,233**	**30,360**	**28,800**	**1,618**
West Thumb	1,560	4,080	2,815	2,520	2,040	796